School of Molecular and Life Sciences

Faculty of Science and Engineering

Electrochemical Detection and Characterization at Liquid/Liquid micro-Interfaces

Gazi Jahirul Islam

This thesis is presented for the degree of
Doctor of Philosophy
of
Curtin University

July 2021

Declaration

To the best of my knowledge and belief, this thesis contains no material previously published by any other person except where due acknowledgement has been made.

This thesis contains no material which has been accepted for the award of any other degree or diploma in any university or institution for higher education.

Gazi Jahirul Islam
PhD Candidate
[26 July 2021]

Table of Contents

I dedicate this work,

To my parents for their unconditional love and support in every stage of my life.

To my loving wife, who makes us happy with her love, care, share, and for her much patience.

To our sons, Gazi Zareef Abdullah and Gazi Jawaad Abdullah, who are the gift and blessings for us from the Almighty Allah.

Acknowledgement

Primarily, all praises and thanks to the Almighty Allah, for his showers of blessings, mercy on me throughout my research journey to complete it successfully.

The arrival of the finishing line of PhD could not have been possible without the assistance and participation of so many people around whose names not all may be specified. Their kind contributions are sincerely appreciated and gratefully acknowledged.

Foremost, I would like to convey my sincerest gratitude to my supervisor Professor Damien Arrigan, for choosing me to join and work in the Electrochemistry and Sensors group at Curtin University. He supported me a lot to cope up in Perth with my family at the very beginning of my study when all was much unknown to me. His constant guidance, assistance, supervision, encouragement, and motivation helped me in all the time throughout my PhD study and research. It would not have been possible to finish my PhD journey without his generosity and patience throughout the duration of my study. He has played the most important part in understanding the electrochemistry and preparing myself as an expert in the field of liquid-liquid electrochemistry gradually. I am fortunate enough to have him as my supervisor and it has been a pleasure to work with Damien and I wish, I could be a great mentor like Damien in future.

I would also like to thank A/Professor Debbie Silvester-Dean, my co-supervisor, for her suggestions, and expert opinions in my work as well as her dedication to research inspires me always. Her insightful comments during my milestones always aided me to think and do further beyond once again.

Then I would extend my gratitude to my thesis committee chair, Dr. Franca Jones, for her support and expert opinions in my research.

Next up a big thanks to entire Electrochmeistry and Sensors Research group for creating an enjoyable place to work in Curtin and supporting directly and indirectly to successfully accomplish my study: Dr. Bren Mark Felisilda for a good discussion about research problems and also personal life during group meeting, coffee break and lunch time. Later, during his post-doctoral period supported me in the ways especially

of the electrochemistry discussion. Dr. Terence Henares for sharing ideas and experiences and be a part one of my thesis work especially sulphate experiments. Dr. Peter Connolly for his thoughtful ideas and discussions. Nasib Kalaei, for showing me the lab induction and research discussion, sharing knowledge in electrochemistry and thesis preparation. Ben Austen, for helping in pipette preparation, SEM experiment, sharing ideas and knowledge about electrochemistry. Hum Lamichhane, for sharing his experience and knowledge. Nazanin Ghaheritabrizi, for discussing electrochemistry in-group meeting and coffee break. Thanks to other Electrochemistry and Sensors group members Dr. Juni, Dr. Ghulam, Simon, Cathy, Fatma, Xinyu, Saghraf for our shared experiences and other happy moments in lab and outside. I would like to thank Manaswini Natarajan for froviding me some PFAS sample, which helped me much.

I am also grateful to Professor Katrina Jolliffe, University of Sydney, for providing us the sulphate ionophores synthesized in her lab, for our sulphate electrochemical research.

I also want to give thanks to all the persons to whom I have worked with outside of our group; my fellow HDR students, all the Honours and project students, the technical staff, all the teaching staff for providing me all the support and necessary things that I have needed to carry out my PhD.

I am grateful to Australian Government and Curtin University for funding (RTP scholarship) to carry out my PhD research. I am also grateful to University of Barisal for approved my study leave and as well as for financial support.

My gratitude also goes to the other colleagues and friends who had made the whole journey memorable by sharing beautiful words, smiling at me from the first day to end of my study, I will definitely remember them.

My gratitude is also for my respected parents, who always pray for me and keep on asking “How is going your study?” They always motivate and encourage me from the far away over the phone since the last few years. Thanks to my siblings (brother and sister) and parents in law for their love and prayers.

I finally, wish to thank my loving wife Shaheda, who is also my colleague as well. I and enough fortunate to get her in my life as a wife and as a researcher in the same lab

under same supervisor. Her continuous support, care and love has strengthen me endeavour my goal. She always motivated to work hard and braced me at every single difficulties in my life. Her continuous motivation helped me a lot to achieve my experimental results at Curtin especially during the critical thesis writing time. She has been taking care of my lovely two sons Gazi Zareef Abdullah and Gazi Jawaad Abdullah. We are on this journey together and I could never be able to finish my PhD study without her endless support. Last but least, special thanks to my elder son Zareef for being such great child throughout this journey. This accomplishment would never been come to happen without them.

Abstract

Electrochemistry at the micro-interface between two immiscible electrolyte solutions (ITIES) has become an important and powerful platform for the detection of a wide variety of organic and inorganic species, because this miniaturization of the liquid/liquid interface improves the sensing capabilities by increasing the rate of mass transport and by reducing the cell resistance. Recently, single μITIES, like a liquid/liquid interface formed at the tip of a micropipette, emerged as a sensitive electrochemical platform not only for the detection of molecules but also for the more accurate study of thermodynamic parameters and kinetics of reactions at the ITIES. This thesis focused on the electrochemical investigation of different types of chemical species at the μITIES formed at the tips of glass micropipettes by applying cyclic voltammetry (CV) and differential pulse voltammetry (DPV).

For this purpose, the first step was to prepare reproducible pipettes. Different sizes of pipettes have been prepared from borosilicate or quartz capillaries by using a P-2000 CO_2 laser-based pipette puller, which has five parameters, namely heat (H), filament (F), velocity (V), delay (D) and pull (P). After preparation of the pipettes, their inner side was silanized by a very simple process to convert it from hydrophilic to hydrophobic to help formation of a stable ITIES at the tip of the pipettes. The electrochemical experiments show the new silanization method works very well by producing reproducible results in a stable ITIES. The reproducibility of the pipettes was examined by electrochemical methods using tetrapropylammonium ion ($TPrA^+$) transfer and by the scanning electron microscopy (SEM). Five different sizes of pipettes were produced by five different pulling programs at different times. Among this, two different size micro-pipettes were examined by both electrochemical and SEM experiments. The other three sets of nano-pipettes were examined by SEM. The average diameter for the first type (pulling parameters H: 400; F: 4; V: 20; D: 200 and P: 70) of eight micro-pipettes measured by electrochemical analysis was 2.81 (± 0.35) μm with 12.3% relative standard deviation (RSD), while the average diameter of 10 micro-pipettes with same pulling parameters measured by SEM was 2.95 (± 0.25) μm with 8.3% RSD. The average diameter of the second type of micro-pipettes with pulling parameters H: 550; F: 2; V: 30; D: 130 and P: 75 measured by electrochemistry and SEM were 2.94 (± 0.25) μm and 2.65 (± 0.21) μm, with RSD 8.6% and 7.8%,

respectively. On the other hand, three different sizes of nanopipettes were examined by SEM, where the average tip diameters were 447.3 (± 32.5) nm, 296 (± 12.7) nm and 129 (± 5.66) nm, with RSD 7.3%, 4.3% and 4.4%, respectively. This experimental and statistical analysis shows that the prepared pipettes were reproducible.

Per- and polyfluoroalkyl (PFAS) substances have unique properties of fluorinated compounds, which makes them highly persistent, toxic and show high levels of accumulation. This creates a globally emerging concern. Four PFAS substances (i.e. perfluorooctanoic acid (PFOA), perfluorobutanesulfonic acid (PFBS), perfluorohexanesulphonic acid (PFHxS) & perfluorooctanesulfonic acid (PFOS)) has been studied in this research work to assess detection and selectivity at the μITIES formed at the tips of the prepared micropipettes. All four PFAS substances were successfully detected at the μITIES by applying CV and DPV as they transfered at different potentials according to their lipophilicity. Diffusion coefficients of PFOS, PFHxS, PFBS and PFOA are 4.43 x 10^{-6}, 4.85 x 10^{-6}, 5.76 x 10^{-6} and 4.71 x 10^{-6} cm^2/s, respectively, in aqueous solution were calculated from steady-state currents recorded in CV experiments using the Saito equation. The limit of detection (LOD) calculated from the CV currents are 1.07, 0.68, 0.22 and 0.61 μM for PFOS, PFHxS, PFBS and PFOA respectively, whereas, the LODs calculated from the DPV peak currents are 0.04, 0.02, 0.03 and 0.05 μM, respectively, which are 7 to 32 times lower compared to the CV data. The selectivity of the ITIES for detection of the PFAS species in mixture solutions has been investigated by DPV. It has been seen that the transfer potential of PFOS, PFHxS, PFBS and PFOA are 0.32, 0.31, 0.25 and 0.22 V, respectively, versus the experimentally-used silver/silver chloride reference electrode. Most of the substances detected form their mixture solutions, however, in PFOA - PFBS and PFHxS - PFOS mixtures, substances were not detected separately. Because their transfer potentials are very close together and resulting one big peak, instead of two separate peaks.

First four generation of Poly(amidoamine), or PAMAM dendrimers were investigated at the μITIES as the models of proteins. Dendrimers are three-dimensional unique macromolecules with well-defined structure, molecular size and surface charge. Dendrimers have three types of amino groups which are protonated at different pH values. This study has been carried out by applying CV and DPV in a wide range of

aqueous phase pH to understand the electrochemical changes of dendrimers while undergoing transfer reactions at the ITIES. CV experiments revealed that all four generation dendrimers (G0 - G3) transfer from aqueous to organic phase by following a diffusion mechanism at all pH, while the back transfer from organic to aqueous phase varies with both pH and the generation of dendrimer. Larger dendrimers G2 and G3 follow an adsorption mechanism at lower pH 3.5, 2.75, 2.25 and 1.75, but transfers follow a diffusion mechanism at higher pH 6, 9, 10 and 11. On the other hand, smaller dendrimers, G0 and G1, always follow a diffusion mechanism and are not impacted by the pH change. However, G0 and G1 did not have any response at very high pH (10, 11) or at very low pH (1.75, 2.25) and maximum current response was shown at pH 3.5, whereas G2 and G3 have better response at lower pH 1.75 and 2.75, respectively. Diffusion coefficients (D) were also investigated at all of those pH values and shows that D decreases with the increase of generation within the same pH but increases gradually with the increase of pH. The LODs by CV analysis are 0.44, 0.24, 0.72 & 0.46 μM for G0 to G3 respectively, while DPV analysis results are 0.07, 0.05, 0.09, & 0.08 μM respectively, which are 5 to 8 times lower than those from CV measurements.

Electrochemical detection of sulphate ion by facilitated transfer across the μITIES at the tip of pipettes using three new squaramide ionophores was investigated by cyclic voltammetry. The sulphate ions have been detected nicely at the ITIES with all ionophores and demonstrated the strong affinity to make bonds between sulphate ions and ionophores although the transfer mechanism were different. Two tripodal ionophores, referred to as tren-bCF_3 and TEB-tri-bCF_3, transfer sulphate ions through the interface following an adsorption mechanism. These system followed the Langmuir adsorption isotherm. Each analysis was done at four different size of micropipettes and a sub-monolayer of complex at the interface was observed for both tripodal ionophores. One the other hand, the dipodal ionophore TEB-bis-CF_3 was seen to transfer sulphate ions at the μITIES by a diffusion-controlled transfer mechanism. The thermodynamic parameter, association constant (K_a) has been investigated at different size of micro-interface and the average log K_a was found 13.7 for TEB-bis-CF_3.

This analysis on electrochemical detection and characterization of various species at μITIES using micropipettes shows that the research on μITIES is a powerful and versatile field in analytical electrochemistry. It overcomes lots of limitations faced in conventional and macro-ITIES. Still there is lots of opportunities to strengthen this research area.

Chapter 1

Introduction

1.1 Electrochemistry at the interface between two immiscible electrolyte solutions (ITIES)

1.1.1 Background of liquid/liquid electrochemistry

The interface between two immiscible electrolyte solutions or the ITIES is formed when two nearly immiscible liquid solvents (one aqueous and the other organic) are brought into contact. About 50 years ago, Gavach and his team recognized that this liquid/liquid interface could be polarized by applying an external potential [1]. This is accepted as the start of modern liquid/liquid interface electrochemistry. Charge (electron and ion) transfer at the liquid/liquid (L/L) interface is one of the most fundamental physicochemical processes.

In the ITIES, a hydrophilic electrolyte salt, usually LiCl or Li_2SO_4, is use in the aqueous phase solvent, while the organic solvent [such as 1,6-dichlorohexane (DCH), 1,2-dichloroethane (DCE)] is polar and has enough dielectric permittivity to dissociate the polar hydrophobic electrolyte salt, commonly bis(triphenylphosphoranylidene)ammonium tetrakis(4-chlorophenyl)borate (BTPPATPBCl) [2-4]. This polarisable interface commonly involves an ion transfer from one phase to the other phase [5-8] or it could be also a redox reaction at this interface [9, 10]. Ion transfer voltammetry at the ITIES overcomes the drawbacks of the solid/liquid (conventional electroanalytical methods) interface, mainly that non-redox-active species may not be detected at solid electrodes immersed in a liquid electrolyte [3], whereas the ITIES can detect non-redox species as well. The liquid/liquid interface system is more flexible as both phases can be changed according to the needs of interesting molecules. But in a conventional solid/liquid electrochemical system, generally the liquid electrolyte can change, while the solid electrode is fixed [11].

Nernst and Riesenfeld started the electrochemical investigations at the ITIES in 1902 [12], when they measured the transport numbers of non-aqueous solvents. They used coloured inorganic electrolytes to observe the transfer of ions across the water/phenol/water interface system [12, 13]. After the 1960s, the studies in this field started to develop, when several investigations were reported on electrochemical ion transfer processes at the ITIES. Blank and Feig proposed a water/oil structure of the

ITIES in 1963 [14] which could serve as a model of half of a biological membrane which is formed by a phospholipid bilayer. In such a biological membrane, the lipophilic chains form the inner layer of the membrane while the polar heads of the bilayer face towards the aqueous intra- or extracellular solutions [15]. Like a phospholipid membrane, one side of ITIES is hydrophilic and other side is hydrophobic, which is why it is described as like half of a biological membrane.

Gavach and co-workers developed the liquid/liquid system by showing that the interface can be polarised by applying voltage and that the charge transfer reactions can control the Galvani potential difference of the two phases [1]. Koryta and co-workers further advanced this polarizability of the ITIES by showing that the mechanism of transport across the ITIES [16] is similar to that of redox processes on solid/liquid electrode surfaces [13, 17]. Samec and his group studied the kinetics of the charge transfer process at the ITIES by developing the concept of the 4-electrode potentiostat with ohmic drop compensation [5, 18].

Nowadays, electrochemistry at the ITIES has become a strong electrochemical method for its versatile applications [11, 19], which covers research on charge transfer processes [20, 21], exploration of mechanisms of extraction processes [22], adsorption-desorption behavior [20, 23], ion pairing systems [24], phase transfer catalysis [11, 25], ion detection by voltammetric and amperometric processes [26-28] and solar energy conversion systems [29]. Electrochemistry at the ITIES has moved forward from simple ion transfer to the detection of biologically significant molecules like proteins [23, 30], peptides [20, 31, 32], amino acids [33], drug delivery system and ionised drugs [34-38], neurotransmitters [39-41], food additives [42], carbohydrates [43] and DNA detection [44]. Studies on electrochemical sensors for the detection of a wide range of inorganic species like heavy metal ions, anions, alkali and alkaline earth metal ions based on ion transfer across the ITIES has developed a lot [45-48].

1.1.2 Physical structure of the ITIES

Verwey and Niessen [49] first described the theoretical electrical double layer of the ITIES as two back-to-back diffuse layers based on the Gouy and Chapman theory [50]. Gavach and co-workers [51] improved the Verwey and Niessen model of the structure

of the ITIES, which is known now as the modified Verwey-Niessen (MVN) model, by introducing a 'compact layer' of orientated dipole molecules to separate the two back-to-back diffuse layers [17].

Girault and Schiffrin [52] investigated the excess of water in the interfacial surface. They observed this surface excess water was less than the equivalent of one monolayer and proposed that ions penetrate into the interfacial region and the interfacial layer should be considered as a mixed solvent layer. Samec and his group reported a similar finding on the mixed solvent layer, where they suggested that ions can move within a certain distance into the inner layer [53]. Schiffrin and his group further studied this degree of the penetration of ions into the layer as a function of the ionic radii [52, 54].

The study on the structure of the liquid/liquid interfacial region is continuing with advanced modern technology. Schlossman and co-workers [55, 56] measured the interfacial widths in the range between 3.5 to 6.0 Å by applying synchrotron x-ray reflectivity, based on the exponential dependence of the reflectivity on the interfacial electron density profile. They confirmed these findings on width measurement by calculating ion distributions and molecular-scale structure in the liquid solution with the help of molecular dynamics (MD) simulations [57]. This group continued their study on ion distributions at microscopic scales to observe the influence of the ion-ion coupling strength [58], which made clear concept for the effect of ion–ion correlations on the ion distributions and the total interfacial excess charge with changing the coupling strength. Scanning electrochemical microscopy (SECM) and neutron reflection were employed to analyse the liquid/liquid interface by Strutwolf et al. [59], where they reported a smooth interface with a root mean square roughness less than 10 Å at a 1,2-dichloroethane/aqueous potassium hydroxide interface, which complies with capillary wave theory and molecular dynamics simulations.

In very recent, Girault and his co-workers [60] have shown that the different types of interfaces spanning liquid–liquid interfaces, metal oxide interfaces, ion-exchange membranes, charged silica–water interfaces, super-capacitors and biological membranes also can be described with a uniform "Discrete Helmholtz" model. In this model structure, there is a layer of discrete charges, those are compensated by another single layer of counter ions, hence makes a sharp potential drop at the interface.

1.1.3 Thermodynamics of the ITIES

As discussed earlier that an ITIES is formed when two immiscible conducting electrolyte liquids are brought into contact. As these two conducting electrolytes have different Galvani potentials ($\Delta_o^w\emptyset$), therefore the charge carriers of these two liquids remain separate between two adjacent phases. The equilibrium Galvani potential difference is defined as the following equation:

$$\Delta_o^w\emptyset = \emptyset^w - \emptyset^o \qquad \text{Equation 1.1.1}$$

where $\emptyset^w$ and $\emptyset^o$ are the aqueous phase (w) and organic phase (o) potentials, respectively. The electrochemical potential of an ion (i) at equilibrium in the ITIES is described as:

$$\bar{\mu}_i^w = \bar{\mu}_i^o \qquad \text{Equation 1.1.2}$$

where $\bar{\mu}_i^w$and $\bar{\mu}_i^o$ are the electrochemical potential of an ion in water (w) and in organic (o) phase, respectively. The work needed to move a species (i) from a vacuum phase to a liquid phase (α) is thermodynamically defined as:

$$\bar{\mu}_i^\alpha = \mu_i^\alpha + z_i F\emptyset^\alpha \qquad \text{Equation 1.1.3}$$

where $\mu_i^\alpha$is the chemical potential of species (i) in phase (α) and z_i is the charge of that species. $z_i F\emptyset^\alpha$ is the electrical contribution in this equation for the electrochemical potential. The electrochemical potential, which becomes equal to the chemical potential for neutral species (z = 0), is defined as follows:

$$\mu_i^\alpha = \mu_i^{\alpha,0} + RTln\alpha_i^\alpha \qquad \text{Equation 1.1.4}$$

where α_i^α is the activity of the ion and $\mu_i^{\alpha,o}$ is the standard chemical potential. The activity of an ion depends on the solution composition, pressure and temperature which can be represented in terms of concentration and activity coefficient (γ_i^α), as below:

$$\alpha_i^\alpha = \gamma_i^\alpha C_i^\alpha \qquad \text{Equation 1.1.5}$$

Equation 1.1.3 can be rewritten as:

$$\bar{\mu}_i^\alpha = \mu_i^{\alpha,0} + RTln\alpha_i^\alpha + z_i F\emptyset^\alpha \qquad \text{Equation 1.1.6}$$

As stated earlier, the thermodynamic equilibrium is established when the electrochemical potential of species i becomes equal in both phases (Equation 1.1.2). Thus, combining Equation 1.1.6 and Equation 1.1.2 gives:

$$\mu_i^{w,0} + RTln\alpha_i^w + z_iF\emptyset^w = \mu_i^{o,0} + RTln\alpha_i^o + z_iF\emptyset^o \qquad \text{Equation 1.1.7}$$

The Galvani potential difference formed at the interface between the two phases will be obtained by rearranging Equation 1.1.7 as below:

$$\Delta_o^w\emptyset = \emptyset^w - \emptyset^o = \frac{\mu_i^{o,0} - \mu_i^{w,0}}{z_iF} + \frac{RT}{z_iF}ln(\frac{\alpha_i^o}{\alpha_i^w}) \qquad \text{Equation 1.1.8}$$

The difference in chemical potentials can be described in terms of a standard ion transfer potential, $\Delta_o^w\emptyset_i^o$ and standard Gibbs energy of ion transfer ($\Delta G_{transfer,i}^{0,w\to o}$) by the following equation:

$$\Delta_o^w\emptyset_i^o = \frac{\Delta G_{transfer,i}^{0,w\to o}}{z_iF} = \frac{\mu_i^{o,0} - \mu_i^{w,0}}{z_iF} \qquad \text{Equation 1.1.9}$$

where $\mu_i^{o,0}$ and $\mu_i^{w,0}$ are the standard chemical potentials of species i in organic (o) and aqueous (w) phases, respectively, while z_i is the charge and F is Faraday's constant.

We get an equation like the Nernst equation by combining Equation 1.1.8 with Equation 1.1.9 for electron transfer reaction, which is equivalent to the classical Nernst equation. As no redox reactions are involved here, hence, equation 1.1.10 can be recognized as the Nernst equation for the ion transfer at the liquid/liquid interface.

$$\Delta_o^w\emptyset = \emptyset^w - \emptyset^o = \Delta_o^w\emptyset_i^o + \frac{RT}{z_iF}ln(\frac{\alpha_i^o}{\alpha_i^w}) \qquad \text{Equation 1.1.10}$$

If the interfacial potential is changed, $\Delta_o^w\emptyset_i^o$ remains constant but the ratio (α_i^o/α_i^w) changes accordingly to reach the equilibrium, which makes the movement of a portion of equilibrated ions across the interface; this movement of charged species produces an electrical current across the interface and which can be determined as a function of the applied potential.

Equation 1.1.10 (Nernst-like equation) could also be presented in terms of activity coefficients and concentration of species i. So, combining Equation 1.1.5 and 1.1.10 results in:

$$\Delta_o^w \emptyset = \Delta_o^w \emptyset_i^o + \frac{RT}{z_i F} ln(\frac{\gamma_i^o C_i^o}{\gamma_i^w C_i^w}) \qquad \text{Equation 1.1.11}$$

Re-arranging Equation 1.1.11 and replacing the activity coefficients and standard Galvani transfer potential with the formal Galvani transfer potential ($\Delta_o^w \emptyset_i^{o'}$) defined as

$$\Delta_o^w \emptyset_i^{o'} = \Delta_o^w \emptyset_i^o + \frac{RT}{z_i F} ln(\frac{\gamma_i^o}{\gamma_i^w}) \qquad \text{Equation 1.1.12}$$

gives the expression for interfacial Galvani potential difference in terms of concentration of species i individually in either phase (w or o) :

$$\Delta_o^w \emptyset_i^o = \Delta_o^w \emptyset_i^{o'} + \frac{RT}{z_i F} ln(\frac{C_i^o}{C_i^w}) \qquad \text{Equation 1.1.13}$$

1.1.4 Polarisable and non-polarisable ITIES

If there is excess positive and negative charge in each of the phases of the two immiscible solutions then polarisation occurs at the liquid-liquid interface [22] and that interface itself acts as a working electrode where the electrochemical process takes place. The polarizability of the interface depends on the electrolyte ions present in the two immiscible phases.

An ideal polarisable interface has the ionic electrolytes with infinite Gibbs transfer energies. In reality, there is no such kind of system as ions have restricted solubility in solvents and that is why the electrolyte ions present dictate the polarizability of that system. A polarisable interface is formed with a very hydrophilic electrolyte (A^+, B^-) in the aqueous phase and with a very hydrophobic electrolyte (C^+, D^-) in the organic phase, as shown in Figure 1.1.4.1. The polarization of the interface happens within a definite potential window which is fixed by the formal ion transfer potentials of the electrolyte ions.

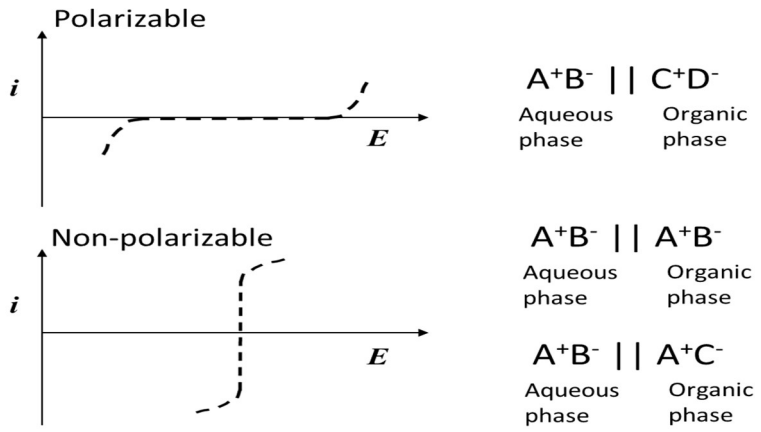

Figure 1.1.4.1: *Schematic representation of polarisable and non-polarisable ITIES. A^+B^- is very hydrophilic while C^+D^- is highly hydrophobic for formation of a polarisable interface. For the non-polarisable interface, (top) A^+B^- would be common in the two phases or (bottom) A^+ is a common ion while B^- is very hydrophilic and C^- is hydrophobic.*

A non-polarisable interface forms if a single binary electrolyte (A^+ B^-) is present in both phases (Figure 1.1.4.1) and the Nernst equation for each of the ions can be written as follows:

$$\Delta_o^w \emptyset = \Delta_o^w \emptyset_{A^+}^o + \frac{RT}{z_{A^+}F} ln(\frac{\alpha_{A^+}^o}{\alpha_{A^+}^w}) \qquad \text{Equation 1.1.14}$$

$$\Delta_o^w \emptyset = \Delta_o^w \emptyset_{B^+}^o + \frac{RT}{z_{B^-}F} ln(\frac{\alpha_{B^-}^o}{\alpha_{B^-}^w}) \qquad \text{Equation 1.1.15}$$

where z_{A^+} = +1 and z_{B^-} = -1 for the cation A^+ and anion B^- respectively.

As the solubility of A^+ is different in both phases, therefore, a distribution potential would be initiated across the interface which is independent of the concentration. So, the Nernst equation can be re-arranged with activity coefficients as the following expression:

$$\Delta_o^w \emptyset = \frac{\Delta_o^w \emptyset_{A^+}^{o'} + \Delta_o^w \emptyset_{B^-}^{o'}}{2} + \frac{RT}{z_i F} ln(\frac{\gamma_{A^+}^o \gamma_{B^-}^w}{\gamma_{A^+}^w \gamma_{B^-}^o}) \qquad \text{Equation 1.1.16}$$

Figure 1.1.4.1 shown another form of non-polarisable interface. This happens when a common ion (A^+) exists in both immiscible phases, whereas B^- is very hydrophilic and C^- is adequately hydrophobic to remain in the aqueous and organic phase respectively. Therefore, the distribution of A^+ ions only controls the Galvani potential difference across the interface and the previous equation simplifies as below:

$$\Delta_o^w \emptyset = \Delta_o^w \emptyset_{A^+}^o + \frac{RT}{F} ln(\frac{\alpha_{A^-}^o}{\alpha_{A^-}^w}) \qquad \text{Equation 1.1.17}$$

1.1.5 Potential window and the voltammetric response of ion transfer at the ITIES

As mentioned earlier, the working potential window at the ITIES is dictated by the formal ion transfer potentials of the electrolytes present in the two liquid solutions. So to create a better polarisable interface at the ITIES for cyclic voltammetry (CV), we use 10 mM lithium chloride (LiCl) as the aqueous electrolyte and 10 mM bis(triphenylphosphoranylidene)ammonium tetrakis(4-chlorophenyl)borate (BTPPATPBCl) as the organic electrolyte shown in Figure 1.1.5.1. Purified water was used as aqueous phase while 1,2-dichloroethane (DCE) was used as organic phase. The potential is applied within two potential limits, starting from a low potential to a more positive value for the forward scan and then back to the starting potential on the reverse scan, and current is measured as the output. Conventionally, if more positive current measured on the forward scan for the applied positive potential (right side of the graph) then this represents the transfer of negative anions from the organic to the aqueous phase and/or the transfer of positively charge ions from the aqueous phase to the organic phase [2]. On the other hand, if negative current increases on the reverse scan, then it represents the back transfer of negatively charged ions from the aqueous into the organic phase and/or the transfer of positively charged ions from the organic to the aqueous phase [2].

Figure 1.1.5.1 shows the CV divided into three separate regions A, B and C. Part A and C are the negative and positive potential regions respectively, whereas region B represents the intermediate (polarised) region. In this experiment, the starting potential is set at the lowest potential in region A and the switching potential is fixed at the most positive potential in region C. The potential starts to scan in the positive direction from the left to the right-hand side and the reversed scan is in opposite direction.

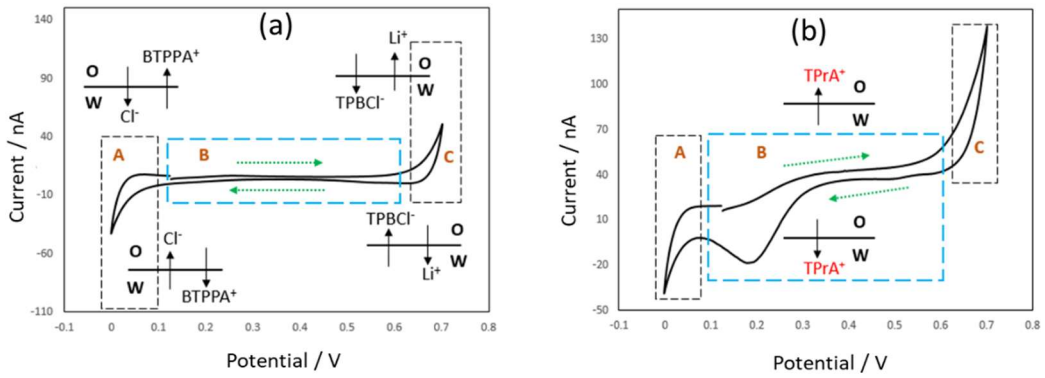

Figure 1.1.5.1: *(a) Cyclic voltammogram of 10 mM LiCl in the aqueous phase and 10 mM BTPPATPBCl in the organic phase 1,1-dichloroethane at 100 micropore array of glass membrane (b) CV of 20 µM tetrapropylammonium in aqueous phase.*

Figure 1.1.5.1 (a) shows that a lower positive potential 0.15 V is applied in region A to start the CV where no transfer of background electrolyte ions (or faradaic process) takes place in the window between 0.15 V to 0.6 V approximately (region B) and this is termed as 'polarisation region'. The current measured in this region is solely contributed by charging current at the ITIES which is a non-faradaic process. The scan continues to the forward direction and a positive increase in the current is observed from approximately 0.6 V to 0.75 V (region C), because of the transfer of the aqueous cation (Li^+) from W (water) to O (organic) phase and the organic anion ($TPBCl^-$) from O to W phase.

When the scan reaches the highest potential 0.75 V, then the scan is subsequently reversed and in the potential region approximately from 0.75 V to 0.6 V, Li^+ and $TPBCl^-$ ions start to back transfer from the organic and aqueous phases respectively. Again, the non-faradaic processes occur at the ITIES while back scanning through the 'polarisation region' from 0.6 V to 0.15 V. $BTPPA^+$ transfers from O to W phase, while Cl^- transfers from W to O phase for the applied potential range from 0.15 V to 0.0 V at the lowest positive potentials region A. The scan direction again changes after reaching the lowest potential 0.0 and stops at 0.15 V by back scanning to complete the cyclic voltammogram where $BTPPA^+$ transfers back to O phase and Cl^- transfers back from O to W phase. Generally, the positive limit at the potential window is fixed by the simultaneous transfer reactions of hydrophilic cation (in this case Li^+) and

hydrophobic anion (in this case $TPBCl^-$) which occur at the positive potential. On the other hand, the limit at the negative end of the potential window is set by the simultaneous transfer reactions of hydrophilic anion (in this case, Cl^-) and hydrophobic cation (in this case, $BTPPA^+$) which occur at the negative potential region.

The transfer of the ionised molecules of interest happens at the ITIES in the polarisation region and that is why the transfer potential of the analyte of interest must fall within that region to get a detectable response without interference with the background response. So, selection of electrolytes for the aqueous and organic phases is very important to get a broad operating potential window for the ionised molecules of interest [4, 61]. Figure 1.1.5.1(b) shows the tetrapropylammonium ($TPrA^+$) ion transfer which falls in the polarization area B and did not interfere with any background ions transfer. The $TPrA^+$ ions start to transfer across the interface when the forward potential scan in the positive direction achieves a positive potential equivalent to the Gibbs energy of $TPrA^+$ ion transfer (approximately at 0.3 V on voltage scale), resulting in an increase in the current in region B, which became steady-state and indicates radial diffusion control of the ion transfer [62, 63]. Conversely, when the applied potential reaches equivalent to the negative value of the Gibbs energy of $TPrA^+$ transfer in the reverse sweep, $TPrA^+$ starts to back transfer from O to W phase producing a negative peak current, indicating linear diffusion of ion transfer [62, 63]. When ions move from aqueous phase to the organic phase then the ions can transport from different directions, which is defined as radial diffusion (Figure 1.1.5.2). One the other hand, when the ions move from organic to aqueous phase (inside the pipette), then ions can migrate only in one direction which is defined as linear diffusion (Figure 1.1.5.2).

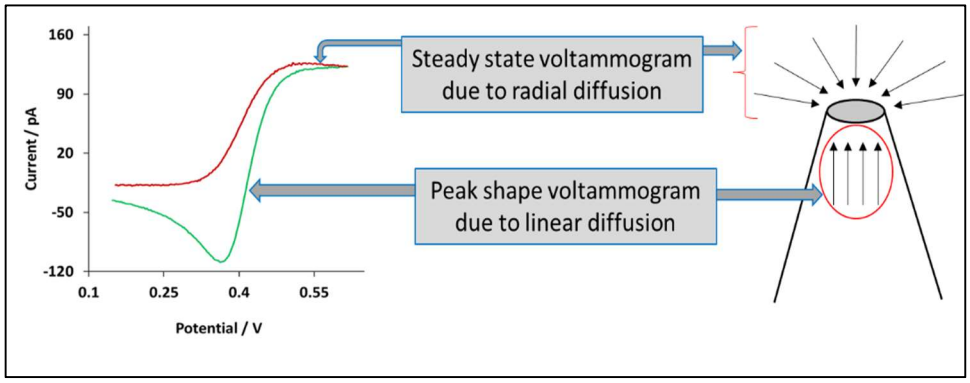

Figure 1.1.5.2: *Shapes of voltammograms based on diffusion moods.*

1.1.6 Types of charge transfer processes

Conventional or solid electrode-electrolyte electrochemistry primarily follows an electron transfer (ET) mechanism, whereas electrochemistry at the ITIES can follow different forms of charge transfer (CT). The first and the simplest CT process is ion transfer (IT), which is the movement of ions from either phase across the interface because of applying an external potential difference and continuing until reaching an equilibrium according to the Nernst equation. When the applied potential difference overcomes the Gibbs free energy of transfer of that ion across the polarised interface then these ions transfer across the ITIES [2, 64]. This transfer potential can be measured if it falls within the potential window set by the transfer of the background electrolytes.

The second charge transfer process is facilitated ion transfer (FIT) [2, 64]. That can be further classified in four categories based on the complexation mechanism between the ion and the ionophore charge transfer [64, 65]. Those are, namely, Transfer by Interfacial Complexation (TIC), Transfer by Interfacial Dissociation (TID), Aqueous Complexation followed by Transfer (ACT) and Transfer to the Organic phase followed by Complexation (TOC). These four assisted ion transfer processes are described in Figure 1.1.6.1(b).

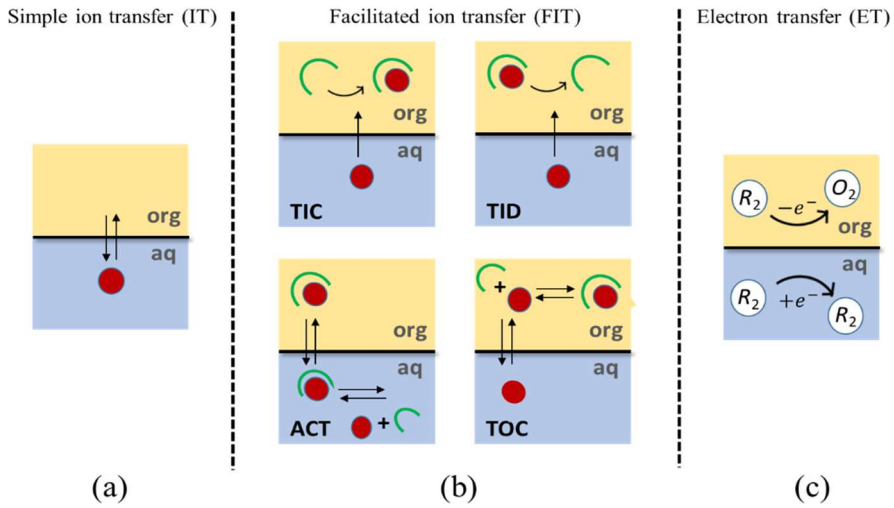

Figure 1.1.6.1: *Schematic presentation of the types of charge transfer process. (a) Simple ion transfer (IT), (b) Facilitated/assisted ion transfer (FIT) and (c) Electron transfer (ET) process.*

The third CT process is electron transfer (ET) [64], which occurs between redox species in each phase and is more complex than other two CT processes. Choosing the redox couples is the difficult part and ideally the redox products should not transfer across the ITIES, otherwise this could produce currents separate from the actual electron transfer process [17].

1.2 Miniaturisation of the ITIES

1.2.1 Benefits of miniaturised ITIES

Miniaturisation of the ITIES from a macro-scale to a micro- or nano-scale offers some advantages with respect to the larger liquid-liquid interfaces. Double layer charging current and IR or Ohmic drop are very important to get the actual signal from the target species and crucial for kinetic parameters. The larger interface creates more charging current and more IR drop, which can inhibit obtaining the actual signal from the analyte. Miniaturisation of the ITIES results in very small currents generated at the ITIES which minimises the effects of Ohmic drop [11, 66, 67]. Furthermore, miniaturised ITIES enhance the diffusional mass transport rate, resulting in greater current densities and hence increase the sensitivity of the analytical response [62, 67-69]. Voltammetric measurements in low polar media or media without supporting electrolytes were also introduced with a single micro- or nano-ITIES [70-72]. This also assists to simplify the conventional four-electrode cell [18] arrangement by replacing it with a two-electrode cell [11]. Electrochemical signals are also enhanced by employing several micro- or nano-ITIES in an array format [66, 69]. Besides, the geometry and the mechanical stability of the interface can be improved by supporting the micro- or nano-ITIES with semi-solid gellified organic phases [66, 68, 69].

1.2.2 History of the development of miniaturised ITIES

Taylor and Girault introduced the concept of the miniaturised ITIES (liquid/liquid interface) in 1986 by transferring tetraethylammonium ion (TEA^+) from the organic phase to the aqueous phase at 25 μm radius tip of pulled glass micropipettes [6]. Afterwards several research groups have also reported their studies on micropipette-based ITIES [7, 73-75]. Asymmetric diffusion was reported by Shao and co-workers in 1991 where they observed spherical diffusion into the micropipette, while 'linear diffusion' is observed out of the micropipette [7]. This asymmetric diffusion results in

the apparently unusual cyclic voltammograms with a steady state current on one half-cycle and a peak-shaped voltammogram on the other half-cycle.

In 1995 Beattie and co-workers [73] made thinner glass micropipettes of borosilicate and quartz materials by using an advanced pipette puller which solves the reproducibility problem of the tip geometry. Shao and Mirkin in 1998 developed a silanization process to change the hydrophilic glass pipette surface to hydrophobic, which makes the ITIES stable at the mouth of the micropipette [75]. In further studies, an array of microITIES formed at membranes containing arrays of microholes (or micropores) was introduced to address the very low signal produced at micropipettes which is not suitable for many applications [76, 77]. The first microhole array based micro-ITIES was reported by Campbell and Girault [78], where 66 microholes was created on micro-machined polyethylene terephthalate (PET) substrate by ablation with a UV excimer laser. Different materials like silicon [31, 68, 79, 80], polymers [77], glass [11, 81] and different techniques like photolithography, electron beam lithography, laser ablation and chemical etching have been explored for preparation of porous membranes [31, 82]. A fast and cheap method for patterned microhole array membrane was reported in 2021 by Poltorak et al. [83], where they used self-adhesive polyimide tape which was punctured by sets of needles to create the array of holes.

Miniaturization research has been continued from the micrometre to the nanometre size. Nano-ITIES supported by glass pipettes in the same way as micro-ITIES are supported by micropipettes were introduced [67, 84]. These studies were followed by the fabrication of nano-ITIES arrays employing alumina membranes [85], track etched membranes [76, 84] and silicon nitride membranes [68, 86-88]. Research is going on in this exciting area from different viewpoints like the miniaturized interface that enables enhanced mass transport, due to dominance of radial diffusion, as well as decrease charging currents and decrease deleterious effects of solution resistance; miniaturized interface is better for mechanistic and kinetic studies, moreover it is more stable compare to larger interface etc. [89, 90].

1.3 Literature review on the ITIES

After the revolutionary work of Taylor and Girault [6], several research groups reported on miniaturised ITIES especially with pipettes for voltammetric studies of

charge-transfer processes at the interface between two immiscible electrolyte solutions because of its numerous advantages compared to a large ITIES. Campbell and Girault reported that the kinetic parameter measurement for the ion transfer reactions, which are very fast, is better in micropipettes for smaller interface size [6, 91], because of its spherical mass transfer pattern which leads to high steady state mass transfer as well as creates a low value of the *IR* drop.

A wide range of investigations on biomolecules at soft polarisable interfaces has been undertaken. DNA detection and characterization is one of the challenging approaches in analytical chemistry. In 1998, Horrocks and Mirkin reported that micropipets provide a simple ion transfer technique for the electrochemical determination of DNA by its binding with non-redox-active cations, where the cation was taken in the organic phase present inside the pipet and DNA (oligonucleotides) were added to the aqueous phase. The cation transfers to the aqueous phase was controlled and facilitated by the DNA present in the aqueous phase [92]. In 2007 Osakai et al. investigated the voltammetric behavior of salmon sperm DNA (purified) and herring sperm DNA at 1,2-dichloroethane (DCE)/water interface in the presence of dimethyldistearylammonium as a cationic surfactant in DCE [44]. Development of a label-free electrochemical DNA sensor was reported by Vagin et al. in 2008 where the flow of nonelectroactive ions was used as an electrochemical probe at the liquid/liquid interface to detect DNA hybridization; they reached a detection limit down to 10 nM [93]. Kivlehan et al. investigated the hybridisation of DNA with acridine-calix[4]arene at the ITIES by sensitive impedance measurements which also enabled the detection of nanomolar double stranded DNA [94]. The interaction of high molecular DNA with drug molecules daunorubicin and dopamine was investigated at water/1,6-dichlorohexane (DCH) microarray interface by Ribeiro et al. in 2015 [95]. Felisilda and Arrigan [96] investigated a synthetic oligonucleotide thrombin-binding aptamer (TBA, 15-mer) at liquid / organogel μITIES interface array. TBA was detected in the presence of cetyltrimethylammonium (CTA^+) in both aqueous and organogel phases. By employing CV, the LOD of TBA reached down to 0.11 μM.

Liquid/liquid interfaces have been employed as a powerful electrochemical platform for the detection and characterization of drug molecules. Arrigan and his group investigated propranolol, which is a cationic β-receptor blocking drug, in artificial

saliva. They employed ion-transfer voltammetry based on arrays of microinterfaces formed at the mouths of silicon micropores between artificial saliva and an organogel phase [97]. They got a LOD of 20 nM by applying differential pulse stripping voltammetry (DPSV) including a preconcentration step. They also investigated the effect of bovine serum albumin on propranolol sensing in the artificial serum matrix when using the same technique [98]. Pereira et al. monitored the electrochemical behavior of anticancer drug daunorubicin (DNR) in both neutral and ionic forms at the water/DCH micro-interface array by imposing CV and differential pulse voltammetry (DPV). They investigated the analytical parameters like lipophilicity, partition coefficients and proposed a DNR sensor based on simple ion transfer at the water/DCH interface [36]. Protonated ractopamine, which is a β-agonist drug, was investigated in artificial serum based on a water / DCH micro-interface array using voltammetric techniques. A LOD of 0.1 µM was successfully achieved by employing stripping voltammetry, which is suitable for real samples as well [99]. Tenofovir was detected at a water / DCE interface by using dibenzo-18-crown-6 in the organic phase as a ligand to facilitate the tenofovir transfer [100]. Hye Jin Lee and her group reported the development of a microscale-ITIES sensor for determining the anticancer drug topotecan in biological samples at a microhole supported water/polyvinyl chloride-2-nitrophenyloctyl ether (PVC-NPOE) gel interface [101]. Osakai et al. [102] studied the oxidation of biologically important L-ascorbic acid at water / DCE) interface in the presence of an electron acceptor (chloranil) in the organic phase by a combination of electrochemical and spectroscopic techniques. They proposed an oxidation mechanism by determining the Galvani potential difference across the interface as well as the distribution of the organic electron acceptor. Ohde et al. [103] reported two different redox reactions between β-nicotinamide adenine dinucleotide (NADH) and quinone derivatives at water / DCE interface, where NADH and quinone were in aqueous and organic phases, respectively. They showed that the mode of redox reaction that occurs at the interface depends on the potential difference at the interface. Very recently, for the first time, the ionizable drug diclofenac has been detected and characterized at water/1,6-dichlorohexane microinterface based on microporous silicon nitride membrane using CV and DPV [104]. Poltorak and his group [105] investigated the electrochemical behavior of four fluoroquinolone antibiotics (ciprofloxacin, enrofloxacin, marbofloxacin and ofloxacin) at both macro and micro supported water / DCE interface using ion–transfer voltammetry (ITV). They detected all of the

molecules within the available potential window where cipofloxacine is the most hydrophilic compound among all four. They calculated lots of thermodynamic and kinetic parameters with the LOD which is around 1 μM. Herzog and his group [106] reported on the proton assisted transfer of an herbicide, ametryn, at a single μITIES as a function of pH. Depending on the pH of the aqueous phase, they observed direct ion transfer as well as proton assisted transfer.

Kataky and Lopes reported [107] the detection of drug enantiomers of ephedrine at a μITIES based on a micropipette, where a cyclodextrin chiral selector was used in the organic phase as a facilitator to transfer the protonated enantiomers. A significant differences of their transfer potentials was recorded, although the difference in association constants of the ephedrinium enantiomers with the cyclodextrin was very small. Lopes and Kataky [108] further investigated interactions of chiral drugs (S)-propranolol and (R)-propranolol with the protein α(1)-acid-glycoprotein at a μITIES formed with a micropipette by employing CV and DPV. In this case, the current response for the transfer of ions decreases differently for the two enantiomers of the drug because of the protein interaction, which makes it possible to calculate the association constants of each enantiomer with the protein [108].

The electrochemical behavior of vitamin B1 at a pipette-based water / nitrobenzene micro-interface was investigated by Huang et al. [109] using stripping voltammetry and enabled to reach a detection limit of 4.6 μM. They also applied potential step chronoamperometry to study the ion transfer process and observed a steady-state current obtained after 15 seconds of the potential step. This observation is important because for applying stripping voltammetry, the pre-electrolysis time need to be set at least 15 seconds. Mono-, di- and tri-adenosine phosphates play an important role in energy metabolism in living systems. Qian et al. [110] investigated their properties at water / 1,2-dichloroethane micro-interface array facilitated by an ionophore N-(2-[bis-(2-(4-tert-butylbenzoyl)-aminoethyl)-amino]ethyl)-t-butylbenzamide and observed distinct ion transfer potentials.

Electrochemical behavior of proteins at the ITIES has been investigated for a long time, however the significant development about the mechanism of protein transfer has been developed since the last decade. The behavior of large biomolecules (ovalbumin and bovine serum albumin) was for the first time reported by Vanysek et

al. at the water/nitrobenzene interface and no ion transfer current was observed that was associated with the proteins, but adsorption occurred [111, 112]. The study of large proteins at the ITIES started its new dimension after 2002 when surfactants were incorporated with more hydrophobic solvents, which explore the label-free detection of proteins at the ITIES for analytical purposes. In 2002, Dryfe's group reported the potential-controlled electron transfer process between cytochrome c and 1, 1′-dimethylferrocene at the ITIES which is close to the in vivo process within the mitochondrial membrane where cytochrome c acts as an electron transfer protein in the electron transfer chain reaction [9]. Amemiya and colleagues in 2003 [20] reported for the first time about the phase transfer of the biological polypeptide protamine at micropipette-based water / 1,2-dichloroethane interface. Protamine is a highly charged macromolecule with 30 amino acids and its isoelectric point (pI) > 12. This charge transfer analysis confirms that each protamine carries at least 20 positive charges at the isoelectric point or lower pH or at physiological pH. This investigation at the ITIES provided a basis for amperometric sensor development for biological macromolecules [20]. Amemiya and coworkers [32] further investigated protamine at water / 1,2-dichloroethane micro-interface by adding dinonylnaphthalenesulfonate (DNNS) as an ionophore in the organic phase. The diffusion coefficient of protamine and its ionised charge were calculated for this interfacial charge transfer process and were in good agreement with previously determined values. Samec's group [113] reported comprehensive studies on the behavior of protamine at the water / 1,2-dichloroethane macro-interface using CV, quasi-elastic light scattering (QELS) and conductometry. This investigation demonstrated important findings about the mechanism of biological targeted macromolecules in a cell. In this study three different anions were used in the organic phase to prove that the transfer of protamine from aqueous to organic phase occurs by the formation of ion-pair between the protamine and the organic anions.

Scanlon et al. [80] investigated the behavior of two biological macromolecules namely insulin and hen-egg-white lysozyme (HEWL) at water / organogel μITIES formed on an array of solid-state micropores in a membrane. They reported that these bio-macromolecules go through an interfacial adsorption in the aqueous side which facilitated the transfer of anions from organic phase to the adsorbed protein layer on the aqueous side, whereas the tetraethylammonium cation (TEA^+) followed a simple ion transfer mechanism [80]. The behavior of myoglobin was also observed at an array

of aqueous / PVC-gelled 1,6-dichlorohexane micro-interfaces by applying CV [114]. This analysis also followed the previous one [80], where myoglobin absorbed at the aqueous side of the interface to facilitate the transfer of the organic phase anions through the interface. However, the reverse process was desorption controlled, confirmed by the voltammetric scan rate of the reverse peak current. As like all other proteins, in this case also pH plays a vital role to detect the myoglobin [114]. Alvarez de Eulate and Arrigan [23] studied HEWL at an array of μITIES and were able to detect 0.03 μM by applying adsorptive stripping voltammetry, which is more than 10 times lower than the previous HEWL detection at the ITIES by CV [80]. These findings provided a new analytical platform for the detection of label-free protein. Booth et al. [115] investigated the structural changes in myoglobin, hemoglobin, cytochrome *c*, and lysozyme by controlled electroadsorption at aqueous / organogel macro interface. Analysis of the second derivative of the amide I peak in FTIR spectra and matrix-assisted laser desorption/ionization time of flight mass spectrometry (MALDI-ToF-MS) showed that the structure of myoglobin, haemoglobin, and cytochrome *c* changed to aggregated antiparallel β-sheet from unfolding of the structure. However, the structure of lysozyme remained unchanged. In a very recent report, investigation on the structure of insulin at liquid-gel soft electrochemical interface was reported by Lamichhane et al. [116]. They also observed that the native secondary structure of insulin changed to α helix secondary structure after interaction with the organic phase at DCE-PVC gelled interface.

Heparin is a highly sulphated polydisperse mixture of carbohydrates and widely used as a blood anticoagulant. Samec and coworkers first investigated the electrochemical behavior of heparin at the ITIES in 2003 [117]. Amemiya and coworkers reported on the behavior and detection of heparin at 1,2-DCE / water (blood plasma) micro-interfaces formed at the tip of a micropipette [43]. In that study, different quaternary ammoniums were used as cationic ionophores to Figure out the structural requirements for heparin-ionophore complex formation. They found that complexation with octadecyltrimethylammonium cations was the best for low detection limits. This was also the first time to study using direct blood samples at the ITIES to investigate the biomedical utility of ion-transfer voltammetry [43]. Voltammetric extraction of heparin with a new ionophore 1-[4-(dioctadecylcarbamoyl)butyl]guanidinium across 1,2-dichloroethane / water single micro-interface at a pipette tip was investigated by

Amemiya and co-workers [118]. They found that the heparin molecule can strongly bind with more than one ionophore to become electrochemically neutral and then this highly lipophilic heparin complex becomes extractable into the nonpolar organic phase. Felisilda et al. [119] investigated two sulphated polysaccharide fucoidans at an array of μITIES where the organic electrolyte phase was gellified. CV experiments showed that the detection process follows an adsorption process when scanned to negative potentials, while it gave a desorption peak on the reverse scan. By applying adsorptive stripping voltammetry (AdSV), they found a LOD of 1.8 μg mL^{-1} for *U. pinnatifida* fucoidan in aqueous phase of 10 mM NaOH and 2.3 μg mL^{-1} in synthetic urine. Felisilda et al. [120] also investigated the electrochemical characterization of sucrose octasulfate (SOS) utilizing voltammetry at a liquid / organogel μITIES array. They found that the detection of SOS depends on the organic cations present in the organic phase. The LOD of SOS was found 0.036 μM with tridodecylmethylammonium ($TDMA^+$) organic phase cation using AdSV.

The products or substrates from enzyme-catalyzed reaction can be detected at the ITIES which creates a new dimension for harnessing the biological selectivity of enzymes for bioanalytical process. Senda et al. [121, 122] and Osborne and Girault [123] introduced this approach by analysing urea. Urea cannot be detected at the ITIES as it is not ionisable or electroactive, however when it undergoes hydrolysis with the enzyme urease then the ammonium cation produced can be detected by transfer across the liquid/liquid interface by a facilitated ion transfer reaction. Pereira et al. [124] developed an amperometric glucose biosensor based on facilitated proton transfer across a gellified microITIES. The protons are generated from the dissociation of gluconic acid, which is a product of the oxidation of glucose by oxygen catalysed by the enzyme glucose oxidase. Lee and coworkers [125, 126] also reported the detection of organophosphate pesticides paraoxon, parathion and methyl parathion at a microhole-based water/organogel interface by a facilitated proton transfer mechanism. In this case, the enzyme organophosphorous hydrolase was added as a reagent in the organic phase which produced protons by hydrolyses with the target analytes and these were subsequently detected by ion transfer voltammetry or amperometry. Akter and Arrigan [127] investigated a label-free nonredox electrochemical detection of the cancer protein biomarker PSMA (prostate specific membrane antigen) at the μITIES array based on assisted proton transfer voltammetry without use of antibodies. The

LOD by applying SWV (square wave voltammetry) was 3.5 pM, which was lower than the reported values [128-131]. Recently Zannah and Arrigan reported label free detection of catalase (CAT) enzyme at liquid/liquid micro interface array [132]. An electroanalytical signal has been found when the aqueous phase pH was lower than the isoelectric point of CAT, proving its electroactivity at the μITIES. CVs of CAT in artificial serum also demonstrated the feasibility of μITIES to detect such large molecules in the presence of various ionic species. The calculated LOD was 3.5 nM, which is lower than that for other proteins reported to date, which further manifested the suitability of L/L μinterface array in practical applications (e.g., biosensor development).

Shen and her group[133] reported the ion transfer of neurotransmitters and neuromodulators, namely acetylcholine (ACh), serotonin (5-HT), and tryptamine (T), across the DCE/water interface by CV and amperometry. This qualitative and quantitative detection for both electrochemically non-redox (ACh) and redox active neurotransmitters (5-HT and T) with nanopipette-based ITIES makes a strong base for sensor probes. Another neurotransmitter, dopamine (DA), has been well studied at the macroITIES [26, 39, 134, 135] and microITIES [40] by Arrigan et al. as well as by Shao's group at microITIES [41]. However Shen and her group [136] reported dopamine transfer across the nanopipette based the 1,2-DCE/water interface facilitated by dibenzo-18-crown-6 ionophore (DB18C6). Shen and her group [137] developed a new method to detect gamma-aminobutyric (GABA) at a nano-ITIES pipette electrode at biological pH 7.0 by pH modulation from the oil phase. They added octanoic acid (OA) to the organic phase 1,2-dichloroethane inside the pipette whereas GABA was in the aqueous phase. GABA was detected upto 22.4 μM by CV. They also confirmed that neither the protons from the OA nor the OA itself come out from the oil phase. Wang et al. [138] reported on the liquid/liquid interface microsensor (LLIM) to monitor the redox-inactive neurochemical choline at cerebrospinal fluid /DCE interface. Choline gave an excellent response in the LLIM with detection limit 0.37 μM.

Scanning electrochemical microscopy (SECM) with the tip of a micro- or nano- pipette has become a useful scanning probe technique for quantitative monitoring of chemical reactivity [139] as well as enabling the imaging of the electrochemical properties of a

surface or interface with an ion. Currently SECM has become a powerful method for chemists to investigate electrochemical process happening in living cells [140, 141]. Bard et al. [142] reported that the tip of a micropipet-supported ITIES can act as a SECM probe to detect silver ions and explore Ag^+ toxicity in living cells. By adding calixarene-based Ag^+ ionophore (IV) into the pipette containing the DCE organic phase, they constructed a Ag^+-selective SECM tip. They monitored the Ag^+ concentration by imaging of the uptake and efflux of Ag^+ by SECM approach curves on living fibroblast cells, which opens a new mode to study cell metabolism, drug delivery and toxicity evaluation by SECM. Shao et al. [143] reported their kinetic analysis of K^+ transfer facilitated by DB18C6 across the water/DCE nano-interface using SECM with a nanopipette tip. Mirkin et al. [144] also reported on their nanopipette ITIES based SECM investigation to characterize rapid ion transfer, as well as information about tip geometry. Shen et al. [145] reported on the high resolution imaging of ion transport through single nanopores by SECM with a 17 nm radius pipette supported ITIES to study the permeability of porous nanocrystalline silicon membranes.

A vast range of inorganic ions have been investigated at the ITIES. Koryta [146] first reported on the facilitated ion transfer (FIT) of potassium and sodium ions at the ITIES by using ionophores DB18C6 and valinomycin, respectively, in the organic phase. That was a pioneering invention for a new path of ion selective sensors development using the ITIES. Osakai and co-workers reported on the development of K^+ ion-selective sensors based on FIT of K^+ at water/PVC membrane microinterfaces using DB18C6 [147]. Shao et al. also reported on FIT of K^+ at water/DCE nano-interface formed at nanopipettes [148]. Kinetic investigation for FIT of Cl^-, Br^-, NO_2^-, and $CH_3CO_2^-$ at micropipette supported water/DCE micro-interfaces has been investigated by Shao et al. using β-octafluoro-*meso*-octamethylcalix[4]pyrrole [149] and detection of ammonium ions was reported at the water/1,6-dichlorohexane micro-interface by a lipophilic cyclodextrin using CV, DPV, SWV [150]. Another investigation of a Cu^{2+} ion selective sensor development was reported at a liquid/organogel micro-interface [151]. For the last few decades, analytical application of the ITIES has been employed to investigate the maximum available inorganic cations and anions in environmental water samples [152]. Highly toxic hexachromic anions Cr(VI) was investigated across a microhole array-supported water/PVC-NPOE interface facilitated by Aliquat 336 to

develop a simple and sensitive detection technique [46]. Radioactive uranyl (dioxouranium, UO_2^{2+}) was investigated by Ding et al. [153] across a water/DCE micro-interface using tributyl phosphate facilitator and they also calculated the Gibbs energy of transfer and the association constant of uranyl-tributyl phosphate complex.

So, it has been seen that, although the electrochemistry at liquid/liquid interfaces is a comparatively new technique, but it has bloomed in lots of research areas, because of its versatile applications and suitability. Especially, the miniaturized ITIES brought a new dimension in research by overcoming the limitations of the larger interfaces. Research on this field is expanding rapidly and there are many opportunities to develop by integrating with other techniques as well.

1.4 Aims of this Work

The general aim of this research is to investigate the electrochemical detection and characterization of different types of micro- and macro species as well as inorganic species at micro-interface between two immiscible electrolyte solutions by applying cyclic voltammetry (CV) and differential pulse voltammetry (DPV). These interfaces were produced at the tip of the glass micro pipettes. The goal was to find electroanalytical behavior that might be useful for detection of different types of molecules. There are many well-established techniques available for the detection and characterization of different ranges of molecules. Gas chromatography-mass spectrometry (GC-MS), high-performance liquid chromatography-mass spectrometry (HPLC-MS), liquid chromatography-tandem mass spectrometry (LC-MS-MS), colourimetric detection, fluorimetric and flow injection analysis are a few of those techniques. These are widely used for ultra-trace analysis and have excellent sensitivity and accuracy. However, those techniques are very complex and based on sophisticated instrumentation, with high costs for establishment and maintenance; they necessitate complicated sample pre-treatment, take a long time to implement and, overall, need highly trained personnel to run those instruments. Most importantly, those techniques are not suitable for in-field data acquisition. Electrochemical techniques could be one of the alternative methods to overcome those difficulties and at the same time keeping low detection limits. Electrochemical techniques that use ion-transfer electrochemistry as the basis for detection open up electrochemical methods to detection of a wider range of target substances that are not easy to oxidise or reduce

(i.e. not redox-active). The sensors or analytical devices constructed by this ion transfer technology are expected to be robust; will cover more variety of analytes; will reduce the cost of instrumentation and maintenance and, more importantly, they will be suitable for infield applications compared to the other available technologies. The objectives for this thesis are as below:

To carry out analysis for different aspects of this research project, the first target was to prepare pipettes from glass capillaries where the μITIES will be formed. The experimental data which has come from analysis by the pipettes would not be reliable if the prepared pipettes do not produce reproducible results. So, the first and most important task is to produce reproducible pipettes. Then the pipettes should be modified to get the reproducible data from that pipette. The modification of the pipettes has been done by a silanization reaction at the inner surfaces of the pipettes. Then the performance and reproducibility of the pipettes was checked by both electrochemical and microscopic techniques.

The detection and investigation of the electrochemical properties of per- and polyfluoroalkyl (PFAS) substances (which became of globally emerging concern because of their serious impact on the environment and on living things) at the μITIES was one of the goals of this research. Four PFAS substances namely Perfluorooctanoic acid (PFOA), Perfluorobutanesulfonic acid (PFBS), Perfluorohexanesulphonic acid (PFHxS) & Perfluorooctanesulfonic acid (PFOS), were studied at the μITIES based on micropipettes employing CV and DPV techniques. Besides the study of the electrochemical behavior, the major objective of the investigation was to assess the selectivity of the μITIES for the detection of PFAS substances in mixtures of different PFAS materials.

Another objective of this thesis was to investigate the electrochemical characterization of PAMAM dendrimers at single μITIES. Dendrimers have well-defined structure, molecular size and surface charges. PAMAM consists of three different types of amino groups and the pKa of those groups are different. For this reason, PAMAM dendrimers are expected to interact differently at ITIES depending on the pH of the solution. The voltammetric behavior of the first four generations of PAMAM dendrimers was investigated at liquid/liquid single micro-interfaces within a wide range of aqueous

phase pH (1.75 to 11.0) so as to understand the change of electrochemical behavior of dendrimers with pH and molecular size.

The detection of sulphate ion at liquid/liquid micro-interfaces by facilitated ion transfer with three new squaramide ionophores was another aim of this research work. The detection of sulphate is important because of its concentration in water and atmosphere increases rapidly from different sources causing increases the acidification levels which became a serious health concerns. Electrochemical characterization of these three ionophores, mechanism of transfer process and kinetic parameters were investigated by utilizing cyclic voltammetry at single μITIES formed at the tip of the pipettes. Four different size of pipettes have been used for each ionophore facilitated transfer to check the effect on size of ITIES.

Chapter 2

Pipette Preparation and Characterization.

2.1 Introduction

The liquid-liquid (L/L) interface was miniaturised by using different size micropipettes or nanopipettes. Pipettes are usually fabricated from borosilicate or quartz capillaries. Taylor and Girault for the first time introduced the idea of miniaturization of L/L interfaces in 1986 [6]. They used pulled glass micropipettes to create micrometre-sized liquid/liquid interfaces. It is also recommended to have a filament inside the nanopipette so it can be filled with solution [154]. For this present work both quartz and borosilicate capillaries were used to make micropipettes and nanopipettes. Nanopipettes were prepared to check the reproducibility of the pipettes only, not for the electrochemical experiments. The electrochemical experiments for this whole research were carried out by micropipettes. A laser pipette puller (e.g., P2000 from Sutter Instruments) was used to pull these capillaries to fabricate pipettes.

The P-2000 is a microprocessor controlled CO_2 laser-based pipette puller, which heats the glass capillaries and pulls it apart to create the micropipette tips employed in experiments. The ultimate size, shape and the quality of a pipette are determined by the parameter values that are programmed in the instrument. Each program consists of one or more cycles (maximum 8) and each cycle consists of five programmable parameters named heat, filament, velocity, delay and pull [154, 155].

Heat ranges from 0 to 999 which specifies the output power of the laser or the amount of energy supplied to the glass. The heat required to melt a piece of glass is a function of the "FILAMENT" that has been selected and the typical starting range of HEAT settings depends on the types/materials of the glass [155].

Filament (FIL) ranges from 0 to 5 specifies the scanning pattern of the laser beam that is used to supply heat to the glass. The P-2000 is preprogramed with scanning pattern values (filament), each of which defines the longitudinal length where the laser heat is applied and the rate of the scan [155].

The velocity (VEL) ranges from 0 to 225 which specifies the velocity at which the puller bar must be moving before the hard pull is executed. Lower values are used for patch and injection pipettes and higher values are used for micropipettes [155].

Pull ranges from 0 to 255 and controls the force of the hard pull. In general, the higher pull is applied for the smaller pipette's tip diameter and for a longer taper. A change of one unit indicates a change of 4 mA of current through the pull parameter. Typically 10 units or more are required to observe an effect [155].

The delay ranges from 0 to 255 and controls the time between when the heat turns off and when the hard pull is activated. The higher the delay value, the cooler the glass will be when the hard pull is executed. Thus, increasing the delay results in decreased taper length and increased tip diameter [155].

In this present work, different sizes of micro / nano pipettes were prepared and checked for reproducibility of the system by both scanning electron microscopy (SEM) and electrochemical measurements. The inner surface of the pipettes was modified by silanization to convert it to a hydrophobic surface from hydrophilic so as to get a stable liquid/liquid interface at the tip of the pipettes for electrochemical analysis.

2.2 Experimental

2.2.1 Reagents and materials

All the reagents were purchased from Sigma-Aldrich Australia Ltd. and used as received, unless otherwise indicated. The organic electrolyte bis(triphenylphosphoranylidene)ammonium tetrakis(4-chlorophenyl)borate (BTPPATPBCl) was prepared by metathesis of equimolar amounts of bis(triphenylphosphoranylidene)ammonium chloride (BTPPACl) and potassium tetrakis(4-chlorophenyl)borate (KTPBCl) as reported earlier [77]. BTPPATPBCl (0.01 M) solutions were prepared in 1,2-dichloroeheane (DCE). Chlorotrimethylsilane was used for silanization of pipettes. Different size of quartz and borosilicate glass capillaries were purchased from Sutter Instrument through SDR Scientific Pty Ltd. All aqueous solutions (e.g. LiCl solution) were prepared in purified water from a USF Pure-lab plus UV (resistivity: 18.2 MΩ cm).

2.2.2 Electrochemical cell setup

Electrochemical measurements were conducted by using an Autolab PGSTAT302N electrochemical analyser (Metrohm Autolab, Utrecht, The Netherlands) running with NOVA software. A typical cell setup with a pipette to form an ITIES at the tip of the

pipette is shown in the Figure 2.2.2.1. The organic electrolyte phase was introduced into the pipette which comes up to the tip and the organic reference solution (saturated BTPPACl in 10 mM LiCl) was placed on the top of the organic phase. Then the pipette was immersed into the aqueous phase so that an ITIES formed at the tip of the pipette. As this was a miniaturized interface, so a two-electrode system was employed for measurements in this electrochemical cell. An Ag/AgCl electrode was in the aqueous solution and another Ag/AgCl electrode used in the organic reference solution. The micro-interface was polarised by imposing a potential difference between these two electrodes. Unless stated otherwise, a 10 mVs^{-1} scan rate was applied to carry out cyclic voltammetry (CV) experiments. The cell is described in the following scheme.

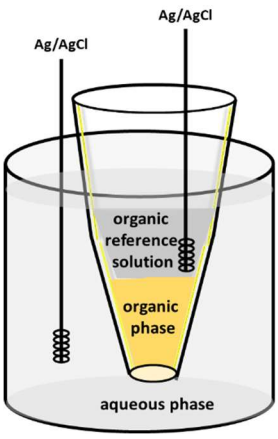

Figure 2.2.2.1: *A typical cell setup to form an ITIES at the tip of the pipette.*

$$\text{Ag}\,\big|\,\text{AgCl}\,\big|\,\begin{matrix}\text{Sat'd BTPPACl}\\ \text{in 10 mM LiCl}\end{matrix}\,\big|\,\begin{matrix}\text{10 mM BTPPATPBCl}\\ \text{in DCE}\end{matrix}\,\big\|\,\begin{matrix}\text{x µM TPrA}^{+}\text{ in}\\ \text{10 mM LiCl}\end{matrix}\,\big|\,\text{AgCl}\,\big|\,\text{Ag}$$

2.2.3 Scanning electron microscopy

The pipettes were characterized by scanning electron microscopy (SEM) to check their size and shape. SEM images were recorded using Neon FIBSEM (model: Neon 40EsB). Neon is a dual-beam Field Emission Scanning Electron Microscope (FESEM). Images of the pipettes were taken with 2 kV beam, 20.00 µm aperture, using the In Lens secondary electron detector. The pore or tip dimensions from the SEM images was calculated using ImageJ software.

2.2.4 Fabrication of glass pipettes

For this research, several programs were used to produce different size and shape of pipettes from quartz (O.D. 1.0 mm; I.D. 0.75 mm) and borosilicate (O.D. 1.0 mm; I.D. 0.75 mm) glass capillaries. It is important to clean the capillaries very well before pulling, because if there is any dust inside the capillaries, it would be very difficult to

clean it after formation of pipettes, especially for nano or small size micropipettes. The capillaries were cleaned with water and acetone for several times and then sonicated in a mixture of water and methanol (50% : 50%) for 10 minutes. Then the dried capillaries were pulled by the pipette puller with the desirable parameters. Figure 2.2.4.1 shows how the laser pipette works. First, the laser heat is applied to the centre of the glass capillary and at the same a time force is applied to the opposite direction as velocity which makes a taper in the centre of the capillary. After the delay, the hard pull is applied and the capillary separates into two pipettes.

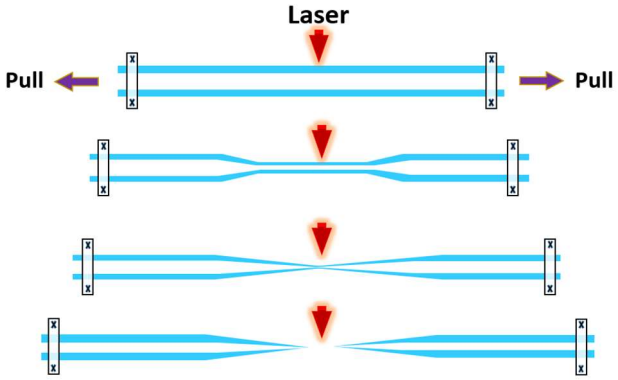

Figure 2.2.4.1: *Schematic representation of pipette fabrication process using a laser-assisted puller. Laser beam is used to heat the centre of the capillary, introducing a taper in the glass capillary. In the second step, a strong pull is applied in opposite direction to separate the two pipettes.*

Figure 2.2.4.2 shows the schematic photos of the P2000 pipette puller and how it works. Figure 2.2.4.2 (1 & 2) shows the photos of the P2000 puller machine outside and inside, respectively. Figure 2.2.4.2 (3 & 4) shows how the glass capillaries are placed inside the puller and tightened by the clamping knob. Figure 2.2.4.2 (5) shows the program selected for a particular pipette. The pull button should be pressed after selecting the program and the laser light on means all five parameters start functioning according to the previous descriptions. Figure 2.2.4.2 (6) shows the separated two pipettes.

Figure 2.2.4.2: *Schematic photos of P2000 pipette puller and how it works. Photos 1 & 2 shows the picture of P2000 puller outside and inside respectively. Photos 3 & 4 shows how the glass capillaries set through the clamps. Photo 5 shows the selecting program and the laser light on indicates pull started and photo 6 shows the two separated pulled pipette.*

2.2.5 Modification of pipettes (silanization)

We used organic solution inside the pipette and aqueous electrolyte outside the pipette to construct an ITIES at the tip of the pipette. The inner surface of the pipettes need to be modified to convert the hydrophilic inner surface into a hydrophobic surface in order to achieve a stable ITIES. Organofunctional alkoxysilanes have been widely used to form high-density self-assembled monolayers (SAMs) on hydroxyl-terminated material surfaces, such as glass, in order to modify the properties or chemical functions of such surfaces [156]. A large range of silane compounds are commercially available, with amino, thiol, carboxyl, epoxide, or other functional groups [156]. In this research,

chlorotrimethylsilane was used to create a hydrophobic layer on the inner glass surface of the pipette via a silanization reaction. Chlorotrimethylsilane was used because with this monochlorosilane, only hydrophobic monolayer is formed by chemical reaction. The reaction mechanism is described in Figure 2.2.5.1.

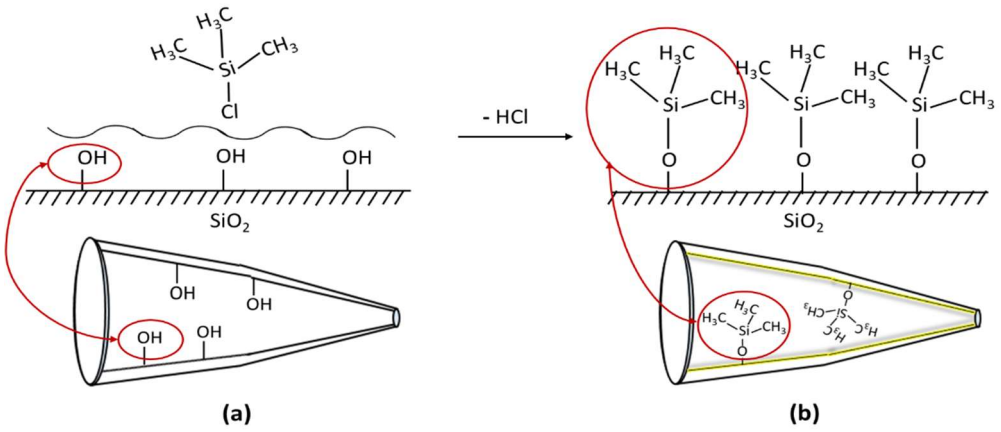

Figure 2.2.5.1: *(a) untreated pipette inner glass surface and introduce of chlorotrimethylsilane (b) silanization reaction creates Si-O-Si bonds in the inner glass surface and makes it hydrophobic.*

The silanization of the inner surface of the pipettes was done at laboratory room temperature with a very simple procedure described in Figures 2.2.5.2 and 2.2.5.3. Here we used a glass jar (70 mm high x 65 mm diameter) with PTFE (Teflon) cap. The cap was joined with 9 tubes (Tygon R3603, I.D. 1 mm x O.D. 3 mm) by drilling small holes in the cap and 9 pipettes were fitted in the 9 tubes, Figure 2.2.5.2 (1 & 2). Then about 0.1 ml or 1-2 drops of chlorotrimethylsilane was added to the glass jar and immediately covered by the cap fitted with pipettes. Chlorotrimethylsilane is a very volatile substance, so the vapour goes to the pipettes very quickly and the silanization reaction with the hydroxyl groups of the pipette glass surface occurs and converts the surface to a hydrophobic character by forming a monolayer. After 30-40 minutes, the pipettes were removed from the tubes and dried for 3-5 hours, as shown in Figure 2.2.5.2 (3). Figure 2.2.5.3 also shows the schematic representation of the silanization procedure used in this research. Chlorotrimethylsilane is a very hazardous substance, so much precautious steps must be taken for handling this chemical and all the silanization process was carried out in a fume hood.

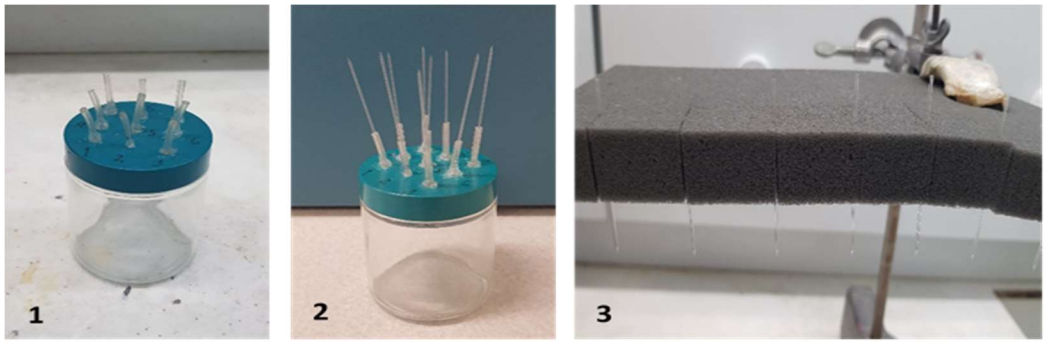

Figure 2.2.5.2: *(1) glass jar with attached tubes on the cap of the jar (2) pipettes fitted in the tube (3) pipettes dried after silanization.*

Figure 2.2.5.3: *Schematic presentation of silanization process of pipette. (1) glass jar with PTFE (Teflon) cap (2) the caps are joined with tubes (3) pipettes fitted in the tube (4) 1/2 drops of chlorotrymethylsilan added into the jar (5) vapour of the chlorotrymethylsilan goes through the pipettes and makes silanization on the inner surface of the pipettes.*

2.3 Results and discussions

2.3.1 Characterization of pipettes

The prepared pipettes were characterized by both SEM and electrochemical measurements. The importance of silanization is investigated electrochemically. Figure 2.3.1.1(a) shows the CVs of blank electrolyte solutions (3 scans) at non-silanized pipettes. These CVs became broader on each subsequent scan and this

indicates the instability of the interface in non-silanized pipettes. This instability may cause the gradual movement of the aqueous phase into the pipette [75]. Figure 2.3.1.1(b) shows the same experiment with the same size silanized pipette. In this case, all three scans completely overlap each other, indicating that the silanized pipette makes a stable ITIES at the tip of the pipette. Figure 2.3.1.1(c) shows the overlayed blank CVs of 3rd scan at silanized and nonsilanized pipettes to illustrate the significance of the modification of the pipette's inner surface.

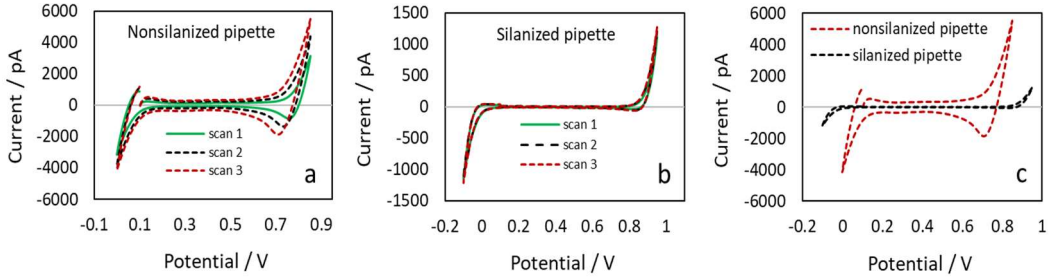

Figure 2.3.1.1: *(a) 3 different scans (scan rate 10 mV/s) of blank at nonsilanized pipette shows the instability of ITIES (b) 3 different scans (scan rate 10 mV/s) of blank at the same size silanized pipette represents very stable interface and (c) combined CVs of blank at the same size silanized and nonsilanized pipettes.*

The μITIES formed at the tip of the pipettes were characterized by cyclic voltammetry of tetrapropylammonium ion ($TPrA^+$) transfer across the water/DCE interface. Because the $TPrA^+$ response is much studied and very well established at the ITIES, it can be referred to as a model example for characterization of liquid-liquid interfaces [157, 158]. The transfer of $TPrA^+$ from the aqueous phase to the organic phase is started when the applied potential difference at the interface reaches the free energy of transfer for $TPrA^+$ ($\Delta G_{TPrA^+}^{O'w\rightarrow DCH} = -8.3$ kJ mol^{-1}) [159]. When the interfacial potential is reduced below $\Delta G_{TPrA^+}^{O'w\rightarrow DCH}$ then the process is reversed, i.e. $TPrA^+$ transfers back to the aqueous phase. Figure 2.3.1.2(a) shows the 40 μM $TPrA^+$ transfer with blank at 2.8 μm diameter pipette tip which represents an ideal $TPrA^+$ voltammogram at a micro-ITIES. The background-subtracted voltammograms (forward scan only) for six concentrations (20, 40, 60, 80, 100 and 120 μM) of $TPrA^+$ are shown in Figure 2.3.1.2(b).

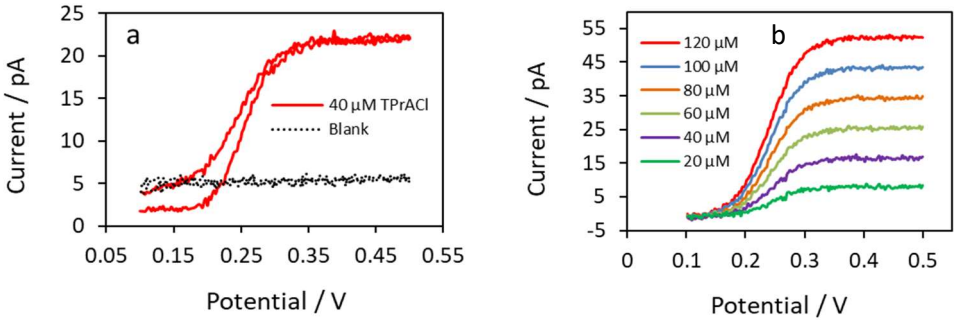

Figure 2.3.1.2: *(a) 40 µM $TPrA^+$ transfer with blank at 2.8 µm diameter pipette tips (b) background-subtracted voltammograms (forward scan only) of 20, 40, 60, 80, 100 and 120 µM $TPrA^+$*

The current increased steadily until a steady-state current reached which is in good agreement with the electrochemical behaviours of miniaturized ITIES reported previously [86, 88, 158]. This experiment proves that the micropipettes working nicely. The diameters/radius of the pipette tips were measured by using the Saito equation [160, 161],

$$I_{ss} = 4|z_i|FD_iC_ir_a \qquad \text{Equation 2.3.1.1}$$

where I_{ss} is the steady state current, F, D, C and r_a are the Faraday constant, diffusion coefficient, concentration and radius of the interface respectively.

Radius of the pipette tips were also measured by the following equations [160, 161],

$$I_{ss} = 3.35\pi|z_i|FD_iC_ir_a \qquad \text{Equation 2.3.1.2}$$

and for hemispherical surface

$$I_{ss} = 2\pi|z_i|FD_iC_ir_a \qquad \text{Equation 2.3.1.3}$$

Throughout the thesis, the pipette radius was used by using the Equation 2.3.1.1 as because this radius matches very closely with SEM measurements. The radius measurement by SEM was done only for chapter 2. However, radius of all pipettes used in this thesis were also calculated using Equation 2.3.1.2 & Equation 2.3.1.3 and presented in appendix B.

The diameter of the pipette for this experiment calculated from Equation 2.3.1.1 is 2.83 µm (Figure 2.3.2.2.2) using a $TPrA^+$ diffusion coefficient value 7.5 x 10^{-6} cm^2s^{-1}

[88, 162], whereas a diameter of 2.85 µm was determined by SEM imaging. These same types of measurement experiments were implemented for different size of pipettes to check the tip size, and for all cases both electrochemical and SEM results were similar. Diffusion coefficient is one of the best criteria to check the system for known substance. Diffusion coefficient for $TPrA^+$ (D_{TPrA^+}) in aqueous phase is calculated 8 x 10^{-6} cm^2s^{-1} which is very close to the literature value 7.5 x 10^{-6} cm^2s^{-1} [88, 162] or 6.2 x 10^{-6} cm^2s^{-1} [81, 163]. This proves that the liquid/liquid interface formed at the tip of the pipettes works very well.

Another well-known experiment is the transfer of K^+ ion transfer facilitated by the ionophore dibenzo-18-crown-6 [73], which is also a model experiment and was investigated to further check the pipettes' performance. Figure 2.3.1.3(a) shows no K^+ transfer from aqueous phase to organic phase without the ionophore, but when dibenzo-18-crown-6 ionophore is added to the organic phase then the K^+ ions transfer and gives a reversible voltammogram.

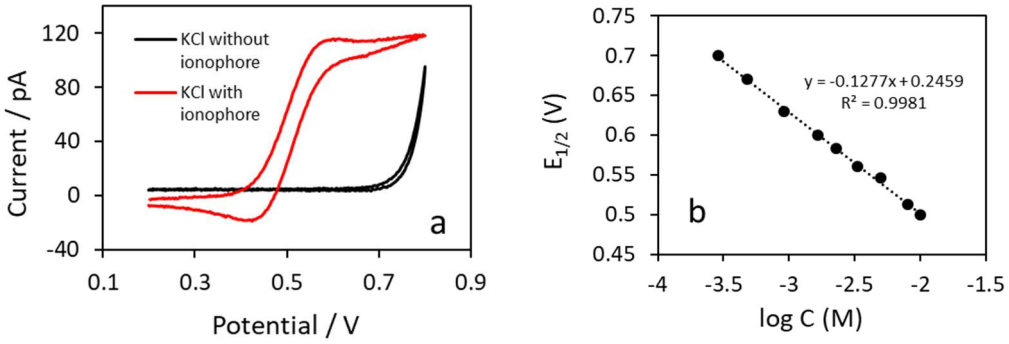

Figure 2.3.1.3: *(a) Assisted ion transfer for K^+ (10 mM) with dibenzo-18-crown-6 and (b) $E_{1/2}$ (V) vs log C (M) for K^+ ion transfer at water/DCE interface with 3.5 µm diameter pipette radius.*

The equilibrium constant (K_a^o) for the complexation reaction between K^+ and dibenzo-18-crown-6 was also calculated for this experiment. K_a^o was studied with an excess of potassium in the aqueous solution ($C_{K^+} >> C_L$) according to the following equation [73]

$$\Delta_o^w E_{1/2} = \Delta_o^w E_{K^+}^{o\prime} - \frac{2.303RT}{zF} \log(K_a^o \, C_{K^+}^w) \qquad \text{Equation 2.3.1.4}$$

where $\Delta_o^w E_{K+}^{o\prime}$ is the formal transfer potential of K^+ ion. According to that equation, plotting the half-wave potential ($\Delta_o^w E_{1/2}$) for the ion transfer process versus $\log(C_{K+}^w)$ will be a straight line. Figure 2.3.1.3(b) shows $E_{1/2}$ (V) vs log concentration (M) of K^+ ions for K^+ ion transfer gave a straight line and K_a^o was calculated from that y-axis intercept. Our calculated log K_a^o is 11.1 by using the formal transfer potential value 0.9 V [164], which is very close to the literature value 9.9 [164].

2.3.2 Reproducibility of the pipettes

Reproducibility of the prepared pipettes is the most important to get the reproducible data for any analysis at the micro-ITIES formed at the tip of the pipettes. Otherwise, no analysis will be reliable. That is why the pipettes' reproducibility was checked throughout our research. Many pipettes of different sizes (with different programs) were prepared for the experiments and to check the pipettes' quality. For most of the cases, the size of the pipettes was checked by both electrochemical experiments and SEM measurements. Electrochemical measurements were done by the CV experiments of $TPrA^+$ transfer and the diameter calculated by using the Saito equation (Equation 2.3.1.1). Here the results for five different types of pipettes prepared from five different programs are shown, to assess the reproducibility of the pipettes and efficiency of P2000 pipette puller.

2.3.2.1 Pipette type 1

Borosilicate glass capillaries were used for these pipettes. The dimension of the capillaries were (O.D. 1.0 mm; I.D. 0.75 mm). The five pulling parameters to make these pipettes were set as below:

Heat	Filament	Velocity	Delay	Pull
400	4	20	200	70

The average time taken to pull these capillaries for these pipettes was ≈ 2.10 s. The dimensions and the quality of 10 pipettes were checked by SEM and another eight pipettes were checked by CV experiments of $TPrA^+$ ion transfer after silanization of the pipettes. The diameters of the pipettes were measured from the forward scan current by using the Saito equation, where the value diffusion coefficient was used as

7.5 x 10^{-6} cm^2s^{-1} [88, 162]. The background subtracted forward CV scans and the respective data for the calculation of the diameter of the eight pipettes are given in the following eight Figures (2.3.2.1.1 - 2.3.2.1.8) and eight Tables (2.3.2.1.1 - 2.3.2.1.8).

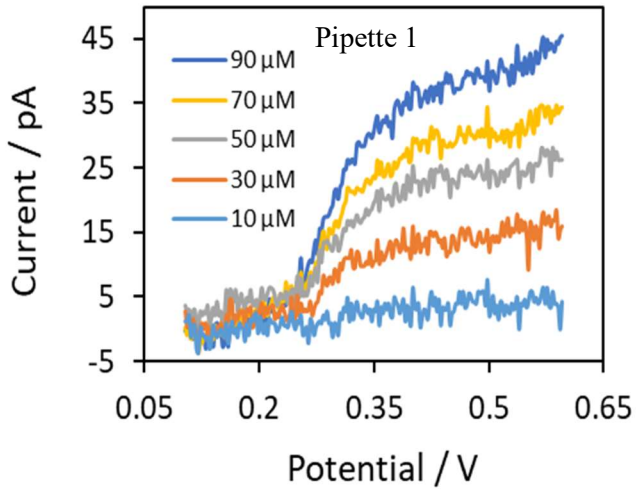

Figure 2.3.2.1.1: *Background subtracted forward CVs of 10 µM, 30 µM, 50 µM, 70 µM and 90 µM $TPrA^+$ ions transfer at water/DCE micro-ITIES formed with pipette 1.*

Figure 2.3.2.1.1 shows the forward cyclic voltammograms of 10 µM, 30 µM, 50 µM, 70 µM and 90 µM $TPrA^+$ ions transfer at water/DCE interface with pipette 1. Table 2.3.2.1.1 shows the average diameter of this pipette tip was 3.10 µm with 6.95% relative standard deviation.

Table 2.3.2.1.1: *Forward currents (i_{ss}) for the CVs of 10 µM, 30 µM, 50 µM, 70 µM and 90 µM $TPrA^+$ ions transfer and the respective data to determine the diameter of the pipette 1.*

i_{ss} (pA)	C (µM)	$4\|z_i\|FDC$	r (cm)	d (µm)	d (average) (µm)	% RSD
5	10	3.0 x 10^{-8}	0.000166	3.32	3.10 (±0.22)	6.95
15	30	9.0 x 10^{-8}	0.000166	3.32		
23	50	15 x 10^{-8}	0.000153	3.06		
30	70	21 x 10^{-8}	0.000142	2.85		
40	90	27 x 10^{-8}	0.000148	2.95		

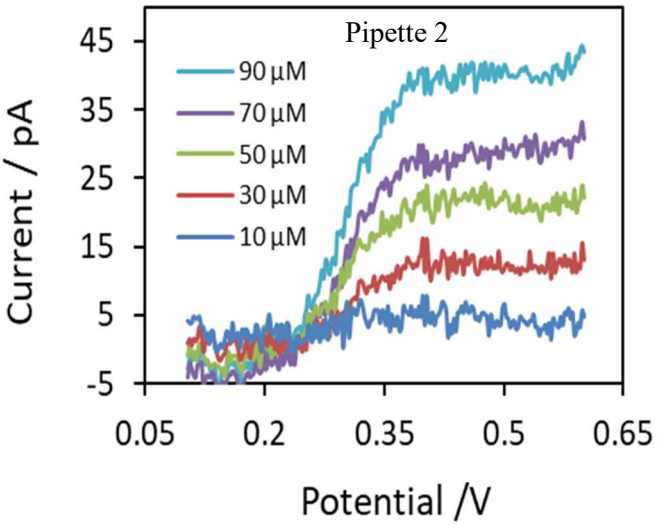

Figure 2.3.2.1.2: *Background subtracted forward CVs of 10 µM, 30 µM, 50 µM, 70 µM and 90 µM $TPrA^+$ ions transfer at water/DCE micro-ITIES formed with pipette 2.*

Figure 2.3.2.1.2 shows the forward cyclic voltammograms of 10 µM, 30 µM, 50 µM, 70 µM and 90 µM $TPrA^+$ ions transfer at water/DCE interface with pipette 2. Table 2.3.2.1.2 shows the average diameter of this pipette tip was 3.12 µm with 2.54% relative standard deviation.

Table 2.3.2.1.2: *Forward currents for the CVs of 10 µM, 30 µM, 50 µM, 70 µM and 90 µM $TPrA^+$ ions transfer and the respective data to measure the diameter of the pipette 2.*

i_{ss} (pA)	C (µM)	$4\|z_i\|FDC$	r (cm)	d (µm)	d (average) (µm)	% RSD
4.5	10	3.0×10^{-8}	0.000149	2.99	3.12 (±0.08)	2.54
14	30	9.0×10^{-8}	0.000155	3.10		
24	50	15×10^{-8}	0.000159	3.19		
33	70	21×10^{-8}	0.000157	3.13		
43	90	27×10^{-8}	0.000159	3.17		

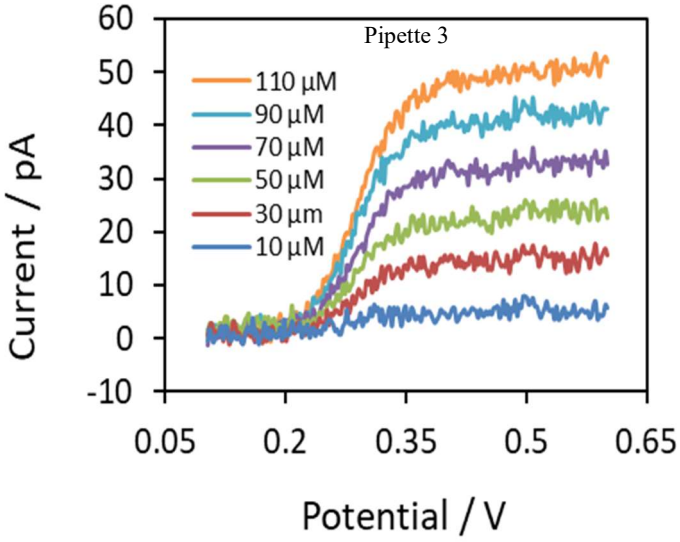

***Figure 2.3.2.1.3**: Background subtracted forward CVs of 10 µM, 30 µM, 50 µM, 70 µM, 90 µM and 110 µM $TPrA^+$ ions transfer at water/DCE micro-ITIES formed with pipette 3.*

Figure 2.3.2.1.3 shows the forward cyclic voltammograms of 10 µM, 30 µM, 50 µM, 70 µM, 90 µM and 110 µM $TPrA^+$ ions transfer at water/DCE interface with pipette 3. Table 2.3.2.1.3 shows the average diameter of this pipette tip was 2.51 µm with 5.56% relative standard deviation.

***Table 2.3.2.1.3:** Forward currents for the CVs of 10 µM, 30 µM, 50 µM, 70 µM and 90 µM $TPrA^+$ ions transfer and the respective data to measure the diameter of the pipette 3.*

i_{ss} (pA)	C (µM)	$4\|z_i\|FDC$	r (cm)	d (µm)	d (average) (µm)	% RSD
4	10	3.0×10^{-8}	0.000133	2.66	2.51 (±0.14)	5.56
12	30	9.0×10^{-8}	0.000133	2.66		
19	50	15×10^{-8}	0.000126	2.52		
26	70	21×10^{-8}	0.000123	2.47		
33	90	27×10^{-8}	0.000122	2.44		
38	110	33×10^{-8}	0.000115	2.30		

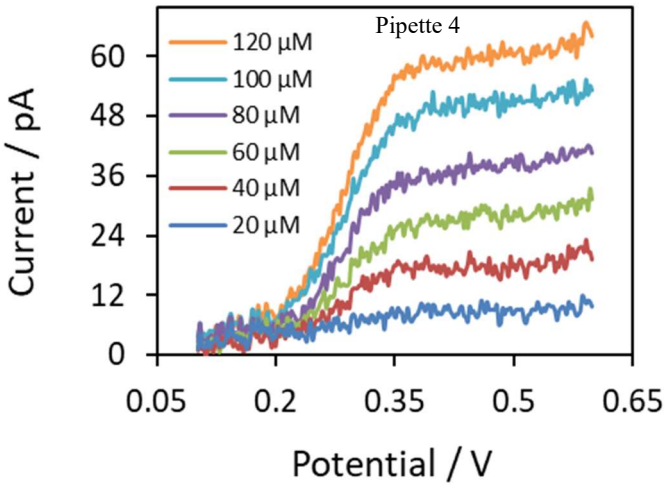

Figure 2.3.2.1.4: *Background subtracted forward CVs of 20 µM, 40 µM, 60 µM, 80 µM, 100 µM and 120 µM $TPrA^+$ ions transfer at water/DCE micro-ITIES formed with pipette 4.*

Figure 2.3.2.1.4 shows the forward cyclic voltammograms of 20 µM, 40 µM, 60 µM, 80 µM, 100 µM and 120 µM $TPrA^+$ ions transfer at water/DCE interface with pipette 4. Table 2.3.2.1.4 shows the average diameter of this pipette tip was 2.28 µm with 3.77% relative standard deviation.

Table 2.3.2.1.4: *Forward currents for the CVs of 20 µM, 40 µM, 60 µM, 80 µM, 100 µM and 120 µM $TPrA^+$ ions transfer and the respective data to measure the diameter of the pipette 4.*

i_{ss} (pA)	C (µM)	$4\|z_i\|FDC$	r (cm)	d (µm)	d (average) (µm)	% RSD
6.5	20	6×10^{-8}	0.000108	2.16	2.28 (±0.09)	3.77
14	40	12×10^{-8}	0.000116	2.33		
21	60	18×10^{-8}	0.000116	2.33		
27	80	24×10^{-8}	0.000112	2.24		
36	100	30×10^{-8}	0.00012	2.39		
40	120	36×10^{-8}	0.000111	2.21		

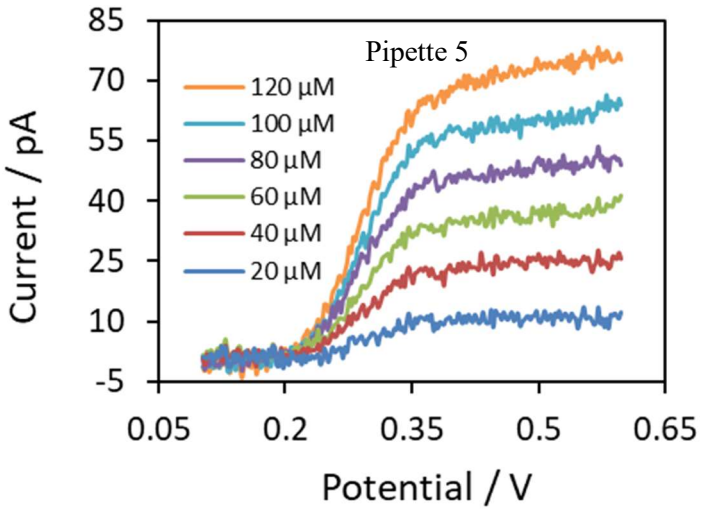

Figure 2.3.2.1.5: *Background subtracted forward CVs of 20 µM, 40 µM, 60 µM, 80 µM, 100 µM and 120 µM $TPrA^+$ ions transfer at water/DCE micro-ITIES formed with pipette 5.*

Figure 2.3.2.1.5 shows the forward cyclic voltammograms of 20 µM, 40 µM, 60 µM, 80 µM, 100 µM and 120 µM $TPrA^+$ ions transfer at water/DCE interface with pipette 5. Table 2.3.2.1.5 shows the average diameter of this pipette tip was 3.12 µm with 4.26% relative standard deviation.

Table 2.3.2.1.5: *Forward currents for the CVs of 20 µM, 40 µM, 60 µM, 80 µM, 100 µM and 120 µM $TPrA^+$ ions transfer and the respective data to measure the diameter of the pipette 5.*

i_{ss} (pA)	C (µM)	$4\|z_i\|FDC$	r (cm)	d (µm)	d (average) (µm)	% RSD
10	20	6×10^{-8}	0.000166	3.32	3.12 (±0.13)	4.26
19	40	12×10^{-8}	0.000158	3.16		
28	60	18×10^{-8}	0.000155	3.10		
35	80	24×10^{-8}	0.000145	2.91		
47	100	30×10^{-8}	0.000156	3.12		
56	120	36×10^{-8}	0.000155	3.10		

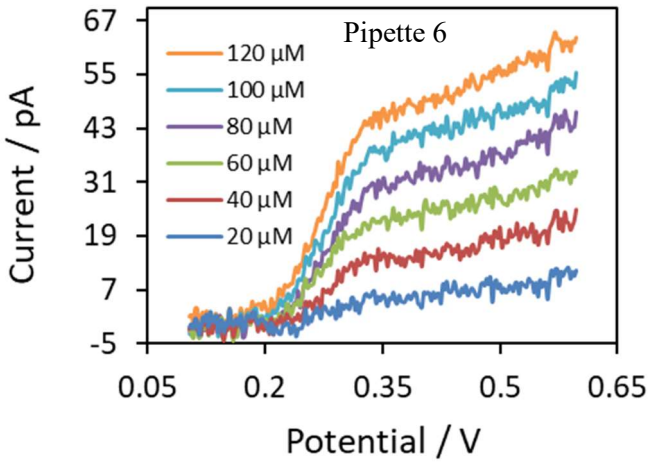

Figure 2.3.2.1.6: *Background subtracted forward CVs of 20 µM, 40 µM, 60 µM, 80 µM, 100 µM and 120 µM $TPrA^+$ ions transfer at water/DCE micro-ITIES formed with pipette 6.*

Figure 2.3.2.1.6 shows the forward cyclic voltammograms of 20 µM, 40 µM, 60 µM, 80 µM, 100 µM and 120 µM $TPrA^+$ ions transfer at water/DCE interface with pipette 6. Table 2.3.2.1.6 shows the average diameter of this pipette tip was 2.82 µm with 4.47% relative standard deviation.

Table 2.3.2.1.6: *Forward currents for the CVs of 20 µM, 40 µM, 60 µM, 80 µM, 100 µM and 120 µM $TPrA^+$ ions transfer and the respective data to measure the diameter of the pipette 6.*

iss (pA)	C (µM)	4|zi|FDC	r (cm)	d (µm)	d (average) (µm)	% RSD
9	20	6×10^{-8}	0.000149	2.99	2.82 (±0.13)	4.47
17	40	12×10^{-8}	0.000141	2.82		
26.5	60	18×10^{-8}	0.000147	2.93		
34	80	24×10^{-8}	0.000141	2.82		
40	100	30×10^{-8}	0.000133	2.66		
49	120	36×10^{-8}	0.000136	2.71		

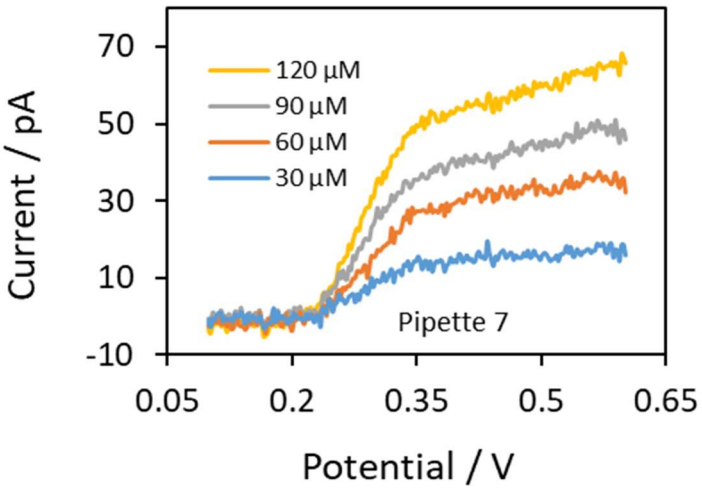

Figure 2.3.2.1.7: *Background subtracted forward CVs of 30 µM, 60 µM, 90 µM and 120 µM $TPrA^+$ ions transfer at water/DCE micro-ITIES formed with pipette 7.*

Figure 2.3.2.1.7 shows the forward cyclic voltammograms of 30 µM, 60 µM, 90 µM and 120 µM $TPrA^+$ ions transfer at water/DCE interface with pipette 7. Table 2.3.2.1.7 shows the average diameter of this pipette tip was 3.09 µm with 5.81% relative standard deviation.

Table 2.3.2.1.7: *Forward currents for the CVs of 20 µM, 40 µM, 60 µM, 100 µM and 120 µM $TPrA^+$ ions transfer and the respective data to measure the diameter of the pipette 7.*

i_{ss} (pA)	C (µM)	$4\|z_i\|FDC$	r (cm)	d (µm)	d (average) (µm)	% RSD
14	30	9×10^{-8}	0.000159	2.96	3.09 (±0.18)	5.81
32	60	18×10^{-8}	0.000177	3.35		
43	90	27×10^{-8}	0.000159	2.98		
59	120	36×10^{-8}	0.000164	3.09		

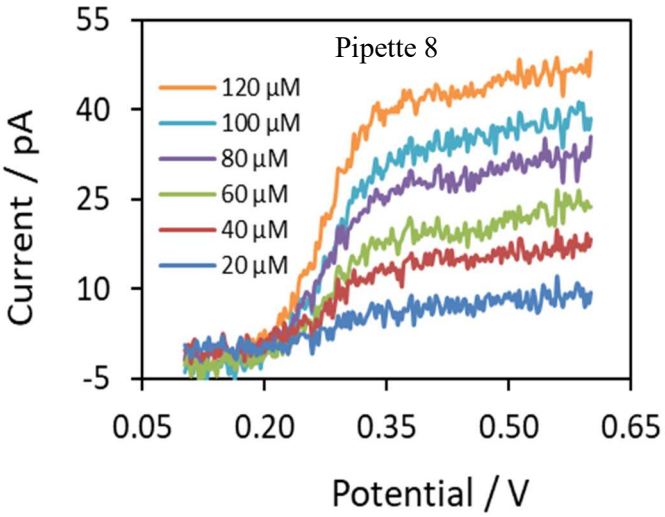

Figure 2.3.2.1.8: *Background subtracted forward CVs of 20 µM, 40 µM, 60 µM, 80 µM, 100 µM and 120 µM $TPrA^+$ ions transfer at water/DCE micro-ITIES formed with pipette 8.*

Figure 2.3.2.1.8 shows the forward cyclic voltammograms of 20 µM, 40 µM, 60 µM, 80 µM, 100 µM and 120 µM $TPrA^+$ ions transfer at water/DCE interface with pipette 8. Table 2.3.2.1.8 shows the average diameter of this pipette tip was 2.47 µm with 6.48% relative standard deviation.

Table 2.3.2.1.8: *Forward currents for the CVs of 20 µM, 40 µM, 60 µM, 80 µM, 100 µM and 120 µM $TPrA^+$ ions transfer and the respective data to measure the diameter of the pipette 8.*

i_{ss} (pA)	C (µM)	$4\|z_i\|FDC$	r (cm)	d (µm)	d (average) (µm)	% RSD
8	20	6×10^{-8}	0.000133	2.66	2.47 (±0.16)	6.48
16	40	12×10^{-8}	0.000133	2.66		
22	60	18×10^{-8}	0.000122	2.44		
29	80	24×10^{-8}	0.00012	2.41		
34	100	30×10^{-8}	0.000113	2.26		
43	120	36×10^{-8}	0.000119	2.38		

Table 2.3.2.1.9 shows the calculated tip diameters from the above eight CV experiments. The average tip diameter was 2.81 and the percentage of their relative standard deviation was calculated as 12.32. Tip diameters for this eight pipettes with their standard deviation plotted in the Figure 2.3.2.1.9. These eight pipettes chosen are prepared in different times and the CV experiments are also done in different days with different potentiostats.

Table 2.3.2.1.9: *Calculated tip diameters from CV experiments and their relative standard deviation (RSD) for pipettes with pulling parameters H: 400; F: 4; V: 20; D: 200 and P: 70.*

Pipette number	Tip diameter (µm)	Average tip diameter (µm)	% RSD
1	3.1	2.81 (±0.35)	12.32
2	3.12		
3	2.51		
4	2.28		
5	3.12		
6	2.82		
7	3.09		
8	2.47		

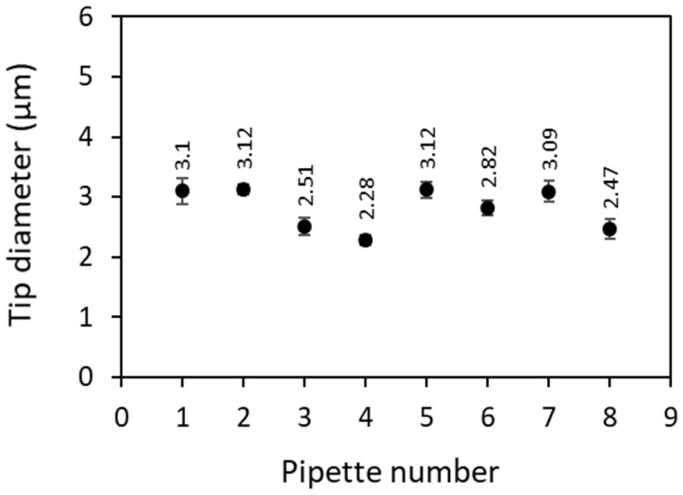

Figure 2.3.2.1.9: *Electrochemical measurement of the tip size of the pipettes those are pulled with pulling parameters H: 400; F: 4; V: 20; D: 200 and P: 70.*

The diameter of the pipettes prepared from the same set of parameters were also investigated by SEM to compare with the results of the electrochemical experiments as well as to check the shapes of the pipette tips.

The following Figure 2.3.2.1.10 shows the size and shape of the nonsilanized pipette tips. Although the size varies a little, they are nearly the same as calculated by the CV analysis. The Figure also shows that the shapes of the tips are not completely circular. This may be because of the parameters or the alignment of the P2000 pipette puller. As the pipette tips are not circular, so to get the pipette diameter, both the long and short diameter was measured and then calculated the average diameter.

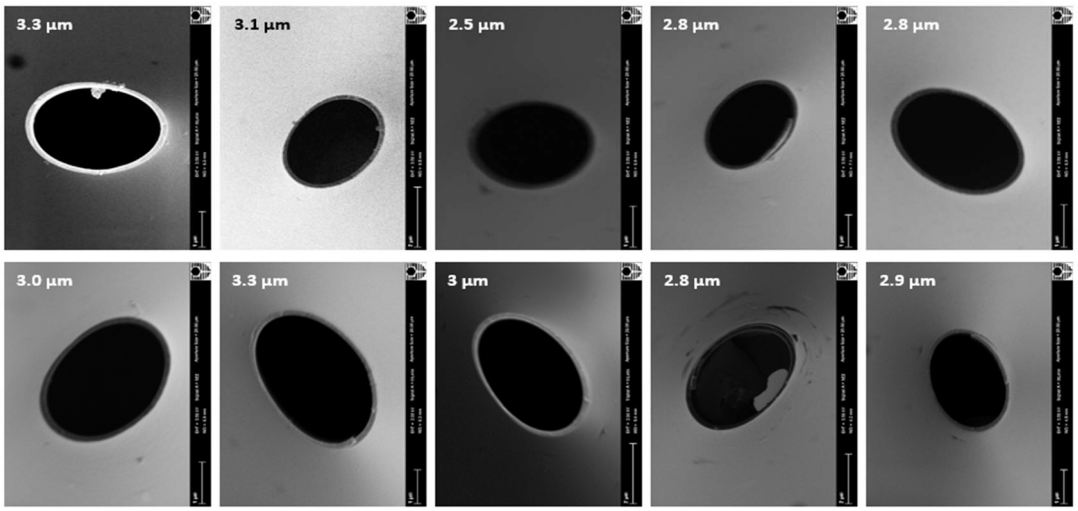

Figure 2.3.2.1.10: *SEM images of the tip of the 10 pipettes those are pulled by P2000 pipette puller with pulling parameters H: 400; F: 4; V: 20; D: 200 and P: 70.*

Table 2.3.2.1.10 shows the 10 pipettes diameter measured from SEM with their average diameter and relative standard deviation. Figure 2.3.2.1.11 shows the graphical representation of these tip diameters with their standard deviation.

Table 2.3.2.1.10: *Measurements of tip diameters from SEM experiments and their relative standard deviation (RSD) for type pipettes with pulling parameters H: 400; F: 4; V: 20; D: 200 and P: 70.*

Pipette number	Tip diameter (µm)	Average tip diameter (µm)	% RSD
1	3.3	2.95 (±0.25)	8.34
2	3.1		
3	2.5		
4	2.8		
5	2.8		
6	3.0		
7	3.3		
8	3.0		
9	2.8		
10	2.9		

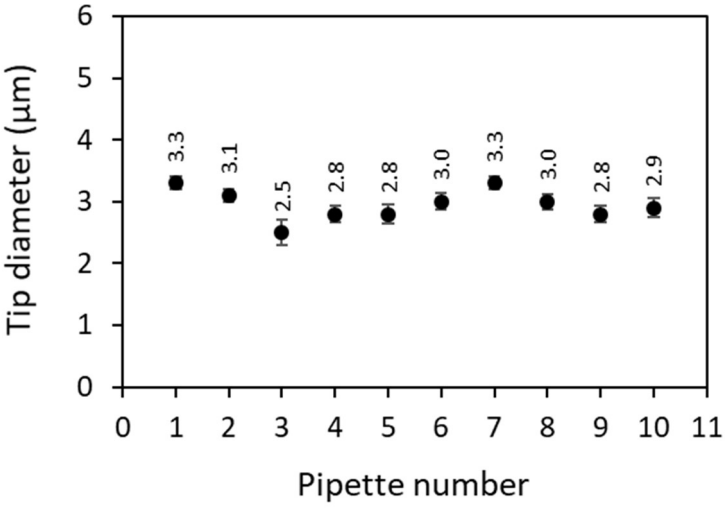

Figure 2.3.2.1.11: *SEM measurement of the tip size of the pipettes those are pulled with pulling parameters H: 400; F: 4; V: 20; D: 200 and P: 70.*

The average diameter of eight pipettes calculated by CV experiments is 2.81 (± 0.35) and their RSD is 12.3%, whereas the average diameter of ten pipettes calculated by SEM measurement is 2.95 (± 0.25) and their RSD is 8.34%. Figure 2.3.2.1.12 shows graphical and statistical representation of CV and SEM results of the tip size for same set of pipette pulling parameters. So, from this comparative analysis of the

electrochemical and SEM measurements, we can say that the pipettes prepared from the set of pulling parameters (H: 400; F: 4; V: 20; D: 200 and P: 70) show very good reproducibility and agreement between the two methods of measurement.

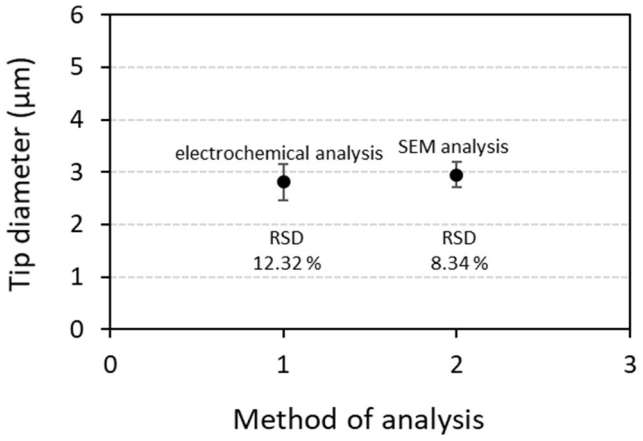

Figure 2.3.2.1.12: *The average diameter of the pipettes by electrochemical and SEM analysis with their standard deviation and relative standard deviation for pulling parameters H: 400; F: 4; V: 20; D: 200 and P: 70.*

2.3.2.2 Pipette type 2

Quartz capillaries were used for these pipettes. The dimension of the capillaries were (O.D. 1.0 mm; I.D. 0.75 mm). The five pulling parameters to make these pipettes were set as below:

Heat	Filament	Velocity	Delay	Pull
500	2	30	130	75

The average time taken to pull these the capillaries for these pipettes was ≈ 3.88 s. Dimension and the quality of 10 pipettes were checked by SEM and another 10 pipettes checked by the CV experiments of $TPrA^+$ ion transfer after silanization of the pipettes. The diameter of the pipettes were measured from the forward current by using the Saito equation. The background subtracted forward CVs and the respective data for the calculation of the diameter of the 10 pipettes are given in the following 10 Figures (2.3.2.2.1-2.3.2.2.10) and Tables (2.3.2.2.1-2.3.2.2.10).

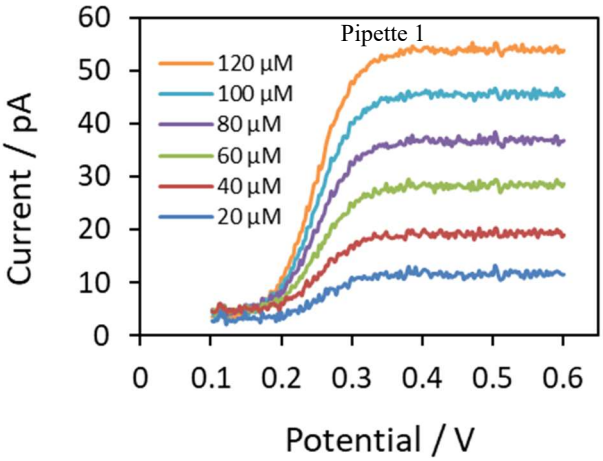

Figure 2.3.2.2.1: *Background subtracted forward CVs of 20 µM, 40 µM, 60 µM, 80 µM, 100 µM and 120 µM $TPrA^+$ ions transfer at water/DCE micro-ITIES formed with pipette 1.*

Figure 2.3.2.2.1 shows the forward cyclic voltammograms of 20 µM, 40 µM, 60 µM, 80 µM, 100 µM and 120 µM $TPrA^+$ ions transfer at water/DCE interface with pipette 1. Table 2.3.2.2.1 shows the average diameter of this pipette tip was 2.72 µm with 4.55% relative standard deviation.

Table 2.3.2.2.1: *Forward currents for the CVs of 20 µM, 40 µM, 60 µM, 80 µM, 100 µM and 120 µM $TPrA^+$ ions transfer and the respective data to measure the diameter of the pipette 1.*

i_{ss} (pA)	C (µM)	$4\|z_i\|FDC$	r (cm)	d (µm)	d (average) (µm)	% RSD
8	20	6×10^{-8}	0.000133	2.66	2.72 (±0.12)	4.55
15	40	12×10^{-8}	0.000125	2.49		
25	60	18×10^{-8}	0.000138	2.77		
34	80	24×10^{-8}	0.000141	2.82		
42	100	30×10^{-8}	0.00014	2.79		
50	120	36×10^{-8}	0.000138	2.77		

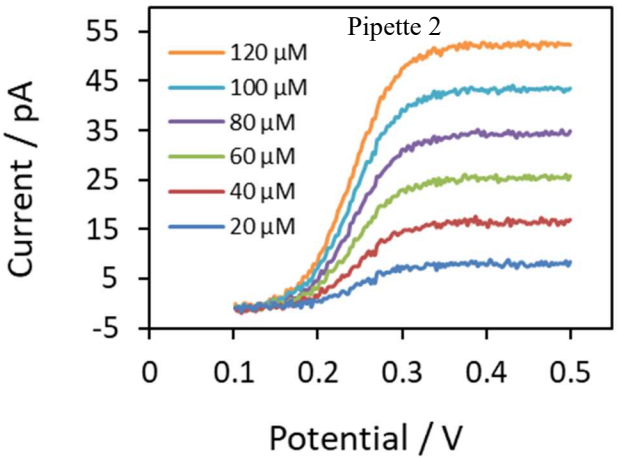

Figure 2.3.2.2.2: *Background subtracted forward CVs of 20 µM, 40 µM, 60 µM, 80 µM, 100 µM and 120 µM $TPrA^+$ ions transfer at water/DCE micro-ITIES formed with pipette 2.*

Figure 2.3.2.2.2 shows the forward cyclic voltammograms of 20 µM, 40 µM, 60 µM, 80 µM, 100 µM and 120 µM $TPrA^+$ ions transfer at water/DCE interface with pipette 2. Table 2.3.2.2.2 shows the average diameter of this pipette tip was 2.83 µm with 4.67% relative standard deviation.

Table 2.3.2.2.2: *Forward currents for the CVs of 20 µM, 40 µM, 60 µM, 80 µM, 100 µM and 120 µM $TPrA^+$ ions transfer and the respective data to measure the diameter of the pipette 2.*

i_{ss} (pA)	C (µM)	$4\|z_i\|FDC$	r (cm)	d (µm)	d (average) (µm)	% RSD
8	20	6×10^{-8}	0.000133	2.66	2.83 (±0.13)	4.67
16	40	12×10^{-8}	0.000133	2.66		
26	60	18×10^{-8}	0.000144	2.88		
35	80	24×10^{-8}	0.000145	2.91		
44	100	30×10^{-8}	0.000146	2.92		
53	120	36×10^{-8}	0.000147	2.93		

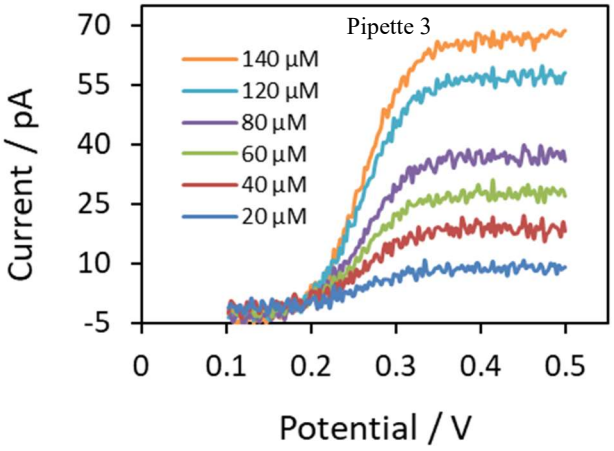

Figure 2.3.2.2.3: *Background subtracted forward CVs of 20 µM, 40 µM, 60 µM, 80 µM, 120 µM and 140 µM $TPrA^+$ ions transfer at water/DCE micro-ITIES formed with pipette 3.*

Figure 2.3.2.2.3 shows the forward cyclic voltammograms of 20 µM, 40 µM, 60 µM, 80 µM, 120 µM and 140 µM $TPrA^+$ ions transfer at water/DCE interface with pipette 3. Table 2.3.2.2.3 shows the average diameter of this pipette tip was 2.98 µm with 5.66% relative standard deviation.

Table 2.3.2.2.3: *Forward currents for the CVs of 20 µM, 40 µM, 60 µM, 80 µM, 120 µM and 140 µM $TPrA^+$ ions transfer and the respective data to measure the diameter of the pipette 3.*

i_{ss} (pA)	C (µM)	$4\|z_i\|FDC$	r (cm)	d (µm)	d (average) (µm)	% RSD
8	20	6×10^{-8}	0.000133	2.66	2.98 (±0.17)	5.66
18	40	12×10^{-8}	0.000149	2.99		
27	60	18×10^{-8}	0.000149	2.99		
36	80	24×10^{-8}	0.000149	2.99		
56	120	36×10^{-8}	0.000155	3.10		
66	140	42×10^{-8}	0.000157	3.13		

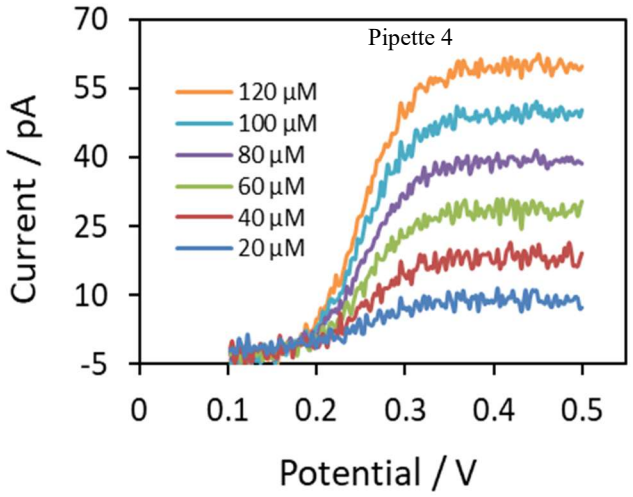

Figure 2.3.2.2.4: *Background subtracted forward CVs of 20 µM, 40 µM, 60 µM, 80 µM, 100 µM and 120 µM $TPrA^+$ ions transfer at water/DCE micro-ITIES formed with pipette 4.*

Figure 2.3.2.2.4 shows the forward cyclic voltammograms of 20 µM, 40 µM, 60 µM, 80 µM, 100 µM and 120 µM $TPrA^+$ ions transfer at water/DCE interface with pipette 4. Table 2.3.2.2.4 shows the average diameter of this pipette tip was 3.09 µm with 7.92% relative standard deviation.

Table 2.3.2.2.4: *Forward currents for the CVs of 20 µM, 40 µM, 60 µM, 80 µM, 100 µM and 120 µM $TPrA^+$ ions transfer and the respective data to measure the diameter of the pipette 4.*

i_{ss} (pA)	C (µM)	$4\|z_i\|FDC$	r (cm)	d (µm)	d (average) (µm)	% RSD
8	20	6×10^{-8}	0.000133	2.66	3.09 (±0.25)	7.92
18	40	12×10^{-8}	0.000149	2.99		
28	60	18×10^{-8}	0.000155	3.10		
39	80	24×10^{-8}	0.000162	3.24		
49	100	30×10^{-8}	0.000163	3.26		
60	120	36×10^{-8}	0.000166	3.32		

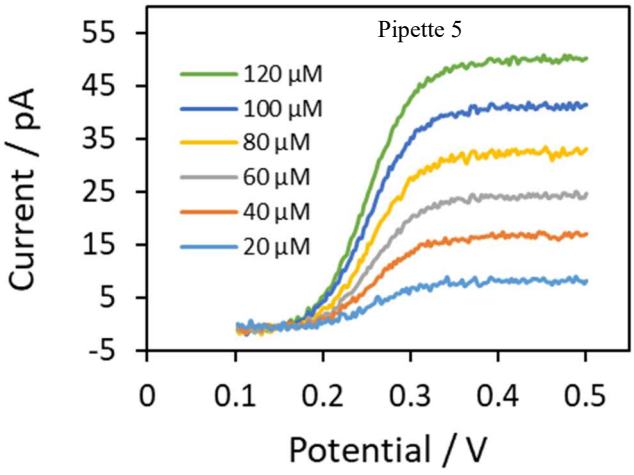

Figure 2.3.2.2.5: *Background subtracted forward CVs of 20 µM, 40 µM, 60 µM, 80 µM, 100 µM and 120 µM $TPrA^+$ ions transfer at water/DCE micro-ITIES formed with pipette 5.*

Figure 2.3.2.2.5 shows the forward cyclic voltammograms of 20 µM, 40 µM, 60 µM, 80 µM, 100 µM and 120 µM $TPrA^+$ ions transfer at water/DCE interface with pipette 5. Table 2.3.2.2.5 shows the average diameter of this pipette tip was 2.72 µm with 1.87% relative standard deviation.

Table 2.3.2.2.5: *Forward currents for the CVs of 20 µM, 40 µM, 60 µM, 80 µM, 100 µM and 120 µM $TPrA^+$ ions transfer and the respective data to measure the diameter of the pipette 5.*

i_{ss} (pA)	C (µM)	$4\|z_i\|FDC$	r (cm)	d (µm)	d (average) (µm)	% RSD
8	20	6×10^{-8}	0.000133	2.66	2.72 (±0.05)	1.87
16	40	12×10^{-8}	0.000133	2.66		
25	60	18×10^{-8}	0.000138	2.77		
33	80	24×10^{-8}	0.000137	2.74		
41	100	30×10^{-8}	0.000136	2.72		
50	120	36×10^{-8}	0.000138	2.77		

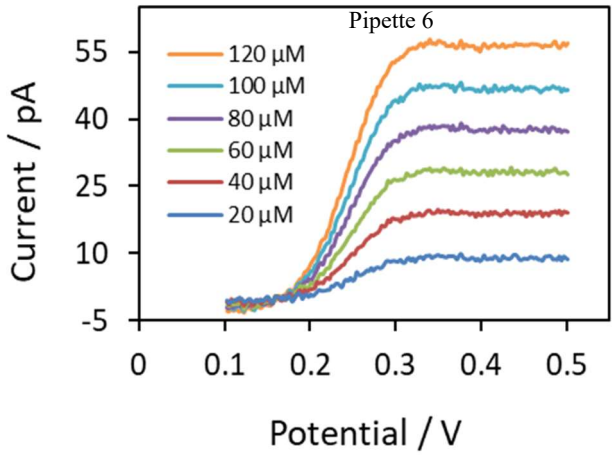

Figure 2.3.2.2.6: *Background subtracted forward CVs of 20 µM, 40 µM, 60 µM, 80 µM, 100 µM and 120 µM $TPrA^+$ ions transfer at water/DCE micro-ITIES formed with pipette 6.*

Figure 2.3.2.2.6 shows the forward cyclic voltammograms of 20 µM, 40 µM, 60 µM, 80 µM, 100 µM and 120 µM $TPrA^+$ ions transfer at water/DCE interface with pipette 6. Table 2.3.2.2.6 shows the average diameter of this pipette tip was 3.06 µm with 6.23% relative standard deviation.

Table 2.3.2.2.6: *Forward currents for the CVs of 20 µM, 40 µM, 60 µM, 80 µM, 100 µM and 120 µM $TPrA^+$ ions transfer and the respective data to measure the diameter of the pipette 6.*

i_{ss} (pA)	C (µM)	$4\|z_i\|FDC$	r (cm)	d (µm)	d (average) (µm)	% RSD
8	20	6×10^{-8}	0.000133	2.66	3.02 (±0.19)	6.23
18	40	12×10^{-8}	0.000149	2.99		
28	60	18×10^{-8}	0.000155	3.10		
38	80	24×10^{-8}	0.000158	3.16		
46	100	30×10^{-8}	0.000153	3.06		
57	120	36×10^{-8}	0.000158	3.16		

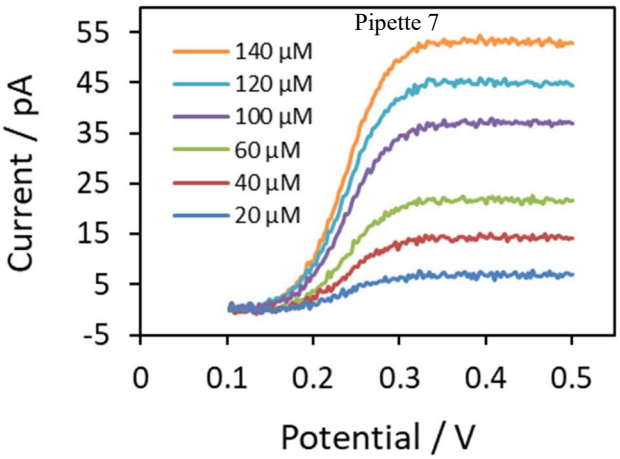

Figure 2.3.2.2.7: *Background subtracted forward CVs of 20 µM, 40 µM, 60 µM, 100 µM, 120 µM and 140 µM $TPrA^+$ ions transfer at water/DCE micro-ITIES formed with pipette 7.*

Figure 2.3.2.2.7 shows the forward cyclic voltammograms of 20 µM, 40 µM, 60 µM, 100 µM, 120 µM and 140 µM $TPrA^+$ ions transfer at water/DCE interface with pipette 7. Table 2.3.2.2.7 shows the average diameter of this pipette tip was 2.46 µm with 3.21% relative standard deviation.

Table 2.3.2.2.7: *Forward currents for the CVs of 20 µM, 40 µM, 60 µM, 80 µM, 100 µM and 120 µM $TPrA^+$ ions transfer and the respective data to measure the diameter of the pipette 7.*

i_{ss} (pA)	C (µM)	$4\|z_i\|FDC$	r (cm)	d (µm)	d (average) (µm)	% RSD
7	20	6×10^{-8}	0.000116	2.33	2.46 (±0.08)	3.21
15	40	12×10^{-8}	0.000125	2.49		
22	60	18×10^{-8}	0.000122	2.44		
37	100	30×10^{-8}	0.000123	2.46		
45	120	36×10^{-8}	0.000125	2.49		
54	140	42×10^{-8}	0.000128	2.56		

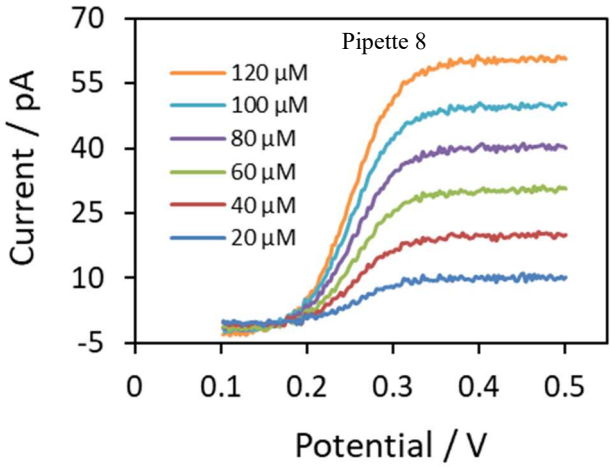

Figure 2.3.2.2.8: *Background subtracted forward CVs of 20 µM, 40 µM, 60 µM, 80 µM, 100 µM and 120 µM $TPrA^+$ ions transfer at water/DCE micro-ITIES formed with pipette 8.*

Figure 2.3.2.2.8 shows the forward cyclic voltammograms of 20 µM, 40 µM, 60 µM, 80 µM, 100 µM and 120 µM $TPrA^+$ ions transfer at water/DCE interface with pipette 8. Table 2.3.2.2.8 shows the average diameter of this pipette tip was 3.31 µm with 2.10% relative standard deviation.

Table 2.3.2.2.8: *Forward currents for the CVs of 20 µM, 40 µM, 60 µM, 80 µM, 100 µM and 120 µM $TPrA^+$ ions transfer and the respective data to measure the diameter of the pipette 8.*

i_{ss} (pA)	C (µM)	$4\|z_i\|FDC$	r (cm)	d (µm)	d (average) (µm)	% RSD
10	20	6×10^{-8}	0.000163	3.26	3.31 (±0.07)	2.10
20	40	12×10^{-8}	0.000165	3.31		
30	60	18×10^{-8}	0.000168	3.36		
39	80	24×10^{-8}	0.00016	3.20		
50	100	30×10^{-8}	0.000166	3.33		
61	120	36×10^{-8}	0.000169	3.39		

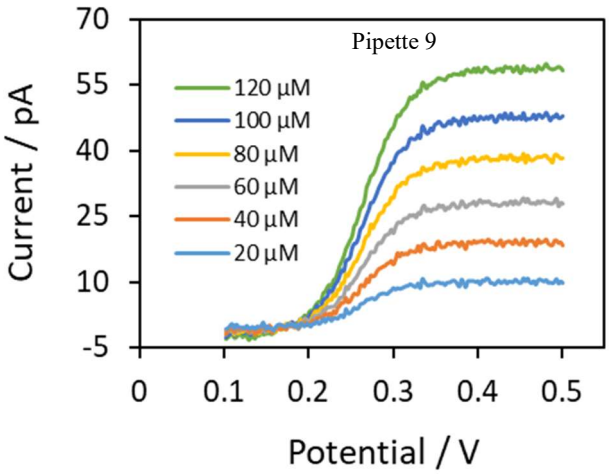

Figure 2.3.2.2.9: *Background subtracted forward CVs of 20 µM, 40 µM, 60 µM, 80 µM, 100 µM and 120 µM $TPrA^+$ ions transfer at water/DCE micro-ITIES formed with pipette 9.*

Figure 2.3.2.2.9 shows the forward cyclic voltammograms of 20 µM, 40 µM, 60 µM, 80 µM, 100 µM and 120 µM $TPrA^+$ ions transfer at water/DCE interface with pipette 9. Table 2.3.2.2.9 shows the average diameter of this pipette tip was 3.13 µm with 3.29% relative standard deviation.

Table 2.3.2.2.9: *Forward currents for the CVs of 20 µM, 40 µM, 60 µM, 80 µM, 100 µM and 120 µM $TPrA^+$ ions transfer and the respective data to measure the diameter of the pipette 9.*

i_{ss} (pA)	C (µM)	$4\|z_i\|FDC$	r (cm)	d (µm)	d (average) (µm)	% RSD
10	20	6×10^{-8}	0.000162	3.24	3.13 (±0.1)	3.29
18	40	12×10^{-8}	0.000151	3.03		
27	60	18×10^{-8}	0.000151	3.02		
37	80	24×10^{-8}	0.000155	3.10		
47	100	30×10^{-8}	0.000156	3.12		
59	120	36×10^{-8}	0.000163	3.27		

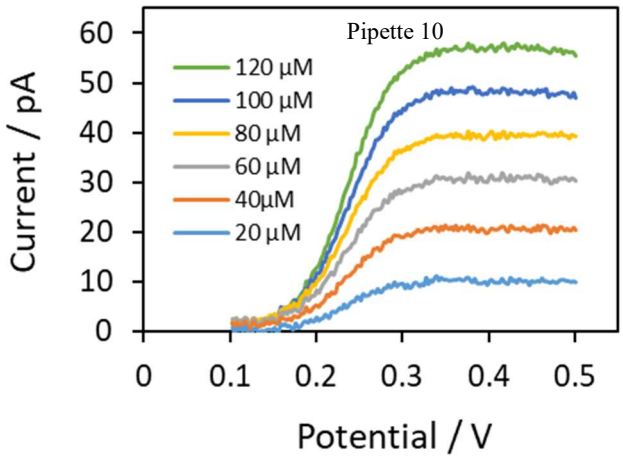

Figure 2.3.2.2.10: *Background subtracted forward CVs of 20 µM, 40 µM, 60 µM, 80 µM, 100 µM and 120 µM $TPrA^+$ ions transfer at water/DCE micro-ITIES formed with pipette 10.*

Figure 2.3.2.2.10 shows the forward cyclic voltammograms of 20 µM, 40 µM, 60 µM, 80 µM, 100 µM and 120 µM $TPrA^+$ ions transfer at water/DCE interface with pipette 10. Table 2.3.2.2.10 shows the average diameter of this pipette tip was 3.11 µm with 4.0% relative standard deviation.

Table 2.3.2.2.10: *Forward currents for the CVs of 20 µM, 40 µM, 60 µM, 80 µM, 100 µM and 120 µM $TPrA^+$ ions transfer and the respective data to measure the diameter of the pipette 10.*

i_{ss} (pA)	C (µM)	$4\|z_i\|FDC$	r (cm)	d (µm)	d (average) (µm)	% RSD
10	20	6×10^{-8}	0.000166	3.32	3.11 (±0.12)	4.00
19	40	12×10^{-8}	0.000158	3.16		
28	60	18×10^{-8}	0.000155	3.10		
37	80	24×10^{-8}	0.000154	3.07		
45	100	30×10^{-8}	0.000149	2.99		
54	120	36×10^{-8}	0.000149	2.99		

Table 2.3.2.2.11 shows the calculated tip diameters from the above ten CV experiments. The average tip diameter was 2.94 and the percentage of their relative standard deviation was calculated as 8.58. Tip diameters for this ten pipettes with their standard deviation plotted in the Figure 2.3.2.2.11. These ten pipettes chosen are prepared in different times and the CV experiments are also done in different days with different potentiostats.

Table 2.3.2.2.11: *Calculated tip diameters from CV experiments and their relative standard deviation (RSD) for pipettes with pulling parameters H: 550; F: 2; V: 30; D: 130 and P: 75.*

Pipette number	Tip diameter (µm)	Average tip diameter (µm)	% RSD
1	2.72	2.94 (± 0.25)	8.58
2	2.83		
3	2.98		
4	3.09		
5	2.72		
6	3.02		
7	2.46		
8	3.31		
9	3.13		
10	3.11		

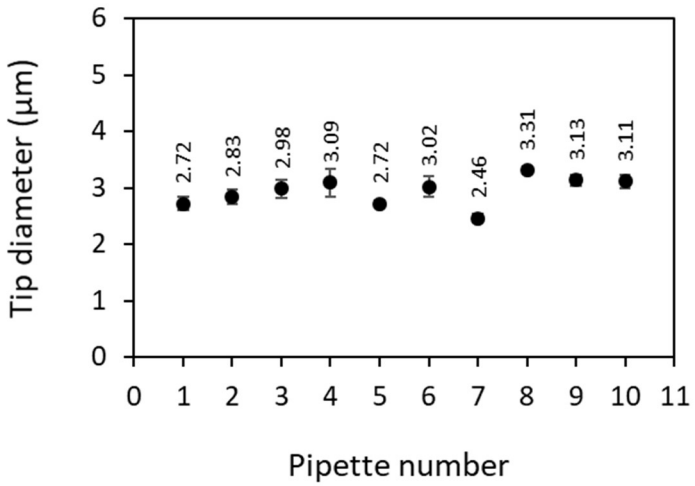

Figure 2.3.2.2.11: *Electrochemical measurement of the tip size of the pipettes prepared with pulling parameters H: 550; F: 2; V: 30; D: 130 and P: 75.*

The diameter of the pipettes prepared from the same set of parameters are also investigated by SEM to compare with the results of electrochemical experiments and to check shape of the pipette tips. The following Figure 2.3.2.2.12 shows the size and shape of the nonsilanized pipette tips. The SEM images shows that the size and shape of the tips of the pipettes are nearly similar and which are also very close to the electrochemical measurements. For this case the shape of the tips are nearly circular. That means the shape depends on the pulling parameters.

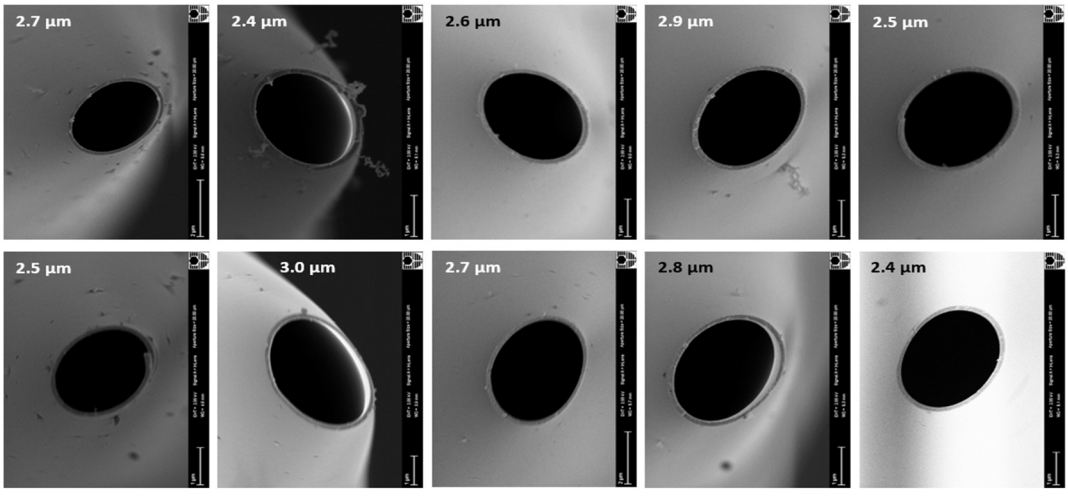

Figure 2.3.2.2.12: *SEM images of the tip of the 10 pipettes those are pulled by P2000 pipette puller with pulling parameters H: 550; F: 2; V: 30; D: 130 and P: 75.*

Table 2.3.2.2.12 shows the 10 pipettes diameter measured from SEM with their average diameter and relative standard deviation. Figure 2.3.2.2.13 shows the graphical representation of this tip diameters with their standard deviation.

Table 2.3.2.2.12: *Measurements of tip diameters from SEM experiments and their relative standard deviation (RSD) for pipettes with pulling parameters H: 550; F: 2; V: 30; D: 130 and P: 75.*

Pipette number	Tip diameter (µm)	Average tip diameter (µm)	% RSD
1	2.7	2.65 (± 0.21)	7.80
2	2.4		
3	2.6		
4	2.9		
5	2.5		
6	2.5		
7	3.0		
8	2.7		
9	2.8		
10	2.4		

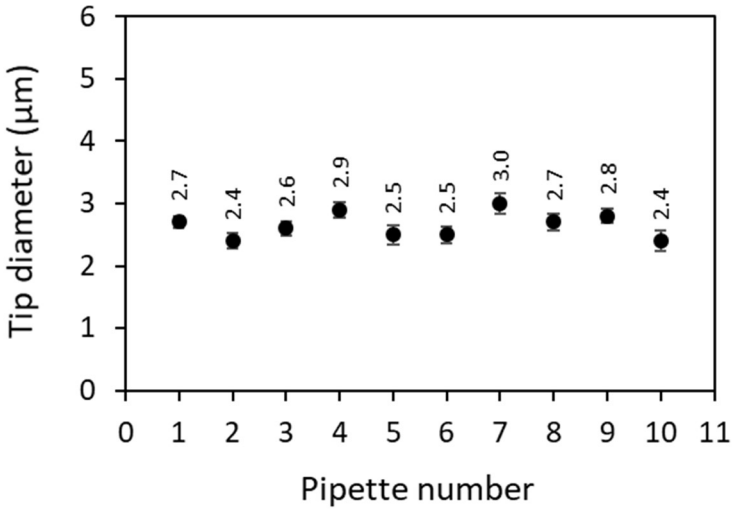

Figure 2.3.2.2.13: *SEM measurement of the tip size of the pipettes those are pulled with pulling parameters H: 550; F: 2; V: 30; D: 130 and P: 75.*

For pulling parameters H: 550; F: 2; V: 30; D: 130 and P: 75, the average diameter of the ten pipettes calculated by CV experiments is 2.94 (± 0.25) and their RSD is 8.58%, whereas the average diameter of ten pipettes calculated by SEM measurement for the same parameters is 2.65 (± 0.21) and their RSD is 7.80%. Figure 2.3.2.2.14 shows graphical and statistical representation of CV and SEM results of the tip size for same set of parameters. So, from this comparative analysis of electrochemical and SEM measurements, we can say that the pipettes prepared from this set of pulling parameters show good reproducibility and agreement between the characterisation methods, making them suitable to carry out the analytical research.

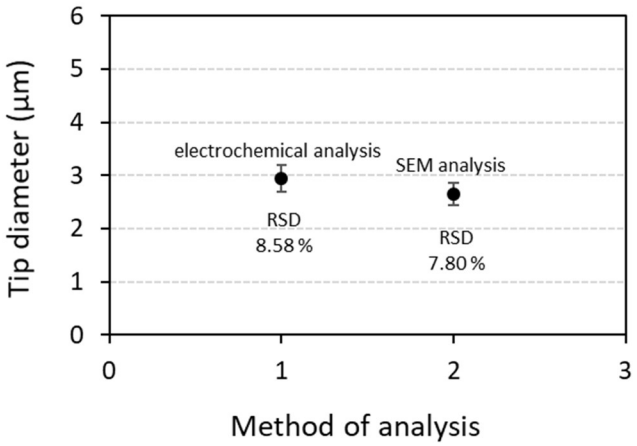

Figure 2.3.2.2.14: *The average diameter of the pipettes by electrochemical and SEM analysis with their standard deviation and relative standard deviation for pulling parameters H: 550; F: 2; V: 30; D: 1300 and P: 75.*

2.3.2.3 Pipette type 3

Four different batch of nanopipettes were also prepared from borosilicate capillaries with dimension O.D. 1.0 mm; I.D. 0.78 mm. We found that nanopipette tips are more circular shaped and more reproducible compared to the micropipettes. Figure 2.3.2.3.1 shows the SEM images of eight nanopipettes. The pulling parameters for these pipettes were set as heat 500, filament 2, velocity 20, delay 155 and pull 70.

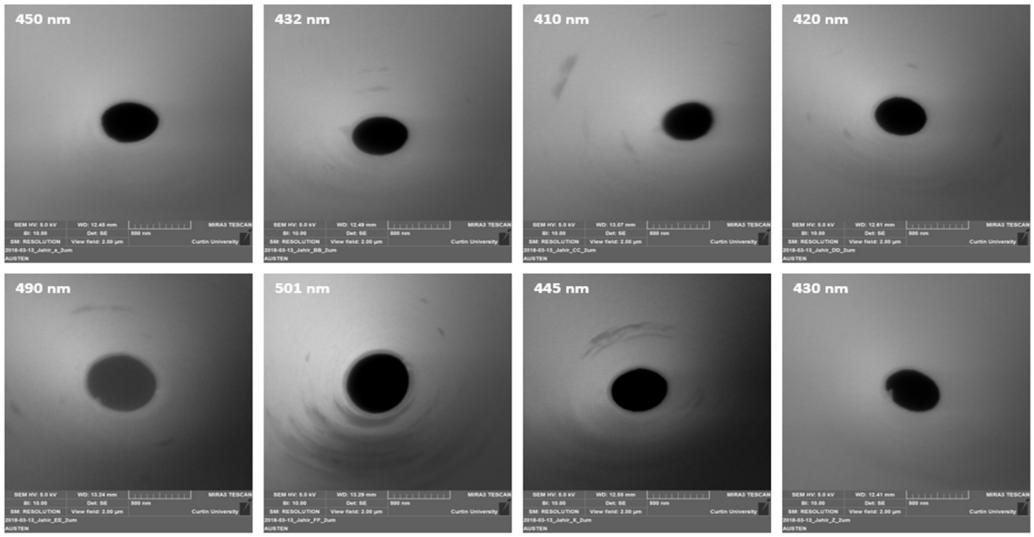

Figure 2.3.2.3.1: *SEM images of the tip of the 8 borosilicate pipettes those are pulled by P2000 pipette puller with pulling parameters H: 500; F: 2; V: 20; D: 155 and P: 70.*

Table 2.3.2.3.1 shows the tip diameters measured from SEM experiments for the pipette type 3, which were prepared at different times. The average tip diameter was 447 nm and the percentage of their relative standard deviation was calculated as 7.26%. The tip diameters for these eight nanopipettes with their standard deviations (deviations from the average tip diameter) are plotted in the Figure 2.3.2.3.2. These experimental data and statistical values proves that the nanopipettes prepared from the pulling parameters H: 500; F: 2; V: 20; D: 155 and P: 70 were reproducible.

Table 2.3.2.3.1: *Measurements of tip diameters from SEM experiments and their relative standard deviation (RSD) for pipettes with pulling parameters H: 500; F: 2; V: 20; D: 155 and P: 70*

Pipette number	Tip diameter (nm)	Average tip diameter (nm)	% RSD
1	450	447 (± 32.5)	7.26
2	432		
3	410		
4	420		
5	490		
6	501		
7	445		
8	430		

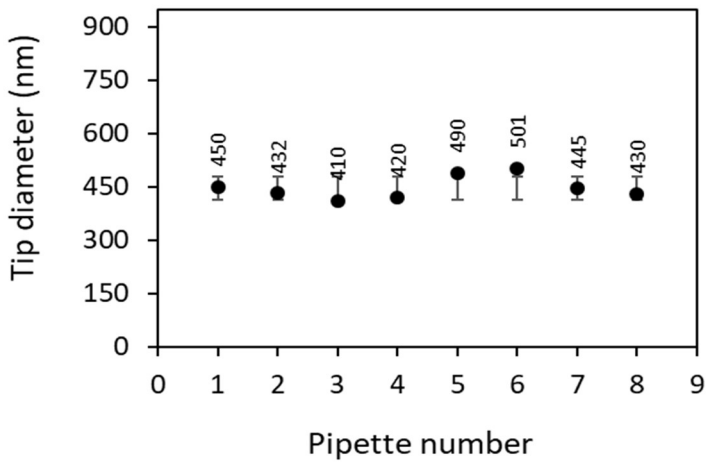

Figure 2.3.2.3.2: *SEM measurement of 8 borosilicate nanopipettes those are pulled by P2000 pipette puller with pulling parameters H: 500; F: 2; V: 20; D: 155 and P: 70 (standard deviation measured based on the average value).*

2.3.2.4 Pipette type 4

Figure 2.3.2.4.1 shows the SEM images of eight nanopipettes prepared from borosilicate capillaries with dimension O.D. 1.0 mm; I.D. 0.78 mm. The pulling parameters for these pipettes were set as heat 450, filament 3, velocity 20, delay 150 and pull 75.

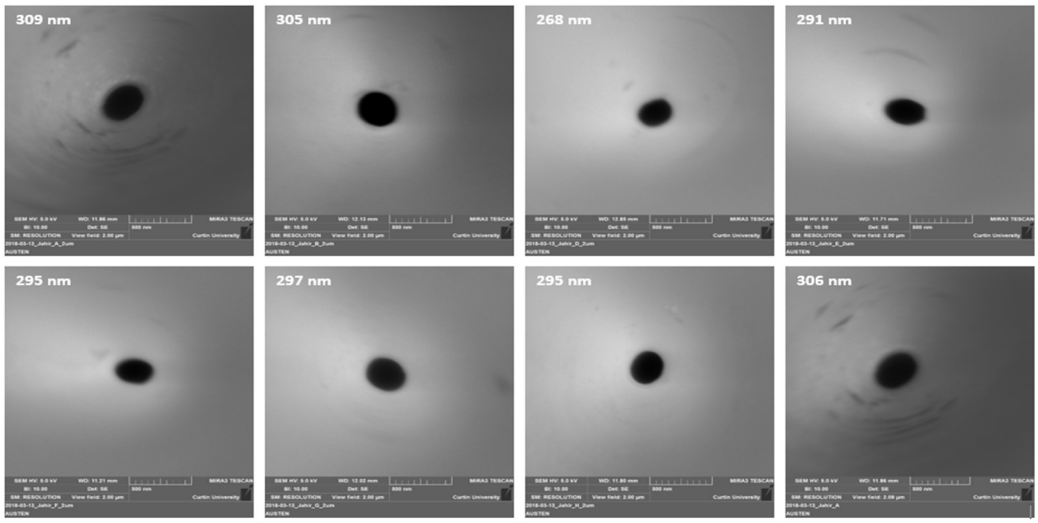

Figure 2.3.2.4.1: *SEM images of the tip of the 8 borosilicate pipettes those are pulled by P2000 pipette puller with pulling parameters H: 450; F: 3; V: 20; D: 150 and P: 75.*

Table 2.3.2.4.1 shows the tip diameters measured from SEM experiments for the pipette type 4, which were prepared at different times. The average tip diameter was 296 nm and the percentage of their relative standard deviation was calculated as 4.30%. Tip diameters for these eight nanopipettes with their standard deviations (deviations from the average tip diameter) are plotted in the Figure 2.3.2.4.2. All these experimental data and statistical values for the nanopipettes prepared from the pulling parameters H: 450; F: 3; V: 20; D: 150 and P: 75, represents that the pipettes were reproducible.

Table 2.3.2.4.1: *Measurements of tip diameters from SEM experiments and their relative standard deviation (RSD) for nanopipettes with pulling parameters H: 450; F: 3; V: 20; D: 150 and P: 75.*

Pipette number	Tip diameter (nm)	Average tip diameter (nm)	% RSD
1	309	296 (± 12.7)	4.30
2	305		
3	268		
4	291		
5	295		
6	297		
7	295		
8	306		

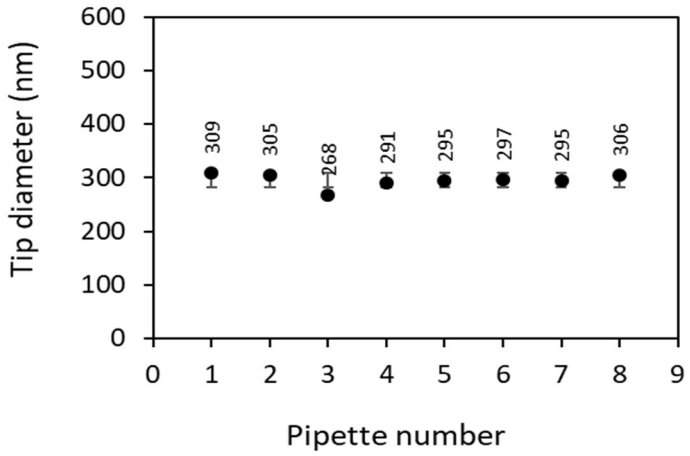

Figure 2.3.2.4.2: *SEM measurement of 8 borosilicate pipettes those are pulled by P2000 pipette puller with pulling parameters H: 450; F: 3; V: 20; D: 150 and P: 75 (standard deviation measured based on the average value).*

2.3.2.5 Pipette type 5

Another type of nanopipettes prepared from borosilicate capillaries (O.D. 1.0 mm; I.D. 0.78 mm) with pulling parameters as heat 350, filament 2, velocity 50, delay 225 and pull 150. Figure 2.3.4.5.1 shows the SEM images of eight nanopipettes for these new parameters. These images shows that the shapes of the pipette tips in this case are also circular or round shape.

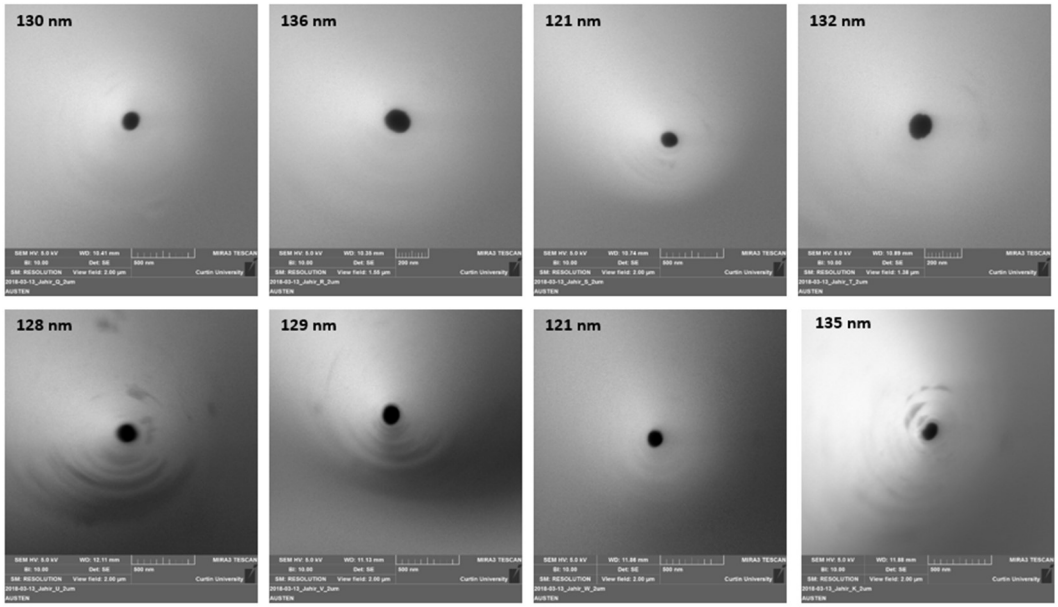

Figure 2.3.2.5.1: *SEM images of the tip of the 8 borosilicate pipettes those are pulled by P2000 pipette puller with pulling parameters H: 350; F: 2; V: 50; D: 255 and P: 150.*

Table 2.3.2.5.1 shows the tip diameters measured from SEM experiments for the pipettes shown in Figure 2.3.2.5.1, which were prepared at different times. The average tip diameter for these pipettes was 129 nm and the percentage of their relative standard deviation was 4.39%. Tip diameters for these eight nanopipettes with their standard deviation (deviations from the average tip diameter), are plotted in the Figure 2.3.2.5.2. It shows that the diameters are very close together or produce reproducible results for pulling parameters H: 350; F: 2; V: 50; D: 255 and P: 150.

Table 2.3.2.5.1: *Measurements of tip diameters from SEM experiments and their relative standard deviation (RSD) for nanopipettes with pulling parameters H: 350; F: 2; V: 50; D: 255 and P: 150.*

Pipette number	Tip diameter (nm)	Average tip diameter (nm)	% RSD
1	130	129 (± 5.66)	4.39
2	136		
3	121		
4	132		
5	128		
6	129		
7	121		
8	135		

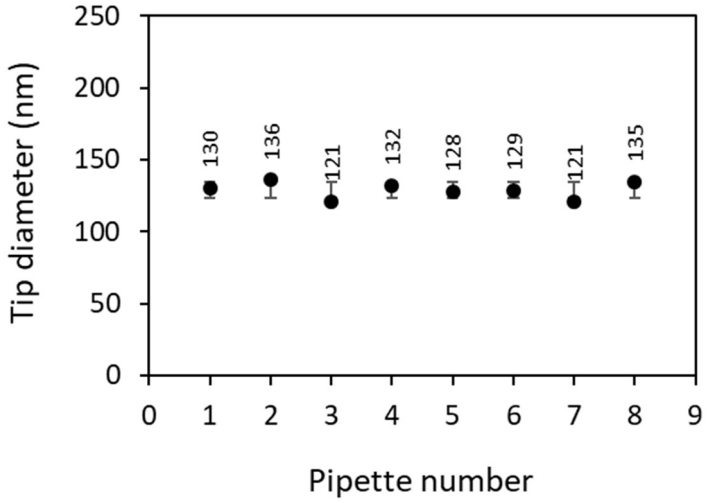

Figure 2.3.2.5.2: *SEM measurement of 8 borosilicate pipettes those are pulled by P2000 pipette puller with pulling parameters H: 350; F: 2; V: 50; D: 255 and P: 150 (standard deviation measured based on the average value).*

Table 2.3.2.5.2: *Variation of tip diameters with different sets of pulling parameters measured by SEM experiments for nanopipettes from borosilicate capillaries.*

Pulling parameters	Average tip diameter (nm)	% RSD
H: 500; F: 2; V: 20; D: 155 and P: 70	447 (± 32.5)	7.26
H: 450; F: 3; V: 20; D: 150 and P: 75	296 (± 12.7)	4.30
H: 350; F: 2; V: 50; D: 255 and P: 150	129 (± 5.66)	4.39

Table 2.3.2.5.2 summarizes the variation of nanopipettes tip diameter with change of pulling parameters, prepared from borosilicate capillaries (O.D. 1.0 mm; I.D. 0.78 mm)

2.4 Comparison with literature

2.4.1 Pipette pulling parameters and tip radius

The pipette pulling parameter values used in the preparation of micropipettes may not be the same for different P-2000 pullers, the instrument used in this work for preparation of pipettes. Moreover, the parameters have to be adjusted occasionally even for the same instrument to produce reproducible pipets of the desired size and shape. Table 2.3.2.5.2 shows that small differences between the pulling parameters have a significant effect on the size of the pipettes. There are lots of data for pipette preparation and characterization available in literature. Some experimental pipette pulling parameters from the literature, which are close to the parameters used here, and their respective pipette radius are presented here to compare with the new results in this chapter. M. V. Mirkin, S. Amemiya and co-authors [165] prepared nanopipettes from 10 cm long quartz capillaries (outer/inner diameter ratio of 1.0/0.70; Sutter Instrument Co., Novato, CA) using the same laser-based pipet puller instrument as used in this thesis (P-2000, Sutter Instrument Co.). Their pulling parameters were Heat = 710, Filament = 4, Velocity = 28, Delay = 120, Pull = 130 and these produced the pipette radius of about 100 nm. From Table 2.3.2.5.2 we can see that a much lower temperature was used in this chapter compared to them because of borosilicate glass use, and hence the pipette radii are bigger, because a higher temperature reduces the tip radius. Mei Shen and co-authors [133] fabricated nanometer scale pipettes from

quartz capillaries (O.D. = 1.0 mm, I.D. = 0.7 mm, length = 10 cm, Sutter Instrument, Novato, CA) using a P-2000 pipette puller instrument, with the parameters Heat = 725, Filament = 4, Velocity = 55, Delay = 130, Pull = 100. This produced pipettes with different tip radius (340 nm, 360 nm and 450 nm). Although the temperature used in this case is higher than the previous example, a larger pipette radius was obtained, showing the variability in methods and the need to establish best parameters in each laboratory location. On the other hand, fabrication of 75 – 100 nm radius pipettes from borosilicate glass capillaries (O.D. 1.2 mm, D.D. 0.69 mm, Harvard Apparatus) using the same type of laser puller was reported by Patrick R. Unwin and his group [166]. They used two lines pulling parameters: Line 1: Heat = 330, Filament = 3, Velocity = 30, Delay = 220, Pull -, and Line 2: Heat = 330, Filament = 3, Velocity = 40, Delay = 180, Pull = 120. As they used borosilicate glass like we used in this chapter and the parameters are comparatively closer to those used for Pipette type 5 values (third row in Table 2.3.2.5.2), the radius is also close to the value obtained here. Although they used two lines of pulling parameters, however, generally we can say that for the same type of glass capillaries and pipette puller, if the pulling parameters are closer then the pipette tip radius also may be closer but not same. Even in the same laboratory with same instruments and same pulling parameters, the shape and size of the pipettes can vary with the change of operating persons.

2.4.2 Silanization process

The silanization process we used here (details in section 2.2.5) is simpler and less time consuming compared to other available processes described in the literature. The two mostly used silanization processes available in literature are summarized here to compare with our new method. S. Amemiya and co-authors [167] applied a vaporization method for silanization of the pipettes. They cleaned the pipettes for 3 min in a plasma cleaner. The clean pipettes were then dried for >1.5 h under vacuum in a mini vacuum desiccator which was placed in a gas-purge desiccator cabinet filled with dry nitrogen. After that, 50 μL of *N*-dimethyltrimethylsilylamine was introduced into the desiccator for silanization and allowed react for about 40 min depending on the temperature and humidity of the atmosphere. After silanization, a vacuum was applied to the mini desiccator for ∼1 min to remove the extra silanization agent. But by this process, both the inner and outer surface of the pipettes were silanized. Y. Shao

and MV.Mirkin [75] silanized the inner surface of the pipette by putting the back of the pipette into the solution of trimethylchlorosilane. Then the solution was pushed towards the pipette tip by a syringe from the back. After 30 min reaction time, the solution was removed from the pipette with a syringe, and the silanized pipette was allowed to dry in the air overnight. The main disadvantage for this method was that there is possibilities to form multilayer silane products, and for smaller nano-pipettes these could block the orifice. On the other hand, in our silanization process, we used a very simple apparatus, which is described in section 2.2.5. The apparatus is made of a glass jar. The cap of that jar was joined with some Tygon polymeric tubes and the pipettes were fitted into those tubes from the back of the pipettes very easily. Then the jar was closed with the pipette fitted cap after adding about 0.1 ml silanizing agent into the jar. The silanizing agent vaporized quickly and goes through the pipettes and modified the inner surface. This whole process was done in fume cupboard under normal laboratory temperature and took 30-40 minutes. So, it is clear from this discussion that our silanization process simpler as this is prompt, easier to implement, and there is less handling of the hazardous silanizing agent.

2.5 Conclusion

In this chapter, the preparation of five different size pipettes using the P2000 pipette puller was demonstrated. Five different sets of pulling parameters were examined and the pipettes were characterized by employing SEM & electrochemical measurements to check the reproducibility of the prepared pipettes. Among the five types of pipettes, two of them were micropipettes and the other three types were nanopipettes. All the electrochemical and SEM results and their statistical analysis showed that the prepared pipettes were reproducible, which was one of the most important tasks for research. This analysis found that the size and shape of the pipettes depends on the five pulling parameters and these parameters are also responsible to make reproducible pipettes. Silanization of the pipettes was another important part of the research to get reproducible electrochemical analysis at the ITIES formed at the tip of the pipettes. The new method used for silanization of the inner side of the pipettes is very simple. All the electrochemical analysis throughout this project shows that the silanization of the pipette works perfectly. This procedure was used to prepare and characterize different size of micropipettes used in all the subsequent chapters of this thesis.

Chapter 3

Electrochemical Detection and Characterization of PFAS Substances.

3.1 Introduction

Per- and polyfluoroalkyl substances (PFAS) are a group of man-made chemicals consisting of long alkyl chains from 4 to 18 carbon atoms, where all or almost all hydrogen atoms are substituted with fluorine atoms with a carboxylic acid, sulfonate or alcohol group at the end of the chain [168, 169]. The C–F bond is one of the strongest bonds found in nature and becomes stronger with increasing hydrogen replacement by fluorine at each carbon. Due to its stable chemical structure, the small size of the fluorine atom, and high electronegativity, makes PFASs high environmentally persistent chemicals with long biological half-lives with more accumulation potential [170, 171]. For its unique physical and chemical properties and stability, they found numerous applications in many areas of daily and industrial use. These substances are well-known constituents of products, such as fire-fighting foams, metal plating, lubricants, paints, polishes, food packaging, aerospace, automotive, construction, electronics, and military [172-177]. These substances are of globally emerging concern because of their high persistence, toxicity, [178, 179] and high levels of accumulation in plants and animals that are linked to immunosuppression and other health conditions such as cancer, liver damage, hormone disruption. [180-183]. The unique properties of fluorinated compounds shows challenges for current analytical techniques, which is motivating the recent surge in research and development to monitor the presence and concentrations of PFAS [184, 185].

At present, a number of methods are available for PFAS detection and monitoring. Gas chromatography-mass spectrometry (GC-MS) [186, 187], high-performance liquid chromatography-mass spectrometry (HPLC-MS) [188, 189], liquid chromatography-tandem mass spectrometry (LC-MS-MS) [190, 191], colourimetric detection [192, 193], fluorimetric flow injection analysis [194] are few of those techniques, which are widely used for ultra-trace elements. Though these high technological methods have achieved excellent sensitivity and accuracy, they have some disadvantages including very complex and sophisticated instrumentation, high costs for establishment & maintenance, complicated sample pre-treatment, long time and overall highly trained personnel to run those instruments. More importantly, those are not suitable for in-field measurements. Electrochemical techniques could be one of the alternative

methods to overcome those difficulties and at the same time keeping low detection limit.

Now a days, a wide range of electrochemical techniques have been successfully applied to determination of environmental pollutants [195-198]. But the chemical stability of the carbon-fluorine bond in PFASs are too strong to detect by direct redox electrochemical techniques. These difficulties could be resolved by employing electrochemistry at the interface between two immiscible electrolyte solutions (ITIES) [3, 65, 66, 125], which depend on the transfer of ionised species across the interface to produce the electrochemical signal. PFASs was investigated by Amemiya and co-workers [199] where they first reported on experimentally quantify lipophilicity of perfluoroalkyl chains with different lengths at the ITIES to measure their lipophilic properties. They also measure the partition coefficients of carboxylates and sulfonates with fluorinated alkyl chain by applying ion-transfer cyclic voltammetry at *n*-octanol/water interface to identify lipophilicities of perfluoroalkyl and alkyl oxoanions with the same chain length. Amemiya's group [200] also reported on PFAS analysis by applying stripping voltammetry at the ITIES formed between aqueous and a thin plasticized polymeric film supported on a gold disc electrode and reported LOD of 50 pM perfluorooctanesulfonate (PFOS). Recently, Arrigan's group [201] also reported on PFOS, where they apply cyclic voltammetry (CV), differential pulse voltammetry (DPV) and differential pulse stripping voltammetry (DPSV) at an array of water/1,2-dichloroethane (DCE) μITIES and achieved a limit of detection (LOD) of 0.03 nM (0.015 μg L^{-1}) in aqueous electrolyte. They also analysed matrix effect and observed the changes in sensitivity and LOD relative to those in pure aqueous electrolyte solutions.

This study was focused on the electrochemical investigations of four PFAS substances, namely perfluorooctanoic acid (PFOA), perfluorobutanesulfonic acid (PFBS), perfluorohexanesulphonic acid (PFHxS) & perfluorooctanesulfonic acid (PFOS), at μITIES formed at the tips of the micropipettes by applying cyclic voltammetry and differential pulse voltammetry. Besides the study of the electrochemical behaviour, the major objective of this investigation was to evaluate the selectivity of the μITIES for the detection of PFAS substances in mixtures of different PFASs. The number of carbon atoms of this chosen four PFAS substances are very close together to better

understand the effect of lipophilicity of this closely related substances and the selectivity in their mixtures.

3.2 Experimental

3.2.1 Reagents

All the reagents were purchased from Sigma-Aldrich Australia Ltd. and used as received unless otherwise indicated. The organic electrolyte bis(triphenylphosphoranylidene)ammonium tetrakis(4-chlorophenyl)borate (BTPPATPBCl) was prepared by metathesis of equimolar amounts of bis(triphenylphosphoranylidene)ammonium chloride (BTPPACl) and potassium tetrakis(4-chlorophenyl)borate (KTPBCl) as reported earlier [77]. BTPPATPBCl (0.01M) solutions were prepared in 1, 2-dichloroethane (DCE). Chlorotrimethylsilane was used for silanization of pipettes. All aqueous solutions (e.g. LiCl solution) were prepared in purified water from a USF Purelab plus UV (resistivity: 18.2 MΩ cm). Pentadecafluorooctanoic acid, 98% (PFOA) and perflurooctanesulphonic acid, potassium salt, 97% (PFOS) were purchased from STREM chemicals. Perfluorobutanesulfonic acid (PFBS) and Perfluorohexanesulfonic acid (PFHxS) are also from Sigma-Aldrich Australia Ltd**.**

3.2.2 Pipette preparation, modification and characterization

The pipettes were prepared according to the method described in section 2.2.4 in chapter two. The inner surface of the pipettes silanized and characterized according the methods described in section 2.2.5 and 2.3.1 respectively. In this case, microscopic characterization has been done along with electrochemical characterization instead of SEM characterization. Difficulties has been faced to prepare comparatively larger tip radius pipettes. The larger tip radius achieved by touching and/or polishing the pipette tips (which were prepared with various pipette pulling parameters) on a very smooth surface like flat glass surface or on relatively softer surface like smooth polystyrene and this depends on what would be the tip radius. This touching and/or polishing has been done after silanization and special care was taken, as the pipette tips are extremely fragile. After touching and/or polishing, the pipette tips were checked by microscope to see the tip orifice smoothness and then electrochemical characterization was done to measure the tip radius.

3.2.3 Electrochemical cell

Electrochemical measurements were conducted by using an Autolab PGSTAT302N electrochemical analyser (Metrohm Autolab, Utrecht, The Netherlands) running with NOVA software. The organic electrolyte phase was introduced into the pipette which comes up to the tip and the organic reference solution (saturated BTPPACl in 10 mM LiCl) was placed on the top of the organic phase. Then the pipette was immersed into the aqueous phase so that an ITIES form at the tip of the pipette. As this was a miniaturized interface, so two-electrode system was employed for this electrochemical cell. An Ag/AgCl electrode was in the aqueous solution and another Ag/AgCl electrode used in the organic reference solution. The micro-interface was polarised by imposing a potential difference between these two electrodes. Unless stated 10 mVs^{-1} scan rate was applied to carried out cyclic voltammetry (CV) experiment. The cell described in the following scheme.

$$\text{Ag}\,|\,\text{AgCl}\,|\,\begin{matrix}\text{Sat'd BTPPACl}\\ \text{in 10 mM LiCl}\end{matrix}\,|\,\begin{matrix}\text{10 mM BTPPATPBCl}\\ \text{in DCE}\end{matrix}\,||\,\begin{matrix}\text{x µM PFAS in}\\ \text{10 mM LiCl}\end{matrix}\,|\,\text{AgCl}\,|\,\text{Ag}$$

3.3 Results and discussions

3.3.1 Cyclic Voltammetry

The transfer of perfluoroalkanesulfonates (PFOS, PFHxS and PFBS) and perfluroalkanecarboxylate (PFOA) across the microinterface between water and DCE formed at the tip of glass micropipette were studied by cyclic voltammetry to analyse the electrochemical behaviour of perfluoroalkyl oxoanions. All the analytes give well-defined voltammograms without any voltammetric sign of their adsorption, emulsification, and or instability of the interface. Figure 3.3.1.1(a) shows the CV of PFOS with the CV of blank. On the forward scan a sigmoidal voltammetric wave or a steady state voltammogram formed corresponding to transfer of the analyte indicates a nonlinear of radial diffusion from the outer aqueous phase to the micrometer-sized interface. On the other hand, the broad peak in the reverse scan confirms the transient linear diffusion of PFOS from the inner DCE phase to the interface or aqueous phase. These findings are similar with the previous investigations applied for the perfluoroalkyl oxoanions by ion-transfer micropipet voltammetry at the interface between 1-octanol/water to find the lipophilic behaviours [199].

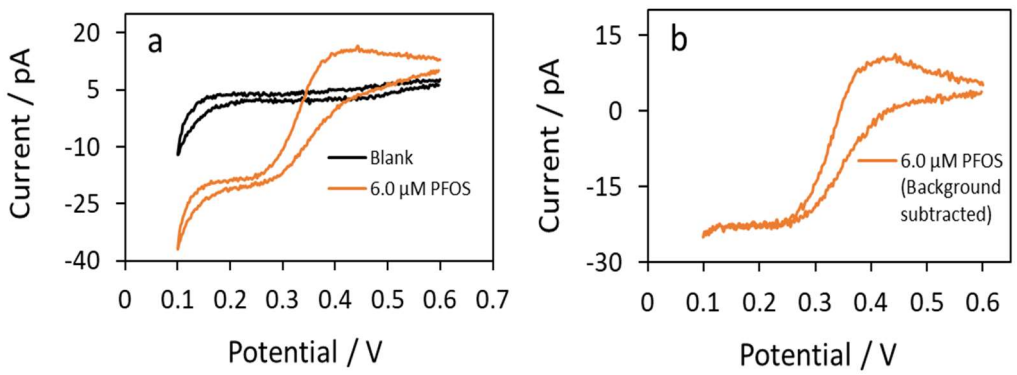

Figure 3.3.1.1: *(a) CV of 6.0 µM PFOS with CV of blank and (b) background subtracted CV of 6.0 µM PFOS at 25 µm radius interface. [Pipette radius with Equations 2.3.1.2 and 2.3.1.3 are also given in Appendix B.]*

Nearly similar behaviour observed for ion-transfer voltammetry of perfluoroalkanesulfonates and perfluoroalkanecarboxylates at the interface between a plasticized polymer membrane and water obtained by using a ~1 µm thick poly(vinyl chloride) membrane plasticized with 2-nitrophenyl octyl ether [200]. Recently similar response was observed for the investigation of PFOS at µITIES array to find out various matrix effect on the ion-transfer behaviour and on detection limit [201].

3.3.2 Cyclic Voltammetry of PFOS

The background subtracted CV profiles of PFOS in the concentration range 1-9 µM are presented in Figure 3.3.2.1. The experiments were carried out under normal condition of LiCl solution (pH ≈ 6). Figure 3.3.1.1(b) shows in forward scan for 6.0 µM PFOS, the ion start transfer at potential 0.44 V and becomes plateau at potential of 0.24 V and for the reverse scan, PFOS ions transfer back to aqueous phase giving a peak at 0.42 V. The calculated half wave potential ($E_{1/2}$) based on forward sweep is 0.34 V. From Figure 3.3.2.1, the steady state forward current (i_f) and backward/reverse peak current (i_b) of 3 scans for each concentration are given in the Table 3.3.2.1. Figure 3.3.2.2 shows current *vs* concentration graph based on those data. The currents on the forward sweeps as well as reverse sweeps of the background-subtracted CVs of PFOS increased linearly with the concentration of PFOS in the aqueous phase. These current vs concentration relation is predicted by the Saito equation [202] for the steady state current and the Randles–Sevcik equation [80, 203]

for the voltammetric peak current for linear diffusion systems. Diffusion coefficient of PFOS (D_{PFOS}) for the aqueous phase calculated as 4.43 x 10^{-6} cm^2/s by using Saito equation, whereas D_{PFOS} was found 5.4 x 10^{-6} cm^2/s in literature measured by capillary method [204]. Irrespective of the diffusion mode, the current is concentration-dependent for both directions. The detection limit is very important parameter for environment pollutants to monitor its increase in the environment and to control it. In this investigation we calculated the lowest detection limit (LOD) by using the regression analysis of the forward currents from the CV experiments and with the help of (3 x σ) / S formula [201], where S is the slope of the calibration curve and σ is the standard deviation of y-intercept of regression line. The values of σ and S was obtained by using the LINEST function in Excel. LINEST function calculates the statistics of a simple line equation (Y = mx + C) which also explains the relationship between the dependent and independent variables using the least square procedure to find the best solution for data used. For this case, the calculated LOD of PFOS was 1.07 µM.

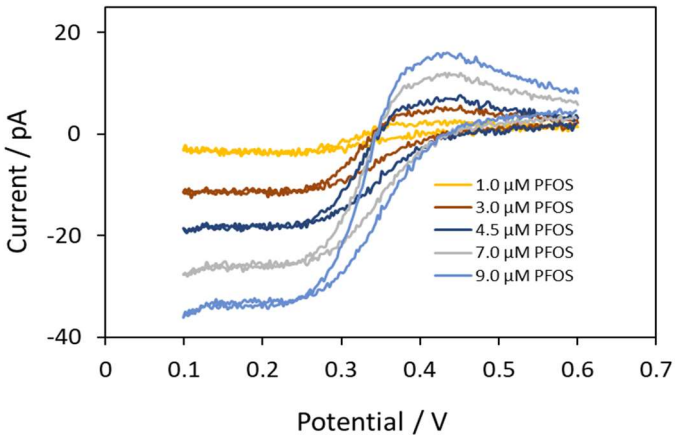

Figure 3.3.2.1: *Background subtracted CV of 1.0 µM, 3.0 µM, 4.5 µM, 7.0 µM and 9.0 µM PFOS at 25 µm radius interface. [Pipette radius with Equations 2.3.1.2 and 2.3.1.3 are also given in Appendix B.]*

Table 3.3.2.1: *Steady state forward currents* (i_f) *and reverse peak currents* (i_b) *with standard deviation (σ) for different concentrations of PFOS*

C / µM	i_{f1} / pA	i_{f2} / pA	i_{f3} / pA	Average i_f / pA	σ
1	-4.18	-6.32	-3.99	-4.83	1.29
3	-11.84	-14.59	-13.72	-13.38	1.41
4.5	-18.65	-20.65	-21.69	-20.33	1.55
7	-26.49	-24.91	-28.55	-26.65	1.83
9	-34.24	-31.47	-35.39	-33.70	2.02
C / µM	i_{b1} / pA	i_{b2} / pA	i_{b3} / pA	Averagei_b / pA	σ
1	6.07	5.66	8.25	6.66	1.39
3	16.33	14.15	17.99	16.16	1.93
4.5	25.58	23.48	27.17	25.41	1.85
7	38.15	36.52	41.31	38.66	2.44
9	49.99	47.65	52.17	49.94	2.26

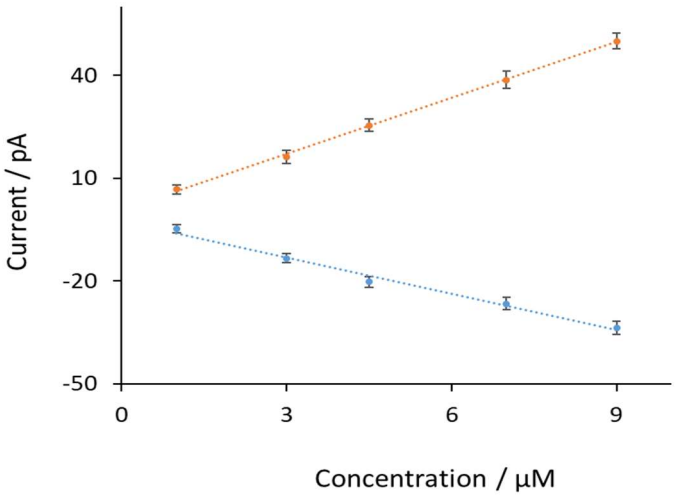

Figure 3.3.2.2: *Current vs concentration graph of PFOS for both forward and reverse direction.*

3.3.3 Cyclic Voltammetry of PFHxS

The transfer of PFHxS across the microinterface between water and DCE formed at the 23 µm radius tip of glass micropipette gives the similar response as PFOS discussed in earlier section 3.3.1. Figure 3.3.3.1(a) shows no response (blank) in the control experiment where all the experimental setup was the same other than no analyte. The response in the lower potential is due to transfer of background electrolyte. The Figure also shows the CV of 6.0 µM PFHxS which gives a sigmoidal voltammetric wave on the forward scan corresponding to transfer of the analyte from the outer aqueous phase to the organic phase through micrometer-sized interface indicates a nonlinear diffusion. On the other hand, the broad peak in the reverse scan confirms the transient linear diffusion of PFHxS ions from the inner DCE to aqueous phase. From the background subtracted CV of 6.0 µM PFHxS (Figure 3.3.3.1 b) shows, the ions start transfer at potential 0.40 V for forward scan as the current start increasing in that potential and becomes a plateau at a potential of 0.22 V. On the other hand, in the reverse scan, PFHxS ions transfer back to aqueous phase giving a peak at 0.36 V. The calculated half wave potential based on forward sweep is 0.32 V.

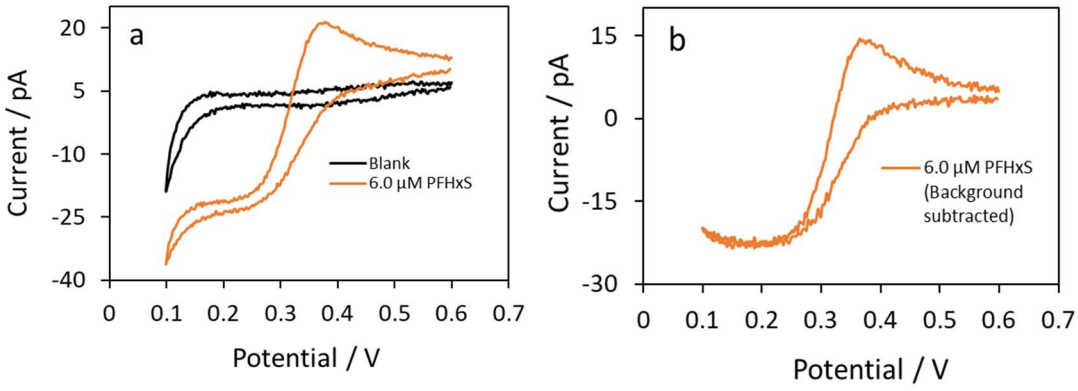

Figure 3.3.3.1: *(a) CV of 6.0 µM PFHxS with CV of blank and (b) background subtracted CV of 6.0 µM PFHxS at 23 µm radius interface. [Pipette radius with Equations 2.3.1.2 and 2.3.1.3 are also given in Appendix B.]*

The Figure 3.3.3.2 shows background subtracted CVs of PFHxS in various concentrations ranging from 2 - 9 µM. Normal LiCl solution of pH ≈ 6.3 was used for this experiment. The data of steady state forward currents (i_f) and backward/reverse peak currents (i_b) of 3 scans for all concentrations are given in the Table 3.3.3.1. Figure 3.3.3.3 shows current *vs* concentration graph based on those data. The currents on the forward sweeps as well as reverse sweeps of the background-subtracted CVs of PFHxS increased linearly with the concentration in aqueous phase. These current vs concentration relation is consistent with the Saito equation [202] for the steady state current and the Randles–Sevcik equation [80, 203] for the voltammetric peak current for linear diffusion systems. Irrespective of the diffusion mode, the current is concentration-dependent for both directions. Diffusion coefficient of PFHxS (D_{PFHxS}) for the aqueous phase calculated as 4.85 x 10^{-6} cm^2/s by using Saito equation, whereas D_{PFHxS} was found 4.5 x 10^{-6} cm^2/s in literature measured by capillary method [204]. For this case LOD was also calculated by using the regression analysis of the forward currents from the CV experiments and with the help of (3 x σ) / S formula and the calculated LOD of PFHxS was 0.68 µM.

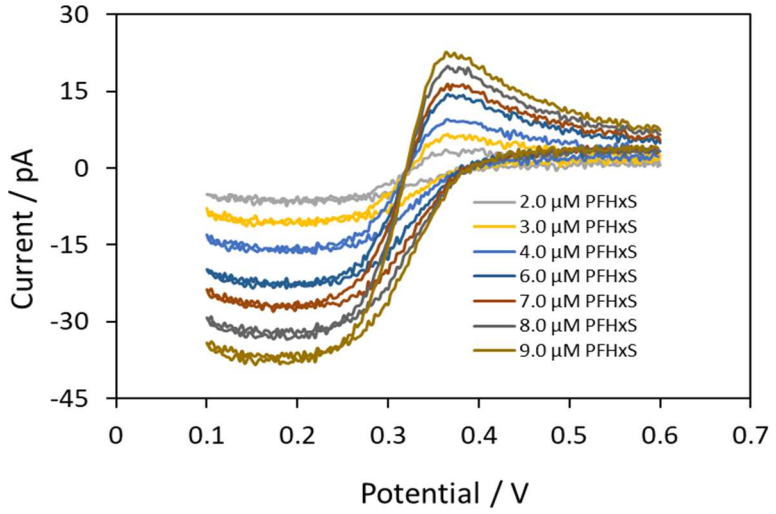

Figure 3.3.3.2: *Background subtracted CV of 2.0 µM, 3.0 µM, 4 µM, 6.0 µM, 7.0 µM, 8.0 µM and 9.0 µM PFHxS at 23 µm radius interface. [Pipette radius with Equations 2.3.1.2 and 2.3.1.3 are also given in Appendix B.]*

Table 3.3.3.1: *Steady state forward currents* (i_f) *and reverse peak currents* (i_b) *with standard deviation (σ) for different concentrations of PFHxS*

C / µM	i_{f1} / pA	i_{f2} / pA	i_{f3} / pA	Averagei_f / pA	σ
2	-7.93	-8.82	-5.84	-7.53	1.53
4	-18.8	-20.21	-16.33	-18.45	1.96
6	-26.77	-28.43	-24.65	-26.62	1.89
7	-30.49	-32.07	-27.89	-30.15	2.11
9	-39.89	-41.89	-37.53	-39.77	2.18
C / µM	i_{b1} / pA	i_{b2} / pA	i_{b3} / pA	Averagei_b / pA	σ
2	10.19	12.31	8.65	10.38	1.84
4	25.79	28.1	23.77	25.89	2.17
6	39.43	41.72	37.49	39.55	2.12
7	44.86	45.89	42.7	44.48	1.63
9	59.63	61.38	57.49	59.50	1.95

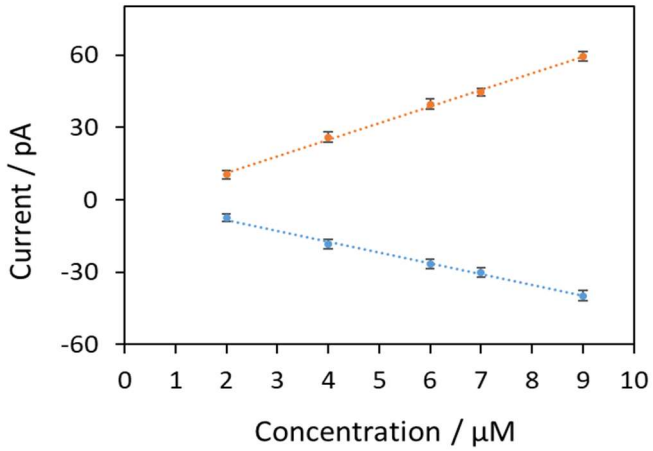

Figure 3.3.3.3: *Current vs concentration graph of PFHxS for both forward and reverse direction.*

3.3.4 Cyclic Voltammetry of PFBS

The transfer of PFBS across the microinterface between water and DCE formed at the tip of 23 µm radius glass micropipette gives the similar response as PFOS & PFHxS discussed in earlier sections. Figure 3.3.4.1 (a) shows no response (blank) in the control experiment where all the experimental setup was the same other than no analyte. The response in the lower potential is due to transfer of background electrolyte. The Figure also shows the CV of 6.0 µM PFBS, which gives a sigmoidal voltammetric wave on the forward scan corresponding to transfer of the analyte from the outer aqueous phase to the organic phase through micrometer-sized interface indicates a nonlinear diffusion. On the other hand, the broad peak in the reverse scan confirms the transient linear diffusion of PFBS ions from the inner DCE to aqueous phase. The background subtracted CV of 6.0 µM PFBS shown in Figure 3.3.4.1 (b), where in forward scan the ions start transfer at potential 0.33 V as the current start increasing in that potential and becomes plateau at potential of 0.17 V. On the other hand, in reverse scan, PFBS ions transfer back to aqueous phase giving a peak at 0.30 V. The half wave potential based on forward sweep is 0.25 V.

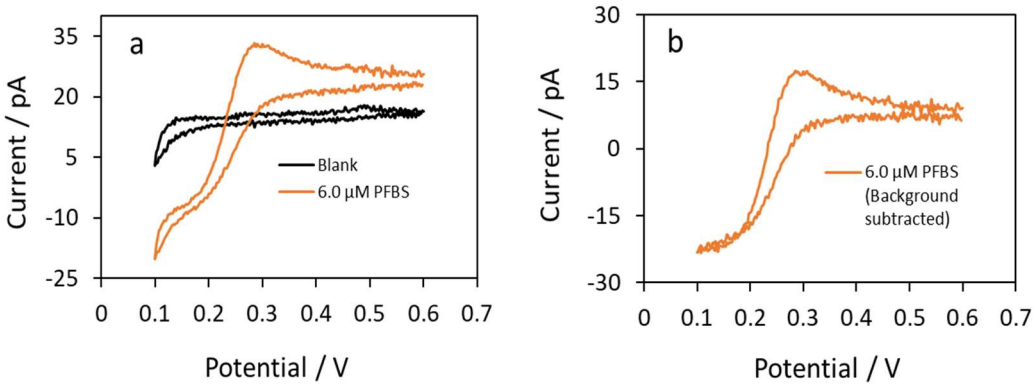

Figure 3.3.4.1: *(a) CV of 6.0 µM PFBS with CV of blank and (b) background subtracted CV of 6.0 µM PFBS at 23 µm radius interface. [Pipette radius with Equations 2.3.1.2 and 2.3.1.3 are also given in Appendix B.]*

The Figure 3.3.4.2 shows background subtracted CVs of PFBS in various concentrations ranging from 2 - 10 µM. Normal LiCl solution of pH ≈ 6.3 was used for this experiment. The data of steady state forward currents (i_f) and backward/reverse peak currents (i_b) of 3 scans for each concentration are given in the Table 3.3.4.1. Figure 3.3.4.3 shows current *vs* concentration graph based on those data. The currents on the forward sweeps as well as reverse sweeps of the background-subtracted CVs of PFBS increased linearly with the concentration in aqueous phase. These current vs concentration relation is consistent with the Saito equation [202] for the steady state current and the Randles–Sevcik equation [80, 203] for the voltammetric peak current for linear diffusion systems. Regardless of the diffusion mode, the current is concentration-dependent for both forward and reverse directions. Diffusion coefficient of PFBS (D_{PFBS}) for the aqueous phase calculated as 5.76 x 10^{-6} cm^2/s by using Saito equation, whereas D_{PFBS} was found 11 x 10^{-6} cm^2/s in literature measured by capillary method [204]. In this case also LOD was calculated by using the regression analysis of the forward currents from the CV experiments and with the help of (3 x σ) / S formula and the calculated LOD of PFBS was 0.22 µM.

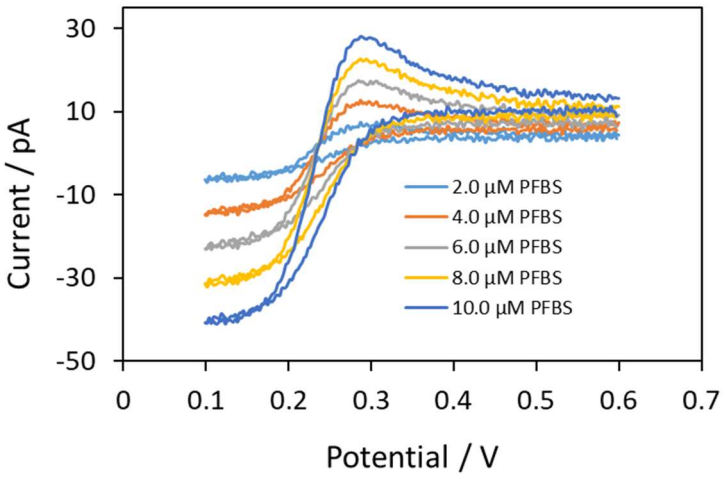

Figure 3.3.4.2: *Background subtracted CV of 2.0 µM, 4.0 µM, 6.0 µM, 8.0 µM and 10.0 µM PFBS at 23 µm radius interface. [Pipette radius with Equations 2.3.1.2 and 2.3.1.3 are also given in Appendix B.]*

Table 3.3.4.1: *Steady state forward currents* (i_f) *and reverse peak currents* (i_b) *with standard deviation (σ) for different concentrations of PFBS*

C / µM	i_{f1} / pA	i_{f2} / pA	i_{f3} / pA	Averagei_f / pA	σ
2	-10.84	-8.42	-12.35	-10.54	1.98
4	-20.15	-18.23	-22.39	-20.26	2.08
6	-31.01	-28.75	-33.15	-30.97	2.20
8	-40.74	-38.61	-41.92	-40.42	1.68
10	-50.23	-47.87	-52.31	-50.14	2.22
C / µM	i_{b1} / pA	i_{b2} / pA	i_{b3} / pA	Averagei_b / pA	σ
2	12.58	10.32	13.99	12.30	1.85
4	25.64	22.84	22.54	23.67	1.71
6	39.83	37.29	42.09	39.74	2.40
8	53.46	51.57	55.47	53.50	1.95
10	67.99	65.34	69.93	67.75	2.30

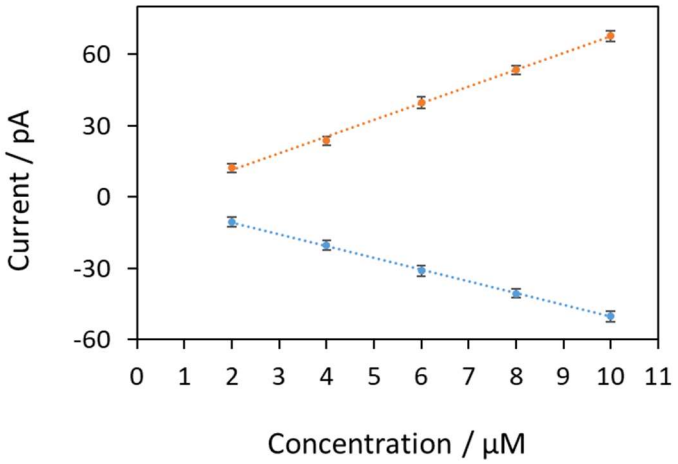

Figure 3.3.4.3: *Current vs concentration graph of PFBS for both forward and reverse direction.*

3.3.5 Cyclic Voltammetry of PFOA

The transfer of PFOA across the microinterface between water and DCE formed at the tip of 24.5 µm radius glass micropipette gives the similar response as PFOS, PFHxS & PFBS discussed in earlier sections. Figure 3.3.5.1(a) shows no response (blank) in the control experiment where all the experimental setup was the same other than no analyte. The response in the lower potential is due to transfer of background electrolyte. The Figure also shows the CV of 6.0 µM PFOA, which gives a sigmoidal voltammetric wave on the forward scan corresponding to transfer of the analyte from the outer aqueous phase to the organic phase through micrometer-sized interface indicates a nonlinear diffusion. On the other hand, the broad peak in the reverse scan confirms the transient linear diffusion of PFOA ions from the inner DCE to aqueous phase. The background subtracted CV of 6.0 µM PFOA shown in Figure 3.3.5.1(b). We ca sea for the forward scan the ions start transfer at potential 0.29 V as the current start increasing in that potential and becomes plateau at potential of 0.16 V. While, PFOA ions transfer back to aqueous phase giving a peak at 0.27 V in reverse scan. The calculated half wave potential based on forward scan is 0.23 V.

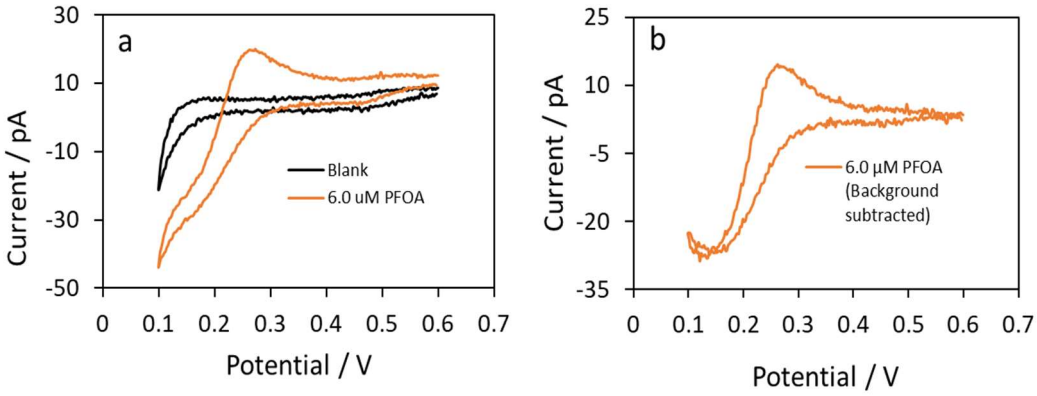

Figure 3.3.5.1: *(a) CV of 6.0 µM PFOA with CV of blank and (b) background subtracted CV of 6.0 µM PFOA at 24.5 µm radius interface. [Pipette radius with Equations 2.3.1.2 and 2.3.1.3 are also given in Appendix B.]*

The Figure 3.3.5.2 shows background subtracted CVs of PFOA in various concentrations ranging from 3.5 – 8.0 µM. Normal LiCl solution of pH ≈ 6.3 was used for this experiment. The data of steady state forward currents (i_f) and backward/reverse peak currents (i_b) of 3 scans for each concentration are given in the Table 3.3.5.1. Figure 3.3.5.3 shows current *vs* concentration graph based on those data. The currents on the forward sweeps as well as reverse sweeps of the background-subtracted CVs of PFOA increased linearly with the concentration in aqueous phase. These current vs concentration relation is predicted by the Saito equation [202] for the steady state current and the Randles–Sevcik equation [80, 203] for the voltammetric peak current for linear diffusion system. Irrespective of the diffusion mode, the current is concentration-dependent for both directions. Diffusion coefficient of PFOA (D_{PFOA}) for the aqueous phase calculated as 4.71 x 10^{-6} cm^2/s by using Saito equation, whereas D_{PFBS} was found 4.9 x 10^{-6} cm^2/s in literature measured by capillary method [204]. However, the increase rate of current in reverse potential is higher than the forward direction. This could be explained by the lipophilic nature of the perfluoroalkanesulfonates [199] . In this case also LOD was calculated by using the regression analysis of the forward currents from the CV experiments and with the help of (3 x σ) / S formula and the calculated LOD of PFOA was 0.61 µM.

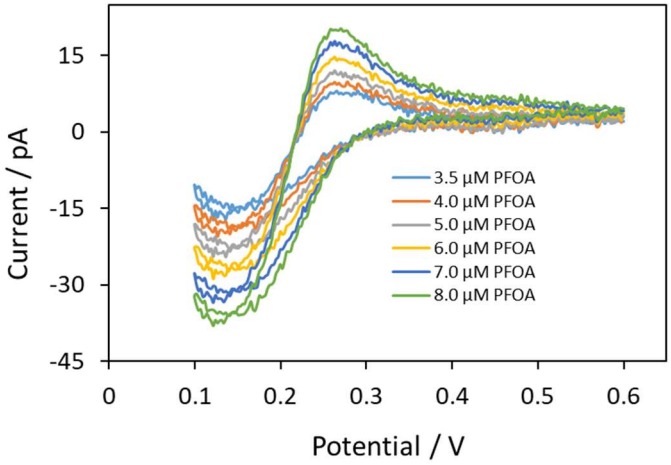

Figure 3.3.5.2: *Background subtracted CV of 3.5 µM, 4.0 µM, 5.0 µM, 6.0 µM, 7.0 µM and 8.0 µM PFOA at 24.5 µm radius interface. [Pipette radius with Equations 2.3.1.2 and 2.3.1.3 are also given in Appendix B.]*

Table 3.3.5.1: *Steady state forward currents* (i_f) *and reverse peak currents* (i_b) *with standard deviation (σ) for different concentrations of PFOA*

C / µM	i_{f1} / pA	i_{f2} / pA	i_{f3} / pA	Averagei_f / pA	σ
3.5	-15.87	-13.05	-16.39	-15.10	1.80
4	-19.32	-16.05	-20.12	-18.50	2.16
5	-22.77	-20.85	-22.69	-22.10	1.09
6	-27.01	-25.91	-28.75	-27.22	1.43
7	-31.22	-29.67	-33.09	-31.33	1.71
8	-35.89	-32.36	-36.45	-34.90	2.22
C / µM	i_{b1} / pA	i_{b2} / pA	i_{b3} / pA	Average3i_b / pA	σ
3.5	22.19	18.29	23.11	21.20	2.56
4	27.80	28.15	23.95	26.63	2.33
5	33.82	30.79	34.52	33.04	1.98
6	40.81	37.72	42.61	40.38	2.47
7	48.07	46.43	49.81	48.10	1.69
8	55.24	53.59	57.29	55.37	1.85

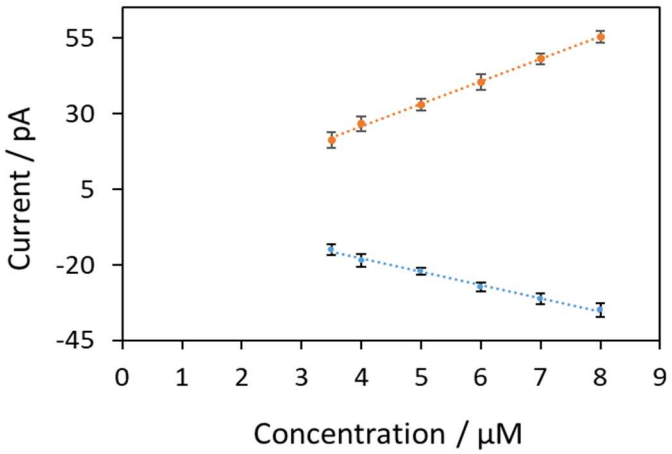

Figure 3.3.5.3: *Current vs concentration graph of PFOA for both forward and reverse direction.*

3.3.6 Comparison of the CVs of PFOS, PFHxS, PFBS and PFOA

From the previous discussions, we see that the transfer energy decreases with the increase of carbon numbers in perfluoroalkanesulfonates. For the case of forward scan for 6.0 µM PFOS (8 carbon chain), PFHxS (6 carbon chain) and PFBS (4 carbon chain), the ion start to transfer at potential 0.44 V, 0.40 V & 0.33 V respectively and becomes steady state current at 0.24 V, 0.22 V & 0.17 V, respectively. The same pattern is seen with the reverse peak at 0.42 V, 0.37 V & 0.30 V, respectively. The calculated half wave potential ($E_{1/2}$) for PFOS, PFHxS, PFBS are 0.34 V, 0.32 V, 0.25 V, respectively. The Figure 3.3.6.1 (a) shows as the forward scan starts from higher potential to lower potential, so, the right hand side of the potential scale indicates lower energy of transfer and the left hand side of the potential scale indicates higher energy of transfer. This Figure 3.3.6.1 is not for the comparison of current densities of PFAS substances as the pipettes used for each substance were not same size.

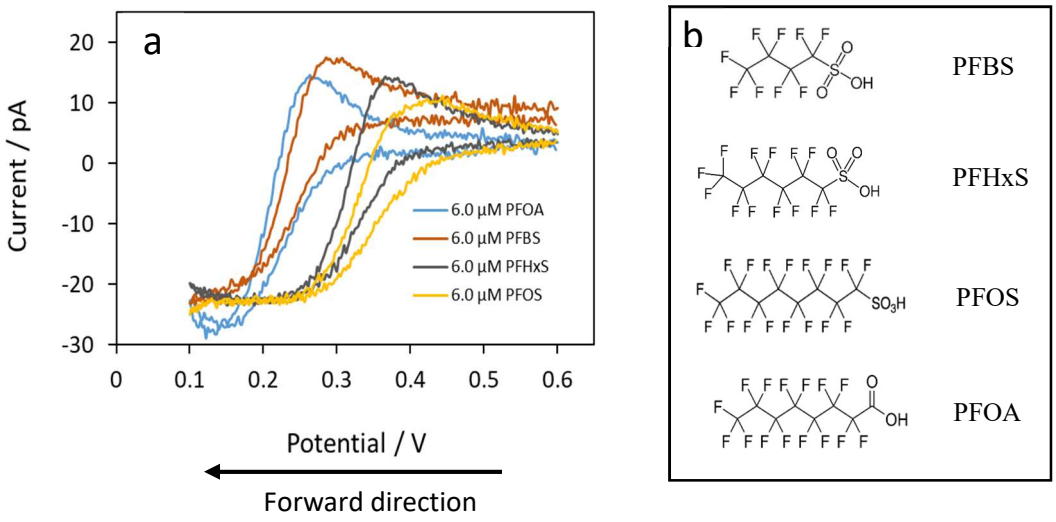

Figure 3.3.6.1 *(a) Background subtracted CV of 6.0 µM PFOA, 6.0 µM PFBS, 6.0 µM PFHxS, and 6.0 µM PFOS at 24.5 µm, 23 µm, 23 µm and 25 µm radius interface respectively. (b) Structures of the respective molecules. [Pipette radius with Equations 2.3.1.2 and 2.3.1.3 are also given in Appendix B.]*

Figure 3.3.6.1 (a) shows that the voltammograms observed the order PFOS < PFHxS < PFBS in case of required energy even though the shape of the voltammograms are more or less similar. This order corresponds to the reversed order of lipophilicity, which confirms that with a longer chain, perfluoroalkanesulfonate is more lipophilic than a shorter one. The similar result was found by Amemiya and his co-workers [200]. They also showed a comparison of PFOS with octanesulfonate (OS^-) which indicates alkanesulfonate is much less lipophilic than perfluoroalkanesulfonate with the same chain length [200]. This is happened because of the electron-withdrawing effects of fluorines in the perfluoroalkyl group, as fluorine is the most electronegative element, thus it reduces the electron density of the adjacent sulfonate group to be less hydrated [199].

One the other hand, the transfer of perfluoroalkanecarboxylates (PFOA) at the same condition was studied by cyclic voltammetry (Figure 3.3.6.1 a). Its half wave potential ($E_{1/2}$) is 0.23 V in the given potential scale. This indicate that it is much less lipophilic in comparison with those of perfluoroalkanesulfonates. Figure 3.3.6.1 (b) shows though the number of carbon chain in PFOA and PFOS are same but PFOA needs much more energy to transfer, even more than PFBS. The lower lipophilicity of perfluoroalkanecarboxylates is due to the stronger hydration energy of the carboxylate group which is smaller and more basic than the sulfonate group [205].

3.3.7 Differential Pulse Voltammetry (DPV)

As observed in previous sections, CV is a very good technique to detect perfluoroalkanesulfonates and perfluoroalkanecarboxylates with micropipette ITIES. The detection limit (LOD) by CV for PFOS, PFHxS, PFBS and PFOA was 1.07 μM, 0.677 μM, 0.223 μM and 0.609 μM respectively. . It has been also seen that the transfer potential of the selected PFAS species were very close together. Therefore, individual PFAS substances could not be detected from the mixture solutions by CV. For this reason, the selectivity was also assessed by differential pulse voltammetry (DPV) experiments, which is a technique that can give a peak-shaped response with better discrimination between species, to support a more thorough evaluation of selectivity and resolution. DPV offers that possibility and that is why it was employed in the study. Getting better LOD is not target of this work. The United States Environmental Protection Agency (EPA) [206] has set a health advisory level of 70 ppt for lifetime exposure of perfluorooctanesulfonic acid (PFOS) and perfluorooctanoic acid (PFOA), which is far away from our detection limit. This is a fundamental research to develop an alternative method, which will be robust and suitable for infield application. DPV was employed to obtain the sharper and better defined peaks at a lower concentration than cyclic voltammetry with a lower charging current and improved resolution. DPV was carried out in reverse scanning from 0.1 to 0.6 V. The conditioning potential, equilibrium time, step potential, modulation amplitude, modulation time and interval time were 0.1 V, 30 s, 0.005 V, 0.05, 0.04 s and 0.5 s respectively. The analyte sample was added from a stock solution to aqueous phase. In the beginning, a blank experiment (without analyte) was recorded and then the background subtraction procedure was applied to further increase the sensitivity of the technique. The LOD calculation was done by $(3 \times \sigma) / S$ formula [201], where S is the slope of the calibration curve and σ is the standard deviation of y-intercepts of regression line. The values of σ and S was obtained by using the LINEST function in Excel as like as CV experiment. LINEST function calculates the statistics of a simple line equation ($Y = mx + C$) which also explains the relationship between the dependent and independent variables using the least square procedure to find the best solution for data used.

3.3.8 Differential Pulse Voltammetry of PFOS

The lowest concentration of PFOS detected was 0.05 µM using background subtracted DPV. Figure 3.3.8.1(a) shows the DPV voltammograms of PFOS concentrations ranging from 0.05 µM to 1.0 µM with blank DPV included, and Figure 3.3.8.1 (b) shows the background subtracted voltammograms. The voltammograms show that the peak current increased as the PFOS concentration increased. Figure 3.3.8.2 shows the calibration curve obtained from the PFOS concentrations and peak currents.

Good linearity in the studied concentration range can be seen in Figure 3.3.8.2 for the peak currents obtained as a function of the PFOS concentration. The linear regression line (y) of best fit shows that the slope, y-intercept, regression coefficient (r^2), standard deviation of slope (STD_{slope}), standard deviation of y-intercept ($STD_{y\text{-}intercept}$) and standard deviation of the regression line (STDy) of this equation are 29.798, 0.381, 0.996, 0.657, 0.389 and 0.674 respectively. The limit of detection (LOD) calculated from these data was found 0.039 µM, whereas the LOD from CV experiment for the same size interface was 1.07 µM. So, DPV gives nearly 27 times lower detection limit than CV for PFOS detection.

Figure 3.3.8.3 shows the calculation of peak width at half height of the peak current ($W_{1/2}$). The $W_{1/2}$ is about 120 mV and for the reversible process, $W_{1/2}$ should be 90.4 mV (z=1) [207]. So, this process is not reversible. The peak potential (E_p) of PFOS for this DPV experiment is 0.32 V, whereas half wave potential ($E_{1/2}$) in CV experiment is 0.34 V, which are very close together.

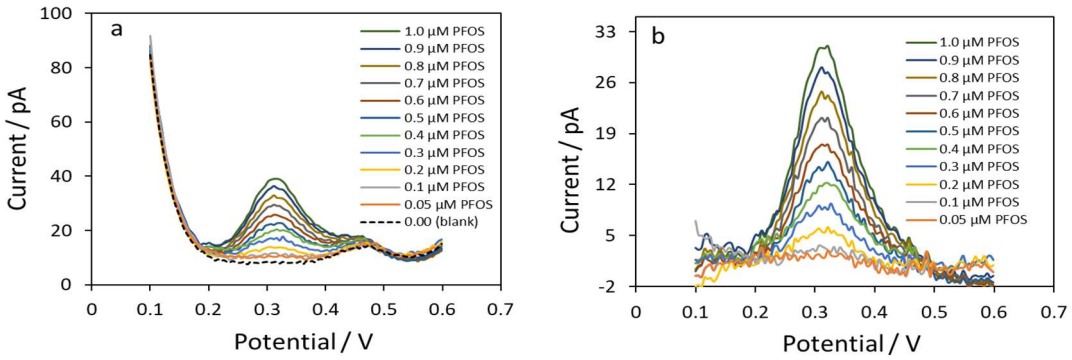

Figure 3.3.8.1: *(a) DPV voltammograms of 0.05, 0.1, 0.2, 0.3, 0.4, 0.5, 0.6, 0.7, 0.8, 0.9 and 1.0 µM PFOS with blank and (b) Background subtracted DPV of 0.05, 0.1, 0.2, 0.3, 0.4, 0.5, 0.6, 0.7, 0.8, 0.9 and 1.0 µM PFOS at 25 µm radius interface. [Pipette radius with Equations 2.3.1.2 and 2.3.1.3 are also given in Appendix B.]*

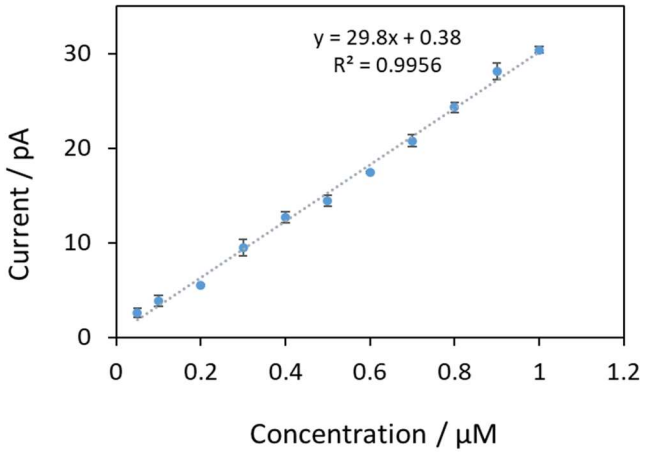

Figure 3.3.8.2: *Current vs concentration graph of 0.05, 0.1, 0.2, 0.3, 0.4, 0.5, 0.6, 0.7, 0.8, 0.9 and 1.0 µM PFOS.*

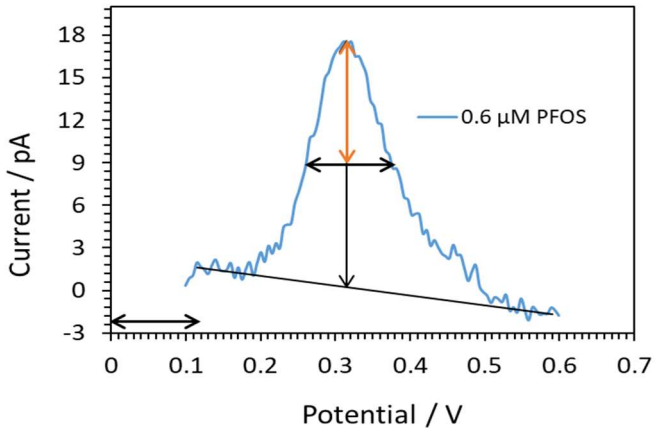

Figure 3.3.8.3: *Calculation of peak width at half height ($W_{1/2}$)*

3.3.9 Differential Pulse Voltammetry of PFHxS

In the case of PFHxS the lowest concentration was detected by DPV is also 0.05 µM. Figure 3.3.9.1 shows the background subtracted voltammograms obtained for the PFHxS concentrations ranging from 0.05 µM to 0.8 µM where the peak current increased linearly with the increase of concentration.

Calibration curve shows (Figure 3.3.9.2) good linearity in the studied concentration range seen for the peak currents obtained as a function of the concentration. For PFHxS the liner regression line (y) of best fit shows that the slope, y-intercept, regression

coefficient (r^2), standard deviation of slope (STD_{slope}), standard deviation of y-intercept ($STD_{y\text{-}intercept}$) and standard deviation of the regression line (STD_y) of this equation are 24.055, 0.705, 0.999, 0.330, 0.157 and 0.248 respectively. The limit of detection (LOD) calculated for PFHxS by DPV was found 0.02 µM. LOD from CV experiment for the same size interface was 0.68 µM. So, DPV gives nearly 34 times lower detection limit than CV for PFHxS detection.

Figure 3.3.9.3 shows the Calculation of peak width at half height of the peak current ($W_{1/2}$). The $W_{1/2}$ is about 95 mV and for the reversible process, $W_{1/2}$ should be 90.4 mV (z=1) [207]. The peak potential (E_p) of PFOS for this DPV experiment is 0.31 V, whereas half wave potential ($E_{1/2}$) in CV experiment is 0.32 V which nearly same.

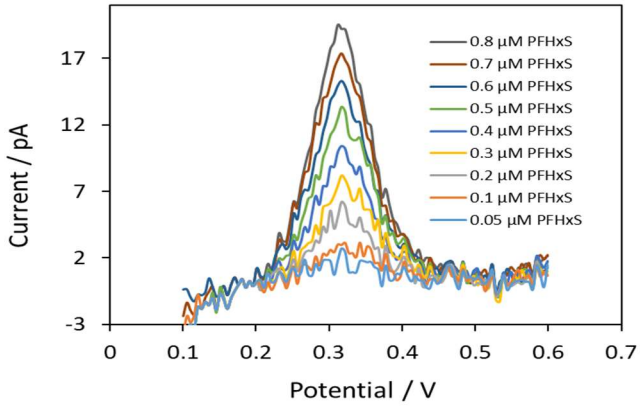

Figure 3.3.9.1: *Background subtracted DPV of 0.05, 0.1, 0.2, 0.3, 0.4, 0.5, 0.6, 0.7 and 0.8 µM PFHxS at 23 µm radius interface. [Pipette radius with Equations 2.3.1.2 and 2.3.1.3 are also given in Appendix B.]*

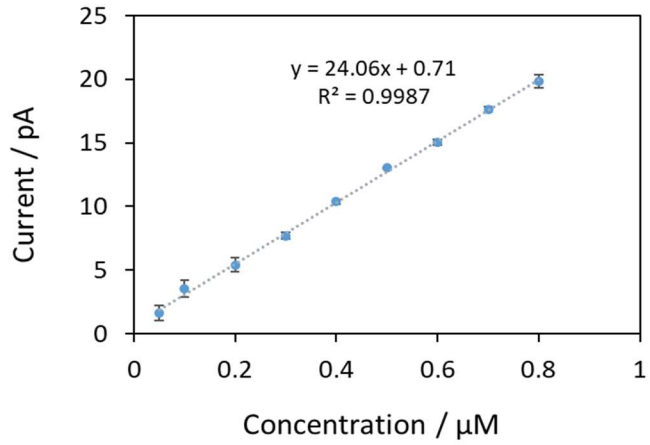

Figure 3.3.9.2: *Current vs concentration graph of 0.05, 0.1, 0.2, 0.3, 0.4, 0.5, 0.6, 0.7 and 0.8 µM PFHxS.*

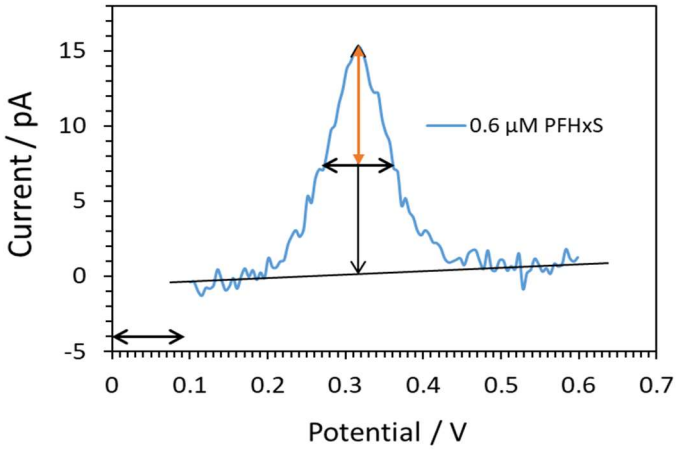

Figure 3.3.9.3: *Calculation of peak width at half height ($W_{1/2}$)*

3.3.10 Differential Pulse Voltammetry of PFBS

The lowest concentration of PFBS was also detected 0.05 µM using background subtracted DPV. Figure 3.3.10.1 shows the background subtracted voltammograms for the PFBS which exhibits the peak current increased linearly as the concentration increased ranging from 0.05 µM to 0.8 µM. The current response is much higher compare to CV experiments.

Calibration graph in that concentration range also shows good linearity obtained for the peak currents *vs* concentration (Figure 3.3.10.2). The liner regression line (y) of best fit for PFBS shows that the slope, y-intercept, regression coefficient (r^2), standard deviation of slope (STD_{slope}), standard deviation of y-intercept ($STD_{y\text{-}intercept}$) and standard deviation of the regression line (STDy) of this equation are 23.63, -0.117, 0.996, 0.539, 0.257 and 0.405 respectively. The limit of detection (LOD) was found 0.03 µM by using (3 x σ) / S formula. One the other hand, LOD from CV experiment for the same size interface was 0.22 µM. So, DPV gives nearly 7 times low detection limit than CV for PFBS detection.

Figure 3.3.10.3 shows the Calculation of peak width at half height of the peak current ($W_{1/2}$). The $W_{1/2}$ is about 90 mV and for the reversible process, $W_{1/2}$ should be 90.4 mV (z=1) [207]. The peak potential (E_p) of PFBS for this DPV experiment is 0.25 V, whereas half wave potential ($E_{1/2}$) in CV experiment is 0.25 V which are same.

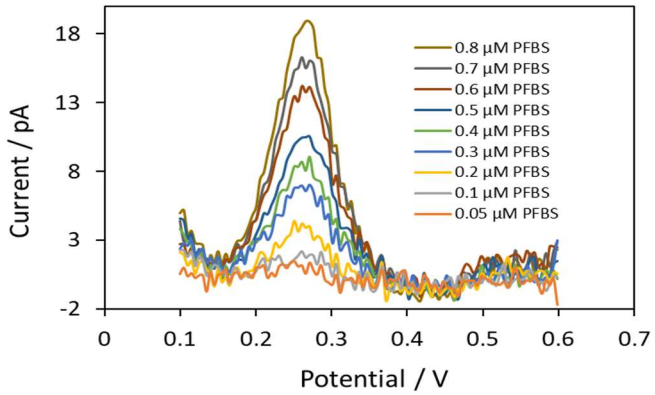

Figure 3.3.10.1: *Background subtracted DPV of 0.05, 0.1, 0.2, 0.3, 0.4, 0.5, 0.6, 0.7 and 0.8 µM PFBS at 23 µm radius interface. [Pipette radius with Equations 2.3.1.2 and 2.3.1.3 are also given in Appendix B.]*

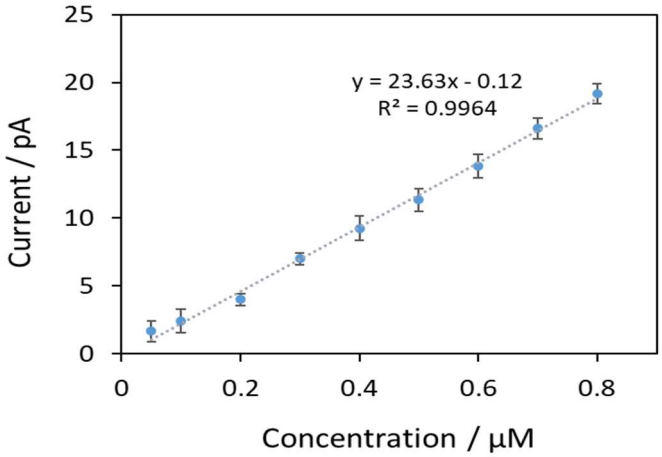

Figure 3.3.10.2: *Current vs concentration graph of 0.05, 0.1, 0.2, 0.3, 0.4, 0.5, 0.6, 0.7 and 0.8 µM PFBS.*

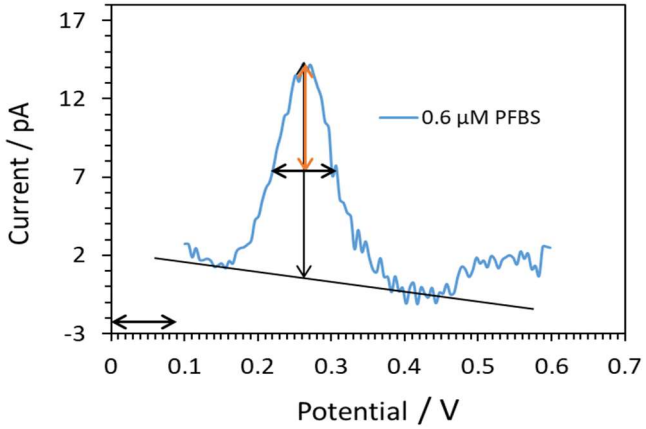

Figure 3.3.10.3: *Calculation of peak width at half height ($W_{1/2}$)*

3.3.11 Differential Pulse Voltammetry of PFOA

The lowest concentration of PFOA was detected 0.1 µM with DPV technique at micropipette ITIES. Figure 3.3.11.1 shows the background subtracted voltammograms for the PFOA which also displays the increase of peak with the increase of concentration within the range of 0.1 µM to 1.2 µM.

Calibration curve in that concentration range also shows good linearity for the peak currents *vs* concentration (Figure 3.3.11.2) with regression coefficient 0.995. The liner regression line (y) of best fit for PFOA shows that the slope, y-intercept, standard deviation of slope (STD_{slope}), standard deviation of y-intercept ($STD_{y\text{-}intercept}$) and standard deviation of the regression line (STDy) for this equation are 27.825, 0.954, 0.669, 0.464 and 0.736 respectively. The limit of detection was found 0.05 µM by using DPV method and LOD from CV experiment for the same size interface was 0.61 µM. So, DPV gives nearly 12 times low detection limit than CV for PFOA detection.

Figure 3.3.11.3 shows the Calculation of peak width at half height of the peak current ($W_{1/2}$). The $W_{1/2}$ is about 100 mV and for the reversible process, $W_{1/2}$ should be 90.4 mV (z=1) [207]. The peak potential (E_p) of PFOA for this DPV experiment is 0.22 V, whereas half wave potential ($E_{1/2}$) in CV experiment is 0.23 V which are nearly same.

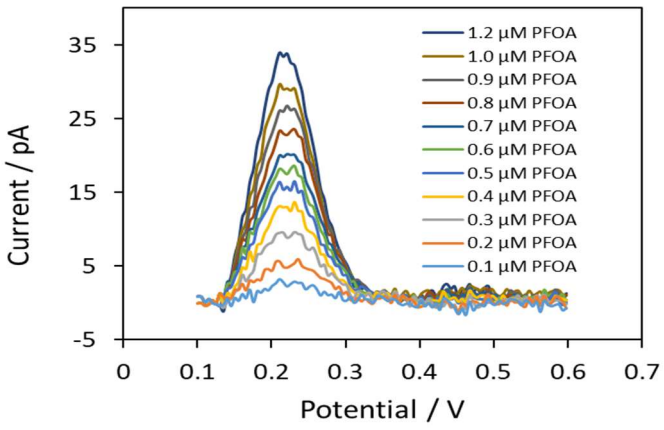

Figure 3.3.11.1: *Background subtracted DPV of 0.1, 0.2, 0.3, 0.4, 0.5, 0.6, 0.7, 0.8, 0.9, 1.0 and 1.2 µM PFOA at 24.5 µm radius interface. [Pipette radius with Equations 2.3.1.2 and 2.3.1.3 are also given in Appendix B.]*

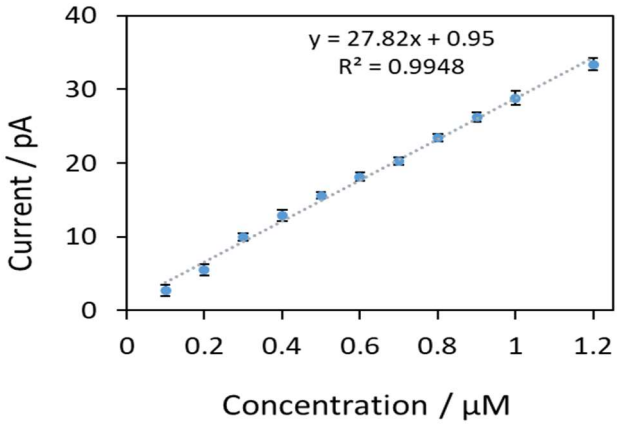

Figure 3.3.11.2: *Current vs concentration graph of 0.1, 0.2, 0.3, 0.4, 0.5, 0.6, 0.7, 0.8, 0.9, 1.0 and 1.2 µM PFOA.*

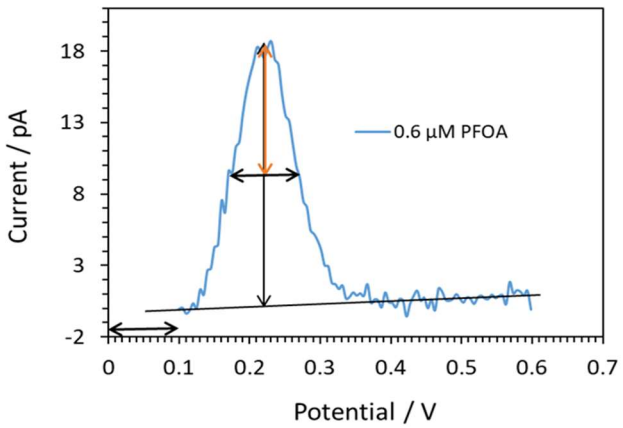

Figure 3.3.11.3: *Calculation of peak width at half height ($W_{1/2}$)*

All the data from the DPV analysis discussed in previous sections are summarized in the Table 3.3.11.1

Table 3.3.11.1: *Data of DPV analysis for the four analytes.*

Analyte	Slope (pA/µM)	STD_{slope} (pA/µM)	Intercept (pA)	$STD_{intercept}$ (pA)	r^2	LOD (µM) (3 x $STD_{intercept}$)/slope
PFOA	27.82	0.669	0.954	0.464	0.995	0.050
PFBS	23.63	0.539	-0.117	0.257	0.996	0.033
PFHxS	24.06	0.330	0.705	0.157	0.999	0.020
PFOS	29.80	0.657	0.381	0.389	0.996	0.039

3.3.12 DPV of the combinations of PFOA, PFBS, PFHxS and PFOS

The mixture of these four PFASs in six different combinations were studied by differential pulse voltammetry at the ITIES by using the same micropipettes. The parameters of the electrochemical and ITIES setup and the DPV technique were the same as mentioned earlier in sections 3.2.3 and 3.3.7 respectively. This mixture study was done to observe the impact on detection and analytical behaviour in presence of different molecules.

At first the mixture PFOA and PFOS were analysed. From the Figure 3.3.12.1, we can see the individual voltammograms of 0.7 µM of PFOA and 0.7 µM of PFOS. Their shapes are nice but overlaps near the half way of their current height. One the other hand, voltammogram of the mixture of 0.7 µM of PFOA and 0.7 µM of PFOS gives a broad peak covering the separate two peaks and give two distinct peaks at the top confirming two different molecules. In the mixture the peaks do not shifts, but their currents are not exactly same as individual PFOA & PFOS response at same concentration. From the Table 3.3.12.1 we can see the currents at different potential for 0.7 µM PFOA and 0.7 µM PFOS and the current for the mixture PFOA & PFOS of same concentration. The summation of the currents of PFOA & PFOS at a particular potential and the current of the mixture at that potential are very close.

Figure 3.3.12.2 shows the voltammogram of 1.0 µM PFOS and others where increase the concentration of PFOA from 0.1 µM to 1.0 µM while keeping the concentration PFOS fixed at 1.0 µM. That means first 1.0 µM PFOS was added and then different PFOA concentration was added to that solution. Figure clearly shows that when the concentration gap between two molecules is high then the voltammogram of DPV does not give any indication of two separate molecules present in the solution. From 0.4 µM PFOA it starts to give a hump in the same potential of PFOA and continue to increase up to 1.0 µM PFOA by giving two separate peak shape as like previous voltammogram of the mixture of 0.7 µM of PFOA and 0.7 µM of PFOS.

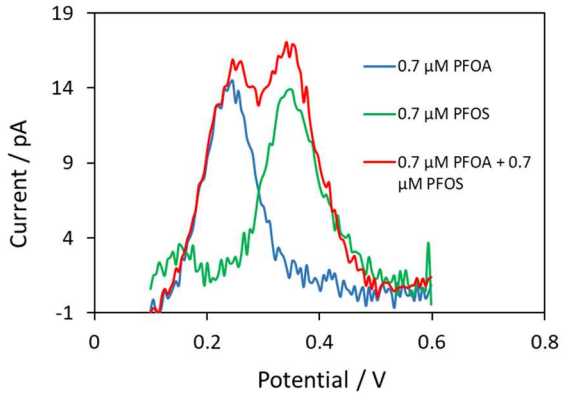

Figure 3.3.12.1: *Background subtracted DPV of 0.7 µM PFOA, 0.7 µM PFOS and mixture of 0.7 µM PFOA + 0.7 µM PFOS at the same micropipette.*

Table 3.3.12.1: *Current at different potential for individual PFOA, PFOS and mixture of them.*

Potential /V	i_{PFOA} (pA)	i_{PFOS} (pA)	$i_{PFOA+PFOS}$ (pA)	$i_{PFOA} + i_{PFOS}$ (pA)
0.24	14.19	2.32	15.62	16.51
0.29	6.93	6.93	12.85	13.86
0.35	2.35	13.85	16.94	16.20

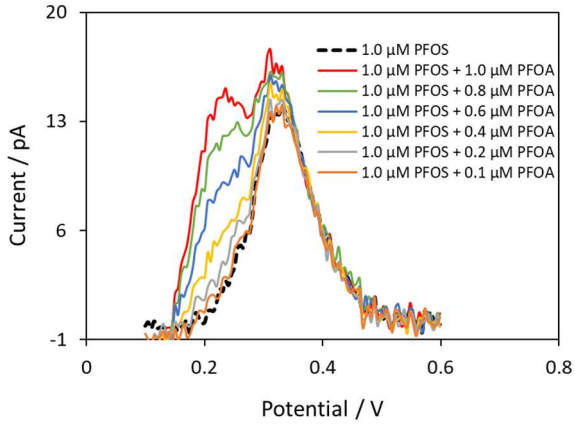

Figure 3.3.12.2: *Background subtracted DPV of 1.0 µM PFOS and 0.1, 0.2, 0.4, 0.6, 0.8, 1.0 µM PFOA with fixed 1.0 µM PFOS.*

Secondly, the mixture PFOA and PFHxS were studied. From the Figure 3.3.12.3, we can see the individual voltammograms of 1.0 μM of PFOA and 1.0 μM of PFHxS. Response for PFHxS is higher than the same concentration of PFOA and the two peaks overlaps near the half way of PFOA current height. One the other hand, voltammogram of the mixture of 1.0 μM of PFOA and 1.0 μM of PFHxS gives a broad peak covering the separate two peaks. Here also give two distinct peaks at the top confirming two different molecules at their individual transfer potential. In the mixture the PFHxS peak little shifts to left and their current are also little bit higher for both PFOA and PFHxS though their concentration remain same. Which indicates in mixture they might have some interaction that enhanced both of their transfer rate at liquid-liquid interface. From the Table 3.3.12.2 we can see the currents at different potential for 1.0 μM PFOA & 1.0 μM PFHxS and the current for the mixture PFOA and PFHxS of same concentration. The summation of the currents of PFOA and PFHxS at a particular potential and the current of the mixture at that potential are changes at the PFHxS region as the peak shifts in mixture.

Figure 3.3.12.4 shows the voltammograms where PFHxS concentration increased from 0.05 μM to 1.0 μM while keeping the concentration PFOA fixed at 1.0 μM. As like as previous discussion we can see that when the concentration gap between two molecules is high then the voltammogram of DPV does not give any indication of two separate molecules present in the solution except little bit broader in the lower area PFHxS. From 0.4 μM PFHxS it starts to develop a hump in the same potential of PFHxS and continue to increase up to 1.0 μM by giving two separate peak shape as like previous voltammogram of the mixture of 1.0 μM of PFOA and 1.0 μM of PFHxS.

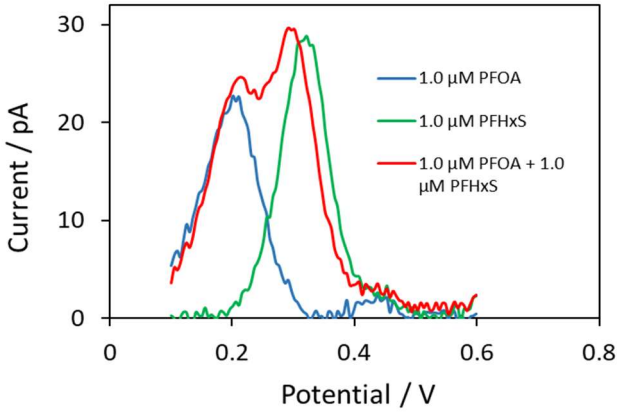

Figure 3.3.12.3: *Background subtracted DPV of 1.0 µM PFOA, 1.0 µM PFHxS and mixture of 1.0 µM PFOA + 1.0 µM PFHxS at the same micropipette.*

Table 3.3.12.2: *Current at different potential for individual PFOA, PFHxS and mixture of them.*

Potential /V	i_{PFOA} (pA)	i_{PFHxS} (pA)	$i_{PFOA+PFHxS}$ (pA)	$i_{PFOA} + i_{PFHxS}$ (pA)
0.23	20.26	2.87	23.22	23.13
0.26	10.28	10.28	24.32	20.56
0.30	2.84	23.99	29.57	26.83

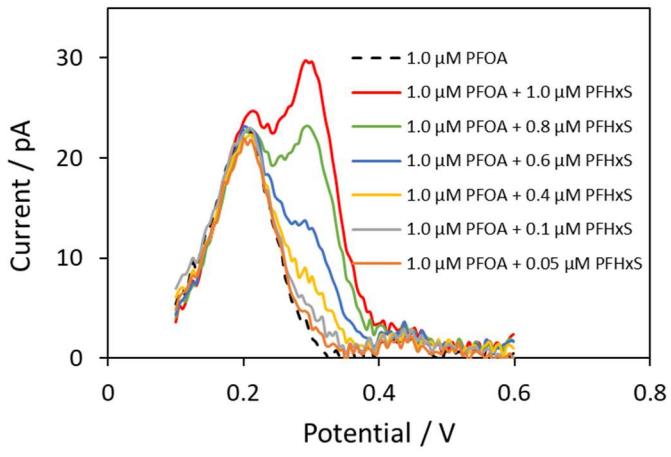

Figure 3.3.12.4: *Background subtracted DPV of 1.0 µM PFOA and 0.05, 0.1, 0.4, 0.6, 0.8, 1.0 µM PFHxS with fixed 1.0 µM PFOA.*

Thirdly, the mixture of PFBS and PFHxS were evaluated. From the Figure 3.3.12.5, we can see the individual voltammograms of 1.0 µM of PFBS and 1.0 µM of PFHxS. The individual peaks are very sharp, but their transfer potentials are closer and that's why they nearly overlaps each other. For the case of 1.0 µM of PFBS and 1.0 µM of PFHxS mixture solution gives a broad peak covering the separate two peaks, but their separation is not good as previous mixtures because of their close transfer potential. In the mixture the PFBS peak little shifts to left and both of their measured currents are also little bit higher for same individual concentration, indicates in mixture they might have some interaction that could have influence on their transfer rate and transfer potential at liquid-liquid interface. From the Table 3.3.12.3 we can see the currents at different potential for 1.0 µM PFBS & 1.0 µM PFHxS and the current for the mixture PFBS & PFHxS of same concentration. The summation of the currents of PFBS & PFHxS at a particular potential and the current of the mixture at that potential changes specially PFBS area as the peak shifts in that area.

Figure 3.3.12.6 shows the voltammograms where PFHxS concentration is fixed at 1.0 µM while the PFBS concentration increased up to 1.0 µM from 0.1 µM. The change of voltammogram while adding the PFBS into the solution gives nearly same result as previous mixtures. The peak becomes broader in PFBS transfer area as the PFBS concentration increases and again starts to develop a hump from 0.4 µM PFBS.

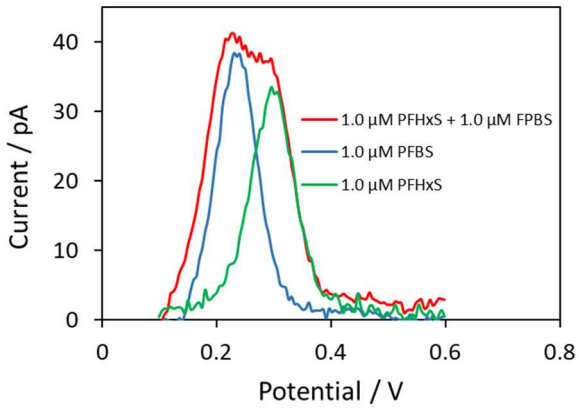

Figure 3.3.12.5: *Background subtracted DPV of 1.0 µM PFHxS, 1.0 µM PFBS and mixture of 1.0 µM PFHxS + 1.0 µM PFBS at the same micropipette.*

Table 3.3.12.3: *Current at different potential for individual PFHxS, PFBS and mixture of them.*

Potential /V	i_{PFBS} (pA)	i_{PFHxS} (pA)	$i_{PFBS+PFHxS}$ (pA)	$i_{PFBS} + i_{PFHxS}$ (pA)
0.20	24.32	3.88	30.64	28.20
0.23	36.87	7.21	41.14	44.08
0.30	5.16	32.56	37.54	37.72

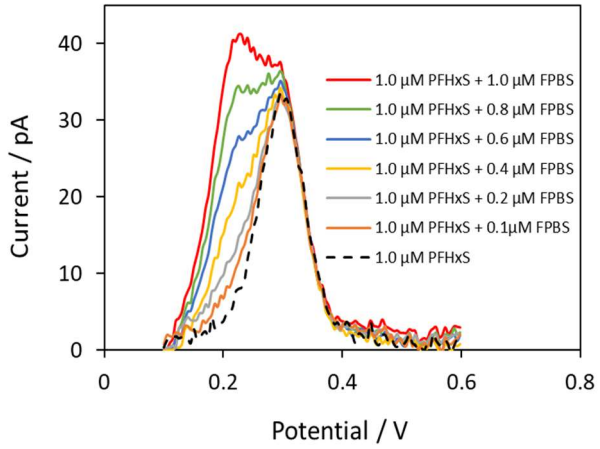

Figure 3.3.12.6: *Background subtracted DPV of 1.0 µM PFHxS and 0.1, 0.2 0.4, 0.6, 0.8, 1.0 µM PFBS with fixed 1.0 µM PFHxS*

Figure 3.3.12.7 shows the voltammograms of DPV analysis of the individual and the mixture of PFOS and PFBS. We can see the current response of 1.0 µM of PFBS is higher than 1.0 µM of PFOS and the two overlapping peaks overlap nearly half of each other. One the other hand, voltammogram of the mixture of 1.0 µM of PFOS and 1.0 µM of PFBS gives a broad peak whose peak area is nearly same as the summations of two individual peaks. But in this case it is difficult to understand the presence of two molecules from the voltammogram equimolecular mixture. From the Table 3.3.12.4 we can see the currents at different potential for 1.0 µM PFBS & 1.0 µM PFOS and the current for the mixture PFBS & PFOS of same concentration. The summation of the currents of PFBS & PFOS at a particular potential and the current of the mixture at that potential are nearly same.

Figure 3.3.12.8 shows the voltammograms where PFBS concentration increased from 0.1 µM to 1.0 µM while keeping the concentration PFOS fixed at 1.0 µM. In this case also, we can see, when the concentration gap between two molecules is high then the voltammogram of DPV does not give any indication of two separate molecules present in the solution except little bit broader peak in the lower area. The hump increases with concentration of PFBS and again diminishes the existence of two peaks when PFBS concentration reaches equivalent to PFOS concentration.

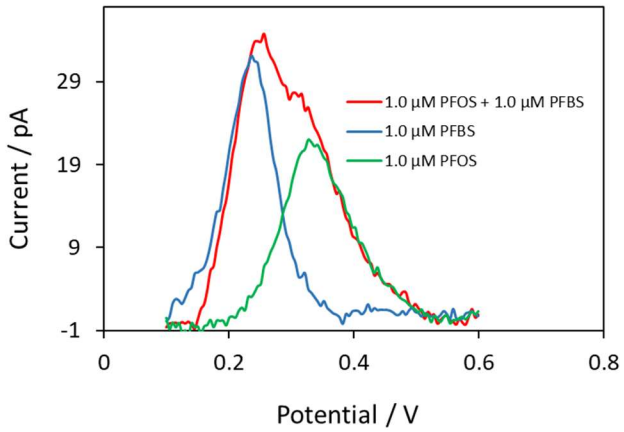

Figure 3.3.12.7: *Background subtracted DPV of 1.0 µM PFBS, 1.0 µM PFOS and mixture of 1.0 µM PFBS + 1.0 µM PFOS at the same micropipette.*

Table 3.3.12.4: *Current at different potential for individual PFBS, PFOS and mixture of them.*

Potential /V	i_{PFBS} (pA)	i_{PFOS} (pA)	$i_{PFBS+PFOS}$ (pA)	$i_{PFBS} + i_{PFOS}$ (pA)
0.24	31.39	3.02	33.84	34.41
0.27	19.62	9.19	31.40	28.81
0.32	5.52	20.80	27.19	26.33

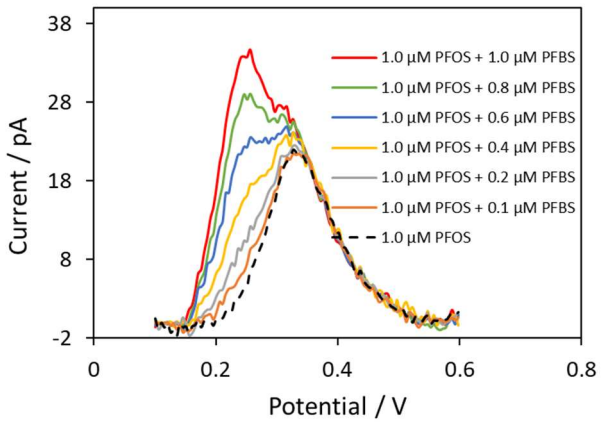

Figure 3.3.12.8: *Background subtracted DPV of 1.0 µM PFOS and 0.1, 0.2 0.4, 0.6, 0.8, 1.0 µM PFBS with fixed 1.0 µM PFOS.*

The mixture of PFOA and PFBS were also analysed, where the transfer potential of them are very close. From the Figure 3.3.12.9, we can see the individual voltammograms of 1.0 µM of PFOA and 1.0 µM of PFBS. As their transfer potential is very close, that's why they completely overlap each other. One the other hand, their equimolar (1.0 µM) mixture gives a big sharp peak just like a single element but the peak area is nearly same as the summation of the two individual peak areas. From the Table 3.3.12.5 we can also see that the summation of the peak currents of the individual PFOA and PFBS at 0.24 V is nearly equal to the mixture peak current at that potential.

Figure 3.3.12.10 shows the voltammograms where increase the concentration of PFOA from 0.1 µM to 1.0 µM while keeping the concentration PFBS fixed at 1.0 µM. For this case, the current increased with the concentration PFOA just like one type of molecule present. So for this mixture it is not possible to know two elements is present in the solution by observing the peak shape only.

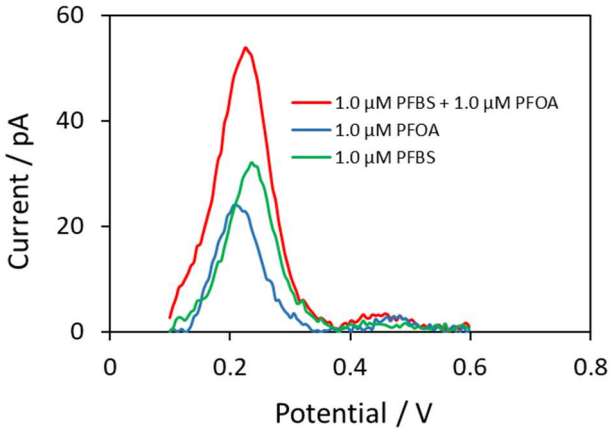

Figure 3.3.12.9: *Background subtracted DPV of 1.0 µM PFOA, 1.0 µM PFBS and mixture of 1.0 µM PFOA + 1.0 µM PFBS at the same micropipette*

Table 3.3.12.5: *Current at potential 0.24 V for individual PFOA, PFBS and mixture of them.*

Potential /V	i_{PFOA} (pA)	i_{PFBS} (pA)	$i_{PFOA+PFBS}$ (pA)	$i_{PFOA} + i_{PFBS}$ (pA)
0.24	21.82	30.98	52.98	52.80

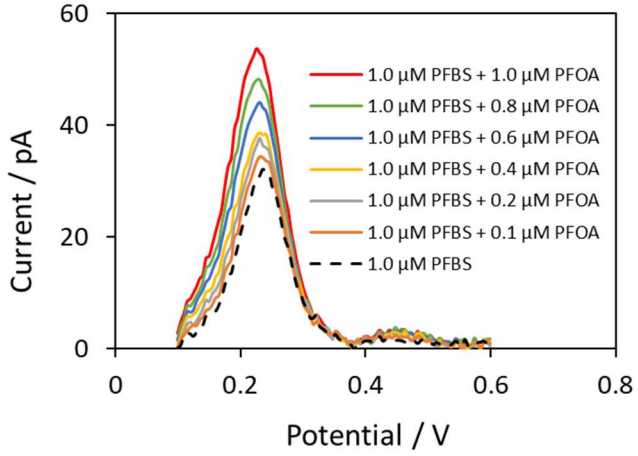

Figure 3.3.12.10: *Background subtracted DPV of 1.0 µM PFBS and 0.1, 0.2 0.4, 0.6, 0.8, 1.0 µM PFOA with fixed 1.0 µM PFBS.*

Finally the mixture of PFOS and PFHxS were investigated, where the transfer potential of them are nearly same. The Figure 3.3.12.11 shows the DPV response of 1.0 µM of PFOS and 1.0 µM of PFHxS where the two peaks are superimposed because of their same transfer potential at liquid-liquid interface. Similarly their equimolar (1.0 µM) mixture gives a big sharp peak just like a single element but the peak area is nearly same as the summation of the two individual peak areas of PFHxS and PFOS. From the Table 3.3.12.6, we can also see that the summation of the peak currents of the individual PFHxS and PFOS at 0.32 V is nearly equal to the mixture peak current at that potential.

Figure 3.3.12.12 shows the voltammograms where gradual increase the concentration of PFHxS from 0.1 µM to 1.0 µM and keeping the concentration PFOS fixed at 1.0 µM. For this case also as assumed the current increased with the concentration PFHxS just like one type of molecule present in the solution. So, for this case also not possible to know two elements is present in the solution by analysing the peak only. From the above discussions, Table 3.3.12.7 summarise whether the two molecules in a mixture, is possible to detect or not.

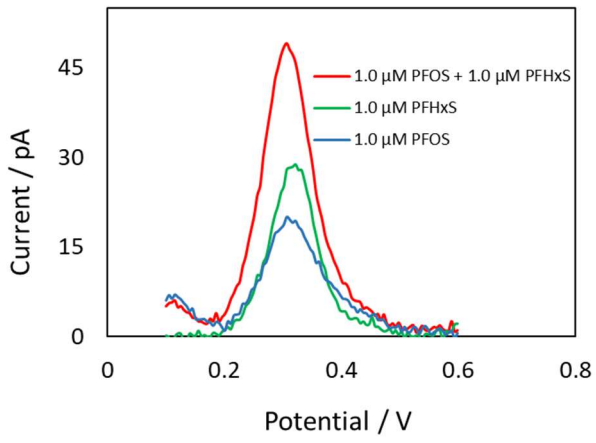

Figure 3.3.12.11: *Background subtracted DPV of 1.0 µM PFHxS, 1.0 µM PFOS and mixture of 1.0 µM PFHxS + 1.0 µM PFOS at the same micropipette.*

Table 3.3.12.6: *Current at potential 0.32 V for individual PFHxS, PFOS and mixture of them*

Potential /V	i_{PFHxS} (pA)	i_{PFOS} (pA)	$i_{PFHxS+PFOS}$ (pA)	$i_{PFHxS} + i_{PFOS}$ (pA)
0.32	27.83	19.07	47.18	46.91

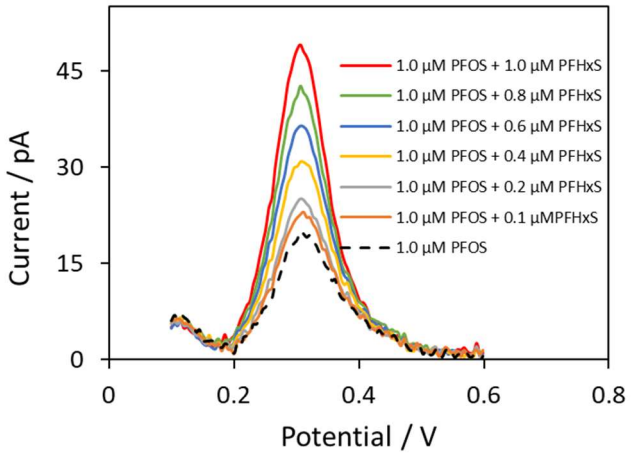

Figure 3.3.12.12: *Background subtracted DPV of 1.0 µM PFOS and 0.1, 0.2 0.4, 0.6, 0.8, 1.0 µM PFHxS with fixed 1.0 µM PFOS.*

Table 3.3.12.7: *The possibilities of the detection of two molecules in a mixture solution in various combination.*

Mixture of the two molecules				**Possibility of individual detection**
Molecule 1	Ep_1 / V	Molecule 2	Ep_2 / V	
PFOA	0.22	PFOS	0.32	yes
PFOA	0.22	PFHxS	0.31	yes
PFBS	0.25	PFHxS	0.31	yes
PFBS	0.25	PFOS	0.32	yes
PFOA	0.22	PFBS	0.25	no
PFHxS	0.31	PFOS	0.32	no

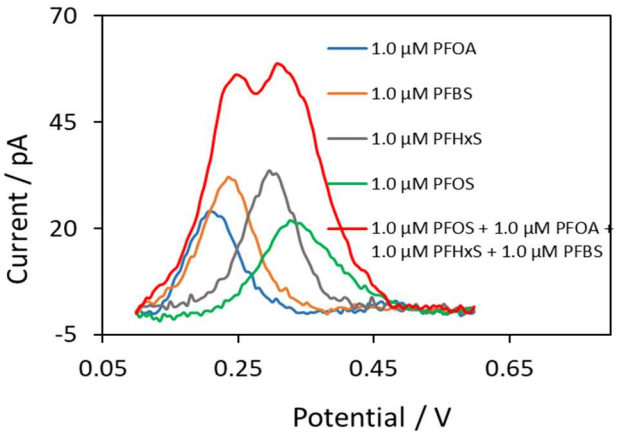

Figure 3.3.12.13: *Background subtracted DPV of 1.0 µM PFOA, 1.0 µM PFBS, 1.0 µM PFHxS, 1.0 µM PFOS and mixture of 1.0 µM PFOA + 1.0 µM PFBS + 1.0 µM PFHxS + 1.0 µM PFOS.*

Figure 3.3.12.13 shows the DPV study of the mixture and individual voltammograms of all four per- and polyfluoroalkyl substances (PFAS). The mixture of 1.0 µM of PFOA, 1.0 µM of PFBS, 1.0 µM of PFHxS and 1.0 µM of PFOS give a wide peak, which area is equal to the summation of all individual peak areas of PFOA, PFBS, PFHxS and PFOS. From this figure, it is clear that, though there are four different molecules present in mixture, but it gives a signal like two molecules present. So, this is a limitation that with DPV experiment we can't exactly say how many molecules are present on a solution if their transfer potential are close together.

3.4 Conclusion

Four per- and polyfluoroalkyl (PFAS) substances (i.e. PFOA, PFBS, PFHxS & PFOS) has been successfully detected at micro-ITIES formed at the tips of the micropipettes by applying cyclic voltammetry and differential pulse voltammetry. All the PFAS substances gave well-defined sigmoidal voltammetric wave or a steady state voltammogram for the forward scan, indicating a nonlinear or radial diffusion of the analytes from the outer aqueous phase to the micrometer-sized interface. On the other hand, a peak shape voltammogram in the reverse scan corresponds to a linear diffusion of PFAS substances from the inner DCE phase to the interface or aqueous phase. It has been also observed that the transfer potentials of four different substances changed

according to their lipophilicity, which depends on the carbon number and also on the functional groups present in that particular substances. Diffusion coefficients of analytes at aqueous phase was calculated from the CV experiments by using Saito equation and found very good agreement with the literature value measured using other methods. LOD was calculated from both CV and DPV results and has been found in range between 0.22 - 1.07 μM from CV and 0.02 - 0.05 μM from DPV technique. Selectivity of this four substances in their mixtures has been also investigated. Although their transfer potentials are very close together, most of the cases of mixtures of two PFAS substances were detected by DPV analysis. But PFOA - PFBS and PFHxS - PFOS mixtures gave one big peak, instead of two separate peaks, because of their transfer potentials are too close together to get separate peaks.

Chapter 4

Electrochemical Characterization of PAMAM Dendrimers.

4.1 Introduction

Dendrimers are unique and non-traditional polymers with well-defined structure, molecular size and surface charge. They are three-dimensional macromolecules with highly symmetric, spherical, hyper-branched, and monodisperse species different from linear polymers [208-213]. In general, a dendrimer is made up of three different parts, namely core, scaffold, and surface structure. The core is the centre part of the molecule and attached with a given number of dendrons or branches. Each and every dendron is composed of a number of branching points or scaffold and surface groups [214]. Figure 4.1.1 (a) shows the structures of dendrimers from generation 0 (G0) to generation 3 (G3). Figure 4.1.1 (b) (source : [215]) shows how the generation number of the dendrimers can be increased by increasing the functional groups on their surfaces or by adding layers to the branches [216, 217]. Because of these properties, they serve as model macromolecules that might tell us more about the electrochemistry of proteins and other biomacromolecules at the ITIES. The number and nature of functional groups of the dendrimer determines the physical and chemical properties of the dendrimer [218].

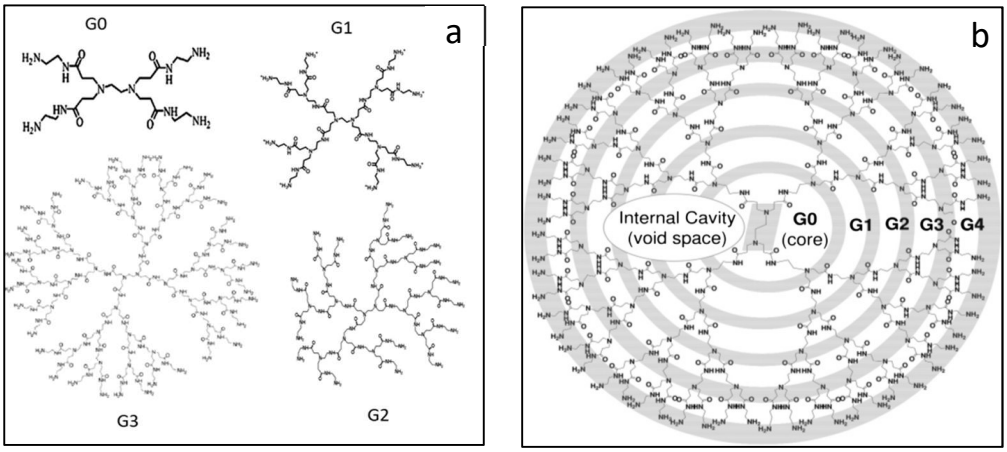

Figure 4.1.1: *(a) Structure of PAMAM dendrimers from G0 to G3 (b) development of higher generation dendrimers with adding functional groups in the surface [Figure b is taken from Abbasi et al. Nanoscale Research Letters 2014, 9:247. This is an open access article, which is licenced under a Creative Common Licence].*

They have many precise and specific properties like solubility, unique viscosity, hydrodynamic cheracter, and versatility [214]. Proteins are bio-macromolecules having different ionisable surface groups, which act differently at different pH, but

they can change their shape as well as charge. Dendrimers do not change their shape, only their charge. That's why dendrimers are now one of the most extensively studied for their distinctive features and used in multi-sectors. Due to the possibility for precise control over their physicochemical properties and their branched polymeric nanoparticle properties, dendrimers have been largely investigated for a wide range of biomedical applications [219-222], such as drug delivery, as unimolecular micelles and as mimics of proteins [223-227], in gene delivery [228-231], in cell membrane interactions [232], and as nanocarriers for RNAi therapeutic cancer treatment [227, 231, 233-235]. Dendrimers are also used as catalysts [236, 237], self-assembled monolayers as models for biological systems [238, 239] and so many applications. Electroactive dendrimers are of great important to understand biological electron-transfer processes [240] and they are also used as electron-transfer mediators for ion sensors or electro-optical devices [241].

Dendrimers like poly(amidoamine) [PAMAM] and poly(propylenimine) [PPI] might have cationic, anionic or neutral moieties at the surface and those are mainly responsible for the high solubility, reactivity and toxicity of the entire molecules [217, 242]. The synthesis and characterization of PAMAM dendrimers with ammonia or ethylenediamine (EDA) cores was first described in 1985 by Donald Tomalia's group [243]. PAMAM dendrimers are one of the best known dendrimers in drug-delivery because of their charged or polar parts in the biological conditions of the body environment [244, 245].

The electrochemical transfer of electrons or ions across the interface between two immiscible electrolyte solutions (ITIES) is one of the well-established fields in electrochemistry [10]. The investigation of voltammetric response of macromolecules and bio-macromolecules such as DNA and proteins at the ITIES has become a powerful and promising technique for their detection. For example, the electrochemical behaviour of insulin [246], haemoglobin [247], myoglobin [114], cytochrome *c* [248, 249] etc. have been investigated at the ITIES and established as a powerful technique to elucidate their electrochemical properties. The electrochemical and physicochemical properties of some dendrimers have been evaluated from their voltammetric behaviour at water/1,2-dichloroethane (DCE) interface. In 2007 Arrigan's group [250] reported on the analysis of different generations of

poly(propylenimine) (DAB-AM-n) and poly(amidoamine) (PAMAM) dendrimers at water/DCE macro-interface. They found that the electrochemical behaviour at ITIES depends on the dendrimer family, the generation number, and the experimental pH. They also observer that the lower generations gave well-defined peaks for both dendrimer families, whereas the higher generations show distorted voltammograms and instability of the interface. Nagatani et al. reported in 2008 [251] that the voltametric behaviour of G4 PAMAM at a water/(DCE) macro-ITIES was significantly depends on pH and also on the concentrations of both the dendrimer and the organic electrolyte. Interfacial mechanism analysis by potential modulated fluorescence (PMF) spectroscopy showed that at pH 7 the dendrimer transferred across the interface along with an adsorption step at the organic side of the interface. Calderon et al. [252] also analysis six dendrimer molecules where they proposed to transfer mechanism depending on the nature of the species and calculated the acid dissociation constants along with hydrophilicity character. G. Herzog et al. [253] investigated the electrochemical response, sensitivity and detection limit of four poly-l-lysine dendrigraft molecules (G2 – G5) at water/(DCE) macro-ITIES and found that the limit of detection decreased (11.10 to 0.65 μM) and the sensitivity increased (1840 to 25 800 nA μM–1) with the increase of generation G2 to G5 respectively. G. Herzog's group [254] further investigated the effects on electrochemical behaviour of PAMAM G0 and G1 at modified liquid/liquid micro arrays with silica. They found that the multi-positively charged dendrimers have electrostatic interaction with negatively charged silica which affects the LOD, sensitivity and diffusion coefficient. Recently, Yuanhua Shao's group [255] investigated facilitated ion transfer (FIT) of PAMAM (G0–G2) by dibenzo-18-crown-6 (DB18C6) at water/DCE μITIES, where they reported that the facilitated transfer potential of PAMAM decreased linearly with the increase of DB18C6 concentration. They also proposed that the higher generation dendrimers might transfer at the interface through deprotonation process.

Our research is a fundamental investigation to observe the electrochemical behaviour of protein-like dendrimer molecules, which do not change their shape at various pH values. The change of functionality / electrochemical properties with pH is very important for detection, as pH changes might influence sensitivity that is unrelated to concentration due to shape changes of proteins. We investigate the electrochemical properties of dendrimer molecules as a model set of molecules that have a simpler

behaviour in comparison to proteins and can tell us about the charge effects controlled by pH.

In this study focused on the voltammetric behaviour of four generations of PAMAM (PAMAM-0, PAMAM-1.0, PAMAM-2.0 and PAMAM-3.0) at single μITIES formed at the tip of the glass pipette. Previous studies used large interfaces, so data analysis might be impacted by uncompensated resistance or capacitance effects. A single μITIES renoves or at least minimises these effects and might reveal a more accurate electrochemical behaviour. Finally, the interest in dendrimers is important because they are ideal macromolecules which can be ionised easily by adjusting the pH of the aqueous phase. Hence, they serve as model macromolecules that might tell us more about the electrochemistry of proteins and other biomacromolecules at the ITIES. The PAMAM dendrimers are non-redox-active and their electrochemistry at the ITIES depends on acid-base behaviour. The pKa of primary amine groups is 9.5 [28] and on the other hand the tertiary amine groups are fully protonated only at pH 3 [29]. So it is expected that at higher pH primary amine will give better response as will be more protonated, whilst sufficiently low pH can lead to protonation of the maximum tertiary amino groups. Due to that, the PAMAM dendrimers are also expected to interact differently with the interface, depending on the pH of the aqueous phase. That is why in this investigation a wide range of aqueous phase pH (1.75 to 11.0) was used for all four PAMAMs to determine the change of electrochemical behaviour with pH.

4.2 Experimental

4.2.1 Reagents

All the reagents were purchased from Sigma-Aldrich Australia Ltd. and used as received unless otherwise indicated. The organic electrolyte bis(triphenylphosphoranylidene)ammonium tetrakis(4-chlorophenyl)borate (BTPPATPBCl) was prepared by metathesis of equimolar amounts of bis(triphenylphosphoranylidene)ammonium chloride (BTPPACl) and potassium tetrakis(4-chlorophenyl)borate (KTPBCl) as reported earlier [77]. BTPPATPBCl (0.01 M) solutions were prepared in 1,2-dichloroeheane (DCE). Chlorotrimethylsilane was used for silanization of pipettes. All aqueous solutions (e.g. LiCl solution) were prepared in purified water from a USF Purelab plus UV (resistivity: 18.2 MΩ cm). The dendrimer kits (generation ‘0’ - ‘3’) are also from Sigma-Aldrich Australia Ltd.

4.2.2 Electrochemical cell

Electrochemical measurements were conducted by using an Autolab PGSTAT302N electrochemical analyser (Metrohm Autolab, Utrecht, The Netherlands) running with NOVA software. The pipettes for the experiments for this chapter were prepared, modified and characterized according to the section 3.3.2 in chapter 3. The organic electrolyte phase was introduced into the pipette which comes up to the tip and the organic reference solution (saturated BTPPACl in 10 mM LiCl) was placed on the top of the organic phase. Then the pipette was immersed into the aqueous phase so that an ITIES formed at the tip of the pipette. As this was a miniaturized interface, so two-electrode system was employed for this electrochemical cell. An Ag/AgCl electrode was in the aqueous solution and another Ag/AgCl electrode used in the organic reference solution. The micro-interface was polarised by imposing a potential difference between these two electrodes. Unless stated 10 mVs^{-1} scan rate was applied to carry out cyclic voltammetry (CV) experiments. The pH of the aqueous LiCl solution was adjusted by using NaOH and HCl solution. The cell is described in the following scheme.

$$\text{Ag}\,|\,\text{AgCl}\,|\,\begin{matrix}\text{Sat'd BTPPACl}\\ \text{in 10 mM LiCl}\end{matrix}\,|\,\begin{matrix}\text{10 mM BTPPATPBCl}\\ \text{in DCE}\end{matrix}\,||\,\begin{matrix}\text{x µM PAMAM in 10 mM}\\ \text{LiCl of controlled pH}\end{matrix}\,|\,\text{AgCl}\,|\,\text{Ag}$$

4.3 Results and discussions:

4.3.1 Cyclic Voltammetry

The transfer of dendrimers across the microinterface between water and DCE formed at the tip of a glass micropipette were studied by cyclic voltammetry to analyse the electrochemical behaviour of PAMAM dendrimers at different pH. The cyclic voltammograms starts from a low potential and the forward scan was in a positive direction. The potential window is limited by the transfer of background electrolyte at low and high potentials. All four generations of dendrimers gave very good CV responses and formed well-defined voltammograms and their position varies a little bit depending on the pH of the aqueous phase. On the forward scan, a sigmoidal voltammetric wave or nearly steady state voltammogram formed at high potential (near to the background transfer), corresponding to transfer of the dendrimers and

indicates a nonlinear or radial diffusion from the outer aqueous phase to the micrometer-sized interface. On the other hand, the peak response in the reverse scan confirms the linear diffusion of dendrimers from the inner DCE phase to the interface or aqueous phase. Shape of the voltammogram is very important to illustrate the possible mechanism for dendrimer behaviour at ITIES. If the cation of the dendrimer and anion of the organic electrolyte form a complex at the interface then we should see a peak for transfer of organic anion form org to aq phase. But a steady-state current is obtained, which means the controlling mass transport is in the aqueous phase, meaning dendrimer transfer occurs.

The molecular charge of the PAMAM dendrimers depends on the experimental pH of dendrimer solution. The approximate charges of these dendrimers based on potentiometric (acid-base) titrations from published data are summarized in Table 4.3.1.1 [244]. Protonation of PAMAM dendrimers first occurs in the primary amino surface groups at the outer rim of the dendrimers at high pH. One the other hand, the interior tertiary amino groups are protonated at lower pH and the central tertiary amine protonated last at even lower pH [244, 250].

Table 4.3.1.1: *Number of amino groups for different generations PAMAM dendrimer.*

Dendrimer	no. of surface amino groups	no. of interior amino groups	Total amino groups
G0	4	2	6
G1	8	6	14
G2	16	14	30
G3	32	30	62

4.3.2 CV of PAMAM dendrimer ‘0’

PAMAM dendrimer generation ‘0’ has 4 surface primary amino groups and 2 interior tertiary amino groups [256]. The Figure 4.3.2.1 shows the structure of PAMAM ‘0’. The cyclic voltammetry experiment gives a very good response for this molecule. The experiment was done at different aqueous phase pH and the pH values were chosen so as to have a distribution across the range studied.

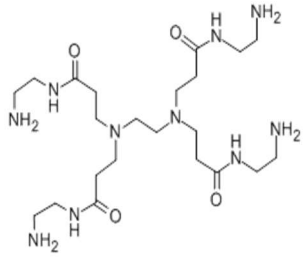

Figure 4.3.2.1: *Structure of PAMAM ‘0’*

CV at pH 2.75

Figure 4.3.2.2(a) shows the voltammogram of the blank where no PAMAM ‘0’ at pH 2.75. Blank shows only the background ion transfers, whereas a very good response for 6 µM PAMAM ‘0’. In forward direction, the current starts to increase and makes a semi steady state voltammogram instead of nice steady state because it transfer near to the background ions transfer. This indicates a radial diffusion of PAMAM ‘0’ ions towards the organic phase from the aqueous phase. However, in reverse scan direction, it gives a peak shape response indicating linear transfer of ions from organic to aqueous phase [257]. Figure 4.3.2.2(b) shows the background subtracted CVs of different concentrations of dendrimer ‘0’. The background subtracted forward currents shows a very good steady state current, which is ideal for micro-interface radial diffusion [257] and the reverse CVs also give peak currents according to ideal linear diffusion from inner organic phase to the aqueous phase through the micro-pipette interface [257]. Figure 4.3.2.2(b) shows the CV of the concentration range of 1-10 µM, where all the forward scan starts ion transfer at potential ≈ 0.67 V and becomes plateau at potential ≈ 0.74 V. While the reverse scan gives peak at ≈ 0.71 V. The calculated half wave potential ($E_{1/2}$) based on the forward scan is 0.71 V.

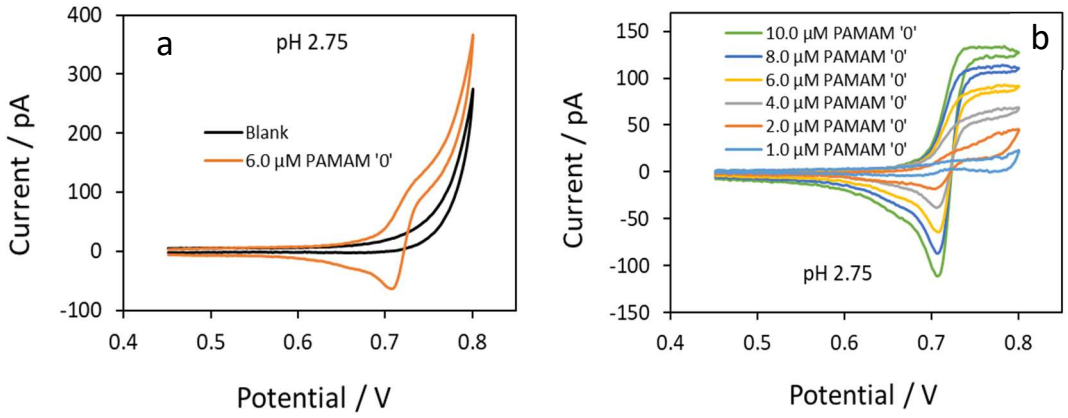

Figure 4.3.2.2: *(a) CV of 6 µM PAMAM '0' with blank and (b) background subtracted CV for 1, 2, 4, 6, 8 & 10 µM PAMAM '0' at pH 2.57 with 23 µm pipette radius. [Pipette radius with Equations 2.3.1.2 and 2.3.1.3 are also given in Appendix B.]*

Table 4.3.29.1: *Steady state forward currents (i_f) and reverse peak currents (i_b) of three scans of CV for 1, 2, 4, 6, 8 & 10 µM PAMAM '0' at pH 2.57.*

C / µM	i_{f1} / pA	i_{f2} / pA	i_{f3} / pA	Average i_f / pA	σ
1	5.2	8.9	9.8	8.0	1.99
2	16.3	20.3	22.8	19.8	2.66
4	46.0	47.2	51.2	48.1	2.21
6	68.2	73.3	74.9	72.1	2.86
8	99.3	103.4	104.6	102.4	2.26
10	120.7	123.8	125.2	123.2	1.86
C / µM	i_{b1} / pA	i_{b2} / pA	i_{b3} / pA	Average i_b / pA	σ
1	-2.8	-3.1	-4.0	-3.3	0.52
2	-11.1	-14.2	-15.7	-13.6	1.92
4	-27.5	-32.1	-31.2	-30.3	1.99
6	-44.3	-47.3	-49.6	-47.0	2.17
8	-62.2	-65.3	-67.4	-65.0	2.15
10	-70.2	-64.2	-76.7	-70.4	5.12

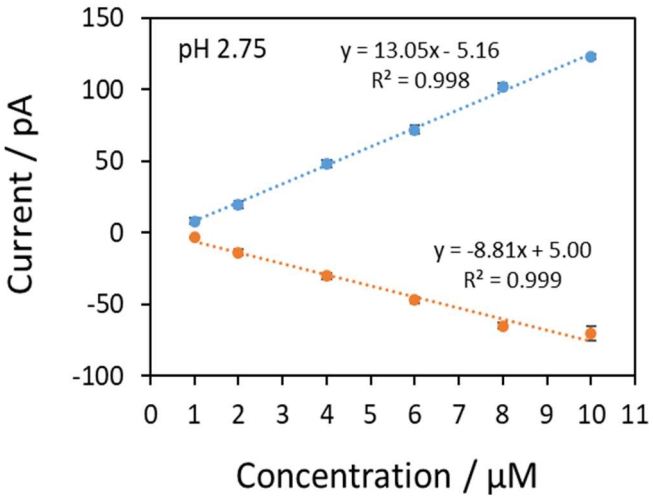

Figure 4.3.2.3: *Current vs concentration graph for both forward and reverse scan for pH 2.75.*

The steady state forward current (i_f) and reverse peak current (i_b) of three scans from the experiment for each concentration are given in the Table 4.3.2.1. Figure 4.3.2.3 shows current *vs* concentration graph based on the data of that Table. The currents on the forward sweeps as well as reverse sweeps of the background-subtracted CVs of dendrimer '0' at pH 2.75 increased linearly with the concentration of analyte in the aqueous phase. These current vs concentration relation is predicted by the Saito equation [202] for the steady state current and the Randles–Sevcik equation [80, 203] for the voltammetric peak current for linear diffusion systems. Irrespective of the diffusion mode, the current is concentration-dependent for both directions. Diffusion coefficient (D) also calculated from the forward current using Saito equation $I_{ss} = 4|z_i|FDCr$. Where I_{ss} is the steady state current, z_i, *F, D, C* and *r* are the charge, Faraday constant, diffusion coefficient, concentration and radius of the interface respectively. Slope (13.05 pA/µM) of current *vs* concentration is used from the Figure 4.3.2.3. Charge 6 for this pH is calculated from the potentiometric titration curves at 0.1 M KCl of dendrimer G0, which is published in 2003 [244]. Radius of the pipette for this case was 23 µm. By using these values diffusion coefficient was calculated 2.45×10^{-6} cm^2/s.

CV at pH 3.5

Figure 4.3.2.4(a) shows the voltammogram of 6 µM PAMAM '0' whereas blank shows only the background ions transfer. At this pH it gives better response than all

other pH. In forward direction, the current starts to increase and makes nearly steady state voltammogram as it transfers near to the background ions transfer. The nearly statedy-state voltammogram indicates a radial diffusion of PAMAM '0' ions towards the organic phase from the aqueous phase. However, it gives a peak shape response in the reverse direction indicating linear transfer of ions from organic to aqueous phase [257]. Figure 4.3.2.4(b) shows the background-subtracted CVs of the concentration range of 0.5-10 µM. Background-subtracted CVs gave very good steady state for forward currents, which is ideal for micro-interface radial diffusion [257] and the reverse CVs also give peak currents according to ideal linear diffusion from inner organic phase to the aqueous phase through the micro-pipette interface [257]. All of the forward scans start ion transfer at potential ≈ 0.67 V and becomes plateau at potential ≈ 0.74 V. While the reverse scan gives peak at ≈ 0.71 V. The calculated half wave potential ($E_{1/2}$) based on the forward scan is 0.71 V. Those parameters are the same as for the results from voltammetry in the aqueous phase with pH 2.75.

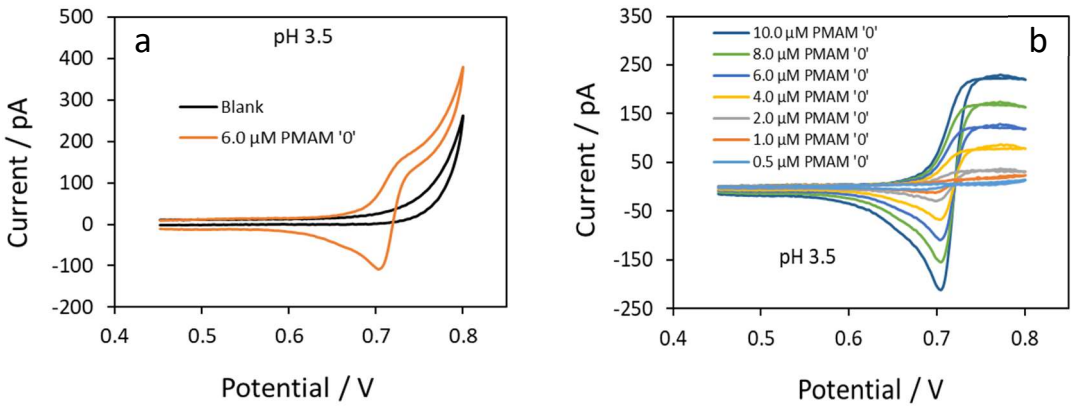

Figure 4.3.2.4: *(a) CV of 6 µM PAMAM '0' with blank and (b) background subtracted CV for 0.5, 1, 2, 4, 6, 8 & 10 µM PAMAM '0' at pH 3.5 with 26 µm pipette radius. [Pipette radius with Equations 2.3.1.2 and 2.3.1.3 are also given in Appendix B.]*

Table 4.3.2.2: *Steady state forward currents (i_f) and reverse peak currents (i_b) of three scans of CV for 1, 2, 4, 6, 8 & 10 µM PAMAM '0' at pH 3.5.*

C / µM	i_{f1} / pA	i_{f2} / pA	i_{f3} / pA	Average i_f / pA	σ
1	9.3	13.9	12.8	12.0	1.94
2	26.2	32.4	30.1	29.6	2.57
4	67.3	74.5	72.2	71.3	3.03
6	103.2	108.7	106.3	106.1	2.26
8	142.7	148.2	147.9	146.3	2.52
10	191.3	197.5	195.5	194.8	2.57
C / µM	i_{b1} / pA	i_{b2} / pA	i_{b3} / pA	Average i_b / pA	σ
1	-8.6	-13.1	-11.6	-11.1	1.87
2	-23.6	-29.4	-26.9	-26.7	2.38
4	-54.4	-61.1	-58.8	-58.1	2.76
6	-94.8	-101.3	-99.7	-98.6	2.79
8	-126.6	-130.6	-129.2	-128.8	1.65
10	-169.5	-177.6	-173.4	-173.5	3.32

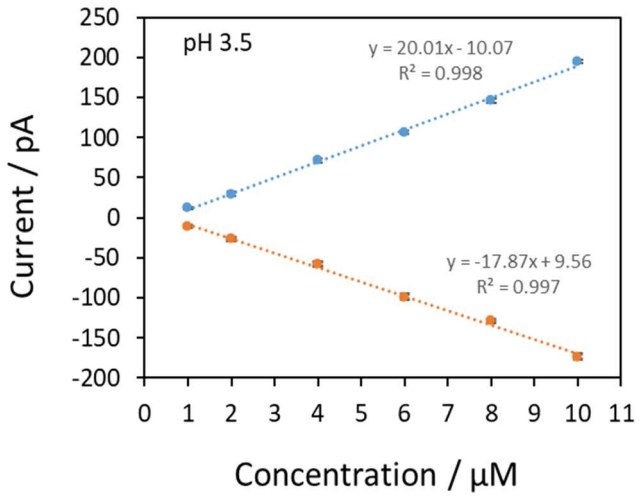

Figure 4.3.2.5: *Current vs concentration graph for both forward and reverse scan for pH 3.5.*

The steady state forward currents (i_f) and reverse peak currents (i_b) of all concentrations are given in the Table 4.3.2.2 and based on these data a current *vs*

concentration graph was drawn which is shown in Figure 4.3.2.5. The currents on the forward sweeps as well as reverse sweeps of the background-subtracted CVs at pH 3.5 increased linearly with the concentration of analyte in the aqueous phase. This current vs concentration relation shows that in both directions the current is concentration-dependent irrespective of the diffusion mode. Like the previous one, diffusion coefficient (D) was calculated from the forward current using Saito equation $I_{ss} = 4|z_i|FDCr$. Slope of current *vs* concentration is 20.01 pA/μM (Figure 4.3.2.5). Charge is 6 for this pH which is calculated from the potentiometric titration curves at 0.1 M KCl of dendrimer G0 [244]. Radius of the pipette for this case was 26 μm. By using these values diffusion coefficient was calculated 3.32 x 10^{-6} cm^2/s.

CV at pH 6.0

PAMAM '0' also gives good response at pH 6.0. Figure 4.3.2.6(a) shows the current starts to increase and produces a nearly steady state voltammogram as it transfer near to the background ions transfer in forward direction for 6 μM PAMAM '0' indicates radial diffusion of ions towards the organic phase from the aqueous phase. As like before, it gives a peak shape response in reverse direction indicating linear transfer of ions from organic to aqueous phase [257]. Figure 4.3.2.6(b) shows the background subtracted CVs of the concentration range of 1-10 μM where the forward scan starts ion transfer at potential ≈ 0.65 V and becomes nearly plateau at potential ≈ 0.72 V. While the reverse scan gives peak at ≈ 0.69 V. So at pH 6.0 the transfer shifts little bit lower potential. The calculated half wave potential ($E_{1/2}$) based on the forward scan is 0.7 V.

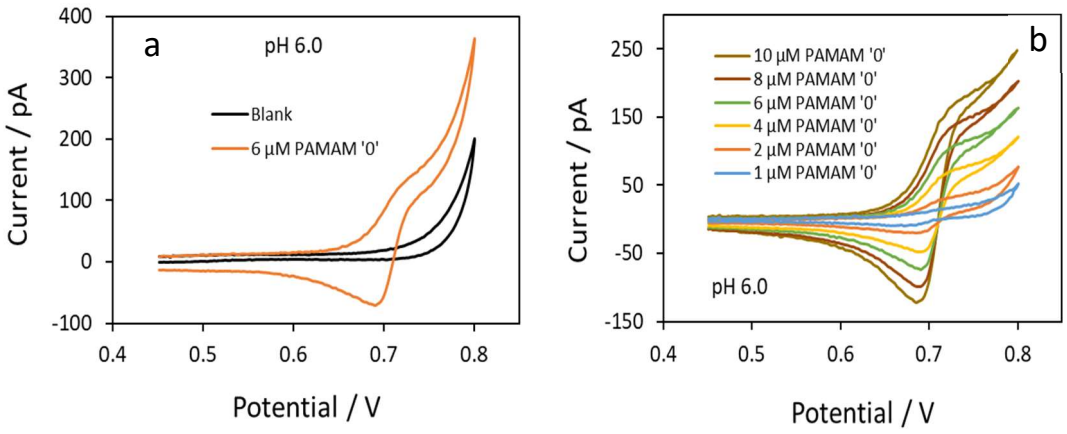

Figure 4.3.2.6: *(a) CV of 6 µM PAMAM '0' with blank and (b) background subtracted CV for 1, 2, 4, 6, 8 & 10 µM PAMAM '0' at pH 6.0 with 23 µm pipette radius. [Pipette radius with Equations 2.3.1.2 and 2.3.1.3 are also given in Appendix B.]*

Table 4.3.2.3: *Steady state forward currents (i_f) and reverse peak currents (i_b) of three scans of CV for 1, 2, 4, 6, 8 & 10 µM PAMAM '0' at pH 6.*

C / µM	i_{f1} / pA	i_{f2} / pA	i_{f3} / pA	Average i_f / pA	σ
1	8.1	10.3	12.7	10.4	1.90
2	21.8	24.3	25.8	24.0	1.62
4	60.5	62.5	65.4	62.8	2.03
6	95.2	97.4	99.8	97.4	1.90
8	127.3	130.2	132.7	130.1	2.19
10	151.3	153.9	155.5	153.6	1.71
C / µM	**i_{b1} / pA**	**i_{b2} / pA**	**i_{b3} / pA**	**Average i_b / pA**	**σ**
1	-5.2	-7.9	-7.5	-6.8	1.18
2	-10.1	-12.3	-12.0	-11.5	1.00
4	-32.2	-35.2	-34.6	-34.0	1.32
6	-49.8	-52.3	-51.5	-51.2	1.02
8	-64.3	-66.8	-65.4	-65.5	1.01
10	-80.4	-83.4	-82.2	-82.0	1.25

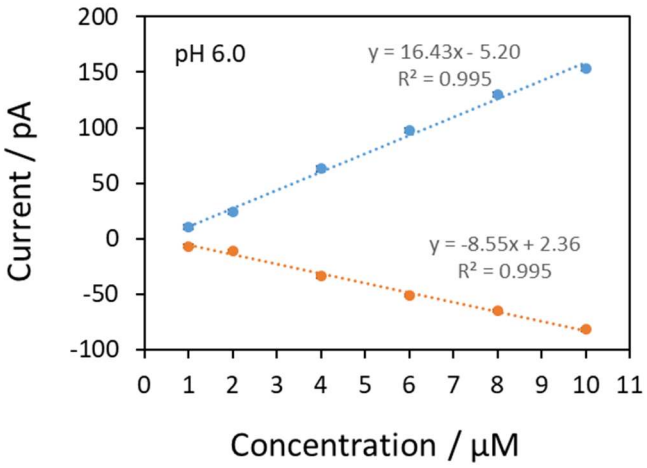

Figure 4.3.2.7: *Current vs concentration graph for both forward and reverse scan for pH 6.0*

The steady state forward currents (i_f) and reverse peak currents (i_b) of all concentrations from Figure 4.3.2.6(b) are given in the Table 4.3.2.3. Based on those data a current *vs* concentration graph was drawn which is shown Figure 4.3.2.7. The currents on the forward sweeps as well as reverse sweeps of the background-subtracted CVs at pH 6.0 increased linearly with the concentration of analyte in the aqueous phase. This current vs concentration relation shows that in both directions the current is concentration-dependent irrespective of the diffusion mode. Diffusion coefficient (D) was calculated from the forward current using Saito equation $I_{ss} = 4|z_i|FDCr$. Slope of current *vs* concentration is 16.43 pA/µM (Figure 4.3.2.7), charge is 5 for this pH which is calculated from the potentiometric titration curves at 0.1 M KCl of dendrimer G0 [244]. Radius of the pipette for this case was 23 µm. By using these values diffusion coefficient was calculated 3.7 x 10^{-6} cm^2/s.

CV at pH 9.0

PAMAM '0' gives response at pH 9.0 also but the response decreased significantly. Figure 4.3.2.8(a) shows the voltammogram for 9 µM PAMAM '0' where the shape of the CV of the forward scan is more or less same as for the other pH indicates radial diffusion of ions towards the organic phase from the aqueous phase. One the other hand, the peak shape changed in the reverse direction becoming broader, although clearly indicating the linear transfer of ions from organic to aqueous phase [257]. Figure 4.3.2.8(b) shows the background subtracted CVs of the concentration range of

2-10 µM where the forward scan starts ion transfer at potential ≈ 0.65 V and becomes nearly plateau at potential ≈ 0.72 V. While the reverse scan gives peak at ≈ 0.69 V. So it transfer at the same potential as at pH 6.0 transfer. The calculated half wave potential ($E_{1/2}$) based on the forward scan is 0.69 V.

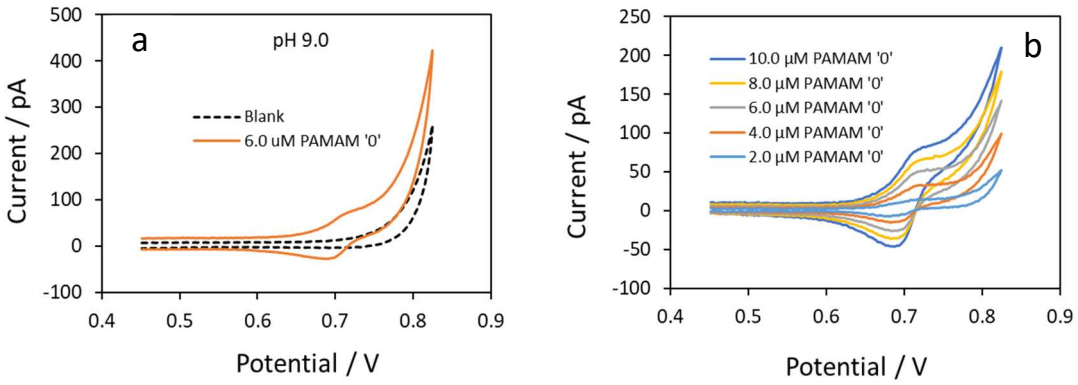

Figure 4.3.2.8: *(a) CV of 6 µM PAMAM '0' with blank and (b) background subtracted CV for 2, 4, 6, 8 & 10 µM PAMAM '0' at pH 9.0 with 23 µm pipette radius. [Pipette radius with Equations 2.3.1.2 and 2.3.1.3 are also given in Appendix B.]*

The steady state forward currents (i_f) and reverse peak currents (i_b) of all concentrations from Figure 4.3.2.8(b) are given in the Table 4.3.2.4. Based on those data a current *vs* concentration graph was drawn which is shown Figure 4.3.2.9. The currents on the forward sweeps as well as reverse sweeps of the background-subtracted CVs at pH 9.0 increased linearly with the concentration of analyte in the aqueous phase. This current vs concentration relation shows that in both directions the current is concentration-dependent irrespective of the diffusion mode. Diffusion coefficient (D) at this pH is 4.06 x 10^{-6} cm^2/s which is calculated from the forward current using Saito equation $I_{ss} = 4|z_i|FDCr$. Slope of current *vs* concentration is 7.2 pA/µM (Figure 4.3.2.9), charge is 2 for this pH which is calculated from the potentiometric titration curves at 0.1 M KCl of dendrimer G0 [244]. Radius of the pipette for this case was 23 µm.

Table 4.3.2.4: *Steady state forward currents (i_f) and reverse peak currents (i_b) of three scans of CV for 2, 4, 6, 8 & 10 µM PAMAM '0' at pH 9.*

C / µM	i_{f1} / pA	i_{f2} / pA	i_{f3} / pA	Average i_f / pA	σ
2	10.4	14.2	13.6	12.7	1.68
4	26.9	29.5	31.4	29.3	1.86
6	41.5	44.2	45.4	43.7	1.60
8	54.4	57.8	58.8	57.0	1.88
10	68.2	71.9	72.6	70.9	1.97
C / µM	i_{b1} / pA	i_{b2} / pA	i_{b3} / pA	Average i_b / pA	σ
2	-7.3	-8.6	-8.7	-8.2	0.63
4	-11.2	-14.1	-13.4	-12.9	1.23
6	-17.3	-19.5	-19.8	-18.9	1.10
8	-23.2	-24.5	-25.2	-24.3	0.83
10	-26.8	-28.1	-29.4	-28.1	1.03

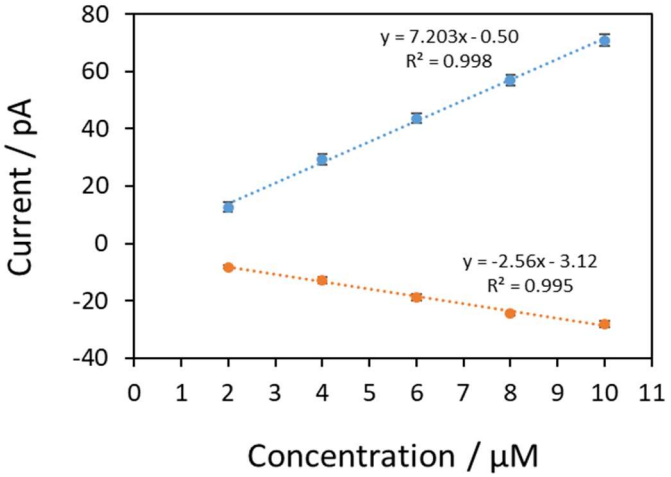

Figure 4.3.2.9: *Current vs concentration graph for both forward and reverse scan for pH 9.0.*

CV at pH 1.75 and pH 10.0

Figure 4.3.2.10 (a) and 4.3.2.10 (b) shows the CV of PAMAM '0' at pH 1.75 and pH 10.0 for 6.0 µM and 10.0 µM respectively. It clearly shows that at pH 1.75 there is no transfer of analyte at all, whether at pH 10.0 small transfer of analyte occurs. This is unusual for lower pH because at this pH all amino groups should be protonated and that's why there should be response at lower pH.

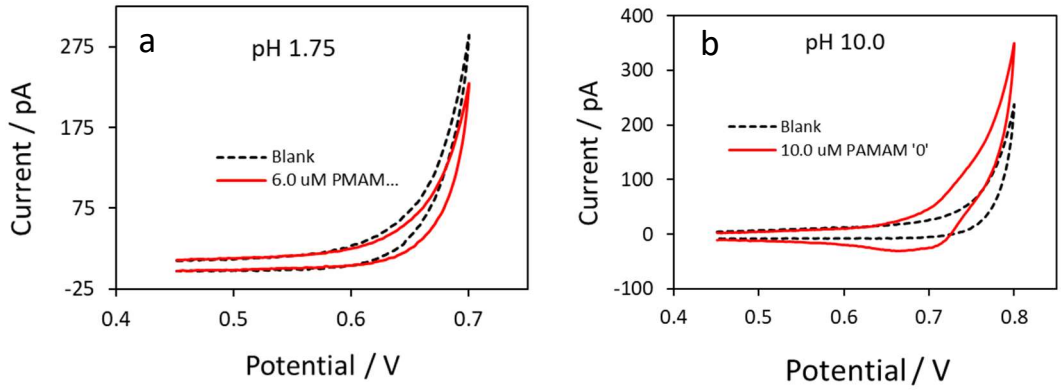

Figure 4.3.2.10: *(a) CV of 6 µM PAMAM '0' with blank at pH 1.75 and (b) CV of 10 µM PAMAM '0' with blank at pH 10.0 with 23 µm pipette radius. [Pipette radius with Equations 2.3.1.2 and 2.3.1.3 are also given in Appendix B.]*

Comparison of CVs at different pH

Figure 4.3.2.11 shows the background subtracted CVs of Dendrimer '0' at different pH. The shape of the CV is nearly same which indicates that the overall mechanism or behaviour of the transfer of PAMAM '0' at different pH is nearly same except the magnitude of the response. PAMAM '0' gives the best response at pH 3.5. The current response at pH lower than 3.5 starts to decrease. Same pattern follows at higher pH than 3.5. Small variation in the shape of the CVs may be because of the different shape of the pipettes.

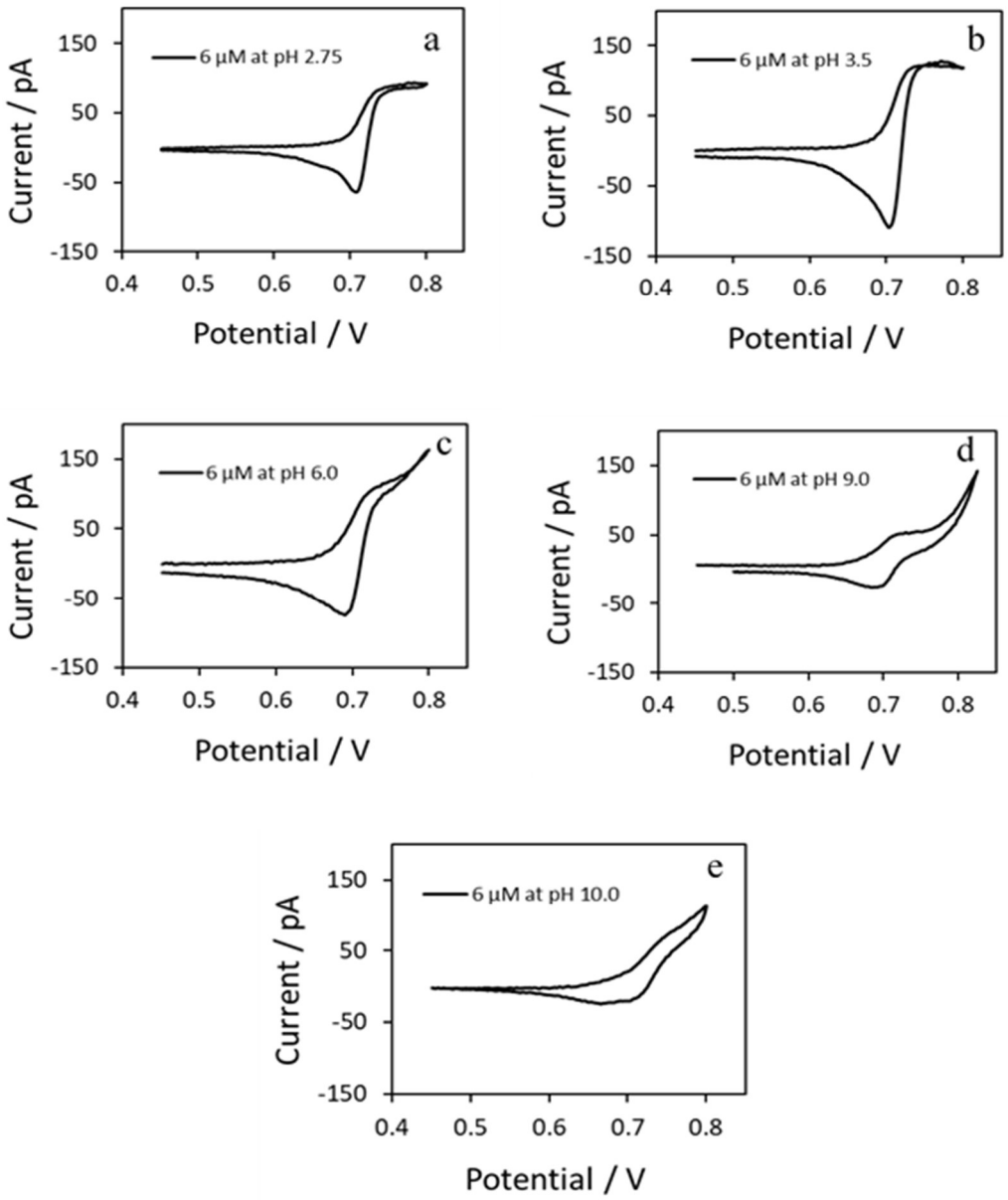

Figure 4.3.2.11: *Background subtracted CVs of Dendrimer '0' at (a) pH 2.75 (b) pH 3.5 (c) pH 6.0 (d) pH 9.0 and (e) pH 10.0*

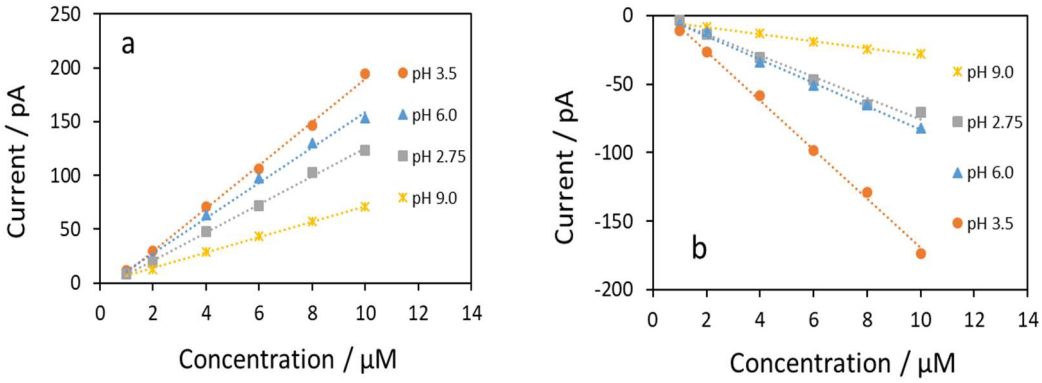

Figure 4.3.2.12: *Current vs concentration at pH 2.75, 3.5, 6.0 and 9.0 for (a) forward scan and (b) reverse scan.*

Table 4.3.2.5: *Diffusion coefficient (D), charge and slope of the regression line at different pH for PAMAM '0'.*

		pH 2.75	pH 3.5	pH 6.0	pH 9.0
D x 10^{-6} / cm^2s^{-1}		2.45	3.32	3.7	4.06
Charge		6	6	5	2
Slope	**forward**	13.1	20	16.4	7.2
pA/µM	**reverse**	-7.8	-17.9	-8.6	-2.6

Figure 4.3.2.12 (a) and 4.3.2.12(b) shows the current verses concentration for both forward and reverse directions at different pH. It shows that if we decrease the pH from the normal LiCl solution (pH 6.0) then initially the current response increased and give highest response at pH 3.5. Then it gradually decreased and at very low pH of 1.75 no response at all (Figure 4.3.2.10 a). On the other hand, current response is always low at higher pH than 6.0 and nearly no response at pH 10 in both directions (Figure 4.3.2.10.b). Table 4.3.2.5 shows the values of diffusion coefficients, charges and slope of the current *vs* concentration calibration curve at different pH. Slope is an important parameter to measure the sensitivity. These behaviour at different pH can be explain by the pK_a and protonation mechanism of primary and secondary amine of PAMAM dendrimer '0'. The protonation of PAMAM dendrimers first involves protonation of primary amine groups at the outer rim of the dendrimer at high pH, while the tertiary amine groups in the dendrimer core protonate at lower pH. The last group to protonate at low pH is a central tertiary amine. The p*Ka* of primary amines ≃

9.0. So, when the pH of the dendrimer solution is ≃ 9, then all the primary amine groups are protonated and both the tertiary amines are deprotonated. When decreasing the pH further and at pH ≃ 6, where all primary groups and one tertiary groups are protonated. At pH ≃ 3.5 all the tertiary amino groups also protonated. According to the protonation mechanism, at pH below than 3.5 all the amino groups are protonated. So the current response should not be less than that of 3.5. But experimentally response is deceased which is unusual.

4.3.3 CV of PAMAM dendrimer '1'

PAMAM dendrimer generation '1' has 8 surface primary amino groups and 6 interior tertiary amine groups [256]. Figure 4.3.3.1 shows the structure of PAMAM '1'. The cyclic voltammetry experiment gives very good response for this molecule also. The experiment started at pH 6.0 then goes to lower pH as 3.5, 2.75, 2.25, 1.75 respectively. After that, experiment was done at higher pH as 9.0, 10.0 & 11.0.

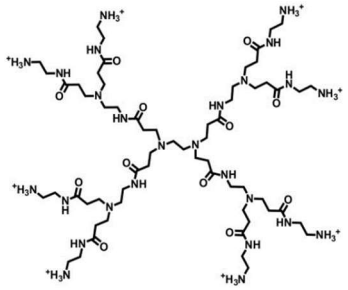

Figure 4.3.3.1: *Structure of PAMAM '1'*

CV at pH 6.0

Figure 4.3.3.2 (a) shows the voltammogram of blank with the 6 µM PAMAM '1' at pH 6.0. Blank gives response only for the background ions transfer, whereas 6 µM PAMAM '1' gives very good response. As like PAMAM '0', in forward direction, the current starts to increase and makes a quasi-steady state voltammogram instead of nice steady state as because it transfer near to the background ions transfer. As observed for PAMAM '0', this indicates a radial diffusion of PAMAM '1' ions towards the organic phase from the aqueous phase. On the other hand, in the reverse direction, it gives a peak shape response indicating linear transfer of ions from organic to aqueous phase [257]. Figure 4.3.3.2 (b) shows the background subtracted CVs of different concentration range of 1-10 µM of dendrimer '1'. All the forward scan starts ion transfer at potential ≈ 0.64 V and starts to become plateau at potential ≈ 0.69 V. The reverse scan gives peak at ≈ 0.67 V. The calculated half wave potential ($E_{1/2}$) based on the forward scan is 0.67 V.

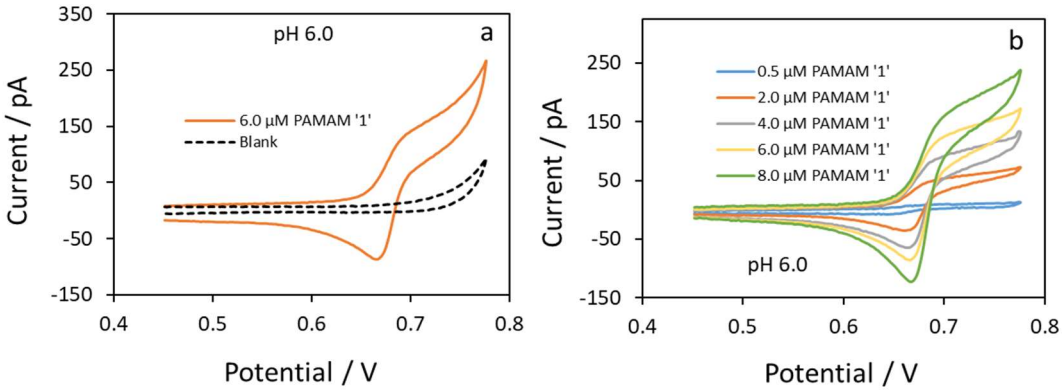

Figure 4.3.3.2: *(a) CV of 6 µM PAMAM '1' with blank and (b) background subtracted CV for 0.5, 2, 4, 6 & 8 µM PAMAM '1' at pH 6.0 with 24 µm radius pipette. [Pipette radius with Equations 2.3.1.2 and 2.3.1.3 are also given in Appendix B.]*

Table 4.3.3.1: *Steady state forward currents (i_f) and reverse peak currents (i_b) of three scans of CV for 1, 2, 3, 4, 5, 6 & 8 µM PAMAM '1' at pH 6.*

C / µM	i_{f1} / pA	i_{f2} / pA	i_{f3} / pA	Average i_f / pA	σ
1	18.2	15.4	21.3	18.3	2.42
2	43.3	37.4	41.6	40.7	2.47
3	62.1	59.4	65.2	62.2	2.36
4	86.3	78.9	88.6	84.6	4.12
5	104.3	100.3	107.9	104.1	3.08
6	119.9	115.1	123.3	119.4	3.36
8	155.2	156.2	168.9	160.1	6.23
C / µM	i_{b1} / pA	i_{b2} / pA	i_{b3} / pA	Average i_b / pA	σ
1	-19.1	-16.1	-23.5	-19.6	3.00
2	-46.9	-42.2	-49.9	-46.3	3.16
3	-68.7	-64.2	-71.8	-68.2	3.09
4	-94.2	-90.2	-99.2	-94.5	3.65
5	-130.5	-120.9	-133.5	-128.3	5.38
6	-140.3	-137.2	-146.8	-141.4	3.98
8	-172.5	-169.1	-178.9	-173.5	4.04

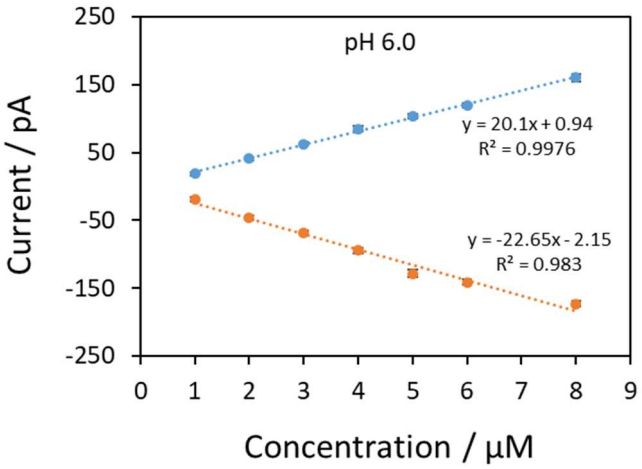

Figure 4.3.3.3: *Current vs concentration graph for both forward and reverse scan for PAMAM '1' at pH 6.0.*

The steady state forward current (i_f) and reverse peak current (i_b) of every 3 scans from the experiment for each concentration are given in the Table 4.3.3.1. Figure 4.3.3.3 shows current *vs* concentration graph based on the data of that Table 4.3.3.1. The currents on the forward sweeps as well as reverse sweeps of the background-subtracted CVs of dendrimer '1' at pH 6.0 increased linearly with the concentration of analyte in the aqueous phase. These current vs concentration relation is predicted by the Saito equation [202] for the steady state current and the Randles–Sevcik equation [80, 203] for the voltammetric peak current for linear diffusion systems. Irrespective of the diffusion mode, the current is concentration-dependent for both directions and the value of the currents of both directions are nearly same. Diffusion coefficient (D) at this pH is 2.41 x 10^{-6} cm^2/s which is calculated from the forward current using Saito equation $I_{ss} = 4|z_i|FDCr$. Slope of current *vs* concentration is 20.1 pA/µM (Figure 4.3.3.3), charge is 9 for this pH which is calculated from the potentiometric titration curves at 0.1 M KCl of dendrimer G1 [244]. Radius of the pipette for this case was 24 µm.

CV at pH 3.5

Figure 4.3.3.4 (a) shows the voltammogram of blank and 8 µM PAMAM '1' at pH 3.5. In this case the PAMAM '1' response is very intense. In forward direction, the current starts to increase and makes nearly steady state voltammogram because of radial diffusion of PAMAM '1' ions towards the organic phase from the aqueous phase. In reverse direction a peak shape response indicate linear transfer of ions from organic to aqueous phase [257]. Figure 4.3.3.4 (b) shows the background subtracted CVs for different concentrations (0.5-10 µM) of dendrimer '1', which gives very good steady state current represents the ideal micro-interface radial diffusion [257] and the reverse CVs also give peak currents according to ideal linear diffusion from inner organic phase to the aqueous phase through the micro-pipette interface [257]. The forward scan starts ion transfer at potential ≈ 0.62 V and becomes plateau at nearly potential ≈ 0.71 V for all concentrations. Whereas the reverse scan gives peak at ≈ 0.67 V, except for 0.5 µM & 0.2 µM those give peaks at 0.64 V & 0.65 V respectively. The calculated half wave potential ($E_{1/2}$) based on the forward scan is 0.67 V.

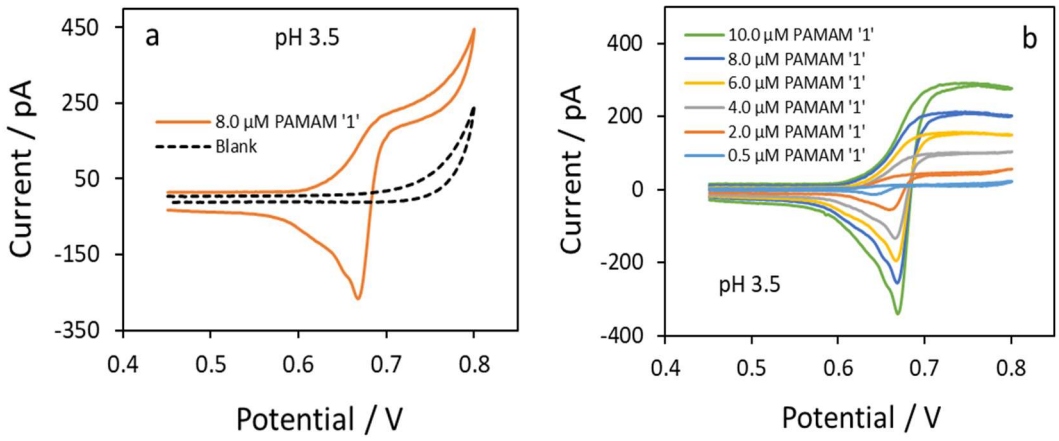

Figure 4.3.3.4: *(a) CV of 8 µM PAMAM '1' with blank and (b) background subtracted CV for 0.5, 2, 4, 6, 8 & 10 µM PAMAM '1' at pH 3.5 with 24 µm radius pipette. [Pipette radius with Equations 2.3.1.2 and 2.3.1.3 are also given in Appendix B.]*

Table 4.3.3.2: *Steady state forward currents (i_f) and reverse peak currents (i_b) of three scans of CV for 0.5, 2, 4, 6, 8 & 10 µM PAMAM '1' at pH 3.5.*

C / µM	i_{f1} / pA	i_{f2} / pA	i_{f3} / pA	Average i_f / pA	σ
0.5	9.7	7.2	13.3	10.1	2.50
2	44.2	42.1	47.8	44.7	2.37
4	96.6	93.1	99.4	96.3	2.59
6	152.2	144.6	158.3	151.7	5.62
8	197.5	193.9	202.2	197.9	3.41
10	254.2	251.4	258.1	254.6	2.72
C / µM	i_{b1} / pA	i_{b2} / pA	i_{b3} / pA	Average i_b / pA	σ
0.5	-10.2	-7.3	-13.5	-10.3	2.52
2	-46.6	-42.3	-48.8	-45.9	2.70
4	-100.8	-96.3	-105.1	-100.7	3.57
6	-168.2	-164.5	-171.0	-167.9	2.64
8	-213.5	-209.6	-217.3	-213.5	3.16
10	-290.3	-287.6	-294.7	-290.9	2.90

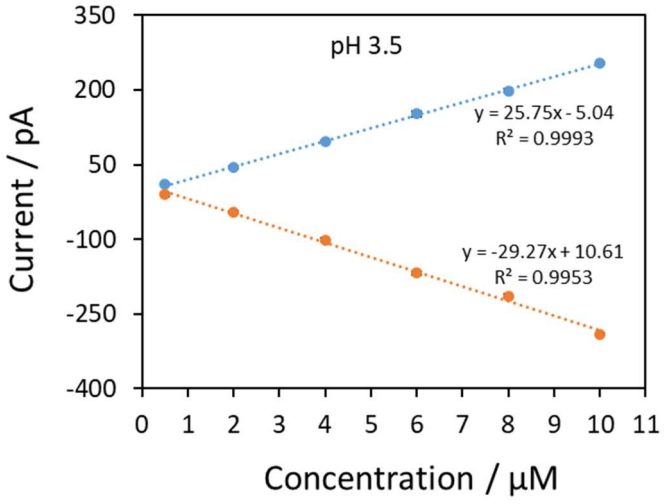

Figure 4.3.3.5: *Current vs concentration graph for both forward and reverse scan for PAMAM '1' at pH 3.5*

The steady state forward current (i_f) and reverse peak current (i_b) of 3 scans from the experiment for each concentration are given in the Table 4.3.3.2. Figure 4.3.3.5 shows current *vs* concentration graph based on the data of that Table 4.3.3.2. The currents on the forward sweeps as well as reverse sweeps of the background-subtracted CVs of dendrimer '1' at pH 3.5 increased linearly with the concentration of analyte in the aqueous phase. These current vs concentration relation is predicted by the Saito equation [202] for the steady state current and the Randles–Sevcik equation [80, 203] for the voltammetric peak current for linear diffusion systems. Irrespective of the diffusion mode, the current is concentration-dependent for both directions. Diffusion coefficient (D) at this pH is 1.99 x 10^{-6} cm^2/s which is calculated from the forward current using Saito equation $I_{ss} = 4|z_i|FDCr$. Slope of current *vs* concentration is 25.75 pA/μM (Figure 4.3.3.5), charge is 14 for this pH which is calculated from the potentiometric titration curves at 0.1 M KCl of dendrimer G1 [244]. Radius of the pipette for this case was 24 μm.

CV at pH 2.75

Figure 4.3.3.6 (a) shows the voltammogram of blank and 8 μM PAMAM '1' at pH 2.75. The PAMAM '1' response is very good but the magnitude of the current is less than in pH 3.5. Same as previous forward current gives steady state voltammogram and peak shape response in reverse direction [257]. Figure 4.3.3.6 (b) shows the background subtracted CVs for concentrations of 2 μM to 10 μM of dendrimer '1'. Nice steady state current in forward direction represents the ideal micro-interface radial diffusion [257] and the reverse peak currents represents the ideal linear diffusion from inner organic phase to the aqueous phase through the micro-pipette interface [257]. Ion transfer starts at potential ≈ 0.61 V in the forward scan and becomes plateau at nearly potential ≈ 0.7 V for all concentrations. The reverse scan gives peak at ≈ 0.67 V for all concentrations. The calculated half wave potential ($E_{1/2}$) based on the forward scan is 0.67 V.

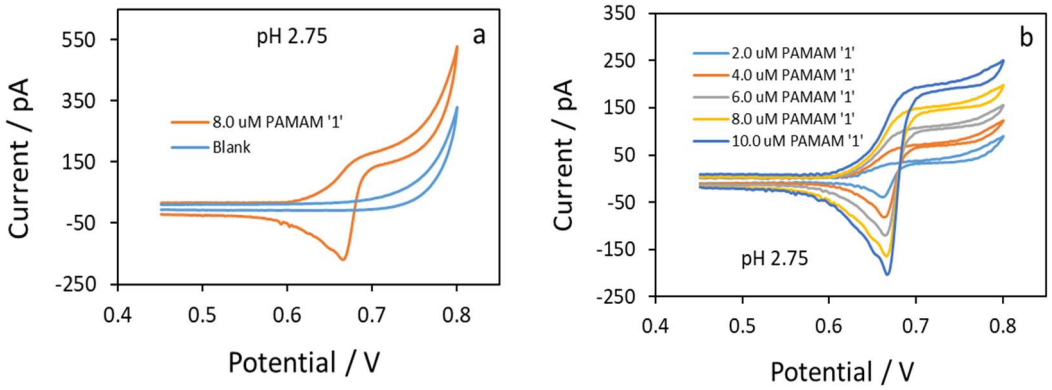

Figure 4.3.3.6: *(a) CV of 8 µM PAMAM '1' with blank and (b) background subtracted CV for 2, 4, 6, 8 & 10 µM PAMAM '1' at pH 2.75 with 24 µm radius pipette. [Pipette radius with Equations 2.3.1.2 and 2.3.1.3 are also given in Appendix B.]*

Table 4.3.3.3: *Steady state forward currents (i_f) and reverse peak currents (i_b) of three scans of CV for 2, 4, 6, 8 & 10 µM PAMAM '1' at pH 2.75.*

C / µM	i_{f1} / pA	i_{f2} / pA	i_{f3} / pA	Average i_f / pA	σ
2	35.1	40.5	38.8	38.1	2.28
4	70.4	73.8	75.1	73.1	1.98
6	110.5	114.2	116.3	113.7	2.37
8	150.9	154.4	156.7	154.0	2.41
10	195.8	198.1	201.3	198.4	2.27
C / µM	**i_{b1} / pA**	**i_{b2} / pA**	**i_{b3} / pA**	**Average i_b / pA**	**σ**
2	-34.9	-38.2	-39.6	-37.6	1.98
4	-71.2	-74.3	-76.1	-73.9	2.05
6	-106.5	-109.7	-112.3	-109.5	2.37
8	-144.5	-148.3	-150.3	-147.7	2.43
10	-180.7	-184.4	-186.8	-183.9	2.51

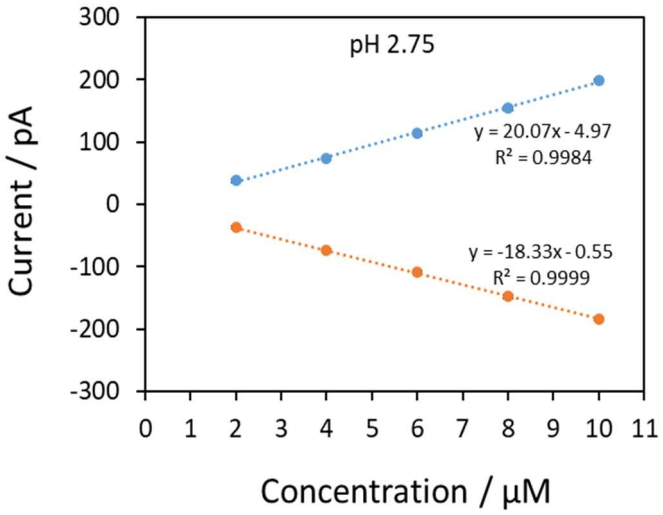

Figure 4.3.3.7: *Current vs concentration graph for both forward and reverse scan for PAMAM '1' at pH 2.75*

The steady state forward current (i_f) and reverse peak current (i_b) from the experiment for each concentration are given in the Table 4.3.3.3. Figure 4.3.3.7 shows current *vs* concentration graph based on that data. The currents on the forward sweeps as well as reverse sweeps of the background-subtracted CVs of dendrimer '1' at pH 2.75 increased linearly with the concentration of analyte in the aqueous phase. These current vs concentration relation is predicted by the Saito equation [202] for the steady state current and the Randles–Sevcik equation [80, 203] for the voltammetric peak current for linear diffusion systems. Irrespective of the diffusion mode, the current is concentration-dependent for both directions. Diffusion coefficient (D) at this pH is 1.55 x 10^{-6} cm^2/s which is calculated from the forward current using Saito equation $I_{ss} = 4|z_i|FDCr$. Slope of current *vs* concentration is 20.07 pA/µM (Figure 4.3.3.7), charge is 14 for this pH which is calculated from the potentiometric titration curves at 0.1 M KCl of dendrimer G1 [244]. Radius of the pipette for this case was 24 µm.

CV at pH 2.25

Figure 4.3.3.8 (a) shows the voltammogram of blank and 8 µM PAMAM '1' at pH 2.25. The PAMAM '1' response is same as before but the magnitude of the current is decreased than pH 2.75. Forward current gives steady state voltammogram and peak shape response in reverse direction. Figure 4.3.3.8 (b) shows the background subtracted CVs for concentrations of 2 µM to 10 µM of dendrimer '1'. Nice steady state current in forward direction represents the ideal micro-interface radial diffusion

[257] and the reverse peak currents represents the ideal linear diffusion from inner organic phase to the aqueous phase through the micro-pipette interface [257]. At higher concentration is shows another peak develops at reverse direction. Ion transfer starts at potential ≈ 0.62 V in the forward scan and becomes plateau at nearly potential ≈ 0.68 V for all concentrations. The reverse scan gives peak at ≈ 0.68 V for all concentrations. The half wave potential ($E_{1/2}$) based on the forward scan is 0.66 V.

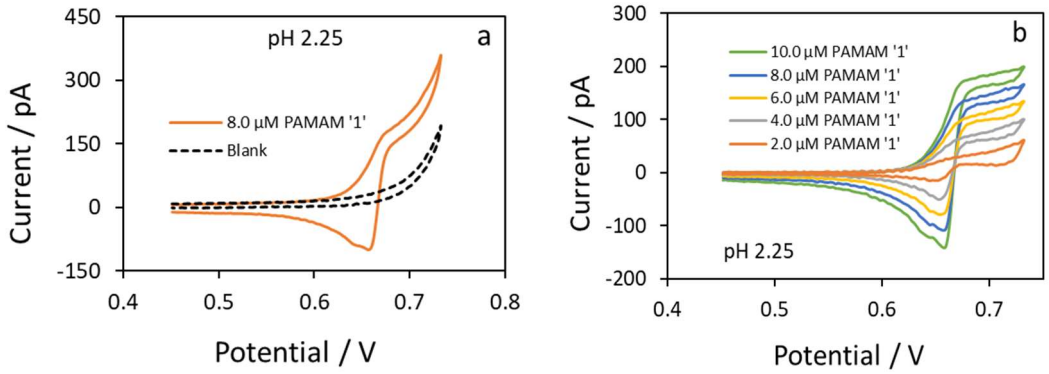

Figure 4.3.3.8: *(a) CV of 8 µM PAMAM '1' with blank and (b) background subtracted CV for 2, 4, 6, 8 & 10 µM PAMAM '1' at pH 2.25 with 24 µm radius pipette. [Pipette radius with Equations 2.3.1.2 and 2.3.1.3 are also given in Appendix B.]*

Table 4.3.3.4: *Steady state forward currents (i_f) and reverse peak currents (i_b) of three scans of CV for 2, 4, 6, 8 & 10 µM PAMAM '1' at pH 2.25*

C / µM	i_{f1} / pA	i_{f2} / pA	i_{f3} / pA	Average i_f / pA	σ
2	29.8	25.3	33.9	29.6	3.49
4	67.9	60.5	70.9	66.5	4.35
6	95.4	85.8	100.9	94.0	6.22
8	136.3	132.6	140.2	136.4	3.12
10	172.7	166.4	177.0	172.0	4.32
C / µM	i_{b1} / pA	i_{b2} / pA	i_{b3} / pA	Average i_b / pA	σ
2	-12.1	-8.6	-16.5	-12.4	3.24
4	-40.8	-36.6	-44.4	-40.6	3.20
6	-65.5	-61.3	-69.0	-65.2	3.12
8	-89.5	-81.1	-93.0	-87.9	4.98
10	-110.9	-106.3	-118.4	-111.9	4.98

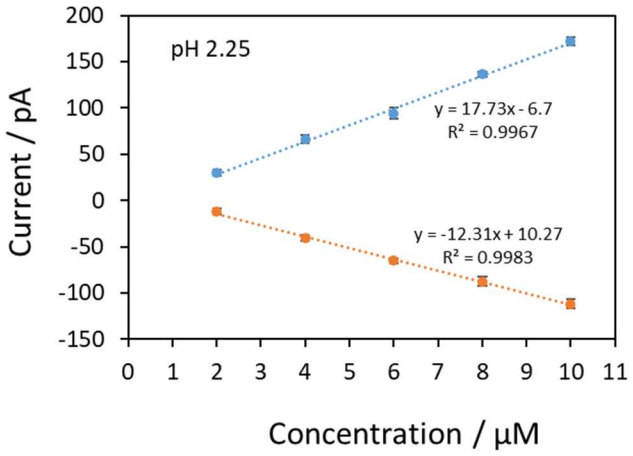

Figure 4.3.3.9: *Current vs concentration graph for both forward and reverse scan for PAMAM '1' at pH 2.25*

The steady state forward current (i_f) and reverse peak current (i_b) from the experiment for each concentration are given in the Table 4.3.3.4. Figure 4.3.3.9 shows current *vs* concentration graph based on that data. The currents on the forward sweeps as well as reverse sweeps of the background-subtracted CVs of dendrimer '1' at pH 2.25 increased linearly with the concentration of analyte in the aqueous phase. These current vs concentration relation is predicted by the Saito equation [202] for the steady state current and the Randles–Sevcik equation [80, 203] for the voltammetric peak current for linear diffusion systems. Irrespective of the diffusion mode, the current is concentration-dependent for both directions. Diffusion coefficient (D) at this pH is 1.37 x 10^{-6} cm^2/s which is calculated from the forward current using Saito equation $I_{ss} = 4|z_i|FDCr$. Slope of current *vs* concentration is 17.73 pA/µM (Figure 4.3.3.9), charge is 14 for this pH which is calculated from the potentiometric titration curves at 0.1 M KCl of dendrimer G1 [244]. Radius of the pipette for this case was 24 µm.

CV at pH 1.75

At very low pH of 1.75 PAMAM '1' also gives response. Figure 4.3.3.10 (a) shows the voltammograms of blank and 8 µM PAMAM '1'. The PAMAM '1' response is same as before but the magnitude of the current is decreased than pH 2.75. Forward current gives steady state voltammogram and peak shape response in reverse direction. Figure 4.3.3.10 (b) shows the background subtracted CVs for concentrations of 2 µM

to 10 µM of dendrimer '1'. Steady state current in forward direction represents the micro-interface radial diffusion [257] and the reverse peak currents represents the ideal linear diffusion from inner organic phase to the aqueous phase through the micro-pipette interface [257]. As like 2.25 pH, with the increase of concentration, another peak develops at reverse direction. Ion transfer starts at potential ≈ 0.62 V in the forward scan and becomes plateau at nearly potential ≈ 0.68 V. The reverse scan gives peak at ≈ 0.67 V for all concentrations and another peak develops at 0.65 V. The half wave potential ($E_{1/2}$) based on the forward scan is 0.67 V.

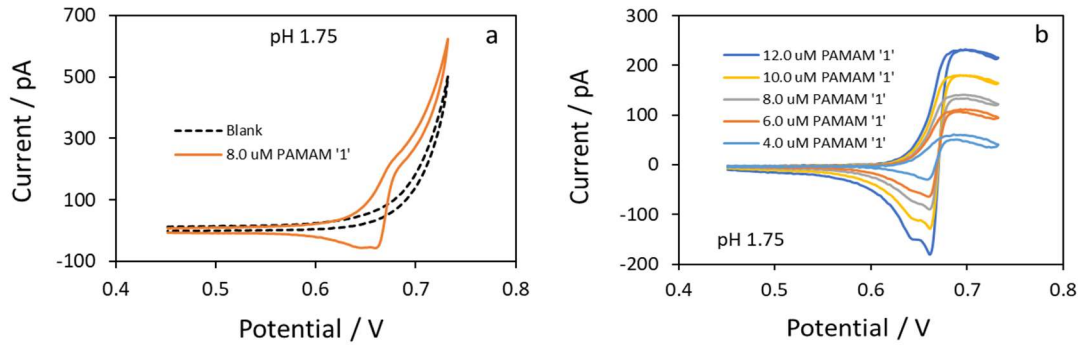

Figure 4.3.3.10: *(a) CV of 8 µM PAMAM '1' with blank and (b) background subtracted CV for 4, 6, 8, 10 & 12 µM PAMAM '1' at pH 1.75 with 24 µm radius pipette. [Pipette radius with Equations 2.3.1.2 and 2.3.1.3 are also given in Appendix B.]*

Table 4.3.3.5: *Steady state forward currents (i_f) and reverse peak currents (i_b) of three scans of CV for 4, 6, 8, 10 & 12 µM PAMAM '1' at pH 1.75*

C / µM	i_{f1} / pA	i_{f2} / pA	i_{f3} / pA	Average i_f / pA	σ
4	57.7	62.3	66.5	62.1	3.58
6	102.3	85.1	84.1	90.5	8.34
8	136.4	131.9	140.5	136.3	3.52
10	172.7	168.8	176.3	172.6	3.07
12	224.1	218.8	229.1	224.0	4.19
C / µM	i_{b1} / pA	i_{b2} / pA	i_{b3} / pA	Average i_b / pA	σ
4	-25.5	-21.6	-29.7	-25.6	3.28
6	-57.5	-53.2	-62.4	-57.7	3.78
8	-78.6	-75.6	-81.2	-78.5	2.28
10	-99.3	-95.2	-103.9	-99.5	3.55
12	-141.2	-137.0	-144.8	-141.0	3.17

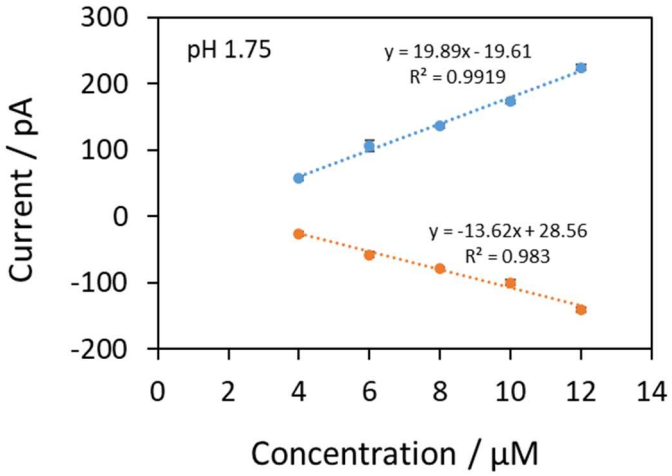

Figure 4.3.3.11: *Current vs concentration graph for both forward and reverse scan for PAMAM '1' at pH 1.75*

The steady state forward current (i_f) and reverse peak current (i_b) for each concentration of CV experiment are given in the Table 4.3.3.5. Figure 4.3.3.11 shows current *vs* concentration graph based on that data. The currents on the forward sweeps as well as reverse sweeps of the background-subtracted CVs of dendrimer '1' at pH 1.75 increased linearly with the concentration of analyte in the aqueous phase. These current vs concentration relation is predicted by the Saito equation [202] for the steady state current and the Randles–Sevcik equation [80, 203] for the voltammetric peak current for linear diffusion systems. Irrespective of the diffusion mode, the current is concentration-dependent for both directions. Diffusion coefficient (D) at this pH is 1.53 x 10^{-6} cm^2/s which is calculated from the forward current using Saito equation $I_{ss} = 4|z_i|FDCr$. Slope of current *vs* concentration is 19.89 pA/µM (Figure 4.3.3.11), charge is 14 for this pH which is calculated from the potentiometric titration curves at 0.1 M KCl of dendrimer G1 [244]. Radius of the pipette for this case was 24 µm.

CV at pH 9.0

We investigate this experiment at high pH also. The Figure 4.3.3.12 (a) shows the voltammograms of blank and 6 µM PAMAM '1' at pH 9.0. The PAMAM '1' response is same as before but the magnitude of the current much decreased even lower than pH 1.75. Figure 4.3.3.12 (b) shows the background subtracted CVs for concentrations of 1 µM to 10 µM of dendrimer '1'. Steady state current in forward direction represents

the micro-interface radial diffusion [257] and the reverse peak currents represents the ideal linear diffusion from inner organic phase to the aqueous phase through the micro-pipette interface [257]. Ion transfer starts at potential ≈ 0.65 V in the forward scan and becomes plateau at nearly potential ≈ 0.69 V. The reverse scan gives peak at ≈ 0.67 V for all concentrations. The half wave potential ($E_{1/2}$) based on the forward scan is 0.67 V.

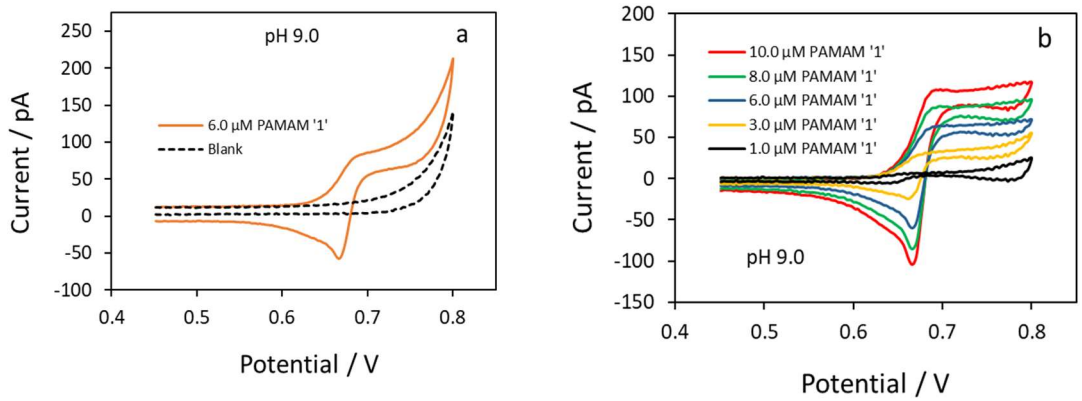

Figure 4.3.3.12: *(a) CV of 6 µM PAMAM '1' with blank and (b) background subtracted CV for 1, 3, 6, 8 & 10 µM PAMAM '1' at pH 9.0 with 22 µm radius pipette.* *[Pipette radius with Equations 2.3.1.2 and 2.3.1.3 are also given in Appendix B.]*

Table 4.3.3.6: *Steady state forward currents (i_f) and reverse peak currents (i_b) of three scans of CV for 1, 2, 3, 4, 6, 8 & 10 µM PAMAM '1' at pH 9.0*

C / µM	i_{f1} / pA	i_{f2} / pA	i_{f3} / pA	Average i_f / pA	σ
1	6.7	4.2	9.5	6.8	2.14
2	18.0	13.8	21.3	17.7	3.08
3	30.8	26.9	34.5	30.7	3.10
4	37.5	34.2	41.1	37.6	2.81
6	60.5	56.3	64.6	60.5	3.37
8	85.9	81.6	88.9	85.5	3.00
10	104.3	100.8	108	104.4	2.91
C / µM	**i_{b1} / pA**	**i_{b2} / pA**	**i_{b3} / pA**	**Average i_b / pA**	**σ**
1	-2.6	-2.0	-3.4	-2.7	0.57
2	-6.6	-4.4	-8.1	-6.4	1.50
3	-18.6	-15.3	-20.5	-18.1	2.17
4	-29.9	-26.3	-32.6	-29.6	2.60
6	-45.4	-42.4	-48.1	-45.3	2.30
8	-60.1	-56.8	-63.5	-60.2	2.74
10	-80.4	-76.3	-84.2	-80.3	3.23

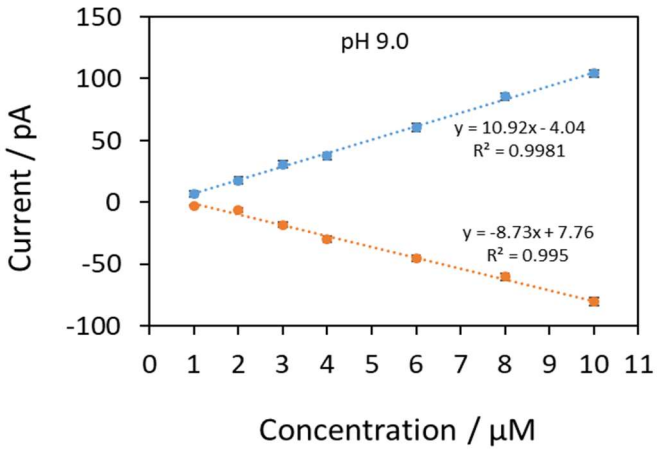

Figure 4.3.3.13: *Current vs concentration graph for both forward and reverse scan for PAMAM '1' at pH 9.0*

The steady state forward current (i_f) and reverse peak current (i_b) for each concentration of CV experiment are given in the Table 4.3.3.6. Figure 4.3.3.13 shows current *vs* concentration graph based on that data. The currents on the forward sweeps as well as reverse sweeps of the background-subtracted CVs of dendrimer '1' at pH 9.0 increased linearly with the concentration of analyte in the aqueous phase. These current vs concentration relation is predicted by the Saito equation [202] for the steady state current and the Randles–Sevcik equation [80, 203] for the voltammetric peak current for linear diffusion systems. Irrespective of the diffusion mode, the current is concentration-dependent for both directions. Diffusion coefficient (D) at this pH is 3.22 x 10^{-6} cm^2/s which is calculated from the forward current using Saito equation $I_{ss} = 4|z_i|FDCr$. Slope of current *vs* concentration is 10.92 pA/µM (Figure 4.3.3.13), charge is 4 for this pH which is calculated from the potentiometric titration curves at 0.1 M KCl of dendrimer G1 [244]. Radius of the pipette for this case was 22 µm.

CV at pH 10.0 and 11.0

CV experiment at pH 10.0 and 11.0 also done to check the change of electrochemical behaviour of PAMAM '1'. At pH 10.0 still gives response but very negligible (Figure 4.3.3.14) and Figure 4.3.3.15 shows no response at all for pH 11.0. It may be because at high pH all amino groups become deprotonated.

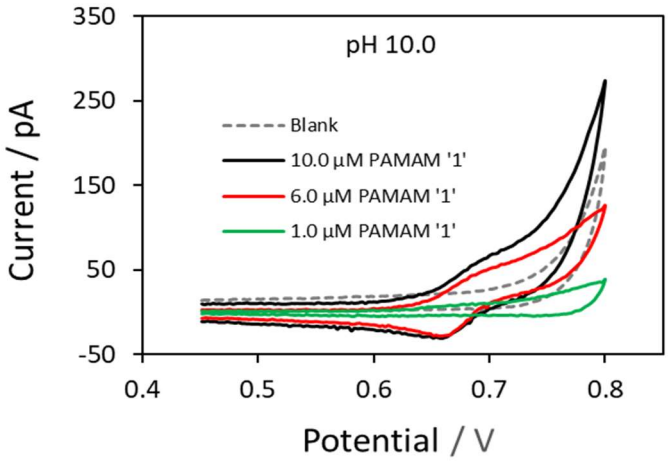

Figure 4.3.3.14: *Background subtracted CV with blank for 1, 6, & 10 µM PAMAM '1' at pH 10.0 with 22 µm radius pipette. [Pipette radius with Equations 2.3.1.2 and 2.3.1.3 are also given in Appendix B.]*

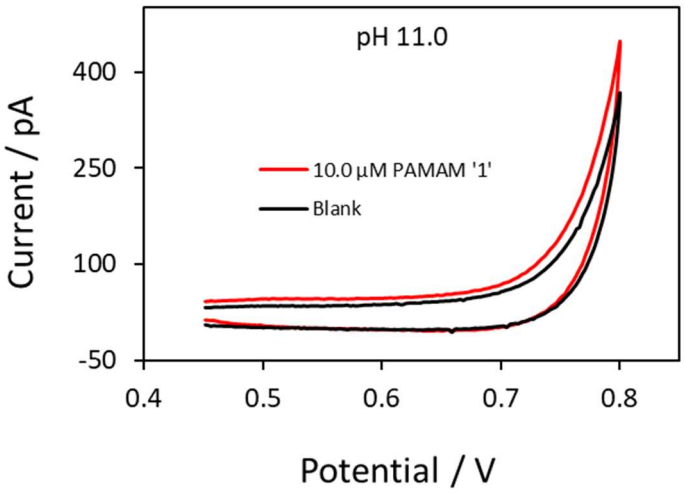

Figure 4.3.3.15: *CV of 10 µM PAMAM '1' and blank at pH 11.0 with 22 µm radius pipette. [Pipette radius with Equations 2.3.1.2 and 2.3.1.3 are also given in Appendix B.]*

Comparison of CVs at different pH

Figure 4.3.3.16 shows the background subtracted CVs of Dendrimer '1' at different pH. It shows that the response at normal LiCl solution (pH 6.0) shifts little bit in both case of high or low pH and the shape of the CV also varies little bit. The small variation

of the shape of the CVs may be because of the different shape of the pipettes and/or for the different time & environment of the experiment.

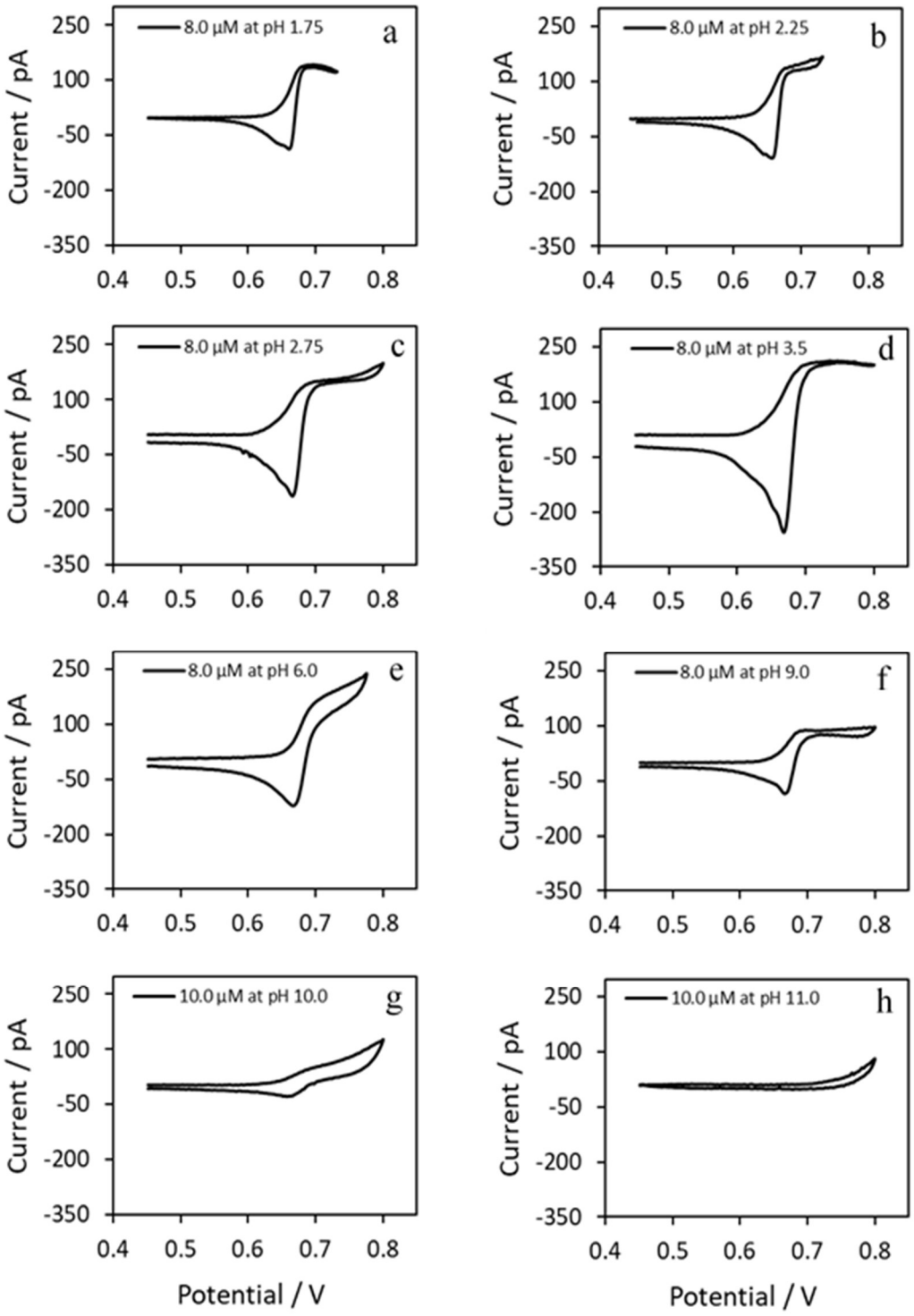

Figure 4.3.3.16: *Background subtracted CVs of 8.0 µM dendrimer '1' at (a) pH 1.75 (b) pH 2.25 (c) pH 2.75 (d) pH 3.5 (e) pH 6.0 (f) pH 9.0 and 10 µM dendrimer '1' at (g) pH 10.0 and (h) pH 11.0*

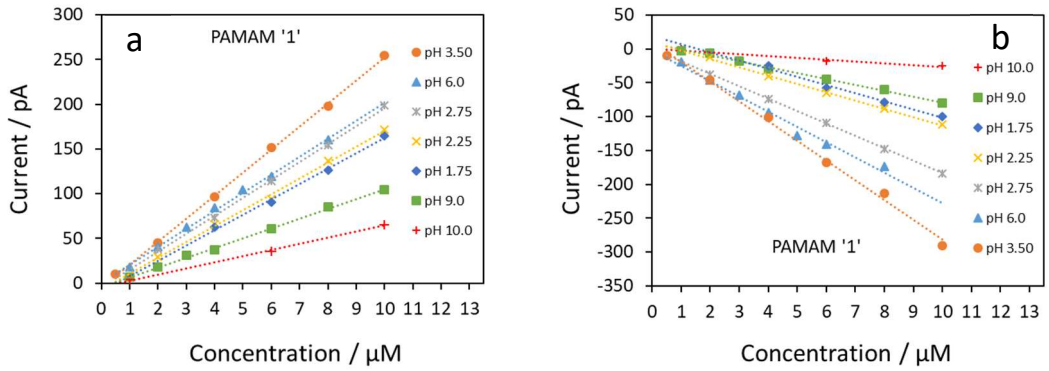

Figure 4.3.3.17: *Current vs concentration graph for PAMAM '1' at pH 1.75, 2.25, 2.75, 3.5, 6.0, 9.0 and 10.0 for (a) forward scan and (b) reverse scan.*

Table 4.3.3.7: *Diffusion coefficient (D), charge and slope of the regression line at different pH for PAMAM '1'.*

		pH 1.75	**pH 2.25**	**pH 2.75**	**pH 3.5**	**pH 6.0**	**pH 9.0**	**pH 10.0**
D x 10^{-6} / cm^2s^{-1}		1.53	1.37	1.55	1.99	2.41	3.22	
Charge		14	14	14	14	9	4	1
Slope	**forward**	17.15	17.73	20.07	25.75	20.10	10.92	6.84
pA/µM	**reverse**	-12.12	-12.31	-18.32	-29.27	-22.65	-8.73	-2.73

Figure 4.3.3.17 shows the current verses concentration for both forward and reverse directions at different pH. Nearly same response like PAMAM '0' is observed for this case also. It shows that if we decrease the pH from the normal LiCl solution (pH 6.0) then initially the current response increased and give highest response at pH 3.5. Then it gradually decreased. After pH 3.5 CV experiment done at 2.75, which gives response less than pH 6.0 and gradually decreased up to pH 1.75. For PAMAM '0' at pH 1.75 there was no response but for PAMAM '1' gives big response. On the other hand, current response is always low at higher pH. At pH 9.0 the response is lower than the lowest pH 1.75 and lowest response gives at pH 10.0. There is no response at all, if we further increase the pH such as at pH 11.0 in both directions (Figure 4.3.3.15). Table 4.3.3.7 also shows the values of diffusion coefficient, charge and slope of the current

vs concentration calibration curve at different pH. Slope is an important parameter to know the sensitivity of the reaction mechanism at that particular pH.

These can be explain by the pK_a and protonation mechanism of primary and secondary amine of dendrimers. The protonation of PAMAM dendrimers first involves protonation of primary amine groups at the outer side of the dendrimer at high pH, while the tertiary amine groups in the dendrimer core protonate at lower pH. The last group to protonate at low pH is a central tertiary amine. The primary amines protonate independently at p$Ka \simeq 9.0$. So, when the pH of the dendrimer solution is $\simeq 9.0$, then all the primary amine groups are protonated and both the tertiary amines are deprotonated. At pH over 9.0 the primary amino groups started deprotonated again and that's why low/no response observed. When decreasing the pH and at pH $\simeq 6$, where all primary groups and one tertiary groups are protonated. At pH $\simeq 3.5$ all the tertiary amino groups also protonated and gives highest response. However like PAMAM '0', it is unusual that at pH lower than 3.5, the response decreased though all the amino groups are protonated.

4.3.4 CV of PAMAM dendrimer '2'

PAMAM dendrimer generation '2' has 16 surface primary amino groups and 14 interior tertiary amino groups [256]. Figure 4.3.4.1 shows the structure of PAMAM dendrimer '2'. This molecule also analysed by cyclic voltammetry experiment at different pH and gives very good response. The experiment started at pH 6.0 then goes to lower pH as 3.5, 2.75, 2.25 and 1.75 respectively. After that, experiment was done at higher pH as 9.0, 10.0 & 11.0.

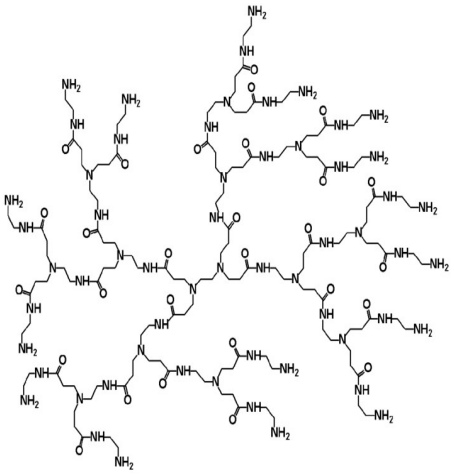

Figure 4.3.4.1: *Structure of PAMAM '2'*

CV at pH 6.0

Figure 4.3.4.2 (a) shows the voltammogram of blank with the 4 µM PAMAM '2' at pH 6.0. Blank gives response only for the background ions transfer, whereas 4 µM PAMAM '2' gives nice response. As like previous dendrimers, in forward direction, the current starts to increase and makes a semi steady state voltammogram instead of nice steady state as because it transfer near to the background ions transfer. Which indicates a radial diffusion of PAMAM '2' ions towards the organic phase from the aqueous phase. On the other hand, it gives a peak shape response in reverse direction indicating linear transfer of ions from organic to aqueous phase [257]. In this case the current response is higher than generation G0 & G1 at same pH. Figure 4.3.4.2 (b) shows the background subtracted CVs of different concentration range of 0.5-6.0 µM of dendrimer '2'. In this case the forward scan starts ion transfer at potential ≈ 0.64 V and starts to become plateau at potential ≈ 0.69 V. The reverse scan gives peak at ≈ 0.66 V but varies little bit with concentrations. The calculated half wave potential ($E_{1/2}$) based on the forward scan is 0.66 V.

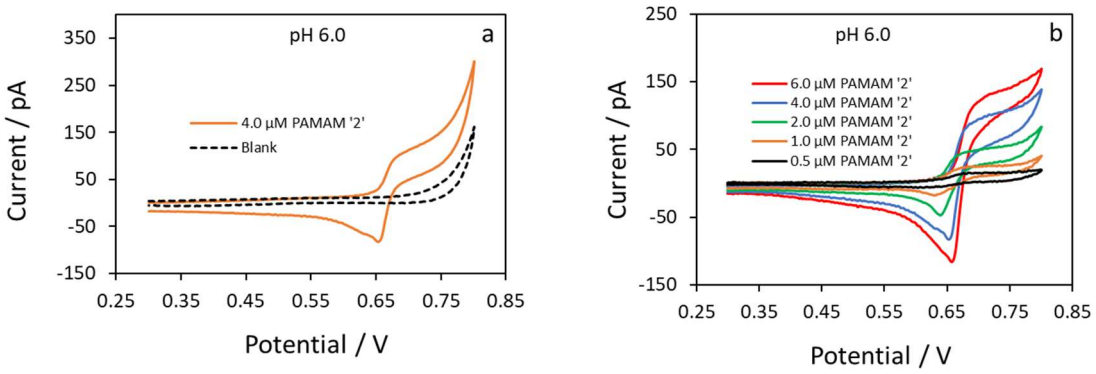

Figure 4.3.4.2: *(a) CV of 4 µM PAMAM '2' with blank and (b) background subtracted CV for 0.5, 1, 2, 4 & 6 µM PAMAM '2' at pH 6.0 with 21 µm radius pipette. [Pipette radius with Equations 2.3.1.2 and 2.3.1.3 are also given in Appendix B.]*

Table 4.3.4.1: *Steady state forward currents (i_f) and reverse peak currents (i_b) of three scans of CV for 1, 2, 3, 4, 5 & 6 µM PAMAM '2' at pH 6.0*

C / µM	i_{f1} / pA	i_{f2} / pA	i_{f3} / pA	Average i_f / pA	σ
1	25	20	29	25	3.4
2	49	45	54	49	3.6
3	75	70	77	74	3.0
4	99	96	104	100	3.0
5	115	110	119	115	3.7
6	135	132	141	136	3.6
C / µM	**i_{b1} / pA**	**i_{b2} / pA**	**i_{b3} / pA**	**Average i_b / pA**	**σ**
1	-21	-18	-25	-21	2.7
2	-58	-56	-61	-58	2.1
3	-85	-82	-89	-85	2.8
4	-117	-113	-120	-117	2.8
5	-138	-136	-140	-138	1.7
6	-174	-170	-181	-175	4.4

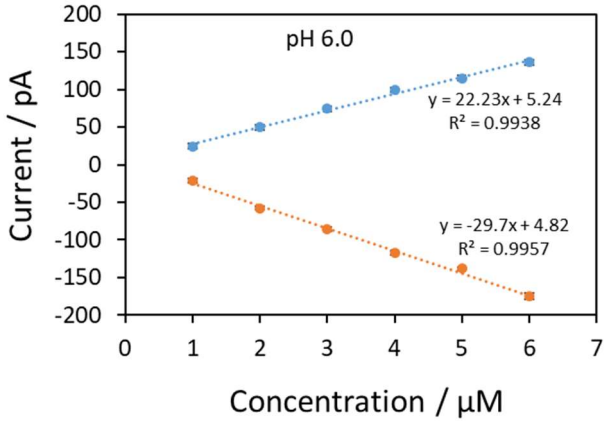

Figure 4.3.4.3: *Current vs concentration graph for both forward and reverse scan for PAMAM '2' at pH 6.0*

Table 4.3.4.1 shows the steady state forward current (i_f) and reverse peak current (i_b) from the experiment for each concentration. Figure 4.3.4.3 shows current *vs* concentration graph based on the data of that Table 4.3.4.1. The currents on the forward sweeps as well as reverse sweeps of the background-subtracted CVs of dendrimer '2' at pH 6.0 increased linearly with the concentration of analyte in the aqueous phase. These current vs concentration relation is predicted by the Saito equation [202] for the steady state current and the Randles–Sevcik equation [80, 203] for the voltammetric peak current for linear diffusion systems. Irrespective of the diffusion mode, the current is concentration-dependent for both directions and the value of the currents of both directions are nearly same. Diffusion coefficient (D) at this pH is 1.83 x 10^{-6} cm^2/s which is calculated from the forward current using Saito equation $I_{ss} = 4|z_i|FDCr$. Slope of current *vs* concentration is 22.23 pA/µM (Figure 4.3.4.3), charge is 15 for this pH which is calculated from the potentiometric titration curves at 0.1 M KCl of dendrimer G2 [244]. Radius of the pipette for this case was 21 µm.

CV at pH 3.5

Figure 4.3.4.4 (a) shows the voltammogram of 3 µM PAMAM '2' with blank at pH 3.5. The shape of the forward CV is nearly same as like previous but much changed in reverse peak shape which becomes very narrow and sharp. This change of shape of the reverse peak suggest that the possible mechanism follows the adsorption behaviour. In this case also the ions transfer towards the organic phase from the aqueous phase

follows radial diffusion and the reverse direction follows linear transfer of ions from organic to aqueous phase [257] via adsorption mechanism. Figure 4.3.4.4 (b) shows the background subtracted CVs of different concentration range of 1.0-8.0 µM of dendrimer '2'. The shape of the forward CVs at higher concentrations changed may be because of the shape of the pipette tip and the experimental conditions at that particular time. The forward scan starts ion transfer at potential ≈ 0.64 V and starts to become plateau at potential ≈ 0.7 V. But the ion transfer shifts to the lower potential for reverse scan which gives peak at ≈ 0.63 V for all concentrations. The calculated half wave potential ($E_{1/2}$) based on the forward scan is 0.69 V.

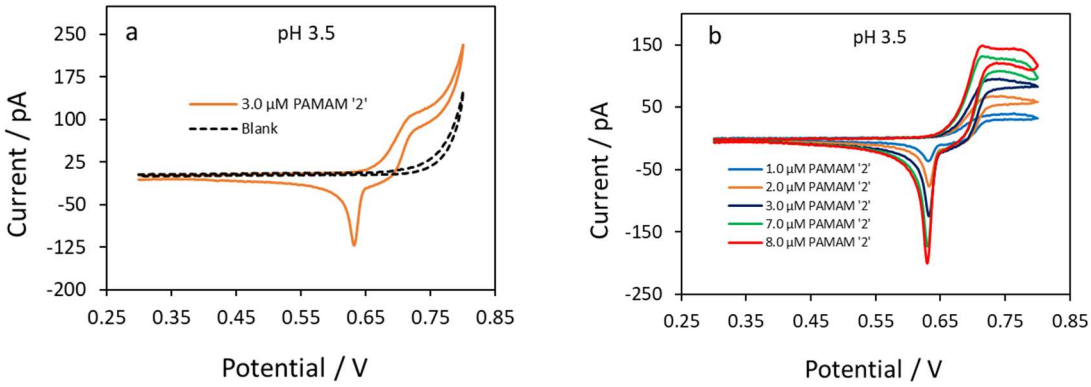

Figure 4.3.4.4: *(a) CV of 3 µM PAMAM '2' with blank and (b) background subtracted CV for 1, 2, 3, 7 & 8 µM PAMAM '2' at pH 3.5 with 22 µm radius pipette. [Pipette radius with Equations 2.3.1.2 and 2.3.1.3 are also given in Appendix B.]*

Table 4.3.4.2: *Steady state forward currents (i_f) and reverse peak currents (i_b) of three scans of CV for 1, 2, 3, 4, 5, 6, 7 & 8 µM PAMAM '2' at pH 3.5*

C / µM	i_{f1} / pA	i_{f2} / pA	i_{f3} / pA	i_f / pA Average	σ	i_{b1} / pA	i_{b2} / pA	i_{b3} / pA	i_b / pA Average	σ
1	37	31	40	36	3.7	-36	-33	-37	-35	2.1
2	60	56	65	60	3.8	-65	-72	-83	-73	7.1
3	79	76	85	80	3.6	-98	-95	-104	-99	3.6
4	88	87	91	89	1.4	-117	-115	-119	-117	1.8
5	101	97	106	101	3.5	-135	-132	-139	-136	3.1
6	117	113	118	116	2.3	-155	-152	-158	-155	2.6
7	133	129	137	133	3.4	-177	-170	-182	-176	4.8
8	144	139	148	143	3.8	-201	-194	-208	-201	5.5

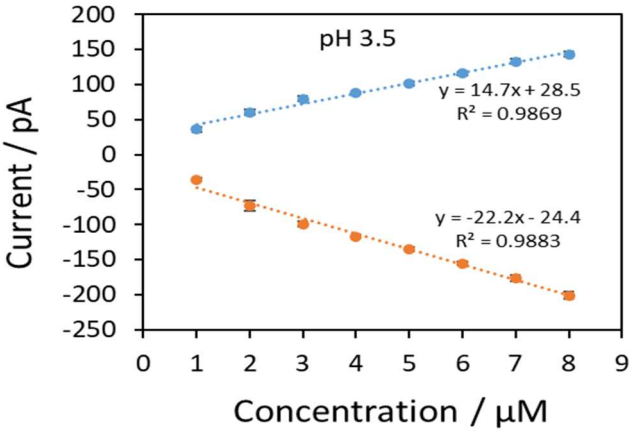

Figure 4.3.4.5: *Current vs concentration graph for both forward and reverse scan for PAMAM '2' at pH 3.5*

Table 4.3.4.2 shows the steady state forward current (i_f) and reverse peak current (i_b) from the CV experiment. Figure 4.3.4.5 shows current *vs* concentration graph based on the data of the Table 4.3.4.2. The currents on the forward sweeps as well as reverse sweeps of the background-subtracted CVs of dendrimer '2' at pH 3.5 increased linearly with the concentration of analyte in the aqueous phase. These current vs concentration relation is predicted by the Saito equation [202] for the steady state current and follows the adsorption mechanism for the voltametric peak current. Irrespective of the diffusion mode or transfer mechanism, the current is concentration-dependent for both directions. Diffusion coefficient (D) at this pH is 0.87 x 10^{-6} cm^2/s which is calculated from the forward current using Saito equation $I_{ss} = 4|z_i|FDCr$. Slope of current *vs* concentration is 14.7 pA/µM (Figure 4.3.4.5), charge is 20 for this pH which is calculated from the potentiometric titration curves at 0.1 M KCl of dendrimer G2 [244]. Radius of the pipette for this case was 22 µm.

CV at pH 2.75

Figure 4.3.4.6 (a) shows the voltammogram of 3 µM PAMAM '2' with blank at pH 2.75. The response is higher than pH 6.0 & 3.5. The shape of the cyclic voltammogram is nearly same as pH 3.5 where the reverse peak is very sharp which is different than G0 and G1. This change of shape of the reverse peak suggest that the possible

mechanism follows the adsorption mechanism and the ions transfer towards the organic phase from the aqueous phase follows radial diffusion [257]. Figure 4.3.4.6 (b) shows the background subtracted CVs of different concentration range of 1.0-9.0 µM of dendrimer '2'. The forward scan starts ion transfer at potential ≈ 0.64 V and starts to become plateau at potential ≈ 0.7 V. The ions transfer lower potential for reverse scan like pH 3.5 and gives peak at ≈ 0.63 V for all concentrations. The calculated half wave potential ($E_{1/2}$) based on the forward scan is 0.69 V.

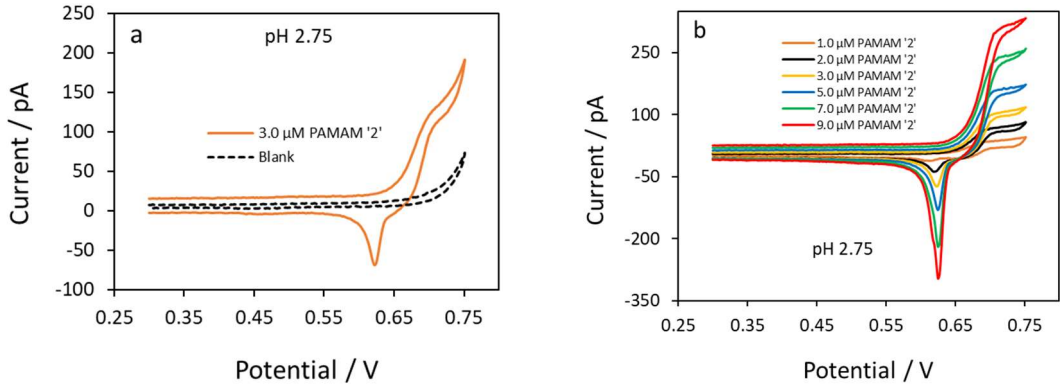

Figure 4.3.4.6: *(a) CV of 3 µM PAMAM '2' with blank and (b) background subtracted CV for 1, 2, 3, 5, 7 & 9 µM PAMAM '2' at pH 2.75 with 22.5 µm radius pipette. [Pipette radius with Equations 2.3.1.2 and 2.3.1.3 are also given in Appendix B.]*

Table 4.3.4.3: *Steady state forward currents (i_f) and reverse peak currents (i_b) of three scans of CV for 1, 2, 3, 5, 7 & 9 µM PAMAM '2' at pH 2.75*

C / µM	i_{f1} / pA	i_{f2} / pA	i_{f3} / pA	i_f / pA Average	σ	i_{b1} / pA	i_{b2} / pA	i_{b3} / pA	i_b / pA Average	σ
1	27	24	34	28	4.1	-12	-9	-16	-13	2.6
2	59	54	62	58	3.2	-37	-32	-40	-36	3.6
3	90	85	94	90	3.8	-74	-68	-79	-74	4.6
5	140	134	144	139	4.0	-135	-130	-141	-135	4.6
7	210	204	214	209	3.9	-210	-204	-216	-210	4.8
9	273	269	279	274	4.0	-273	-269	-277	-273	3.3

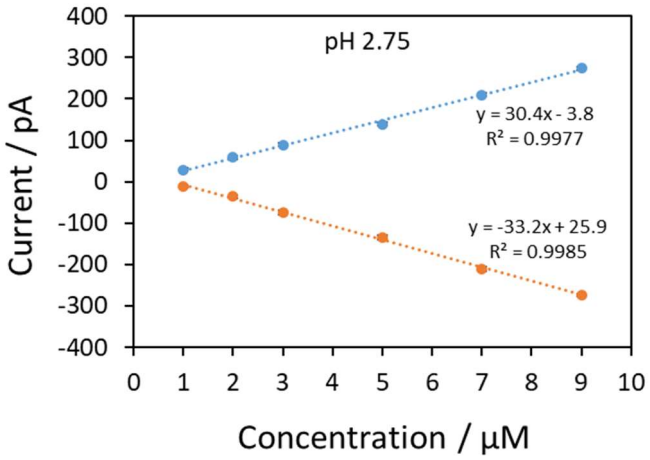

Figure 4.3.4.7: *Current vs concentration graph for both forward and reverse scan for PAMAM '2' at pH 2.75*

Table 4.3.4.3 shows the steady state forward current (i_f) and reverse peak current (i_b) from the CV experiment. Figure 4.3.4.7 shows current *vs* concentration graph based on the data of the Table 4.3.4.3. The currents on the forward sweeps as well as reverse sweeps of the background-subtracted CVs of dendrimer '2' at pH 2.75 increased linearly with the concentration of analyte in the aqueous phase. These current vs concentration relation is predicted by the Saito equation [202] for the steady state current and follows adsorption mechanism for the voltametric peak current. Irrespective of the transfer mode, the current is concentration-dependent for both directions. Diffusion coefficient (D) at this pH is 1.17 x 10^{-6} cm^2/s which is calculated from the forward current using Saito equation $I_{ss} = 4|z_i|FDCr$. Slope of current *vs* concentration is 30.4 pA/µM (Figure 4.3.4.7), charge is 30 for this pH which is calculated from the potentiometric titration curves at 0.1 M KCl of dendrimer G2 [244]. Radius of the pipette for this case was 22.5 µm.

CV at pH 2.25

Figure 4.3.4.8 (a) shows the voltammogram of 4 µM PAMAM '2' with blank at pH 2.25. The shape of the cyclic voltammogram is nearly same as pH 2.75, but the response is more intense than in pH 2.75. Especially the reverse peak current increased much more than the forward current and the peak is very sharp also which suggests this is adsorption controlled. So the CV indicates the ions transfer towards the organic

phase from the aqueous phase follows radial diffusion and the reverse direction follows adsorption mechanism from organic to aqueous phase [257]. Figure 4.3.4.8 (b) shows the background subtracted CVs of different concentration range of 1.0-8.0 µM of dendrimer '2'. The forward scan starts ion transfer at potential ≈ 0.63 V and starts to become plateau at potential ≈ 0.69 V. While the reverse scan gives peak at ≈ 0.64 V for all concentrations. The calculated half wave potential ($E_{1/2}$) based on the forward scan is 0.67 V.

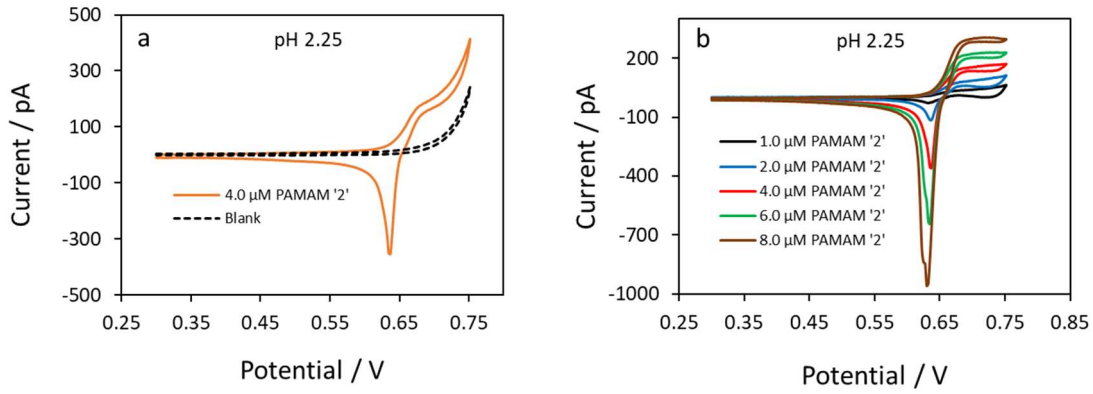

Figure 4.3.4.8: *(a) CV of 4 µM PAMAM '2' with blank and (b) background subtracted CV for 1, 2, 4, 6 & 8 µM PAMAM '2' at pH 2.25 with 22.5 µm radius pipette. [Pipette radius with Equations 2.3.1.2 and 2.3.1.3 are also given in Appendix B.]*

Table 4.3.4.4: *Steady state forward currents (i_f) and reverse peak currents (i_b) of three scans of CV for 1, 2, 3, 4, 5, 6, 7 & 8 µM PAMAM '2' at pH 2.25*

C / µM	i_{f1} / pA	i_{f2} / pA	i_{f3} / pA	i_f / pA Average	σ	i_{b1} / pA	i_{b2} / pA	i_{b3} / pA	i_b / pA Average	σ
1	20	15	25	20	4.0	-27	-22	-30	-26	3.1
2	86	81	91	86	4.0	-116	-107	-120	-114	5.6
3	122	118	124	121	2.4	-219	-216	-224	-220	3.5
4	153	149	156	153	2.9	-327	-321	-332	-327	4.6
5	191	187	195	191	3.2	-450	-445	-456	-450	4.6
6	223	220	227	223	3.0	-592	-585	-597	-591	4.8
7	268	262	272	267	3.9	-735	-728	-742	-735	5.6
8	301	294	306	300	4.7	-859	-850	-866	-858	6.8

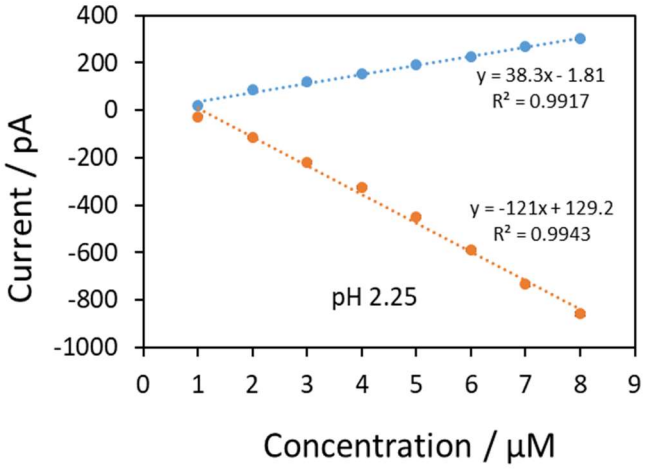

Figure 4.3.4.9: *Current vs concentration graph for both forward and reverse scan for PAMAM '2' at pH 2.25*

Table 4.3.4.4 shows the steady state forward current (i_f) and reverse peak current (i_b) from the CV experiment. Figure 4.3.4.9 shows current *vs* concentration graph based on the data of the Table 4.3.4.4. The currents on the forward sweeps as well as reverse sweeps of the background-subtracted CVs of dendrimer '2' increased linearly with the concentration of analyte in the aqueous phase. But the increase rate is much higher for reverse peak current as assumed adsorption occurred. These current vs concentration relation is predicted by the Saito equation [202] for the steady state current and for the voltametric peak current adsorption mechanism follows. Irrespective of the transfer mode, the current is concentration-dependent for both directions. Diffusion coefficient (D) at this pH is 1.47 x 10^{-6} cm^2/s which is calculated from the forward current using Saito equation $I_{ss} = 4|z_i|FDCr$. Slope of current *vs* concentration is 38.3 pA/µM (Figure 4.3.4.9), charge is 30 for this pH which is calculated from the potentiometric titration curves at 0.1 M KCl of dendrimer G2 [244]. Radius of the pipette for this case was 22.5 µm.

CV at pH 1.75

Figure 4.3.4.10 (a) shows the voltammogram of 6 µM PAMAM '2' with blank at pH 1.75. The shape of the cyclic voltammogram is nearly same as pH 2.25. In this case also, the reverse peak current increased much more than the forward current and the peak is very sharp as assumed it follows adsorption mechanism. So the CV indicates

the ions transfer towards the organic phase from the aqueous phase follows radial diffusion and the reverse direction follows adsorption mechanism from organic to aqueous phase [257]. Figure 4.3.4.10 (b) shows the background subtracted CVs of different concentration range of 2.0-9.0 µM of dendrimer '2'. The forward scan starts ion transfer at potential ≈ 0.62 V and starts to become plateau at potential ≈ 0.69 V. While the reverse scan gives peak in between ≈ 0.64 V - 0.62 V. The calculated half wave potential ($E_{1/2}$) based on the forward scan is 0.65 V.

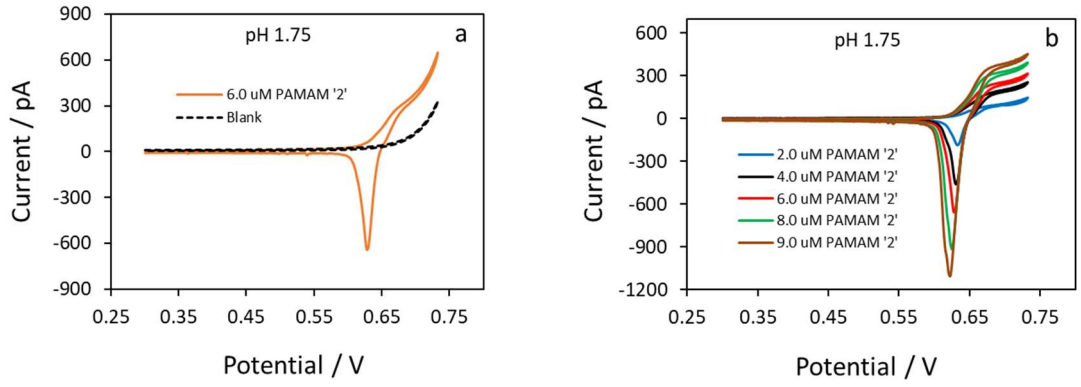

Figure 4.3.4.10: *(a) CV of 6 µM PAMAM '2' with blank and (b) background subtracted CV for 2, 4, 6, 8 & 9 µM PAMAM '2' at pH 1.75 with 25 µm radius pipette. [Pipette radius with Equations 2.3.1.2 and 2.3.1.3 are also given in Appendix B.]*

Table 4.3.4.5: *Steady state forward currents (i_f) and reverse peak currents (i_b) of three scans of CV for 1, 2, 3, 4, 5, 6, 7 & 8 µM PAMAM '2' at pH 1.75*

C / µM	i_{f1} / pA	i_{f2} / pA	i_{f3} / pA	i_f / pA Average	σ	i_{b1} / pA	i_{b2} / pA	i_{b3} / pA	i_b / pA Average	σ
2	90	82	96	89	5.5	-178	-171	-184	-178	5.2
3	138	130	145	138	5.9	-273	-266	-277	-272	4.9
4	196	191	200	195	3.7	-448	-444	-454	-449	4.1
5	219	214	225	220	4.6	-514	-507	-520	-514	5.3
6	255	248	262	255	5.4	-641	-634	-647	-641	5.6
7	286	280	293	286	5.2	-761	-758	-765	-761	3.0
8	325	320	327	324	2.9	-893	-887	-898	-893	4.6
9	382	376	389	383	5.4	-1072	-1060	-1079	-1070	7.6

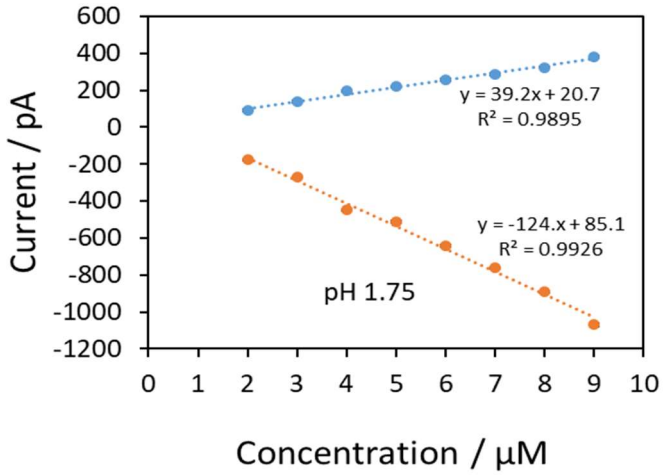

Figure 4.3.4.11: *Current vs concentration graph for both forward and reverse scan for PAMAM '2' at pH 1.75*

Table 4.3.4.5 shows the steady state forward current (i_f) and reverse peak current (i_b) from the CV experiment at pH 1.75. Figure 4.3.4.11 shows current *vs* concentration graph based on the data of the Table 4.3.4.5. The currents on the forward sweeps as well as reverse sweeps of the background-subtracted CVs of dendrimer '2' at pH 1.75 increased linearly with the concentration of analyte in the aqueous phase. But the increase rate is much higher for reverse peak current like pH 2.25. These current vs concentration relation is predicted by the Saito equation [202] for the steady state current and follows adsorption mechanism for voltametric peak current. Irrespective of the transfer mode, the current is concentration-dependent for both directions. Diffusion coefficient (D) at this pH is 1.35 x 10^{-6} cm^2/s which is calculated from the forward current using Saito equation $I_{ss} = 4|z_i|FDCr$. Slope of current *vs* concentration is 39.2 pA/µM (Figure 4.3.4.11), charge is 30 for this pH which is calculated from the potentiometric titration curves at 0.1 M KCl of dendrimer G2 [244]. Radius of the pipette for this case was 25 µm.

CV at pH 9.0

We investigate the electrochemical properties at high pH also. Like low pH electrochemical response increases with the increase of pH. Figure 4.3.4.12 (a) shows the voltammogram of 6 µM PAMAM '2' with blank at pH 9.0. This case the shape of the cyclic voltammogram is as like as the CV at pH 6.0. That means at this pH the reverse transfer follows diffusion controlled. Similar to others, the shape of the CV

indicates ions transfer towards the organic phase from aqueous phase follows radial diffusion and the reverse direction follows linear transfer of ions from organic to aqueous phase [257]. Figure 4.3.4.12 (b) shows the background subtracted CVs of different concentration range of 2.0 - 10.0 µM of dendrimer '2'. The forward scan starts ion transfer at potential ≈ 0.65 V and starts to become plateau at potential ≈ 0.7 V. While the reverse scan gives peak at ≈ 0.65 V. The calculated half wave potential ($E_{1/2}$) based on the forward scan is 0.67 V.

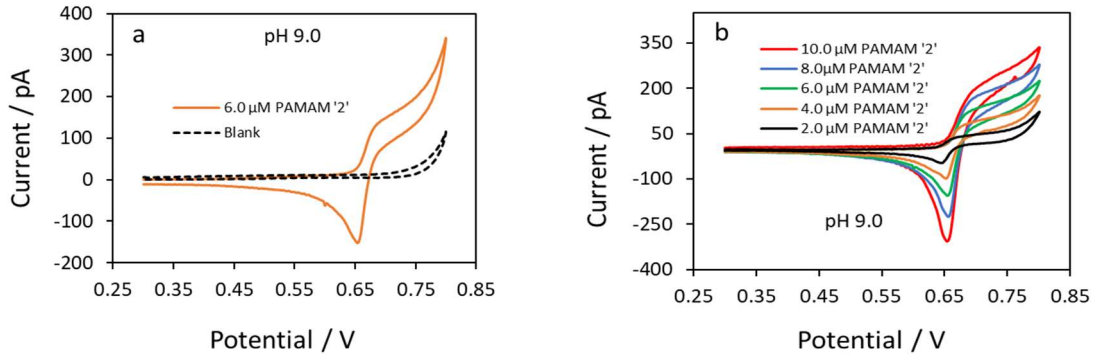

Figure 4.3.4.12: *(a) CV of 6 µM PAMAM '2' with blank and (b) background subtracted CV for 2, 4, 6, 8 & 10 µM PAMAM '2' at pH 9.0 with 25 µm radius pipette.*

[Pipette radius with Equations 2.3.1.2 and 2.3.1.3 are also given in Appendix B.]

Table 4.3.4.6: *Steady state forward currents (i_f) and reverse peak currents (i_b) of three scans of CV for 1, 2, 3, 4, 5, 6, 7, 8 & 9 µM PAMAM '2' at pH 9.0*

C / µM	i_{f1} / pA	i_{f2} / pA	i_{f3} / pA	i_f / pA Average	σ	i_{b1} / pA	i_{b2} / pA	i_{b3} / pA	i_b / pA Average	σ
1	15	13	19	16	2.3	-12	-11	-15	-13	1.8
2	48	45	51	48	2.5	-54	-51	-57	-54	2.5
3	75	74	78	76	2.0	-87	-82	-90	-86	3.3
4	93	90	110	98	8.9	-115	-112	-118	-115	2.7
5	124	121	126	123	2.4	-163	-158	-166	-162	3.2
6	146	143	150	146	2.7	-189	-185	-207	-194	9.5
7	172	167	175	172	3.3	-234	-228	-238	-233	4.2
8	198	195	203	199	3.5	-280	-276	-284	-280	3.3
9	221	215	229	222	5.4	-330	-316	-335	-327	8.2

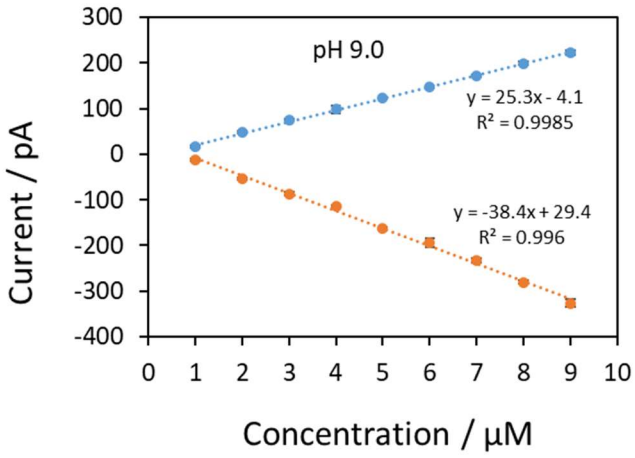

Figure 4.3.4.13: *Current vs concentration graph for both forward and reverse scan for PAMAM '2' at pH 9.0*

Table 4.3.4.6 shows the steady state forward current (i_f) and reverse peak current (i_b) from the CV experiment at pH 9.0. Figure 4.3.4.13 shows current *vs* concentration graph based on the data of the Table 4.3.4.6. The currents on the forward sweeps as well as reverse sweeps of the background-subtracted CVs of dendrimer '2' at pH 9.0 also increased linearly with the concentration of analyte in the aqueous phase like previous. These current vs concentration relation is predicted by the Saito equation [202] for the steady state current and the Randles–Sevcik equation [80, 203] for the voltametric peak current for linear diffusion systems. Irrespective of the diffusion mode, the current is concentration-dependent for both directions. Diffusion coefficient (D) at this pH is 2.91 x 10^{-6} cm^2/s which is calculated from the forward current using Saito equation $I_{ss} = 4|z_i|FDCr$. Slope of current *vs* concentration is 25.3 pA/µM (Figure 4.3.4.13), charge is 9 for this pH which is calculated from the potentiometric titration curves at 0.1 M KCl of dendrimer G2 [244]. Radius of the pipette for this case was 25 µm.

CV at pH 10.0

Figure 4.3.4.14 (a) shows the voltammogram of 3 µM PAMAM '2' with blank at pH 10.0. Cyclic voltammogram is as like as the CV at pH 9.0 and indicates ions transfer towards the organic phase from aqueous phase follows radial diffusion and the reverse direction follows linear diffusion transfer of ions from organic to aqueous phase [257]. There is no response for PAMAM '0' and very small response for PAMAM '1' at pH

10, whereas very big response gives PAMAM '2' at this pH. Figure 4.3.4.14 (b) shows the background subtracted CVs of different concentration range of 1.0 - 10.0 µM of dendrimer '2'. The forward scan starts ion transfer at potential ≈ 0.64 V and starts to become plateau at potential ≈ 0.7 V. While the reverse scan gives peak at ≈ 0.64 V. The calculated half wave potential ($E_{1/2}$) based on the forward scan is 0.67 V.

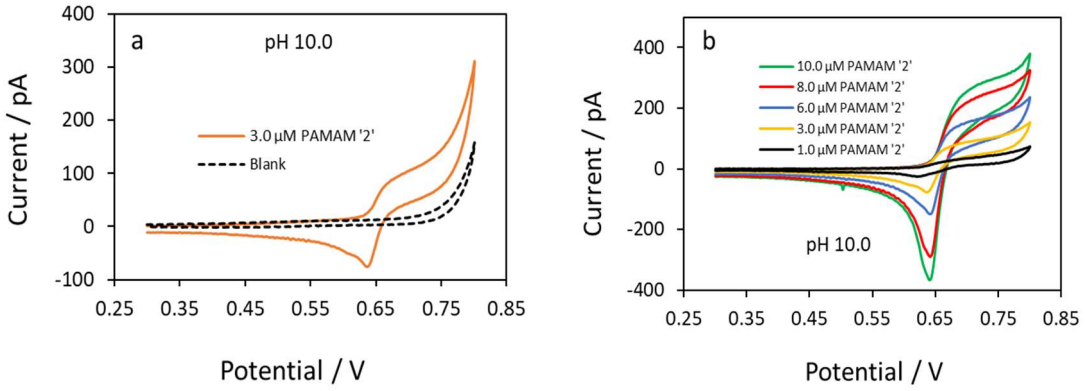

Figure 4.3.4.14: *(a) CV of 3 µM PAMAM '2' with blank and (b) background subtracted CV for 1, 3, 6, 8 & 10 µM PAMAM '2' at pH 10.0 with 25 µm radius pipette. [Pipette radius with Equations 2.3.1.2 and 2.3.1.3 are also given in Appendix B.]*

Table 4.3.4.7: *Steady state forward currents (i_f) and reverse peak currents (i_b) of three scans of CV for 1, 2, 3, 4, 6, 8 & 10 µM PAMAM '2' at pH 10.0*

C / µM	i_{f1} / pA	i_{f2} / pA	i_{f3} / pA	i_f / pA Average	σ	i_{b1} / pA	i_{b2} / pA	i_{b3} / pA	i_b / pA Average	σ
1	18	14	20	17	2.4	-27	-23	-28	-26	2.1
2	39	36	44	40	3.1	-63	-60	-66	-63	2.4
3	76	72	80	76	3.3	-95	-92	-98	-95	2.4
4	110	107	115	111	3.6	-137	-135	-142	-138	2.9
6	149	145	167	154	9.5	-203	-214	-225	-214	8.8
8	223	205	226	218	9.0	-328	-312	-327	-322	7.3
10	246	245	267	252	10.0	-405	-401	-380	-395	10.9

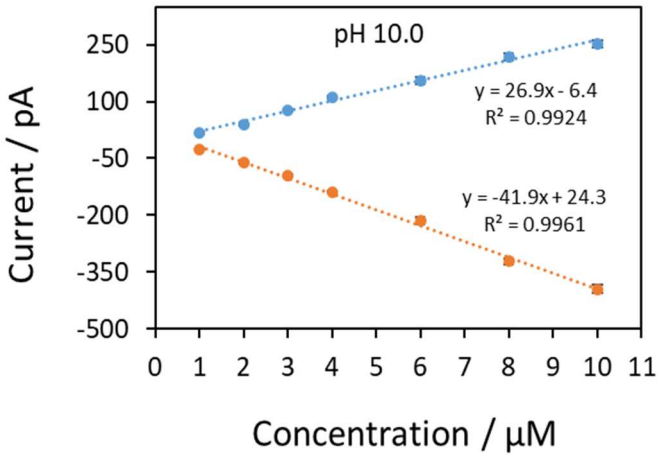

Figure 4.3.4.15: *Current vs concentration graph for both forward and reverse scan for PAMAM '2' at pH 10.0*

Table 4.3.4.7 shows the steady state forward current (i_f) and reverse peak current (i_b) from the CV experiment at pH 10.0. Figure 4.3.4.15 shows current *vs* concentration graph based on the data of the Table 4.3.4.7. The currents on the forward sweeps as well as reverse sweeps of the background-subtracted CVs of dendrimer '2' at pH 10.0 increased linearly with the concentration of analyte in the aqueous phase other pH. These current vs concentration relation is predicted by the Saito equation [202] for the steady state current and the Randles–Sevcik equation [80, 203] for the voltametric peak current for linear diffusion systems. Irrespective of the diffusion mode, the current is concentration-dependent for both directions. Diffusion coefficient (D) at this pH is 9.3 x 10^{-6} cm^2/s which is calculated from the forward current using Saito equation $I_{ss} = 4|z_i|FDCr$. Slope of current *vs* concentration is 26.9 pA/µM (Figure 4.3.4.15), charge is 3 for this pH which is calculated from the potentiometric titration curves at 0.1 M KCl of dendrimer G2 [244]. Radius of the pipette for this case was 25 µm.

CV at pH 11.0

PAMAM '2' gives good electrochemical response at very high pH 11.0 also. Figure 4.3.4.16 (a) shows the voltammogram of 4 µM PAMAM '2' with blank at pH 11.0. In this case the ion transfer shifts to high potential that very close to background ion transfer. The CV at this pH also indicates ions transfer towards the organic phase from aqueous phase follows radial diffusion and the reverse direction follows linear transfer of ions from organic to aqueous phase [257]. There is no response for PAMAM '0' and PAMAM '1' at pH 11 at all, whereas PAMAM '2' gives very big response. May

be because at this pH it is still little bit protonated according to potentiometric titration curves. Figure 4.3.4.16 (b) shows the background subtracted CVs of different concentration range of 2.0 - 10.0 µM of dendrimer '2'. The forward scan starts ion transfer at potential ≈ 0.71 V and it does not give steady state current as ions transfer very close to background ions transfer. The reverse scan gives peak at ≈ 0.72 V for 4 µM and goes to lower potential with the increase of concentration. The calculated half wave potential ($E_{1/2}$) based on the forward scan is 0.74 V.

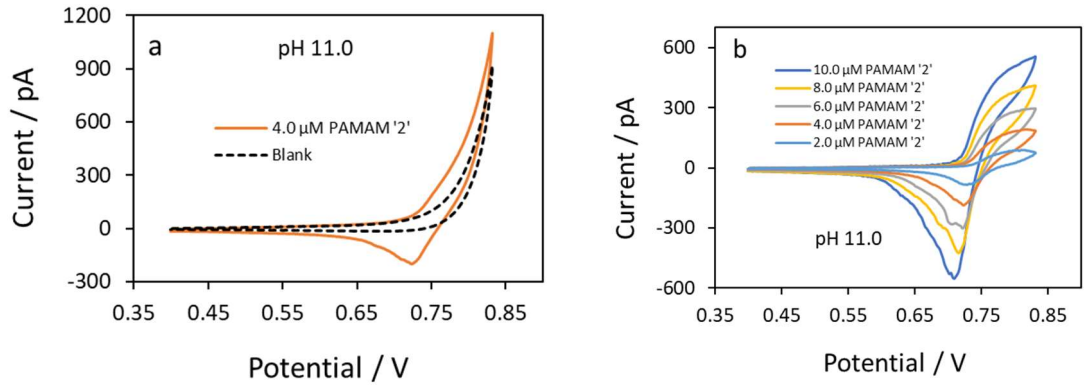

Figure 4.3.4.16: *(a) CV of 4 µM PAMAM '2' with blank and (b) background subtracted CV for 2, 4, 6, 8 & 10 µM PAMAM '2' at pH 11.0 with 27 µm radius pipette. [Pipette radius with Equations 2.3.1.2 and 2.3.1.3 are also given in Appendix B.]*

Table 4.3.4.8: *Steady state forward currents (i_f) and reverse peak currents (i_b) of three scans of CV for 2, 4, 6, 8 & 10 µM PAMAM '2' at pH 11.0*

C / µM	i_{f1} / pA	i_{f2} / pA	i_{f3} / pA	i_f / pA Average	σ	i_{b1} / pA	i_{b2} / pA	i_{b3} / pA	i_b / pA Average	σ
2	68	65	73	68	3.3	-69	-65	-71	-68	2.5
4	136	132	138	135	2.6	-140	-138	-144	-141	2.5
6	211	205	214	210	3.6	-228	-221	-232	-227	4.3
8	268	265	270	268	2.2	-293	-286	-295	-291	4.0
10	330	327	335	331	3.4	-351	-343	-356	-350	5.4

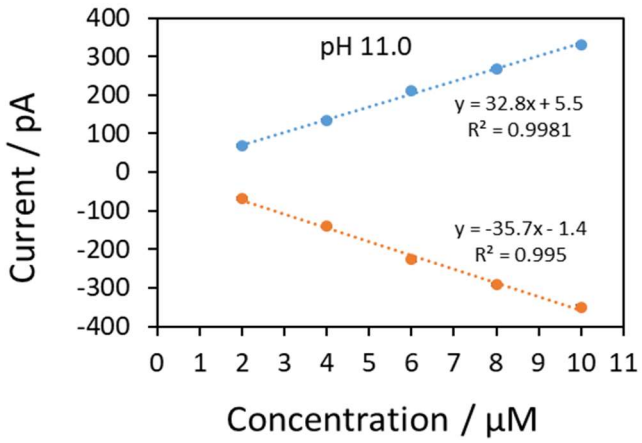

Figure 4.3.4.17: *Current vs concentration graph for both forward and reverse scan for PAMAM '2' at pH 11.0*

Table 4.3.4.8 shows the steady state forward current (i_f) and reverse peak current (i_b) from the CV experiment at pH 11.0. Figure 4.3.4.17 shows current *vs* concentration graph based on the data of the Table 19. The currents on the forward sweeps as well as reverse sweeps of the background-subtracted CVs of dendrimer '2' at pH 11.0 increased linearly with the concentration of analyte in the aqueous phase other pH. These current vs concentration relation is predicted by the Saito equation [202] for the steady state current and the Randles–Sevcik equation [80, 203] for the voltametric peak current for linear diffusion systems. Irrespective of the diffusion mode, the current is concentration-dependent for both directions. Diffusion coefficient (D) at this pH is 15.7 x 10^{-6} cm^2/s which is calculated from the forward current using Saito equation $I_{ss} = 4|z_i|FDCr$. Slope of current *vs* concentration is 32.8 pA/µM (Figure 4.3.4.17), charge is 2 for this pH which is calculated from the potentiometric titration curves at 0.1 M KCl of dendrimer G2 [244]. Radius of the pipette for this case was 27 µm.

Comparison of CVs at different pH

Figure 4.3.4.18 shows the background subtracted CVs of Dendrimer '2' at different pH. The shape of the CV for forward potential are nearly same whereas lots of variation observed in the reverse direction. From the Figure 4.3.4.18 it is clearly seen that the reverse peak current from pH 6.0 to pH 11.0 are diffusion controlled. On the other hand at lower pH from 3.5 the reverse peak current follows adsorption mechanism. The current response increased more as the pH go down more. Which is opposite than the case of G0 & G1. The ion transfer potential at pH 11.0 shifts to higher

whereas for other pH it very small variation observed. The small variation of the shape of the CVs may be because of the different shape of the pipettes and/or for the different time & environment of the experiment.

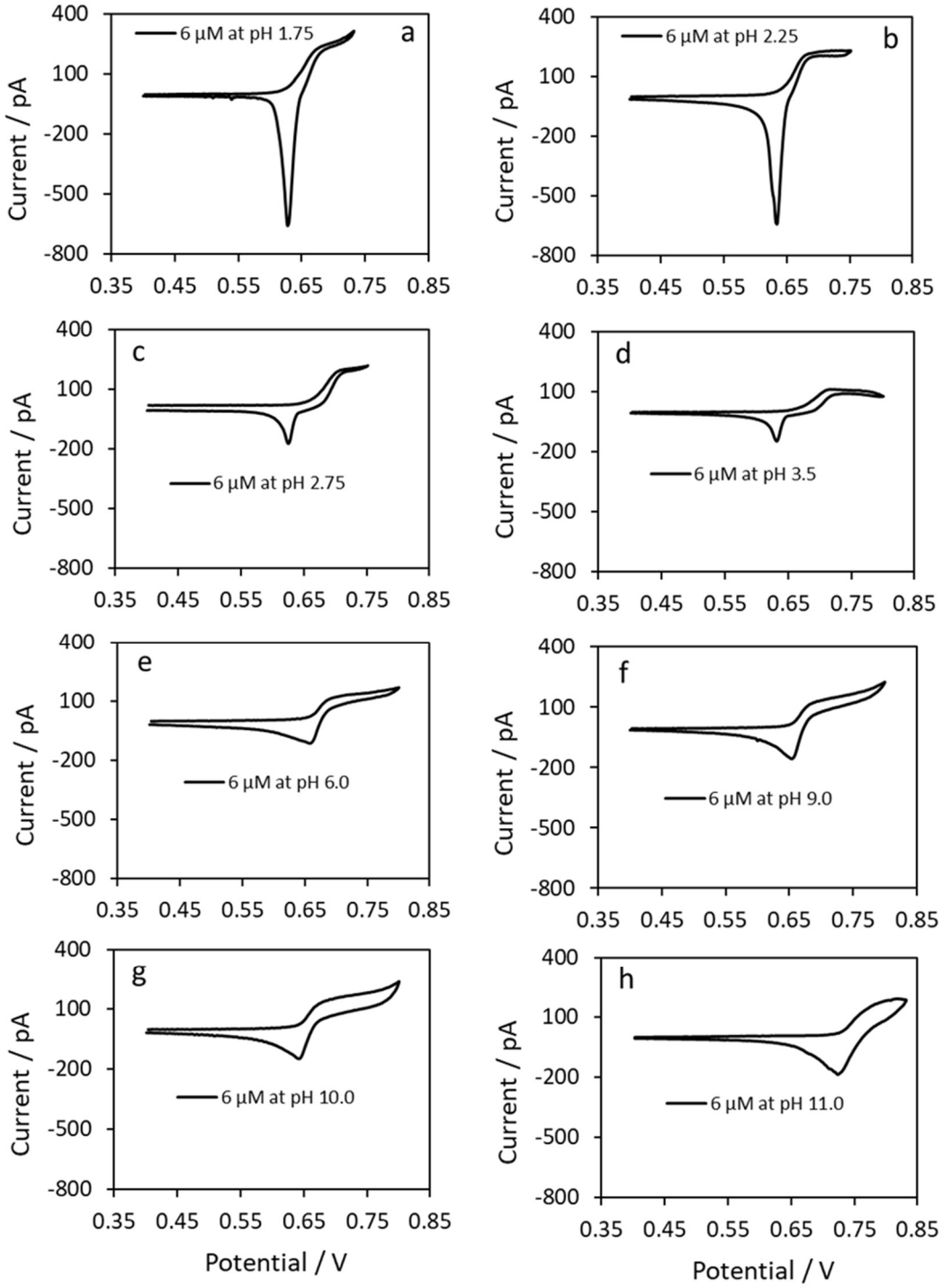

Figure 4.3.4.18: *Background subtracted CVs of 6 µM dendrimer '2' at (a) pH 1.75 (b) pH 2.25 (c) pH 2.75 (d) pH 3.5 (e) pH 6.0 (f) pH 9.0, (g) pH 10.0 and (h) pH 11.0*

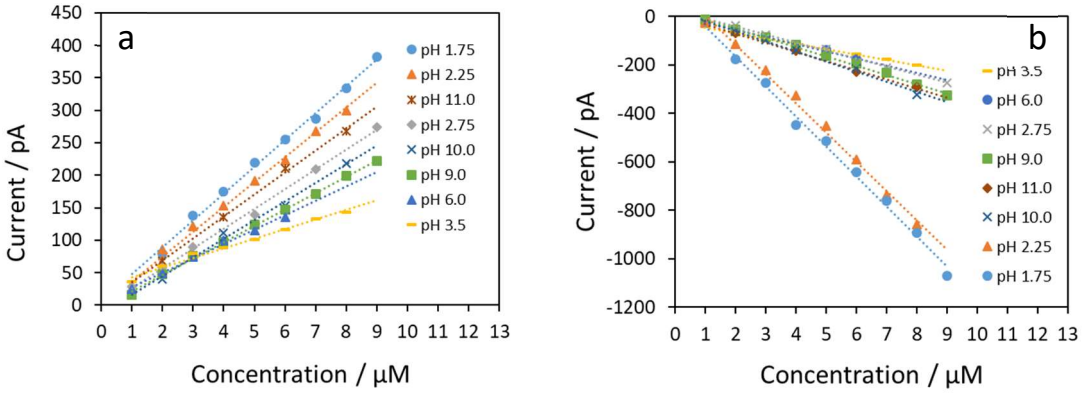

Figure 4.3.4.19: *Current vs concentration graph for PAMAM '2' at pH 1.75, 2.25, 2.75, 3.5, 6.0, 9.0, 10.0 and 11.0 for (a) forward scan and (b) reverse scan.*

Table 4.3.4.9*: Diffusion coefficient (D), charge and slope of the regression line at different pH for PAMAM '2'.*

		pH 1.75	**pH 2.25**	**pH 2.75**	**pH 3.5**	**pH 6.0**	**pH 9.0**	**pH 10**	**pH 11**
D x 10^{-6} / cm^2s^{-1}		1.35	1.47	1.17	0.87	1.83	2.91	9.30	15.7
Charge		30	30	30	20	15	9	3	1
Slope pA/µM	**forward**	41.3	38.2	30.4	14.8	22.2	25.3	28.6	33.6
	reverse	-124	-121	-33.2	-22.1	-29.9	-38.4	-41.7	-37.7

Figure 4.3.4.19 shows the current verses concentration for both forward and reverse directions at different pH. It shows that in both case of very low pH and in very high pH PAMAM '2' gives very high electrochemical response. The highest response for both forward and reverse directions are for pH 1.75 and then for pH 2.25. But the reverse peak give exceptionally high current for these two pH. Lowest response got at pH 3.5 for both case. For PAMAM '0' at pH 1.75 there was no response but for PAMAM '1' gives response. The response increased with the increase of pH from pH 6.0 up to pH 11.0. On the other hand, for PAMAM '1' lowest response gives at pH 10.0 and no response at pH 11.0.

According to p*Ka* and protonation mechanism it is assumed that at lower pH the current will be high also. But for G0 and G1 at lower pH response was low. Again for the high pH the response increased which is also unusual because the charge decrease with increase of pH (Table 4.3.4.9). The table 4.3.4.9 also shows how the diffusion coefficient, charge and slope changes with pH.

4.3.5 CV of PAMAM dendrimer '3'

PAMAM dendrimer generation '3' has 32 surface primary amino groups and 30 interior tertiary amino groups [256]. Figure 4.3.5.1 shows the structure of PAMAM '3'. The cyclic voltammetry experiment of this molecule gives best response among others PAMAM dendrimers. The experiment started at pH 6.0 then goes to lower pH as 3.5, 2.75, 2.25, 1.75 respectively. After that experiment was done at higher pH as 9.0, 10.0 & 11.0.

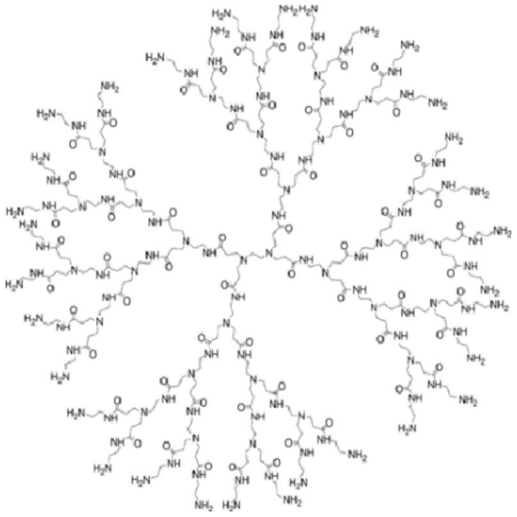

Figure 4.3.5.1: *Structure of PAMAM '3' dendrimer*

CV at pH 6.0

Figure 4.3.5.2 (a) shows the voltammogram of blank with the 4 µM PAMAM '3' at pH 6.0. 4 µM PAMAM '3' gives very big response compare to other PAMAM dendrimers at pH 6.0. As like previous dendrimers, in forward direction, the CV makes a semi steady state voltammogram which indicates a radial diffusion of PAMAM '3' ions towards the organic phase from the aqueous phase and the peak shape response in reverse direction indicating linear transfer of ions from organic to aqueous phase [257]. Figure 4.3.5.2 (b) shows the background subtracted CVs of different concentration range of 1.0 - 6.0 µM of dendrimer '3'. In this case the forward scan starts ion transfer at potential ≈ 0.66 V and starts to become plateau at potential ≈ 0.7 V. The reverse scan gives peak at ≈ 0.61 V nearly for all concentrations. The calculated half wave potential ($E_{1/2}$) based on the forward scan is 0.68 V.

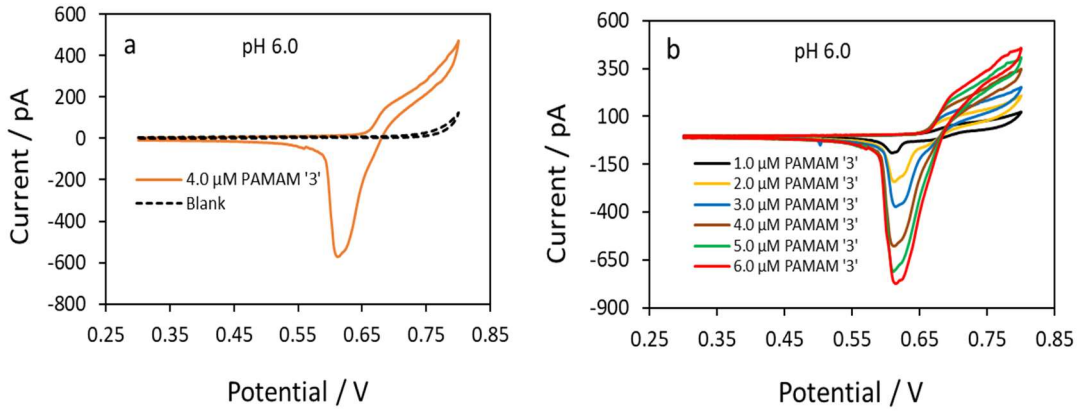

Figure 4.3.5.2: *(a) CV of 4 µM PAMAM '3' with blank and (b) background subtracted CV for 1, 2, 3, 4, 5 & 6 µM PAMAM '3' at pH 6.0 with 23.5 µm radius pipette. [Pipette radius with Equations 2.3.1.2 and 2.3.1.3 are also given in Appendix B.]*

Table 4.3.5.1: *Steady state forward currents (i_f) and reverse peak currents (i_b) of three scans of CV for 1, 1.5, 2, 2.5, 3, 3.5, 4, 5 & 6 µM PAMAM '3' at pH 6.0*

C / µM	i_{f1} / pA	i_{f2} / pA	i_{f3} / pA	i_f / pA Average	σ	i_{b1} / pA	i_{b2} / pA	i_{b3} / pA	i_b / pA Average	σ
1	70	60	65	65	4.0	-90	-85	-93	-89	3.2
1.5	89	93	84	89	3.6	-144	-138	-150	-144	5.0
2	113	109	118	113	3.5	-241	-237	-243	-240	2.5
2.5	134	130	138	134	3.4	-294	-296	-310	-300	6.8
3	159	153	162	158	3.6	-372	-373	-382	-376	4.6
3.5	190	184	191	188	3.2	-492	-480	-483	-485	5.2
4	211	208	215	211	3.2	-574	-559	-555	-563	8.2
5	248	242	254	248	4.9	-710	-698	-719	-709	8.3
6	280	275	285	280	4.0	-774	-786	-795	-785	8.9

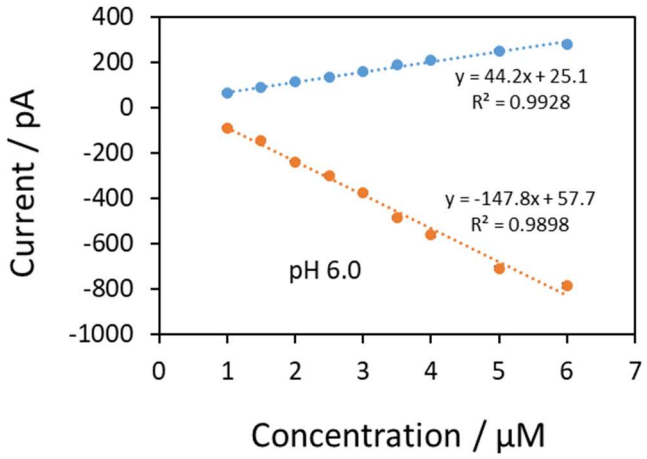

Figure 4.3.5.3: *Current vs concentration graph for both forward and reverse scan for PAMAM '3' at pH 6.0*

Table 4.3.5.1 shows the steady state forward current (i_f) and reverse peak current (i_b) for different concentrations. Figure 4.3.5.3 shows current vs concentration graph based on the data of that Table 4.3.5.1. The currents on the forward sweeps as well as reverse sweeps of the background-subtracted CVs of dendrimer '3' at pH 6.0 increased linearly with the concentration of analyte in the aqueous phase. But the peak current in the reverse phase is much higher than the forward direction. Same as before this current vs concentration relation follow the Saito equation [202] for the steady state current and the Randles–Sevcik equation [80, 203] for the voltammetric peak current for linear diffusion systems. Diffusion coefficient (D) at this pH is 1.32 x 10^{-6} cm^2/s which is calculated from the forward current using Saito equation $I_{ss} = 4|z_i|FDCr$. Slope of current *vs* concentration is 44.2 pA/µM (Figure 4.3.5.3), charge is 37 for this pH which is calculated from the potentiometric titration curves at 0.1 M KCl of dendrimer G3 [244]. Radius of the pipette for this case was 23.5 µm.

CV at pH 3.5

After CV experiment at pH 6.0 the pH was gradually decreased. Figure 4.3.5.4 (a) shows the voltammogram of blank with the 4 µM PAMAM '3' at pH 3.5. The response increased with the decrease of pH especially for reverse direction. Similarly like others, the CV makes steady state voltammogram in forward direction which indicates a radial diffusion of PAMAM '3' ions [257] and the response in reverse direction clearly shows that the peak shape and intensity completely changed which indicates the ions follow adsorption mechanism from organic to aqueous phase. Figure 4.3.5.5

(b) shows the background subtracted CVs of different concentration range of 1.0 - 5.0 µM of dendrimer '3'. The reverse peak is very big and sharp. Forward scan starts ion transfer at potential ≈ 0.68 V and starts to become plateau at potential ≈ 0.74 V and the reverse scan gives peak at ≈ 0.61 V. The calculated half wave potential ($E_{1/2}$) based on the forward scan is 0.7 V.

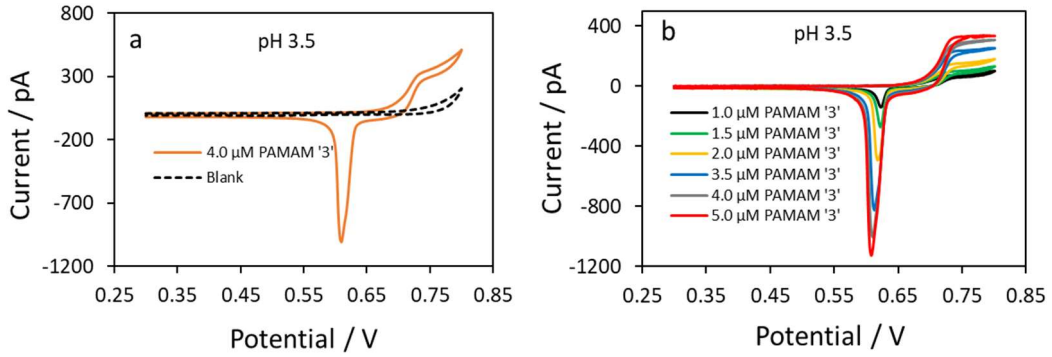

Figure 4.3.5.4: *(a) CV of 4 µM PAMAM '3' with blank and (b) background subtracted CV for 1, 1.5, 2, 3.5, 4 & 5 µM PAMAM '3' at pH 3.5 with 23.5 µm radius pipette. [Pipette radius with Equations 2.3.1.2 and 2.3.1.3 are also given in Appendix B.]*

Table 4.3.5.2: *Steady state forward currents (i_f) and reverse peak currents (i_b) of three scans of CV for 1, 1.5, 2, 2.5, 3, 3.5, 4, 5 & 6 µM PAMAM '3' at pH 3.5*

C / µM	i_{f1} / pA	i_{f2} / pA	i_{f3} / pA	i_f / pA Average	σ	i_{b1} / pA	i_{b2} / pA	i_{b3} / pA	i_b / pA Average	σ
1	76	71	78	75	3.1	-137	-131	-143	-137	5.0
1.5	106	100	108	105	3.5	-271	-265	-270	-269	2.7
2	136	131	139	135	3.7	-496	-476	-486	-486	7.9
2.5	163	157	164	161	3.1	-618	-607	-610	-612	4.9
3	202	199	205	202	2.7	-709	-702	-708	-706	3.2
3.5	229	225	233	229	3.1	-826	-823	-837	-829	5.9
4	291	286	292	290	2.6	-1006	-984	-992	-994	8.9
5	331	328	339	332	4.7	-1128	-1115	-1126	-1123	5.5
6	370	367	378	372	4.6	-1278	-1269	-1279	-1275	4.8

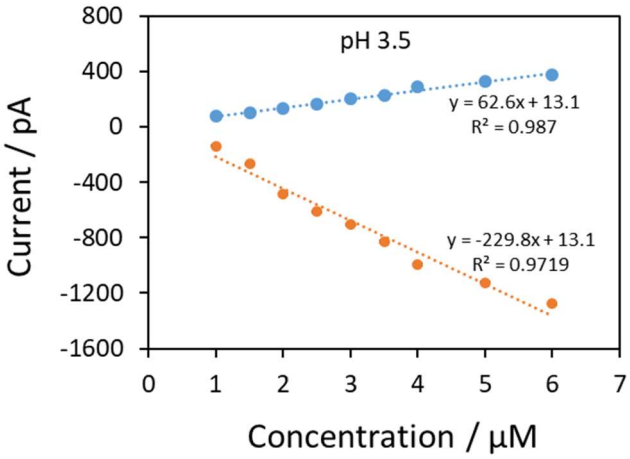

Figure 4.3.5.5: *Current vs concentration graph for both forward and reverse scan for PAMAM '3' at pH 3.5*

Table 4.3.5.2 shows the steady state forward current (i_f) and reverse peak current (i_b) for different concentrations. Figure 4.3.5.5 shows current vs concentration graph based on the data of that Table 4.3.5.2. The currents on the forward sweeps as well as reverse sweeps of the background-subtracted CVs of dendrimer '3' at pH 3.5 increased linearly with the concentration of analyte, but as like as at pH 6.0 the peak current in the reverse phase is much higher than the forward direction. This current vs concentration relation follow the Saito equation [202] for the steady state current and adsorption mechanism for the voltammetric peak current. Diffusion coefficient (D) at this pH is 1.15 x 10^{-6} cm^2/s which is calculated from the forward current using Saito equation $I_{ss} = 4|z_i|FDCr$. Slope of current *vs* concentration is 62.6 pA/µM (Figure 4.3.5.5), charge is 60 for this pH which is calculated from the potentiometric titration curves at 0.1 M KCl of dendrimer G3 [244]. Radius of the pipette for this case was 23.5 µm.

CV at pH 2.75

Figure 4.3.5.6 (a) shows the voltammogram of blank with the 4 µM PAMAM '3' at pH 2.75. At this pH the peak current again increased. Similarly like pH 3.5, the CV makes steady state voltammogram in forward direction which indicates a radial diffusion of PAMAM '3' ions [257] and the peak shape response in reverse direction indicating adsorption mechanism occurs from organic to aqueous phase. The

background subtracted CVs of different concentration range of 1.0 - 5.0 µM of dendrimer '3' are shown in Figure 4.3.5.6 (b). Forward scan starts ion transfer at potential ≈ 0.67 V and starts to become plateau at potential ≈ 0.72 V and the reverse scan gives peak at ≈ 0.6 V. The calculated half wave potential ($E_{1/2}$) based on the forward scan is 0.7 V.

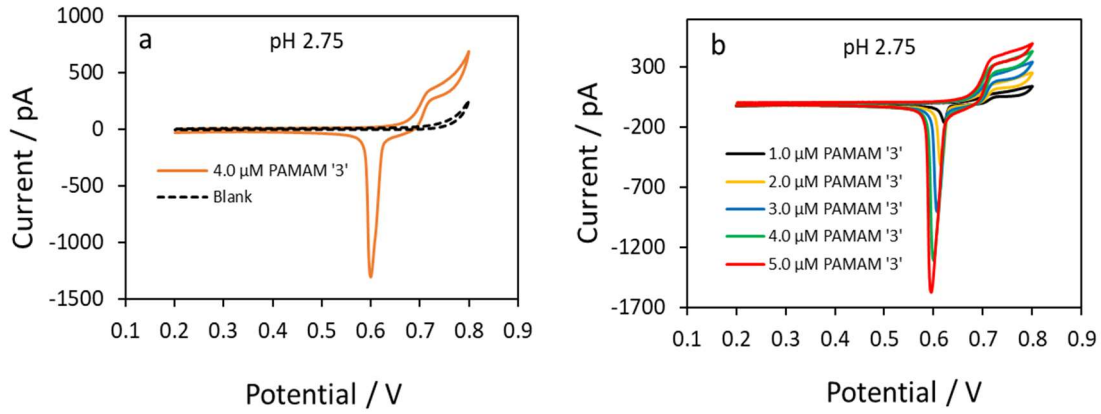

Figure 4.3.5.6: *(a) CV of 4 µM PAMAM '3' with blank and (b) background subtracted CV for 1, 2, 3, 4 & 5 µM PAMAM '3' at pH 2.75 with 25 µm radius pipette. [Pipette radius with Equations 2.3.1.2 and 2.3.1.3 are also given in Appendix B.]*

Table 4.3.5.3: *Steady state forward currents (i_f) and reverse peak currents (i_b) of three scans of CV for 1, 1.5, 2, 2.5, 3, 3.5, 4, 5 & 6 µM PAMAM '3' at pH 2.75*

C / µM	i_{f1} / pA	i_{f2} / pA	i_{f3} / pA	i_f / pA Average	σ	i_{b1} / pA	i_{b2} / pA	i_{b3} / pA	i_b / pA Average	σ
1	85	80	88	85	3.3	-161	-151	-170	-161	7.5
1.5	131	124	133	129	4.0	-343	-333	-349	-342	6.5
2	169	165	174	169	3.8	-521	-512	-525	-519	5.2
2.5	206	201	211	206	4.3	-730	-727	-736	-731	3.9
3	242	235	249	242	5.3	-900	-887	-913	-900	10.7
3.5	313	304	319	312	6.1	-1179	-1160	-1175	-1172	8.1
4	338	332	341	337	3.4	-1305	-1291	-1310	-1302	7.9
5	414	411	423	416	5.3	-1575	-1586	-1592	-1584	7.3
6	444	440	448	444	3.3	-1782	-1787	-1809	-1793	12.0

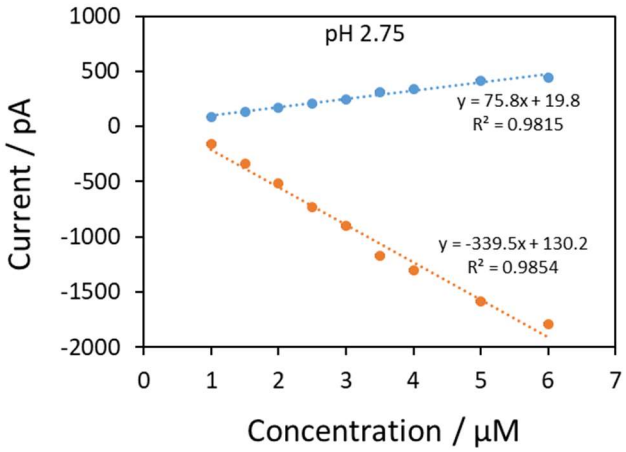

Figure 4.3.5.7: *Current vs concentration graph for both forward and reverse scan for PAMAM '3' at pH 2.75*

Current vs concentration graph was drown in Figure 4.3.5.7 based on the steady state forward current (i_f) and reverse peak current (i_b) for different concentrations in Table 4.3.5.3. The currents on the forward sweeps as well as reverse sweeps of the background-subtracted CVs of dendrimer '3' at pH 2.75 increased linearly with the concentration of analyte and as like for pH 3.5 the peak current in the reverse phase is much higher than the forward direction. Same as all others this current vs concentration relation follow the Saito equation [202] for the steady state current [80, 203] and adsorption mechanism for the voltammetric peak current. Diffusion coefficient (D) at this pH is 1.27 x 10^{-6} cm^2/s which is calculated from the forward current using Saito equation $I_{ss} = 4|z_i|FDCr$. Slope of current *vs* concentration is 75.8 pA/µM (Figure 4.3.5.7), charge is 62 for this pH which is calculated from the potentiometric titration curves at 0.1 M KCl of dendrimer G3 [244]. Radius of the pipette for this case was 25 µm.

CV at pH 2.25

Figure 4.3.5.8 (a) shows the voltammogram of blank with the 4 µM PAMAM '3' at pH 2.25. CV makes steady state voltammogram in forward direction which indicates a radial diffusion of PAMAM '3' ions [257] and the peak shape response in reverse direction indicating adsorption controlled mechanism from organic to aqueous phase like pH 3.5 and pH 2.75. The background subtracted CVs of different concentration range of 1.0 - 6.0 µM of dendrimer '3' are shown in Figure 4.3.5.8 (b). Forward scan

starts ion transfer at potential ≈ 0.62 V and starts to become plateau at potential ≈ 0.67 V and the reverse scan gives peak at ≈ 0.6 V. The calculated half wave potential ($E_{1/2}$) based on the forward scan is 0.65 V.

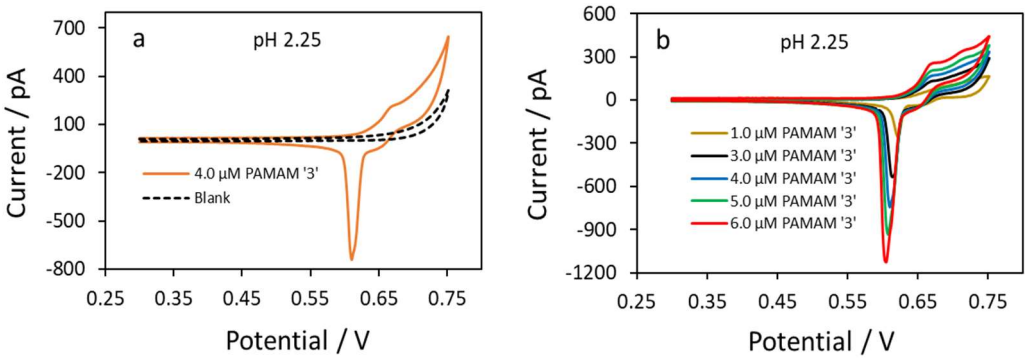

Figure 4.3.5.8: *(a) CV of 4 µM PAMAM '3' with blank and (b) background subtracted CV for 1, 3, 4, 5 & 6 µM PAMAM '3' at pH 2.25 with 23.5 µm radius pipette. [Pipette radius with Equations 2.3.1.2 and 2.3.1.3 are also given in Appendix B.]*

Table 4.3.5.4: *Steady state forward currents (i_f) and reverse peak currents (i_b) of three scans of CV for 1, 1.5, 2, 2.5, 3, 3.5, 4, 5 & 6 µM PAMAM '3' at pH 2.25*

C / µM	i_{f1} / pA	i_{f2} / pA	i_{f3} / pA	i_f / pA Average	σ	i_{b1} / pA	i_{b2} / pA	i_{b3} / pA	i_b / pA Average	σ
1	79	74	82	78	3.5	-240	-253	-233	-242	8.1
1.5	110	102	114	108	5.1	-325	-318	-327	-323	4.2
2	122	116	127	122	4.3	-411	-405	-419	-412	5.7
2.5	131	127	134	131	2.6	-474	-466	-480	-473	5.9
3	143	150	144	145	2.9	-532	-539	-543	-538	4.5
4	174	170	178	174	3.1	-741	-732	-743	-739	4.7
5	219	210	226	218	6.6	-932	-925	-930	-929	2.7
6	257	251	265	258	5.9	-1125	-1106	-1122	-1118	8.4

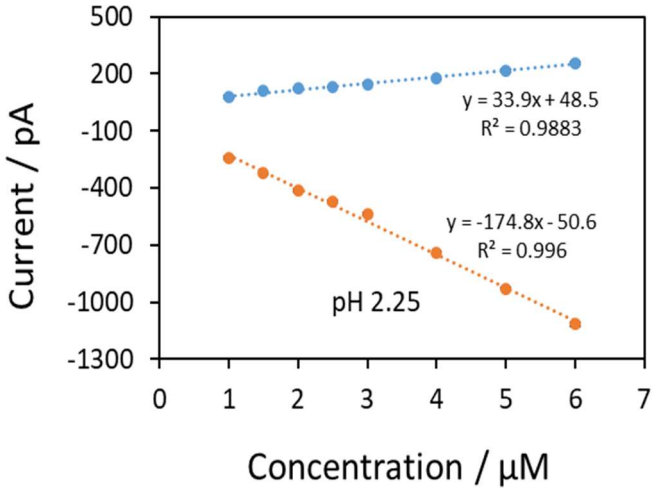

Figure 4.3.5.9: *Current vs concentration graph for both forward and reverse scan for PAMAM '3' at pH 2.25*

Figure 4.3.5.9 shows current vs concentration graph based on the steady state forward current (i_f) and reverse peak current (i_b) for different concentrations from Table 4.3.5.4. The currents on the forward sweeps as well as reverse sweeps of the background-subtracted CVs of dendrimer '3' at pH 2.25 increased linearly with the concentration of analyte and the peak current in the reverse phase is higher than the forward direction. In this case also current vs concentration relation follow the Saito equation [202] for the steady state current and the adsorption mechanism for the voltammetric peak. Diffusion coefficient (D) at this pH is 0.603 x 10^{-6} cm^2/s which is calculated from the forward current using Saito equation $I_{ss} = 4|z_i|FDCr$. Slope of current *vs* concentration is 33.9 pA/µM (Figure 4.3.5.9), charge is 62 for this pH which is calculated from the potentiometric titration curves at 0.1 M KCl of dendrimer G3 [244]. Radius of the pipette for this case was 23.5 µm.

CV at pH 1.75

Figure 4.3.5.10 (a) shows the voltammogram of blank with the 3 µM PAMAM '3' at pH 1.75. CV makes steady state voltammogram in forward direction which indicates a radial diffusion of PAMAM '3' ions [257] and the peak shape response in reverse direction indicating adsorption controlled behaviour of ions from organic to aqueous phase. The background subtracted CVs of different concentration range of 1.0 - 5.0 µM of dendrimer '3' are shown in Figure 4.3.5.10 (b). Forward scan starts ion transfer at potential ≈ 0.63 V and starts to become plateau at potential ≈ 0.68 V and the reverse

scan gives peak at ≈ 0.61 V. The calculated half wave potential ($E_{1/2}$) based on the forward scan is 0.66 V.

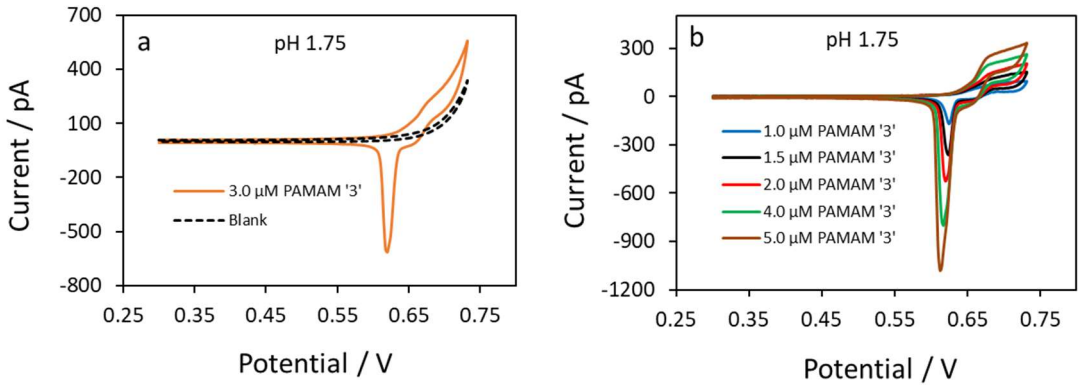

Figure 4.3.5.10: *(a) CV of 3 µM PAMAM '3' with blank and (b) background subtracted CV for 1, 1.5, 2, 4 & 5 µM PAMAM '3' at pH 1.75 with 25 µm radius pipette. [Pipette radius with Equations 2.3.1.2 and 2.3.1.3 are also given in Appendix B.]*

Table 4.3.5.5: *Steady state forward currents (i_f) and reverse peak currents (i_b) of three scans of CV for 1, 1.5, 2, 2.5, 3, 3.5, 4, 5 & 6 µM PAMAM '3' at pH 1.75*

C / µM	i_{f1} / pA	i_{f2} / pA	i_{f3} / pA	i_f / pA Average	σ	i_{b1} / pA	i_{b2} / pA	i_{b3} / pA	i_b / pA Average	σ
1.0	83	80	86	83	2.5	-171	-166	-177	-172	4.7
1.5	116	110	120	115	3.9	-260	-257	-264	-260	3.0
2.0	137	134	141	137	2.9	-405	-399	-411	-405	5.2
2.5	150	148	153	150	2.2	-471	-465	-476	-470	4.5
3.0	178	171	184	177	5.2	-620	-610	-626	-619	6.5
4.0	222	217	227	222	4.0	-803	-796	-808	-802	5.1
5.0	285	281	290	285	3.7	-1080	-1069	-1087	-1079	7.4
6.0	329	327	337	331	4.3	-1213	-1202	-1219	-1211	6.7

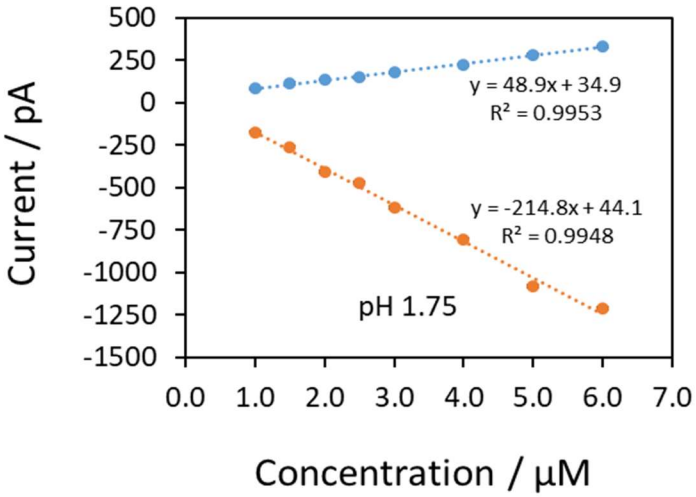

Figure 4.3.5.11: *Current vs concentration graph for both forward and reverse scan for PAMAM '3' at pH 1.75*

Current vs concentration graph based on the steady state forward current (i_f) and reverse peak current (i_b) for different concentrations was drawn (Figure 4.3.5.11) based on Table 4.3.5.5. The currents on the forward sweeps as well as reverse sweeps of the background-subtracted CVs of dendrimer '3' at pH 1.75 increased linearly with the concentration of analyte and the peak current in the reverse phase is higher than the forward direction. In this case also current vs concentration relation follow the Saito equation [202] for the steady state current and adsorption controlled for the voltammetric peak current. Diffusion coefficient (D) at this pH is 0.81 x 10^{-6} cm^2/s which is calculated from the forward current using Saito equation $I_{ss} = 4|z_i|FDCr$. Slope of current *vs* concentration is 48.9 pA/µM (Figure 4.3.5.11), charge is 37 for this pH which is calculated from the potentiometric titration curves at 0.1 M KCl of dendrimer G3 [244]. Radius of the pipette for this case was 25 µm.

CV at pH 9.0

After electrochemical investigation at low pH we also investigate it at higher pH. Figure 4.3.5.12 (a) shows the voltammogram of blank with the 3 µM PAMAM '3' at pH 9.0 a big response compare with response at pH 6.0 the peak shape indicates the forward direction is radial diffusion and reverse direction is linear diffusion transfer [257]. Figure 4.3.5.12 (b) shows the background subtracted CVs of different concentration range of 1.0 - 6.0 µM of dendrimer '3'. In this case the forward scan

starts ion transfer at potential ≈ 0.64 V and starts to become plateau at potential ≈ 0.68 V. The reverse scan gives peak at ≈ 0.62 V nearly for all concentrations. The calculated half wave potential ($E_{1/2}$) based on the forward scan is 0.66 V.

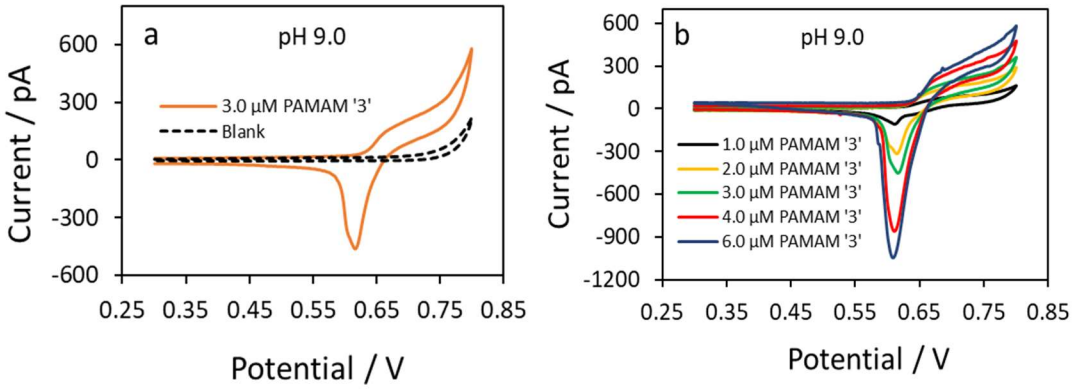

Figure 4.3.5.12: *(a) CV of 3 µM PAMAM '3' with blank and (b) background subtracted CV for 1, 2, 3, 4 & 6 µM PAMAM '3' at pH 9.0 with 26 µm radius pipette.* *[Pipette radius with Equations 2.3.1.2 and 2.3.1.3 are also given in Appendix B.]*

Table 4.3.5.6: *Steady state forward currents (i_f) and reverse peak currents (i_b) of three scans of CV for 1, 1.5, 2, 2.5, 3, 4, 5 & 6 µM PAMAM '3' at pH 9.0*

C / µM	i_{f1} / pA	i_{f2} / pA	i_{f3} / pA	i_f / pA Average	σ	i_{b1} / pA	i_{b2} / pA	i_{b3} / pA	i_b / pA Average	σ
1	79	74	84	79	3.7	-111	-104	-117	-111	5.1
1.5	112	109	116	112	3.0	-198	-191	-205	-198	5.8
2	148	140	156	148	6.4	-314	-308	-320	-314	4.9
2.5	171	165	178	171	5.0	-397	-390	-402	-396	4.8
3	205	199	212	205	5.5	-494	-482	-491	-489	5.1
4	260	255	266	260	4.6	-756	-739	-736	-744	8.9
5	304	294	311	303	7.1	-978	-966	-959	-968	7.6
6	321	326	329	326	3.3	-1088	-1025	-1047	-1053	26.1

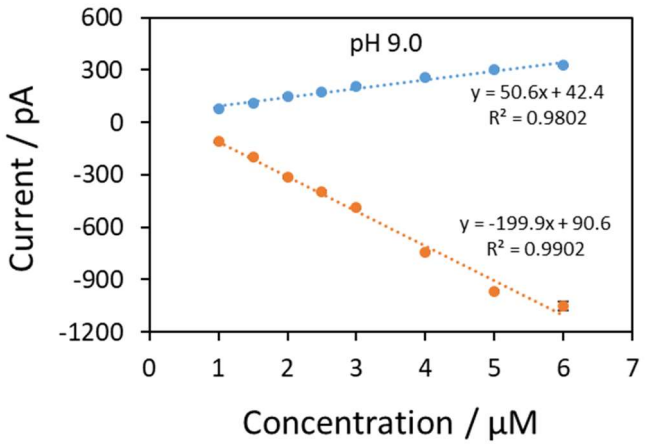

Figure 4.3.5.13: *Current vs concentration graph for both forward and reverse scan for PAMAM '3' at pH 9.0*

Figure 4.3.5.13 shows current vs concentration graph for steady state forward current (i_f) and reverse peak current (i_b) for different concentrations at pH 9.0 based on Table 4.3.5.6. The currents on the forward sweeps as well as reverse sweeps of the background-subtracted CVs of dendrimer '3' at this pH increased linearly with the concentration of analyte and the peak current in the reverse phase is higher than the forward direction. In this case also current vs concentration relation follow the Saito equation [202] for the steady state current and the Randles–Sevcik equation [80, 203] for the voltammetric peak current for linear diffusion systems. Diffusion coefficient (D) at this pH is 2.52 x 10^{-6} cm^2/s which is calculated from the forward current using Saito equation $I_{ss} = 4|z_i|FDCr$. Slope of current *vs* concentration is 50.6 pA/µM (Figure 4.3.5.13), charge is 20 for this pH which is calculated from the potentiometric titration curves at 0.1 M KCl of dendrimer G3 [244]. Radius of the pipette for this case was 26 µm.

CV at pH 10.0

The pH was again increased and at pH 10.0 the electrochemical response decreased. Figure 4.3.5.14 (a) shows the voltammogram of 3 µM PAMAM '3' with blank at pH 10.0. Electrochemical response in forward direction is radial diffusion controlled and reverse direction is controlled by linear diffusion transfer [257] of the ions. At this pH the ion transfers shifts to the higher potential. Figure 4.3.5.14 (b) shows the background subtracted CVs of different concentration range of 1.0 - 5.0 µM of

dendrimer '3'. In this case the forward scan starts ion transfer at potential ≈ 0.67 V and starts to become plateau at potential ≈ 0.71 V. The reverse scan gives peak at ≈ 0.66 V nearly for all concentrations. The calculated half wave potential ($E_{1/2}$) based on the forward scan is 0.69 V.

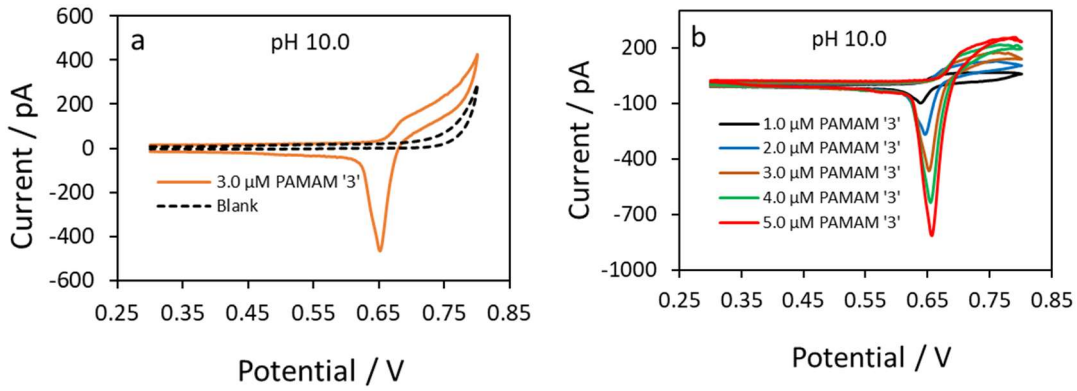

Figure 4.3.5.14: *(a) CV of 3 µM PAMAM '3' with blank and (b) background subtracted CV for 1, 2, 3, 4 & 5 µM PAMAM '3' at pH 10.0 with 27 µm radius pipette.* *[Pipette radius with Equations 2.3.1.2 and 2.3.1.3 are also given in Appendix B.]*

Table 4.3.5.7: *Steady state forward currents (i_f) and reverse peak currents (i_b) of three scans of CV for 1, 1.5, 2, 2.5, 3, 4, 5 & 6 µM PAMAM '3' at pH 10.0*

C / µM	i_{f1} / pA	i_{f2} / pA	i_{f3} / pA	i_f / pA Average	σ	i_{b1} / pA	i_{b2} / pA	i_{b3} / pA	i_b / pA Average	σ
1	67	61	71	66	3.9	-98	-92	-102	-97	4.2
1.5	97	92	100	96	3.5	-180	-173	-187	-180	5.7
2	123	119	128	123	3.7	-270	-262	-277	-269	6.0
2.5	150	146	155	150	3.6	-372	-364	-377	-371	5.4
3	169	163	175	169	4.8	-464	-458	-467	-463	3.6
4	200	195	205	200	4.0	-638	-634	-642	-638	3.3
5	233	229	238	234	3.7	-816	-801	-807	-808	6.3
6	274	267	280	274	5.5	-915	-930	-925	-923	6.0

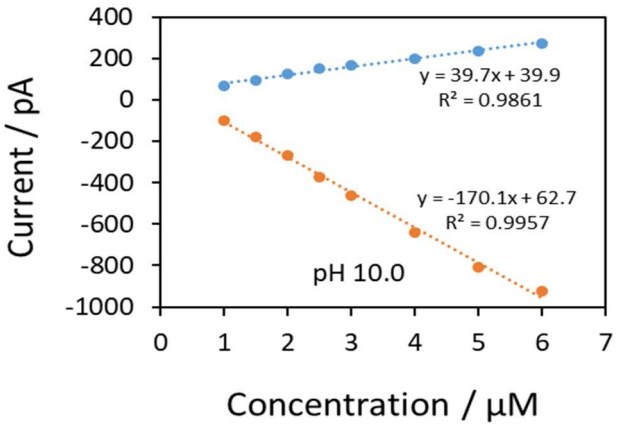

Figure 4.3.5.15: *Current vs concentration graph for both forward and reverse scan for PAMAM '3' at pH 10.0*

Figure 4.3.5.15 shows current vs concentration graph for steady state forward current (i_f) and reverse peak current (i_b) for different concentrations at pH 10.0 based on Table 4.3.5.7. The currents on the forward sweeps as well as reverse sweeps of the background-subtracted CVs of dendrimer '3' at this pH increased linearly with the concentration of analyte and the peak current in the reverse phase is higher than the forward direction. Current vs concentration relation follow the Saito equation [202] for the steady state current and the Randles–Sevcik equation [80, 203] for the voltammetric peak current for linear diffusion systems. Diffusion coefficient (D) at this pH is 9.6 x 10^{-6} cm^2/s which is calculated from the forward current using Saito equation $I_{ss} = 4|z_i|FDCr$. Slope of current *vs* concentration is 39.7 pA/µM (Figure 4.3.5.15), charge is 4 for this pH which is calculated from the potentiometric titration curves at 0.1 M KCl of dendrimer G3 [244]. Radius of the pipette for this case was 27 µm.

CV at pH 11.0

The potential vs current response again decreased at very high pH 11. Figure 4.3.5.16 (a) shows the voltammogram of 5 µM PAMAM '3' with blank at pH 11. Electrochemical response in forward direction is radial diffusion controlled and flow if ions in the reverse direction is linear diffusion controlled [257]. At this pH the ion transfers shifts to the higher potential significantly. Figure 4.3.5.16 (b) shows the background subtracted CVs of different concentration range of 1.0 - 6.0 µM of dendrimer '3'. In this case the forward scan starts ion transfer at potential ≈ 0.73 V and starts to become plateau at potential ≈ 0.77 V. The reverse scan gives peak at ≈ 0.72 V

nearly for all concentrations. The calculated half wave potential ($E_{1/2}$) based on the forward scan is 0.74 V.

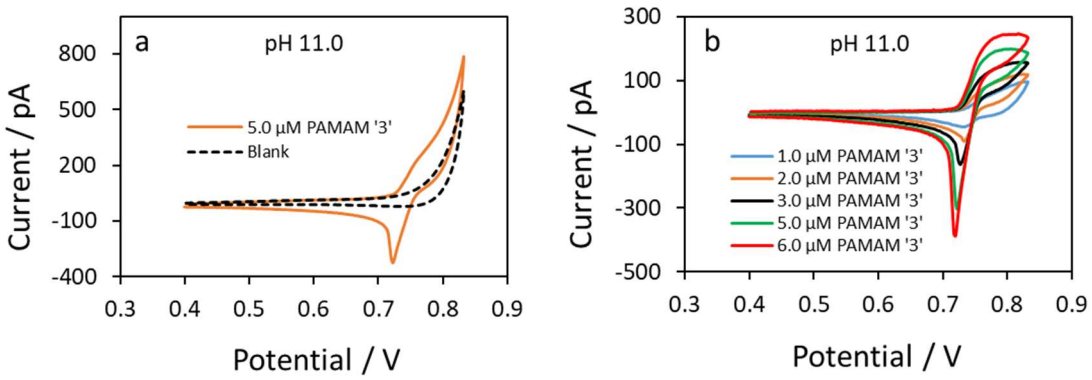

Figure 4.3.5.16: *(a) CV of 5 µM PAMAM '3' with blank and (b) background subtracted CV for 1, 2, 3, 5 & 6 µM PAMAM '3' at pH 11.0 with 27 µm radius pipette.*

[Pipette radius with Equations 2.3.1.2 and 2.3.1.3 are also given in Appendix B.]

Table 4.3.5.8: *Steady state forward currents (i_f) and reverse peak currents (i_b) of three scans of CV for 1, 2, 3, 4, 5 & 6 µM PAMAM '3' at pH 11.0*

C / µM	i_{f1} / pA	i_{f2} / pA	i_{f3} / pA	i_f / pA Average	σ	i_{b1} / pA	i_{b2} / pA	i_{b3} / pA	i_b / pA Average	σ
1	58	42	46	49	6.8	-45	-38	-47	-43	3.7
2	76	72	81	76	3.6	-89	-86	-94	-90	3.2
3	107	104	109	107	2.2	-163	-158	-168	-163	4.0
4	149	140	142	144	3.6	-237	-233	-242	-237	3.6
5	178	176	182	178	2.4	-306	-298	-311	-305	5.6
6	235	221	235	230	6.6	-387	-380	-396	-388	6.3

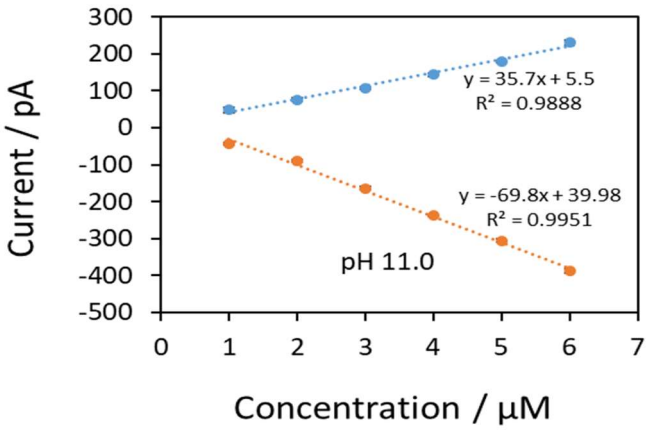

Figure 4.3.5.17: *Current vs concentration graph for both forward and reverse scan for PAMAM '3' at pH 10.0*

Figure 4.3.5.17 shows current vs concentration graph for steady state forward current (i_f) and reverse peak current (i_b) for different concentrations at pH 11.0 based on data in Table 4.3.5.8. The currents on the forward sweeps as well as reverse sweeps of the background-subtracted CVs of dendrimer '3' at this pH increased linearly with the concentration of analyte and interestingly the peak current in the reverse phase at this pH is nearly same to forward current. Current vs concentration relation follow the Saito equation [202] for the steady state current and the Randles–Sevcik equation [80, 203] for the voltammetric peak current for linear diffusion systems. Diffusion coefficient (D) at this pH is 17.1 x 10^{-6} cm^2/s which is calculated from the forward current using Saito equation $I_{ss} = 4|z_i|FDCr$. Slope of current *vs* concentration is 35.7 pA/μM (Figure 4.3.5.17), charge is 2 for this pH which is calculated from the potentiometric titration curves at 0.1 M KCl of dendrimer G3 [244]. Radius of the pipette for this case was 27 μm.

Comparison of CVs of PAMAM '3' at different pH

Figure 4.3.5.18 shows the background subtracted CVs of Dendrimer '3' at different pH. The shape of the CV for forward potential are nearly same whereas lots of variation observed in the reverse direction. From the Figure 4.3.5.18 it is clearly seen that the reverse peak current from pH 6.0 to pH 11.0 are diffusion controlled and on the other hand at lower pH from 3.5 the reverse peak current follows adsorption mechanism like PAMAM '2'. In general the current response increased as the pH go down more. Again as like PAMAM '2' at higher pH the current response increased with pH except at pH 11.0. At higher pH the ion transfer shifts to the higher potential. The Figure shows the ion transfer shifts to the higher potential at pH 10 and again shifts much higher potential at pH 11. Whereas for other pH ions transfer nearly at same potential. The small variation of the shape of the CVs may be because of the different shape of the pipettes and/or for the different time & environment of the experiment.

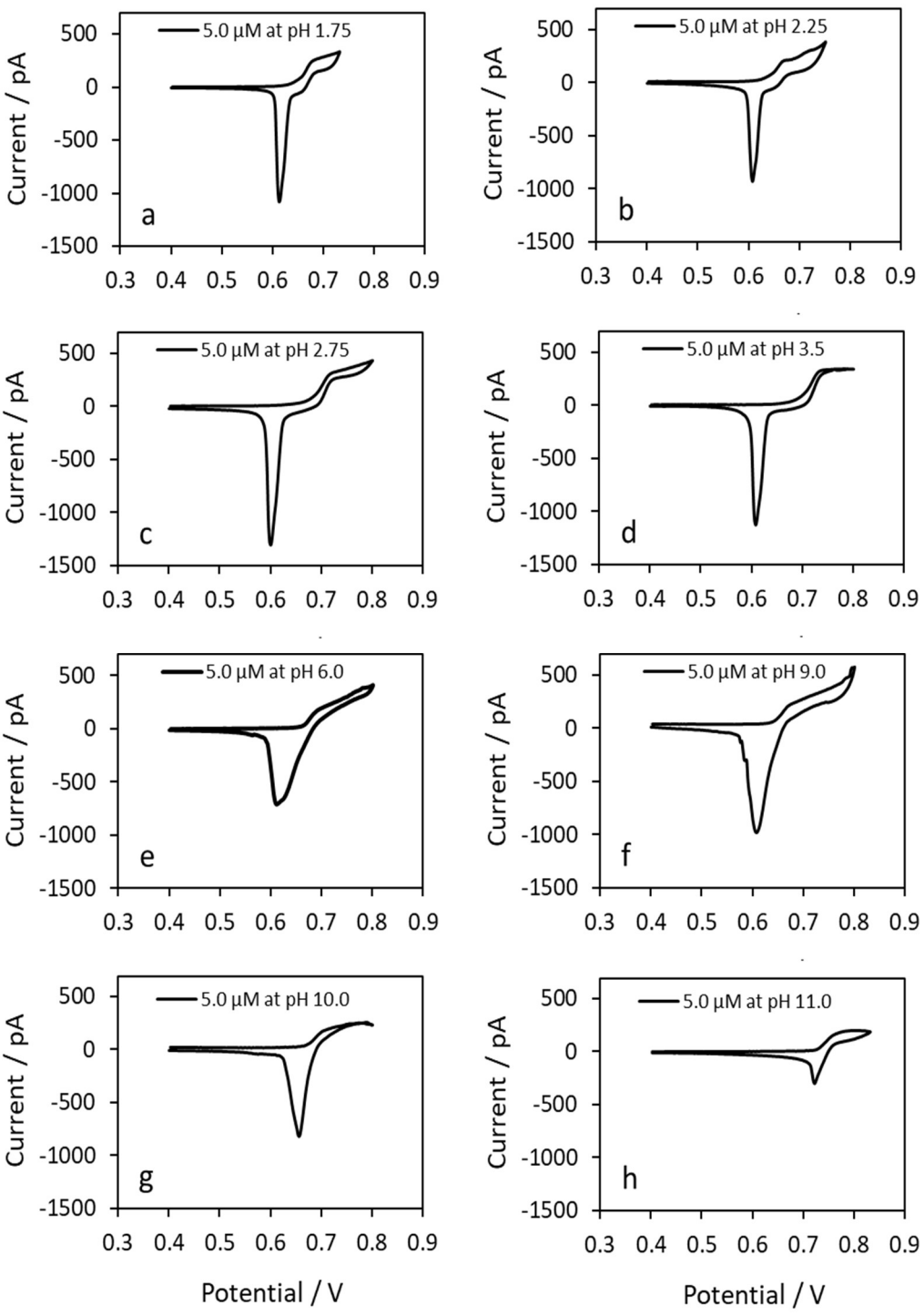

Figure 4.3.5.18: *Background subtracted CVs of 5 µM dendrimer '3' at (a) pH 1.75 (b) pH 2.25 (c) pH 2.75 (d) pH 3.5 (e) pH 6.0 (f) pH 9.0, (g) pH 10.0 and (h) pH 11.0*

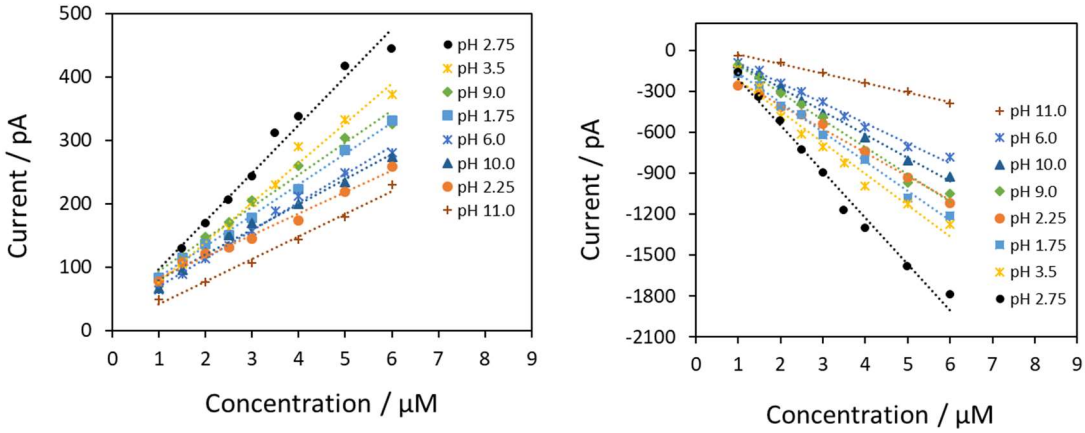

Figure 4.3.5.19: *Current vs concentration graph for PAMAM '3' at pH 1.75, 2.25, 2.75, 3.5, 6.0, 9.0, 10.0 and 11.0 for (a) forward scan and (b) reverse scan.*

Table 4.3.5.9: *Diffusion coefficient (D), charge and slope of the regression line at different pH for PAMAM '3'.*

		pH 1.75	**pH 2.25**	**pH 2.75**	**pH 3.5**	**pH 6.0**	**pH 9.0**	**pH 10**	**pH 11**
D x 10^{-6} / cm^2s^{-1}		0.81	0.60	1.27	1.15	1.32	2.52	9.60	17.1
Charge		62	62	62	60	37	20	4	2
Slope pA/µM	**forward**	48.9	33.9	75.8	62.6	44.2	50.6	39.7	35.7
	reverse	-214	-173	-339	-230	-148	-200	-170	-70

Figure 4.3.5.19 shows the current verses concentration for both forward and reverse directions at different pH. It shows that PAMAM '3' gives very high electrochemical response at very low pH. The highest response for both forward and reverse directions are for pH 2.75 and then for pH 3.5. The electrochemical response at pH 9.0 is also higher than the normal lithium chloride solution of pH 6.0. After that with the increase of pH the response decreased and give lowest response at pH 11.0, which is also big response. The Table 4.3.5.9 shows how the diffusion coefficient, charge and slope changes with pH. According to p*Ka* and protonation mechanism, it is assumed that at lower pH the current will be high also. However, for G0 and G1 at lower pH response was low. Again, for the high pH the response increased which is also unusual because the charge decrease with increase of pH (Table 4.3.4.9).

The general electrochemical trend with this CV experiments shows that the lower generation PAMAM (G0 & G1) follows diffusion controlled mechanism for both directions at all pH. Both of this PAMAM do not give any electrochemical response at very high and very low pH. On the other hand G2 & G3 follows adsorption mechanism for reverse peak at lower pH (3.5 to 1.75) and shows very high electrochemical response for both low and high pH.

4.3.6. Diffusion coefficient

The diffusion coefficient (D) for all four generations (G0 – G4) are summarised in Table 4.3.6.1. From that data we can see that the D varies with the change of pH and also varies with generation. It is assumed that the D will be decrease with the increase of molecular size. From our experiment we can also see this trend (Table 4.3.6.1 and Figure 4.3.6.1). We analyse the D in large variation of pH scale which gives very important findings as well. From Figure 4.3.6.1 we can see that with the increase of pH, D increases and the increase rates are nearly same for all four generations.

Table 4.3.6.1: *Diffusion coefficients of PAMAM dendrimer generations G0 to G3 at different pH*

Dendrimer	**Diffusion coefficient (D) x 10^{-6} / cm^2s^{-1}**							
	pH 1.75	**pH 2.25**	**pH 2.75**	**pH 3.5**	**pH 6.0**	**pH 9.0**	**pH 10.0**	**pH 11.0**
G0			2.45	3.32	3.7	4.06		
G1	1.53	1.37	1.55	1.99	2.41	3.22		
G2	1.35	1.47	1.17	0.87	1.83	2.91	9.30	15.7
G3	0.81	0.60	1.27	1.15	1.32	2.52	9.60	17.1

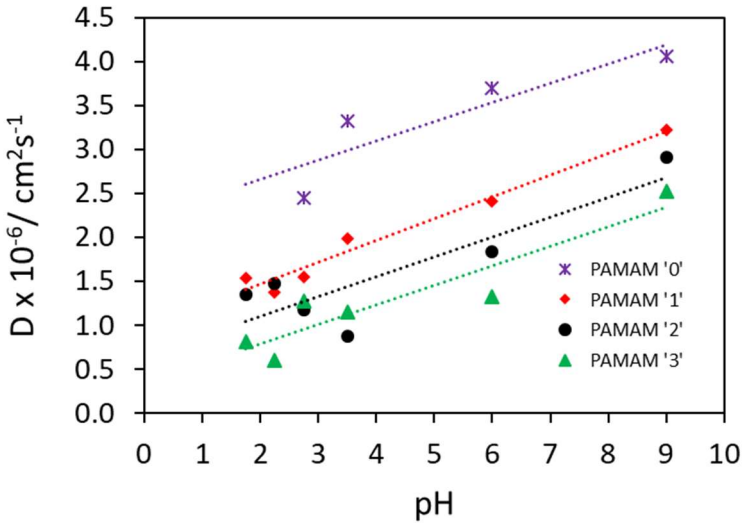

Figure 4.3.6.1: *Diffusion coefficient vs pH for PAMAM dendrimer generations G0, G1, G2 amd G3*

From the data in Table 4.3.6.1 shows that D increase at regular rate up to pH 9.0. After that for G2 & G3 the diffusion coefficient suddenly increased by many folds for pH 10 & pH 11. After pH 9 the dendrimers becomes nearly neutral. So, from these dada we can say that the diffusion coefficient is low at high protonated state and high at low protonated state. For neutral dendrimer it becomes very high. This investigation is very much consistent with published data though there is no published data for D with lots of pH variation. Veronica, Jose and Joel calculated diffusion coefficients for G0 - G3 by DOSY-NMR spectroscopy in infinite dilution aqueous solution at high and neutral pH Their calculated diffusion coefficients are 3.13, 2.14, 1.32, 0.82 x 10^{-6} cm^2s^{-1} for G0 - G3 respectively at pH 7 [258]. Those values are very close to our calculated diffusion coefficients at pH 6.

4.4 Differential Pulse Voltammetry (DPV)

We already saw that CV is a very good technique to detect and characterise dendrimers of different generations with micropipette ITIES. CV revels the response mechanism as well as dendrimers diffusion coefficient if it is diffusion controlled. The detection limit (LOD) by CV experiment for PAMAM '0', PAMAM '1', PAMAM '2' and PAMAM '3' was 0.44 µM, 0.24 µM, 0.71 µM and 0.46 µM respectively at pH 3.5. To improve the detection limit (LOD) and sensitivity of the analyte we use more Differential Pulse Voltammetry which is more sensitive voltammetric technique. DPV gives sharper and better defined peaks and improved signal changes for the change of pH at a lower concentration compared to cyclic voltammetry with a lower charging current and improved resolution. For this reason, it helps to elucidate the electrochemical properties more precisely, easily and clearly. In this case, DPV was carried out in forward scanning from 0.5 V to 0.78 V, because in forward direction it gives a better response than the reverse direction (Figure 4.4.1). pH of the solution for DPV experiments for all PAMAM dendrimers was 3.5. Because G0 & G1 gives highest response at this pH and G2 & G3 also give very good response at pH 3.5. The conditioning potential, equilibrium time, step potential, modulation amplitude, modulation time and interval time were 0.1 V, 30 s, 0.005 V, 0.05, 0.04 s and 0.5 s respectively. The analyte sample was added from a stock solution 0to aqueous phase. In the beginning, a blank experiment (without analyte) was recorded and then the background subtraction procedure was applied to further increase the sensitivity of the technique. The LOD calculation was done by (3 x σ) / S formula [201], where S is the slope of the calibration curve and σ is the standard deviation of the y-intercept of the regression line. The values of σ and S was obtained by using the LINEST function in Excel as like as CV experiment. LINEST function calculates the statistics of a simple line equation (Y = mx + C) which also explains the

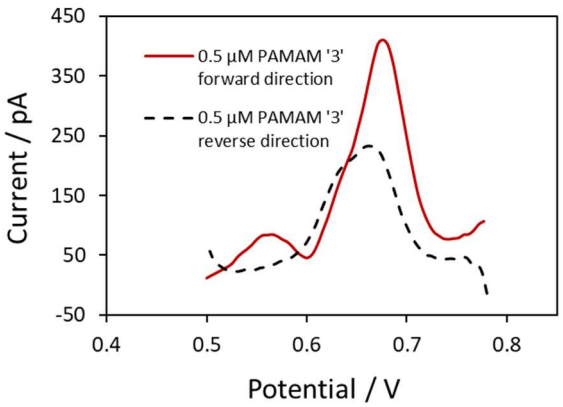

Figure 4.4.1: *DPV of PAMAM '3' in two different directions*

relationship between the dependent and independent variables using the least square procedure to find the best solution for data used.

4.4.1 Differential Pulse Voltammetry of PAMAM '0'

The lowest concentration of PAMAM '0' detected was 0.2 µM using background-subtracted DPV. Figure 4.4.1.1 and 4.4.1.2 shows the voltammograms and calibration curve obtained for the PAMAM '0' concentrations ranging from 0.2 µM to 0.9 µM respectively. Voltammograms exhibits that the peak current increased linearly as the dendrimer concentration increased.

Good linearity in the studied concentration range can be seen in Figure 4.4.1.2 for the peak currents obtained as a function of the PAMAM '0' concentration. The linear regression line (y = mx + c) of best fit shows that the slope, y-intercept, regression coefficient (r^2), standard deviation of slope (STD_{slope}), standard deviation of y-intercept ($STD_{y\text{-}intercept}$) and standard deviation of the regression line (STDy) of this equation are 117.8, -7.5, 0.99, 4.3, 2.8 and 3.3 respectively. The limit of detection (LOD) calculated from these data was found 0.07 µM, whereas the LOD from CV experiment for the same size interface was 0.44 µM. So, DPV gives nearly 6 times lower detection limit than CV for PAMAM '0' detection.

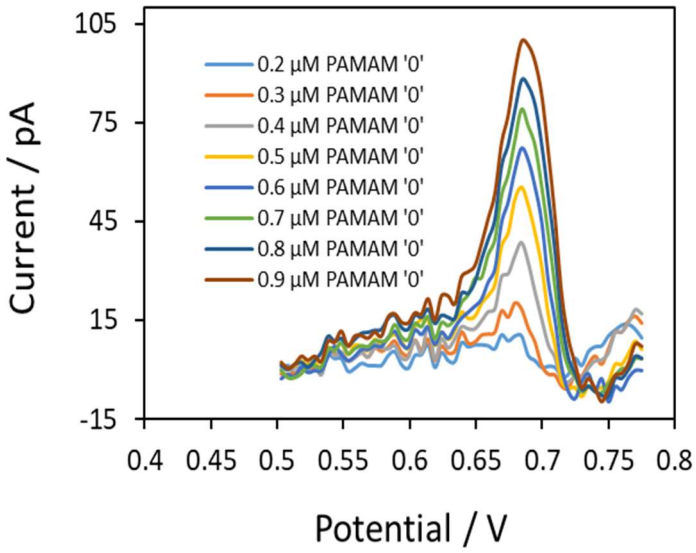

***Figure 4.4.1.1**: Background subtracted DPV of 0.2, 0.3, 0.4, 0.5, 0.6, 0.7, 0.8 and 0.9 µM PAMAM '0' at 25 µm radius interface. [Pipette radius with Equations 2.3.1.2 and 2.3.1.3 are also given in Appendix B.]*

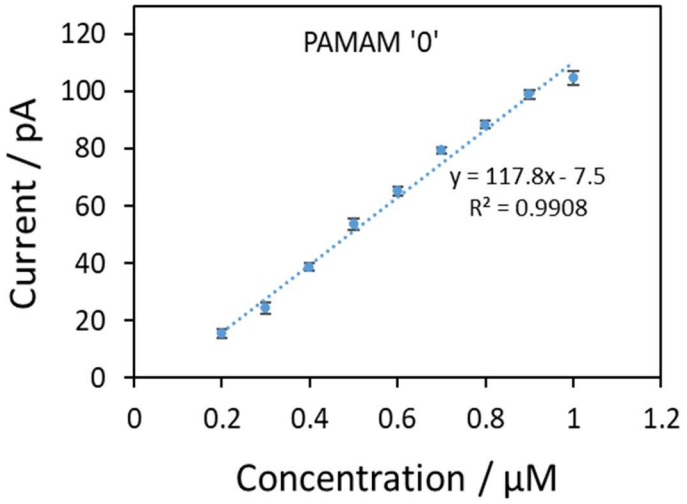

Figure 4.4.1.2: *Current vs concentration graph of 0.2, 0.3, 0.4, 0.5, 0.6, 0.7, 0.8, 0.9 and 1.0 µM PAMAM '0'.*

4.4.2 Differential Pulse Voltammetry of PAMAM '1'

For the case of PAMAM '1', the lowest concentration detected 0.2 µM using background subtracted DPV. Figure 4.4.2.1 shows the background subtracted voltammograms for the PAMAM '1' which exhibits the peak current increased linearly as the concentration increased ranging from 0.2 µM to 1.0 µM. The current response is higher compare to CV experiments.

Calibration graph in that concentration range also shows good linearity obtained for the peak currents *vs* concentration (Figure 4.4.2.2). The liner regression line (y) of best fit shows that the slope, y-intercept, regression coefficient (r^2), standard deviation of slope (STD_{slope}), standard deviation of y-intercept ($STD_{y\text{-}intercept}$) and standard deviation of the regression line (STDy) of this equation are 150.9, -5.3, 0.995, 3.98, 2.6 and 3.1 respectively. The limit of detection (LOD) calculated from these data was found 0.05 µM, whereas the LOD from CV experiment for the same size interface was 0.24 µM. So, DPV gives nearly 5 times low detection limit than CV for PAMAM '1' detection.

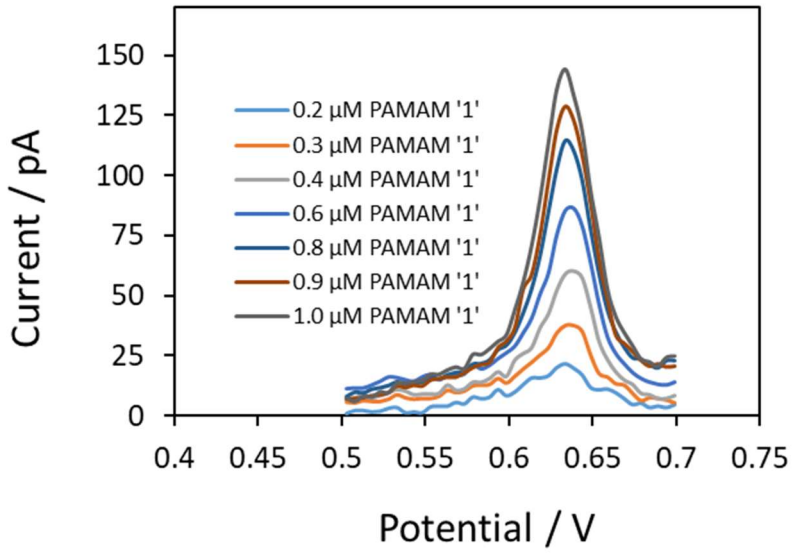

Figure 4.4.2.1: *Background subtracted DPV of 0.2, 0.3, 0.4, 0.6, 0.8, 0.9 and 1.0 µM PAMAM '1' at 25 µm radius interface. [Pipette radius with Equations 2.3.1.2 and 2.3.1.3 are also given in Appendix B.]*

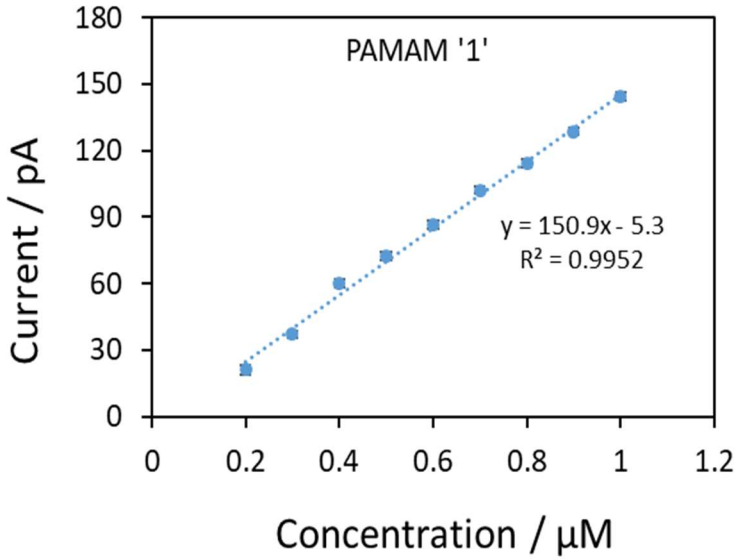

Figure 4.4.2.2: *Current vs concentration graph of 0.2, 0.3, 0.4, 0.5, 0.6, 0.7, 0.8, 0.9 and 1.0 µM PAMAM '1'.*

4.4.3 Differential Pulse Voltammetry of PAMAM '2'

In the case of PAMAM '2' the lowest concentration was detected by DPV is 0.3 µM. Figure 4.4.3.1 shows the background subtracted voltammograms obtained for the PAMAM '2' concentrations ranging from 0.2 µM to 1.0 µM where the peak current increased linearly with the increase of concentration. Calibration curve shows (Figure 4.4.3.2) good linearity in the studied concentration range seen for the peak currents obtained as a function of the concentration. For PAMAM '2' the liner regression line (y) of best fit shows that the slope, y-intercept, regression coefficient (r^2), standard deviation of slope (STD_{slope}), standard deviation of y-intercept ($STD_{y\text{-}intercept}$) and standard deviation of the regression line (STD_y) of this equation are 549.7, -19.2, 0.986, 24.3, 15.9 and 18.8 respectively. The limit of detection (LOD) calculated for PAMAM '2' by DPV was found 0.09 µM. LOD from CV experiment for the same size interface was 0.72 µM. So, DPV gives 8 times low detection limit than CV for PAMAM '2' detection.

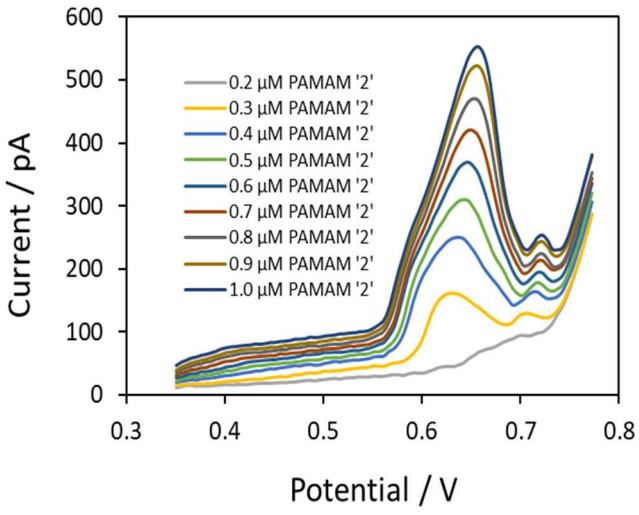

Figure 4.4.3.1: *Background subtracted DPV of 0.2, 0.3, 0.4, 05, 0.6, 0.7, 0.8, 0.9 and 1.0 µM PAMAM '2' at 22 µm radius interface. [Pipette radius with Equations 2.3.1.2 and 2.3.1.3 are also given in Appendix B.]*

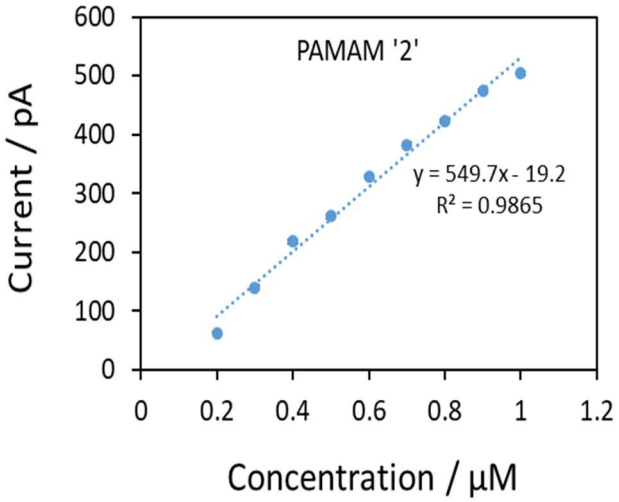

Figure 4.4.3.2: *Current vs concentration graph of 0.2, 0.3, 0.4, 0.5, 0.6, 0.7, 0.8, 0.9 and 1.0 µM PAMAM '2'.*

4.4.4 Differential Pulse Voltammetry of PAMAM '3'

The lowest concentration of PAMAM '3' detected was 0.1 µM using background subtracted DPV. Figure 4.4.4.1 and 4.4.4.2 shows the voltammograms and calibration curve obtained for the PAMAM '0' concentrations ranging from 0.1 µM to 1.0 µM respectively. Voltammograms exhibits that the peak current increased linearly as the dendrimer concentration increased.

Good linearity in the studied concentration range can be seen in Figure 4.4.4.2 for the peak currents obtained as a function of the PAMAM '3' concentration. The liner regression line (y) of best fit shows that the slope, y-intercept, regression coefficient (r^2), standard deviation of slope (STD_{slope}), standard deviation of y-intercept ($STD_{y\text{-}intercept}$) and standard deviation of the regression line (STDy) of this equation are 479.1, 7.02, 0.99, 23.2, 12.9 and 18.0 respectively. The limit of detection (LOD) calculated from these data was found 0.08 µM, whereas the LOD from CV experiment for the same size interface was 0.46 µM. So, DPV gives nearly 6 times low detection limit than CV for PAMAM '3' detection.

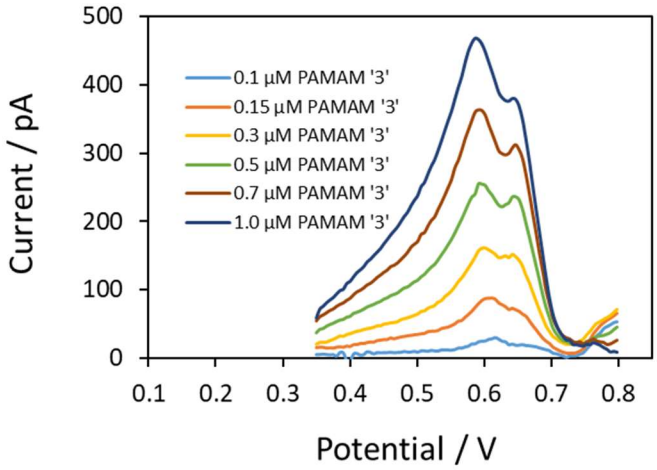

Figure 4.4.4.1: *Background subtracted DPV of 0.1, 0.15, 03, 0.5, 0.7, and 1.0 µM PAMAM '3' at 22 µm radius interface. [Pipette radius with Equations 2.3.1.2 and 2.3.1.3 are also given in Appendix B.]*

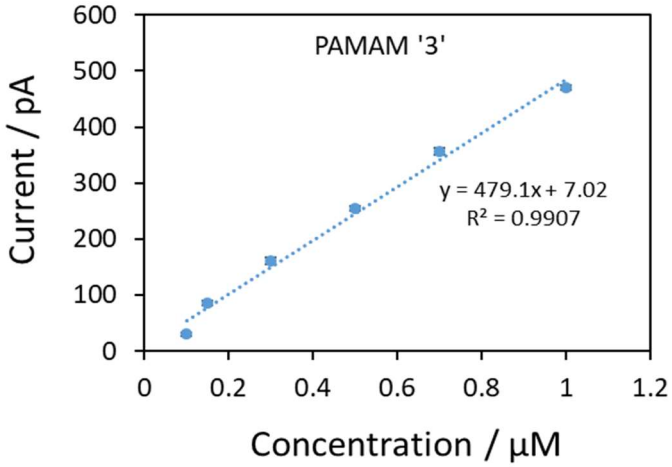

Figure 4.4.4.2: *Current vs concentration graph of 0.1, 0.15, 03, 0.5, 0.7, and 1.0 µM PAMAM '3'.*

Table 4.4.4.1: *LOD of PAMAM dendrimer generations G0 to G3.*

Analyte	LOD by CV (µM) (3 x $STD_{intercept}$)/slope	LOD by DPV(µM) (3 x $STD_{intercept}$)/slope
PAMAM '0'	0.44	0.07
PAMAM '1'	0.24	0.05
PAMAM '2'	0.72	0.09
PAMAM '3'	0.46	0.08

4.5 Conclusions

This is the first time electrochemical investigation of four generations of PAMAM dendrimers at ITIES formed at micropipettes over a wide range of pH. In this analysis we focused on how different generations of dendrimers changed their electrochemical propertied with pH. Because each dendrimer has amine groups which are protonated in aqueous solution at different pH, according to the p*Ka* value of that particular amino group, this makes them enable to transfer across the interface. Cyclic voltammetry nicely detects the PAMAM dendrimers and gives important information about the transfer mechanism, kinetic parameters like diffusion coefficient. This CV analysis shows that the transfer from aqueous to organic for all generation dendrimers follow diffusion mechanism at all pH. In contrast, transfer from organic to aqueous phase for G2 & G3 at pH 3.5 to more lower pH follow adsorption mechanism and show diffusion controlled transfer for pH 6.0 to higher pH. But G0 & G1 follow diffusion mechanism for reverse transfer at all pH. Electrochemical response for G0 & G1 is found better at pH 3.5 and this two low generation dendrimers do not show any response at very high or at very low pH. On the other hand, G2 & G3 show better response at lower pH at 1.75 and 2.75 respectively. Sometimes higher generation dendrimer does not follow a general trend for an analysis, which may be because of their larger size and much more charges on it makes them more complicated than lower generations. Previous studies also found that sometimes the charges of the higher generation dendrimers were neutralized by electrolyte anions from the aqueous phase which could be a reason for variation from a general trend [250]. Another important observation shows that generally the diffusion coefficient follows a trend with the change of pH and with different generation dendrimers. Analysis shows D increases gradually with the increase of pH and decreases with the increase of generation within the same pH. CV analysis gives a LOD range 0.24 – 0.72 μM for G0 to G3, whereas DPV analysis gives 5 to 8 times lower LOD (0.05 – 0.09 μM) which is very impressive compared to previous published data [250]. There are lots of opportunities for further study on the electrochemical behaviour of these dendrimers based on charge-transfer at ITIES.

Chapter 5

Electrochemical Detection of Sulphate Ions.

5.1 Introduction

Sulphate is one of the leading species in aquatic environments. Sulphate concentration increases in water and the atmosphere from different sources. Some of the major sources are sulphate salts in soil because of their high solubility, decaying plant and animal matter, chemical products like fertilizer, insecticides and industrial by-products or untreated effluents. Acidification of water bodies indicates the increasing of sulphate levels in water which causing a serious health concerns [259, 260]. That is why scientists are trying to develop a precise and consistent method for sulphate ion detection and measurement. However, the design of anion receptors is more challenging than that of cation receptors because of their various geometries, varying protonation states at different pH values and their often comparably low charge to radius ratio [261-264]. For example, ionophores for sulphate are of interest as this double negatively charged oxoanion is challenging to extract from water due to its large hydration energy [265].

Current methods for sulphate detection have several problems like being time consuming, not adequate for low concentrations, laboriousness and insufficient selectivity and poor reproducibility. For example ion chromatography (IC) is a common method for the determination of sulphate in aqueous samples up to $\geq 1.5 \times 10^{-6}$ M (144 ng ml^{-1}) [263] but it is expensive and time consuming. Capillary electrophoresis is also very complex and require high equipment cost [266, 267]. Park and Simmons started experiments of anion coordination chemistry to develop macrobicyclic ammonium cages for halide anions [268] and the interaction of the methoxide anion with a diboron ligand was reported by Shriver and Biallas [269]. Recently scientists focused on colorimetry [270] and fluorimetry [271, 272] for sensor development to detect the anions like sulphate. In some cases they used cysteine-modified gold nanoparticles for catalytic reactions [273]. Similarly, for photochemical measurements in the presence of pH sensitive chromoionophores, polystyrene microspheres have been used to support ionophores [274].

Ion-selective electrodes (ISEs) especially with ion carriers in polymeric membrane are now established as a strong analytical tools for analysis because of their several advantages, such as robustness, simple preparation method, better selectivity, wide range of concentration and also low cost [275, 276]. The ionophore can interact

specifically with the particular analyte and the response is measured as the electromotive force (EMF) relative to the activity of the ion of interest. A range of ionophores based on guanidinium [277], ferroceneamide [278], polyazacycloalkane [279], tris-urea [280, 281], bis-thiourea [281, 282] and squaramide [283, 284] recognition groups have been designed for sulphate detection in ISE membranes.

Very few investigations have been conducted for anion detection by dynamic electrochemistry at the interface formed between two immiscible electrolyte solutions (ITIES). Ion transfer (IT) and facilitated ion transfer (FIT) processes at the ITIES could be a promising method for anion detection. For example, to assist the transfer of monovalent anions at water/dichloroethane microinterfaces, a calix-pyrrole ligand was used by Shao's group [149]. Calixarenes with bis-thiourea moieties were implemented at the ITIES for phosphate [285, 286] and sulphate [287] recognition, while Dryfe's group [288] employed cholapod receptors to investigate halides by FIT at the ITIES.

The aim of this work was to electrochemically characterise some new squaramide sulphate ionophores at water/o-nitrophenyloctylether (W/NPOE) interface developed in micropipette tips. Earlier the micro-ITIES array was employed to study the ionophore-facilitated sulphate transfer at the W/NPOE interface using the commercially available ionophore 1,3-[Bis(3-phenylthioureidomethyl)]benzene [289], which has been used previously in ISEs and in the dropping electrolyte ITIES format [282, 290].

5.2 Experimental

5.2.1 Reagents

All the reagents were purchased from Sigma-Aldrich Australia Ltd. and used as received unless otherwise indicated. The organic electrolyte bis(triphenylphosphoranylidene)ammonium tetrakis(4-chlorophenyl)borate (BTPPATPBCl) was prepared by metathesis of equimolar amounts of bis(triphenylphosphoranylidene)ammonium chloride (BTPPACl) and potassium tetrakis(4-chlorophenyl)borate (KTPBCl) as reported earlier [77]. BTPPATPBCl (0.01 M) solutions were prepared in o-nitrophenyloctylether (NPOE) in the presence or absence of the ionophores. Commercial sulphate ionophore 1,3-[Bis(3-phenylthioureidomethyl)] benzene was from Sigma and the new ionophores tren-

bCF_3, TEB-tri-bCF_3 and TEB-bis-CF_3 were supplied from the School of Chemistry, University of Sydney (group of Prof. K. A. Jolliffe). Tetrahydrofuran (THF) was used to dissolve the ionophores in NPOE. Chlorotrimethylsilane was used for silanization of pipettes. All aqueous solutions (like LiCl, Li_2SO_4) were prepared in purified water from a USF Purelab plus UV (resistivity: 18.2 MΩ cm).

5.2.2 Electrochemical cell

Electrochemical measurements were conducted by using an Autolab PGSTAT302N electrochemical analyser (Metrohm Autolab, Utrecht, The Netherlands) running with NOVA software. The pipettes for the experiments for this chapter were prepared, modified and characterized according to the section 3.3.2 in chapter 3. The organic electrolyte phase was introduced into the pipette which comes up to the tip and the organic reference solution (saturated BTPPACl in 10 mM LiCl) was placed on the top of the organic phase. The ionophores were not dissolved directly in the organic phase NPOE. First the ionophores were dissolved in THF and then added to the NPOE. After that the THF was removed by using vacuum desiccator as THF is a volatile substance. Then the pipette was immersed into the aqueous phase so that an ITIES form at the tip of the pipette. As this was a miniaturized interface, so a two-electrode system was employed for this electrochemical cell. A polished Ag wire was in the aqueous solution and Ag/AgCl electrode used in the organic reference solution. The micro-interface was polarised by imposing a potential difference between these two electrodes. Unless stated 10 mVs^{-1} scan rate was applied to carried out cyclic voltammetry (CV). The cell is described in the following scheme.

$$\mathrm{Ag}\left|\mathrm{AgCl}\right|\begin{array}{c}\text{Sat'd BTPPACl}\\ \text{in 10 mM LiCl}\end{array}\left|\begin{array}{c}\text{10 mM BTPPATPBCl \& 0.25}\\ \text{mM ionophore in NPOE}\end{array}\right|\left|\text{x mM } Li_2SO_4\right|\mathrm{Ag}$$

Tetraethylammonium (TEA^+) ion was used as an internal reference to determine the halfwave and formal transfer potentials on the Galvani potential scale using equation 5.2.2.1.

$$\Delta_o^w\phi_{1/2,\ A^{z-}(exp)} - \Delta_o^w\phi_{A^{z-}}^{o'} = \Delta_o^w\phi_{1/2,\ TEA^+(exp)} - \Delta_o^w\phi_{TEA^+}^{o'} \qquad \text{(Eq. 5.2.2.1)}$$

where $\Delta_o^w\phi_{1/2,\ A^{z-}(exp)}$ and $\Delta_o^w\phi_{1/2,\ TEA^+(exp)}$ are the experimental half-wave potentials, while $\Delta_o^w\phi_{A^{z-}}^{o'}$ and $\Delta_o^w\phi_{TEA^+}^{o'}$ are the formal transfer potentials of the anion

A^- and TEA^+ respectively. $\Delta_o^w\phi_{TEA^+}^{o'}$ was calculated as -3 mV [291] based on the tetraphenylarsonium tetraphenylborate (TATB) for W/NPOE interfaces and all the data in this chapter reported on the Galvani scale.

5.3 Result and Discussions

5.3.1 Cyclic voltammetry experiment with tri-squaramide tren-bCF$_3$ ionophore

Figure 5.3.1.1 shows the structure of new synthesized squaramide ionophore tren-bCF$_3$ and Figure 5.3.1.2 illustrates the facilitated transfer of sulphate anions with this ionophore from the aqueous phase (8.0 mM SO_4^{-2} ion) to the organic phase at 25 µm radius tip. 0.25 mM ionophore was introduced in the organic phase for this process. This sulphate ion transfers with the formation of ionophore-sulphate complex under electrochemical control. Figure 5.3.1.2 (a) shows the voltammograms of 8 mM sulphate ions and for the background electrolytes. Figure 5.3.1.2 (b) shows the background subtracted cyclic voltammogram (CV). The potential axis was calibrated with TEA^+. If a cation transfer from aqueous phase to organic phase or an anion transfer from the organic phase to the aqueous phase, then by convention, the transfer current is defined as positive current. Similarly, a negative current is defined as transfer of a cation from the organic phase to the aqueous phase or an anion from the aqueous phase to the organic phase [2]. Therefore, increase the negative current at -0.24 V is recognized as the ionophore-facilitated transfer of sulphate from water to organic phase (Figure 5.3.1.2a). As this transfer of ions produced a peak shape voltammogram in the forward sweep, the result suggest an interfacial complexation between sulphate and the ionophore, where the ionophore transfers to the interface linearly inside the pipette. This ion transfer process is controlled by the ionophore concentration in the organic phase (0.25 mM) as its concentration is much lower (32 times) than the concentration of sulphate (8.0 mM) in the aqueous phase.

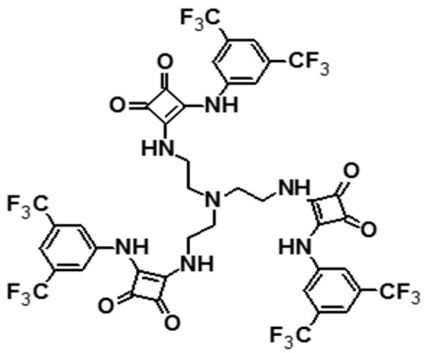

Figure 5.3.1.1: *Structure of tri-squaramide sulphate ionophore Tren-bCF$_3$*

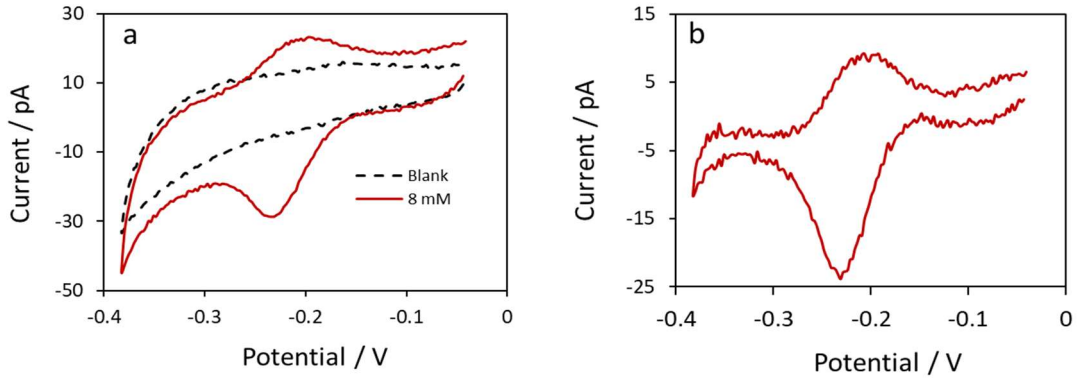

Figure 5.3.1.2: *(a) Cyclic Voltammograms of 8.0 mM sulphate ions with 0.25 mM tren-bCF₃ ionophore and background CV (black dotted) and (b) background subtracted CV at 25 µm radius pipette. [Pipette radius with Equations 2.3.1.2 and 2.3.1.3 are also given in Appendix B.]*

Scan rate of the experiment is very important parameter for electroanalytical experiments. It controls how fast the applied potential is scanned. Higher currents are observed for faster scan rates because it leads to a decrease in the size of the diffusion layer [292, 293]. According to the Randles-Sevcik equation 5.3.1.1, the peak current (i_p) isexpected to be proportional to the square root of the scan rate ($v^{1/2}$) for a linear diffusion process.

$$i_p = 268{,}600\ z^{3/2} AD^{1/2} Cv^{1/2} \qquad \text{(Eq. 5.3.1.1)}$$

where z is the charge of the transferring species, A is the area of the interface, C is the concentration and D is the diffusion coefficient of the species controlling the transfer process. In a micropipette-based ITIES, linear diffusion is expected to occur inside the pipette, as was shown in the Figure 2.5.2 (chapter 2) for tetrapropylammonium ion transfer. Analytes can also adsorb to the liquid-liquid interface [292]. For that case, the current response is described by equation 5.3.1.2.

$$i_p = \frac{z^2F^2}{4R} vA\Gamma^* \qquad \text{(Eq. 5.3.1.2)}$$

where Γ^* is the surface coverage of the adsorbed species in mol cm^{-2} and other parameters have their usual meanings Equation 5.3 shows that for adsorbed species the current response varies linearly with the scan rate. An analyte which is thought to be a diffusing species can deviate from the linearity in plots of i_p vs. $v^{1/2}$. This can happen if the process is either (a) electrochemical quasi-reversible or (b) the transfer

may be occurring via surface adsorption. For electrochemically quasi-reversible process, the peak-to-peak separation shifts with scan rate and for surface adsorbed species no peak-to-peak separation is observed [294].

Figure 5.3.1.3 (a) shows voltammograms of sulphate ions transfer at different scan rate and Figure 5.3.1.3 (b) shows that both negative and positive current linearly increased with scan rate variation, but they gave curved lines for peak current *vs* square root of scan rate for both forward and reverse direction. Therefore, according to the previous discussions (Equation 5.3.1.2) this process is adsorption controlled rather than diffusion controlled. The forward and the backward current ratio is nearly 2.3 and the peak-to-peak separation is 31 mV.

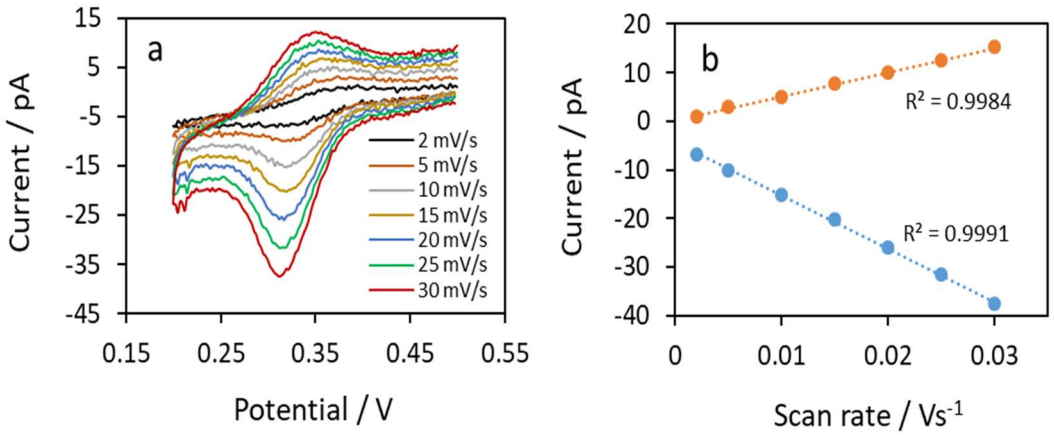

Figure 5.3.1.3: *(a) Cyclic voltammograms of 5 mM sulphate ions at different scan rates at 11 µm radius pipette and (b) current vs scan rate for both forward and reverse scan. [Pipette radius with Equations 2.3.1.2 and 2.3.1.3 are also given in Appendix B.]*

Surface coverage is an important parameter for adsorption process. Several parameters such as charge transfer kinetics of the adsorbed molecules, adsorption coefficient and the nature of the produced current are directly or indirectly affected by the degree of the surface coverage [295]. We calculate the surface coverage (Γ), by using the formula $\Gamma = \frac{m}{\text{area of interface}}$ [296, 297], where m = $\frac{Q}{zi \,.\, F}$ = moles of adsorbed ions at ITIES, Q = total charge or peak area [298], z_i = charge of ion and F = Faraday constant.

According to the Langmuir isotherm [299-301], which is described by equation 5.3.1.3.

$$\Gamma_{SO_4^{-2}}/(\Gamma_{Sat} - \Gamma_{SO_4^{-2}}) = \beta\,[SO_4^{-2}] \qquad \text{(Eq. 5.3.1.3)}$$

where $\Gamma_{SO_4^{-2}}$ (pmol/cm^2) is the surface coverage for a particular concentration, Γ_{Sat} is the saturation surface coverage or limiting surface coverage, $[SO_4^{-2}]$ is the concentration of sulphate in aqueous solution and β is the adsorption coefficient or energy parameter. Rearranging the equation 5.3.1.3 we can write as

$$\frac{[SO_4^{-2}]}{\Gamma_{SO_4^{-2}}} = \frac{[SO_4^{-2}]}{\Gamma_{Sat}} + \frac{1}{\beta.\Gamma_{Sat}} \qquad \text{(Eq. 5.3.1.4)}$$

Equation 5.3.1.4 is the linearized form of the Langmuir isotherm. We can obtain the saturation surface coverage from the slope of the plot $[SO_4^{-2}]/\Gamma_{SO_4^{-2}}$ *vs* $[SO_4^{-2}]$ and β can also be calculated from the intercept of that graph [302, 303].

This experiment was done with four different size of pipettes to check how the electrochemical properties changes with the size of interface. Figure 5.3.1.4 shows the non-background subtracted voltammograms of different concentrations of SO_4^{-2} with 0.25 mM tren-bCF$_3$ ionophore at an 4 μm radius of pipette. Table 5.3.1.1 shows many different concentrations used for this experiment; all experiments for each concentrations are done at least three times. From the background subtracted CVs of different concentrations, the total charge or peak area (Q) and moles of adsorbed ions (m) are calculated and those are used to calculate the surface coverage (Γ) for both forward and reverse directions. Data listed in the Table 5.3.1.1 are the average data which are calculated from three different experiments for each concentration.

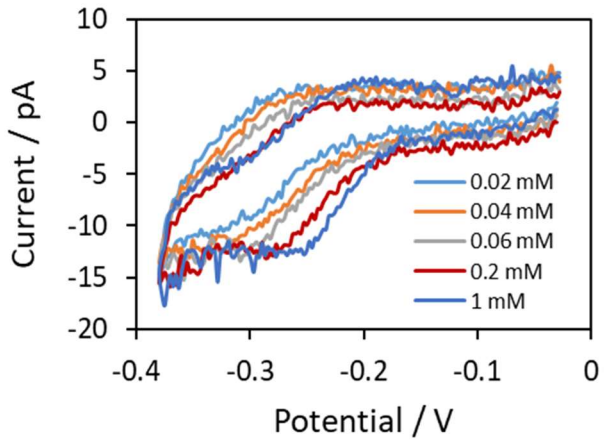

Figure 5.3.1.4: *Cyclic Voltammograms of sulphate ions of concentration 0.02, 0.04, 0.06, 0.2 and 1.0 mM with 0.25 mM trenbCF₃ ionophore at 4 µm radius pipette.*

[Pipette radius with Equations 2.3.1.2 and 2.3.1.3 are also given in Appendix B.]

Table 5.3.1.1: *Charge or area of the peak, number of molecules and surface coverage for both forward and reverse peaks for CV experiments of sulphate ions at different concentrations with 0.25 mM tren-bCF₃ ionophore at 4 µm radius pipette.*

Conc. (mM)	average area of the forward peak, Q^f x 10^{-13} (coulomb)	average area of the reverse peak, Q^r x 10^{-13} (coulomb)	average number of moles $m^f = Q^f/Z_i F$ x 10^{-19}	average number of moles $m^r = Q^r/Z_i F$ x 10^{-19}	surface coverage, $\Gamma^f = m^f$/area of the surface (p.mol/cm²)	surface coverage, $\Gamma^r = m^r$/area of the surface (p.mol/cm²)
0.02	0.86	0.56	4.39	2.88	0.91	0.59
0.04	1.15	0.96	6.21	4.97	1.21	1.01
0.06	1.31	1.04	6.87	5.39	1.39	1.10
0.08	1.24	1.05	6.39	5.43	1.31	1.11
0.10	1.35	1.05	7.04	5.46	1.43	1.11
0.20	1.55	1.16	8.06	5.99	1.64	1.22
0.30	1.89	1.42	9.80	7.36	2.00	1.50
0.40	1.94	1.49	10.11	7.74	2.05	1.58
0.60	2.04	1.65	10.55	8.54	2.16	1.74
1.00	2.06	1.64	10.77	8.50	2.18	1.73
3.00	2.08	1.64	10.73	8.51	2.20	1.73
6.00	2.15	1.66	11.32	8.61	2.28	1.76
10.0	2.14	1.68	11.09	8.70	2.26	1.77

By using the data of Table 5.3.1.1 surface coverage vs sulphate ion concentration was plotted for both forward and reverse direction, as shown in Figure 5.3.1.5. From this Figure we can say that sulphate transfer facilitated by tren-bCF₃ follows the Langmuir

isotherm. An exponential curve has been fitted to the data as a guide to the eye only. Parameters to characterise the adsorption process (e.g. adsorption coefficient, saturation surface coverage) were determined by linear fitting to the linearised form of the Langmuir isotherm. At very low concentration, surface coverage increased sharply with the increase of concentration and became a plateau after a certain concentration for both scan directions. Typical surface coverage data for adsorption at the ITIES include monolayer formation for a phospholipid at W/DCE interface of 2.3×10^{-10} mol/cm^2 [304], 2.71×10^{-10} mol/cm^2 [305] and 2.5×10^{-10} mol/cm^2. So from the data of Figure 5.3.1.5 we can say that the sulphate-ionophore transfer process forms a sub-monolayer for data extracted from scans in both directions.

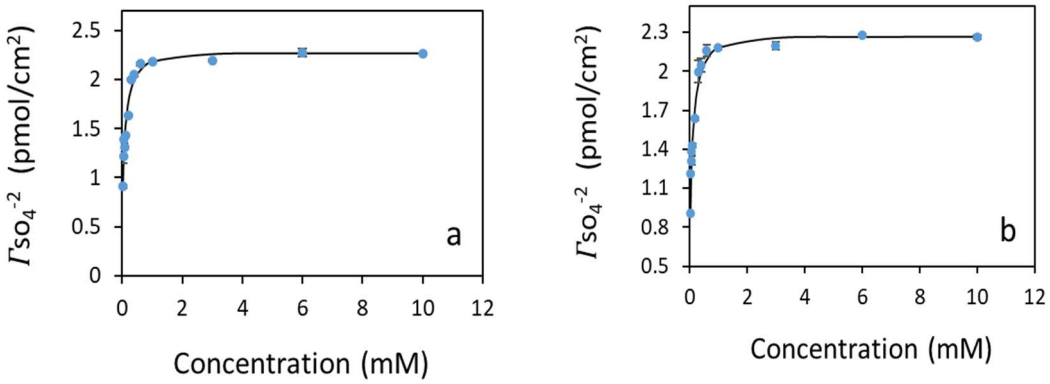

Figure 5.3.1.5: *Surface coverage vs sulphate ion concentration for both (a) forward and (b) reverse scan with tren-bCF$_3$ ionophore at 4 µm radius pipette.*
[Pipette radius with Equations 2.3.1.2 and 2.3.1.3 are also given in Appendix B.]

The plot of current response *vs* concentration of sulphate ions (Figure 5.3.1.6) shows that at very low concentration (lower than the ionophore concentration), the current increased very rapidly and the increase rate decreases as the sulphate ion concentration became closer to the ionophore concentration 0.25 mM. When the sulphate ion concentration exceeded the ionophore concentration, then the current reached a plateau. This observation confirms that the facilitated sulphate ions transfer by the formation of ionophore-sulphate complex was depended on the ionophore concentration, not on the sulphate ion concentrations.

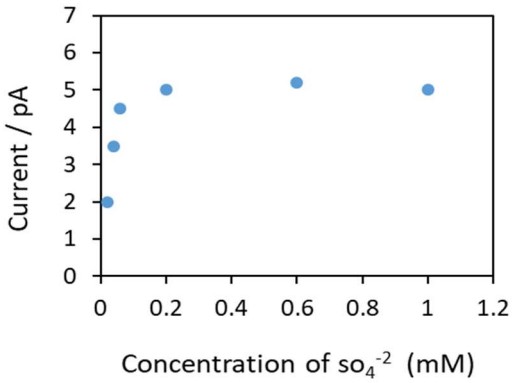

Figure 5.3.1.6: *Current vs sulphate ion concentration for forward scan with tren-bCF₃ ionophore at 4 µm radius pipette. [Pipette radius with Equations 2.3.1.2 and 2.3.1.3 are also given in Appendix B.]*

Figure 5.3.1.7 shows $[SO_4^{-2}]/\Gamma_{SO_4^{-2}}$ *vs* $[SO_4^{-2}]$ graph which gives a straight line according to the linearization of the Langmuir isotherm. We calculated the saturation surface coverage for both forward and reverse scan from the slope of the graph, which are 2.28 and 1.78 pmol/cm^2 respectively. The adsorption coefficients (β) for both scans also calculated from the intercept of the graphs, which are 21 x 10^6 cm^3/mol and 21 x 10^6 cm^3/mol respectively.

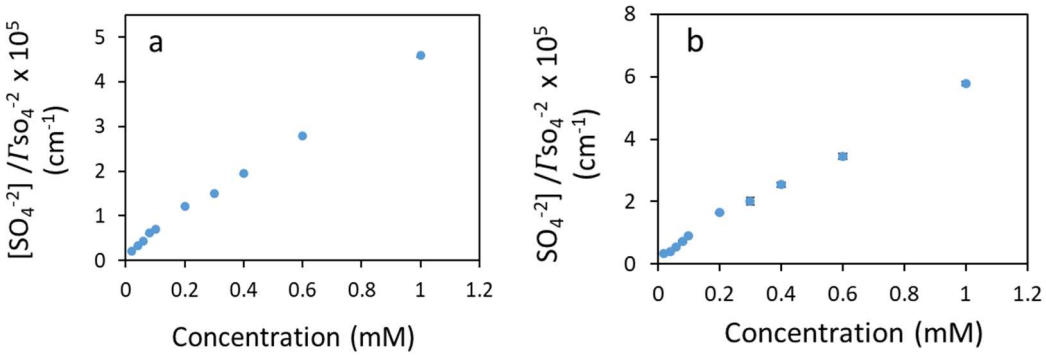

Figure 5.3.1.7: $[SO_4^{-2}]/\Gamma_{SO_4^{-2}}$ *vs sulphate ion concentration for both (a) forward and (b) reverse scan with tren-bCF₃ ionophore at 4 µm radius pipette. [Pipette radius with Equations 2.3.1.2 and 2.3.1.3 are also given in Appendix B.]*

Figure 5.3.1.8 (a) shows the background subtracted voltammograms of different concentrations of sulphate ions with 0.25 mM tren-bCF$_3$ ionophore at an 9 µm radius pipette. Figure 5.3.1.8 (b) shows the current linearly dependent with scan rate which shows this process is adsorption controlled. The total charge or peak area (Q) and moles of adsorbed ions (m) are calculated from the background subtracted CVs of

different concentrations and these are used to calculate the surface coverage (Γ) for both forward and reverse scan directions. Data listed in the Table 5.3.1.2 are the average data that are calculated from three different experiments for each concentration.

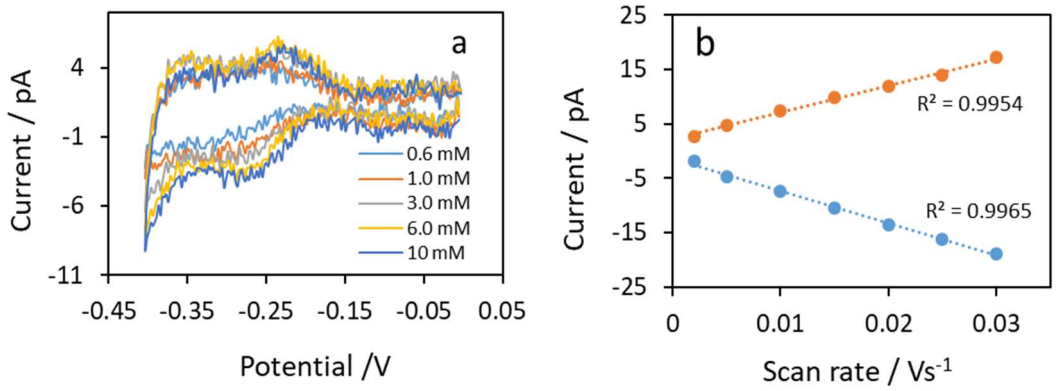

Figure 5.3.1.8: *(a) Cyclic Voltammograms of sulphate ions of concentration 0.6, 1.0, 3.0, 6.0 and 10.0 mM and (b) current vs scan rate with 0.25 mM tren-bCF₃ ionophore at 9 µm radius pipette. [Pipette radius with Equations 2.3.1.2 and 2.3.1.3 are also given in Appendix B.]*

Table 5.3.1.2: *Charge or area of the peak, number of molecules and surface coverage for both forward and reverse peaks for CV experiments of sulphate ions at different concentrations with 0.25 mM tren-bCF₃ ionophore at 9 µm radius pipette.*

Conc. (mM)	average area of the forward peak, Q^f x 10^{-14} (coulomb)	average area of the reverse peak, Q^r x 10^{-14} (coulomb)	average number of moles, $m^f = Q^f/Z_i F$ x 10^{-19}	average number of moles, $m^r = Q^r/Z_i F$ x 10^{-19}	surface coverage, $\Gamma^f = m^f$/area of the surface (p.mol/cm^2)	surface coverage, $\Gamma^r = m^r$/area of the surface (p.mol/cm^2)
0.6	5.25	4.02	2.72	2.08	0.11	0.08
0.4	4.18	2.38	2.16	1.23	0.08	0.05
0.2	3.04	1.80	1.57	0.93	0.06	0.04
0.8	5.61	4.30	2.91	2.23	0.12	0.08
1	7.29	4.45	3.78	2.30	0.14	0.09
2	7.67	5.88	3.98	3.05	0.15	0.11
3	7.50	6.12	3.89	3.17	0.16	0.12
4	7.91	6.18	4.10	3.20	0.15	0.12
5	8.12	6.10	4.21	3.16	0.16	0.12
6	8.69	6.11	4.50	3.17	0.16	0.12
7	8.11	6.13	4.20	3.18	0.16	0.12
8	8.62	6.04	4.47	3.13	0.16	0.12
10	8.00	5.77	4.15	2.99	0.16	0.12

Figure 5.3.1.9 (a) and (b) shows surface coverage *vs* sulphate ion concentration graph for forward and reverse scan respectively. From Figure 5.3.1.9 we can say, sulphate transfer facilitated by tren-bCF$_3$ ideally follows the Langmuir isotherm in this case also. At very low concentration, surface coverage increased sharply with the increase of concentration and became a plateau after a certain concentration for both directions. In previous discussions we saw that it was reported 2.3 × 10^{-10} mol/cm^2 to form a monolayer of phospholipid at W/DCE interface [304]. So, from the Figure 5.3.1.9 and the data extracted from scans in both directions, we can say that the sulphate-ionophore transfer process forms a sub-monolayer at the interface for this case also.

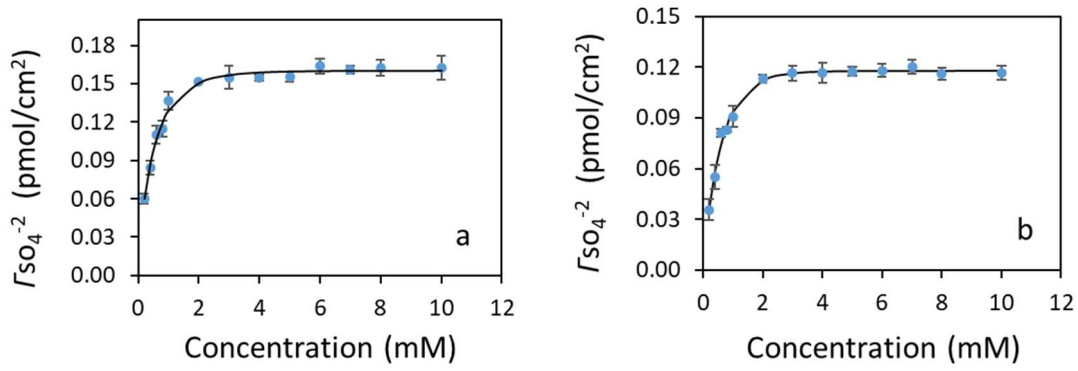

Figure 5.3.1.9: *Surface coverage vs sulphate ion concentration for both (a) forward and (b) reverse scan with tren-bCF$_3$ ionophore at 9 µm radius pipette. [Pipette radius with Equations 2.3.1.2 and 2.3.1.3 are also given in Appendix B.]*

Figure 5.3.1.10 shows $[SO_4^{-2}]/\Gamma_{SO_4^{-2}}$ *vs* $[SO_4^{-2}]$ graph gives a straight line which follows the linearization of the Langmuir isotherm. Calculated saturation surface coverage for both forward and reverse scan from the slope of the graphs are 0.17 and 0.12 pmol/cm^2 respectively. Adsorption coefficients (β) for both scans also calculated from the intercept of the graphs which are 3 x 10^6 cm^3/mol and 3 x 10^6 cm^3/mol respectively.

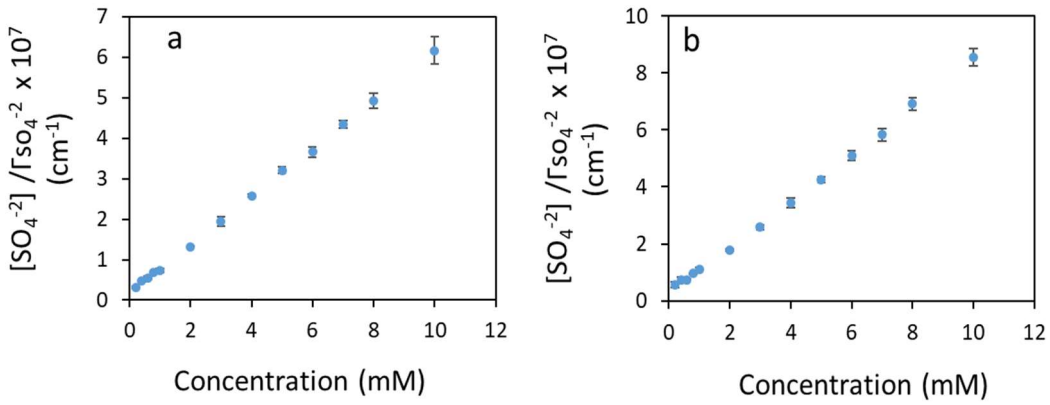

Figure 5.3.1.10: *$[SO_4^{-2}]/\Gamma_{SO_4^{-2}}$ vs sulphate ion concentration for both (a) forward and (b) reverse scan with tren-bCF$_3$ ionophore at 9 µm radius pipette. [Pipette radius with Equations 2.3.1.2 and 2.3.1.3 are also given in Appendix B.]*

Similar experiments have been done with different radius of pipettes. Figure 5.3.1.11 (a) shows the background subtracted voltammograms of different concentrations of sulphate ions with 0.25 mM of tren-bCF$_3$ ionophore at a pipette of 11 µm radius. Figure 5.3.1.11 (b) shows the current linearly dependent with the scan rate which shows this process is adsorption controlled. The total charge or peak area (Q) and moles of adsorbed ions (m) are calculated from the background subtracted CVs of different concentrations those are used to calculate the surface coverage (Γ) for both forward and reverse directions. Data listed in the Table 5.3.1.3 are the average data calculated from three different experiments for each concentration.

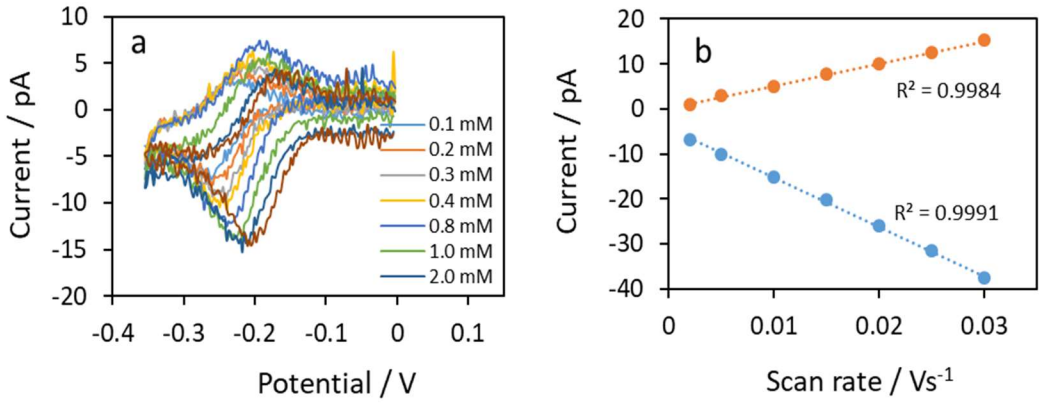

Figure 5.3.1.11: *(a) Cyclic Voltammograms of sulphate ions of concentration 0.1, 0.2, 0.3, 0.4, 0.8, 1.0 and 2.0 mM and (b) current vs scan rate with 0.25 mM tren-bCF$_3$ ionophore at 11 µm radius pipette. [Pipette radius with Equations 2.3.1.2 and 2.3.1.3 are also given in Appendix B.]*

Table 5.3.1.3: *Charge or area of the peak, number of molecules and surface coverage for both forward and reverse peaks for CV experiments of sulphate ions at different concentrations with 0.25 mM tren-bCF$_3$ ionophore at 11 µm radius pipette.*

Conc. (mM)	average area of the forward peak, Q^f x 10^{-13} (coulomb)	average area of the reverse peak, Q^r x 10^{-13} (coulomb)	average number of moles, $m^f = Q^f/Z_i F$ x 10^{-18}	average number of moles, $m^r = Q^r/Z_i F$ x 10^{-18}	surface coverage, $\Gamma^f = m^f$/area of the surface (p.mol/cm^2)	surface coverage, $\Gamma^r = m^r$/area of the surface (p.mol/cm^2)
0.1	2.28	1.33	1.18	0.69	0.28	0.15
0.2	2.79	1.77	1.45	0.92	0.34	0.22
0.3	3.43	2.51	1.78	1.30	0.42	0.30
0.4	4.50	2.63	2.33	1.36	0.56	0.36
0.8	5.52	3.07	2.86	1.59	0.73	0.40
1	6.09	3.66	3.15	1.90	0.78	0.44
2	6.71	3.60	3.48	1.86	0.85	0.47
3	6.56	3.90	3.40	2.02	0.85	0.49
5	6.94	3.83	3.60	1.99	0.86	0.48
7	6.78	3.88	3.51	2.01	0.86	0.49

Figure 5.3.1.12 (a) and (b) shows surface coverage *vs* sulphate ion concentration graph for forward and reverse scan respectively. As like before, from this Figure we can say that sulphate transfer facilitated by tren-bCF$_3$ ideally follows the Langmuir isotherm. At very low concentration, surface coverage increased sharply with the increase of sulphate concentration and became plateau after a certain concentration for both directions. So, from the Figure 5.3.1.12 and the data extracted from scans in both directions and according to the previous discussion, we can say that the sulphate-ionophore transfer process forms a sub-monolayer at the interface for this case also.

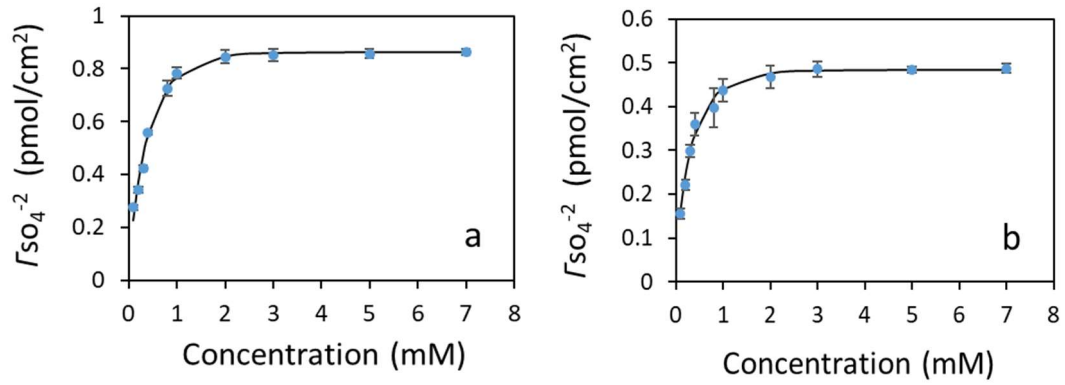

Figure 5.3.1.12: *Surface coverage vs sulphate ion concentration for both (a) forward and (b) reverse scan with tren-bCF₃ ionophore at 11 µm radius pipette. [Pipette radius with Equations 2.3.1.2 and 2.3.1.3 are also given in Appendix B.]*

Figure 5.3.1.13 shows $[SO_4^{-2}]/\Gamma_{SO_4^{-2}}$ *vs* $[SO_4^{-2}]$ graph gives a straight line which follows linearization of the Langmuir isotherm. Calculated saturation surface coverage for both forward and reverse scan from the slope of the graph are 0.9 and 0.5 pmol/cm^2 respectively. Adsorption coefficients (β) for both scans also calculated from the intercept of the graphs which are 4 x 10^6 cm^3/mol and 5 x 10^6 cm^3/mol respectively.

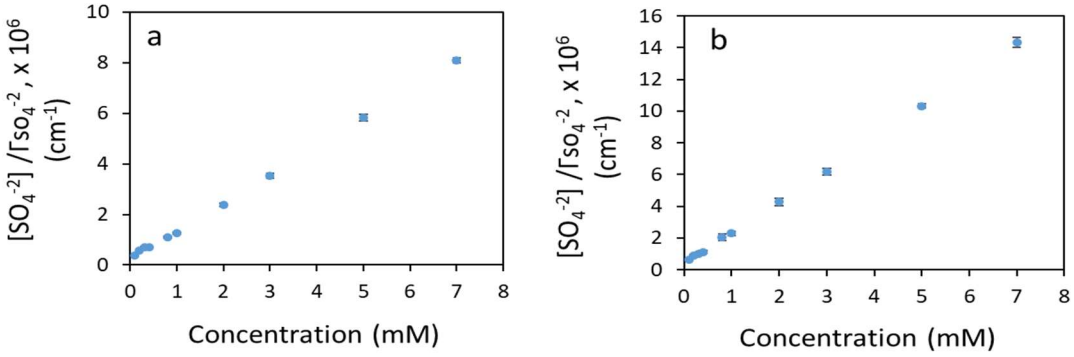

Figure 5.3.1.13: $[SO_4^{-2}]/\Gamma_{SO_4^{-2}}$ *vs sulphate ion concentration for both (a) forward and (b) reverse scan with tren-bCF₃ ionophore at 11 µm radius pipette. [Pipette radius with Equations 2.3.1.2 and 2.3.1.3 are also given in Appendix B.]*

The same experiment was done on another pipette of radius 27.5 µm. Figure 5.3.1.14(a) shows the background subtracted voltammograms of different concentrations sulphate ions with 0.25 mM tren-bCF$_3$ at that pipette. Figure 5.3.1.14(b) shows the current linearly dependent with scan rate which proves this process is also adsorption controlled. The total charge or peak area (Q) and moles of adsorbed ions (m) are calculated from the background subtracted CVs of different

concentrations those are used to calculate the surface coverage (Γ) for both forward and reverse directions. Data listed in the Table 5.3.1.4 are the average data those are calculated from three different experiments for each concentration.

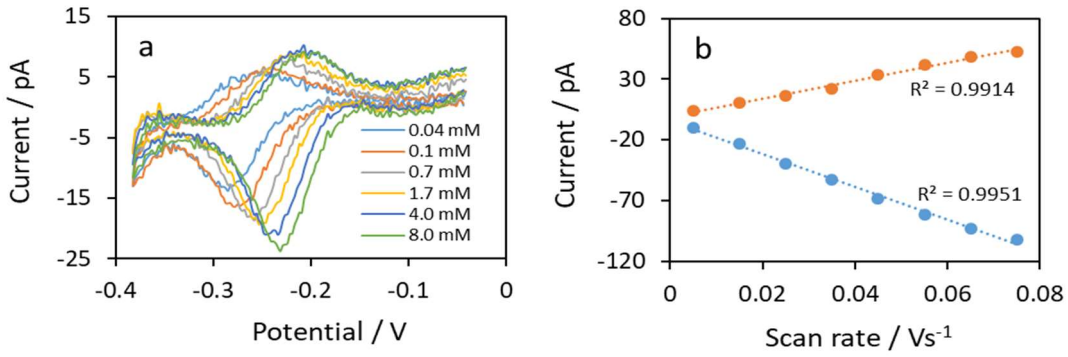

Figure 5.3.1.14: *(a) Cyclic Voltammograms of sulphate ions of concentration 0.04, 0.1, 0.7, 1.7, 4.0 and 8.0 mM and (b) current vs scan rate with 0.25 mM tren-bCF₃ ionophore at 27.5 µm radius pipette. [Pipette radius with Equations 2.3.1.2 and 2.3.1.3 are also given in Appendix B.1*

Table 5.3.1.4: *Charge or area of the peak, number of molecules and surface coverage for both forward and reverse peaks for CV experiments of sulphate ions at different concentrations with 0.25 mM tren-bCF₃ ionophore at 27.5 µm radius pipette.*

Conc. (mM)	average area of the forward peak, Q^f x 10^{-13} (coulomb)	average area of the reverse peak, Q^r x 10^{-13} (coulomb)	average number of moles, $m^f = Q^f/Z_i F$ x 10^{-18}	average number of moles, $m^r = Q^r/Z_i F$ x 10^{-18}	surface coverage, $\Gamma^f = m^f$/area of the surface (p.mol/cm²)	surface coverage, $\Gamma^r = m^r$/area of the surface (p.mol/cm²)
0.04	3.60	2.98	1.87	1.55	0.080	0.066
0.1	5.37	3.56	2.78	1.85	0.119	0.079
0.3	6.06	3.99	3.14	2.07	0.134	0.088
0.65	7.07	4.84	3.66	2.51	0.156	0.107
1.67	7.94	5.24	4.11	2.72	0.175	0.116
2.8	8.37	5.51	4.34	2.86	0.185	0.122
4	8.82	5.46	4.57	2.83	0.195	0.120
6	9.25	5.54	4.79	2.87	0.204	0.122
8	9.25	5.60	4.79	2.90	0.204	0.124
10	9.57	5.65	4.96	2.93	0.211	0.125

Figure 5.3.1.15 (a) and (b) shows surface coverage *vs* sulphate ion concentration graph for forward and reverse scan respectively. From this Figure we can say, sulphate ions

transfer facilitated by tren-bCF$_3$ ideally follows the Langmuir isotherm in this case also. At very low concentration, surface coverage increased sharply with the increase of concentration and became plateau after a certain concentration for both directions. As like before, from the Figure 5.3.1.15 we can say that the sulphate-ionophore transfer process forms a sub-monolayer.

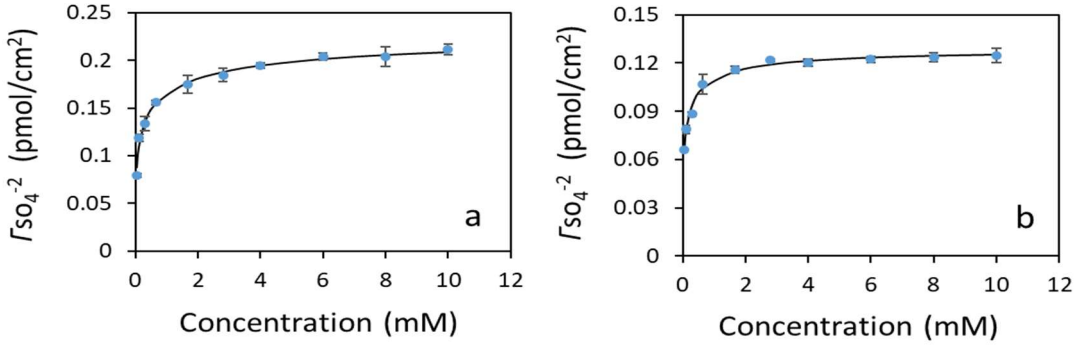

Figure 5.3.1.15: *Surface coverage vs sulphate ion concentration for both (a) forward and (b) reverse scan with tren-bCF$_3$ ionophore at 27.5 µm radius pipette. [Pipette radius with Equations 2.3.1.2 and 2.3.1.3 are also given in Appendix B.]*

Figure 5.3.1.16 shows $[SO_4^{-2}]/\Gamma_{SO_4^{-2}}$ *vs* $[SO_4^{-2}]$ graph gives a straight line which follows the linearization of Langmuir isotherm. Calculated saturation surface coverage for both forward and reverse scan from the slope of the graphs are 0.21 and 0.13 pmol/cm^2 respectively. Adsorption coefficients (β) for both scans also calculated from the intercept of the graphs which are 5 x 10^6 cm^3/mol and 11 x 10^6 cm^3/mol respectively.

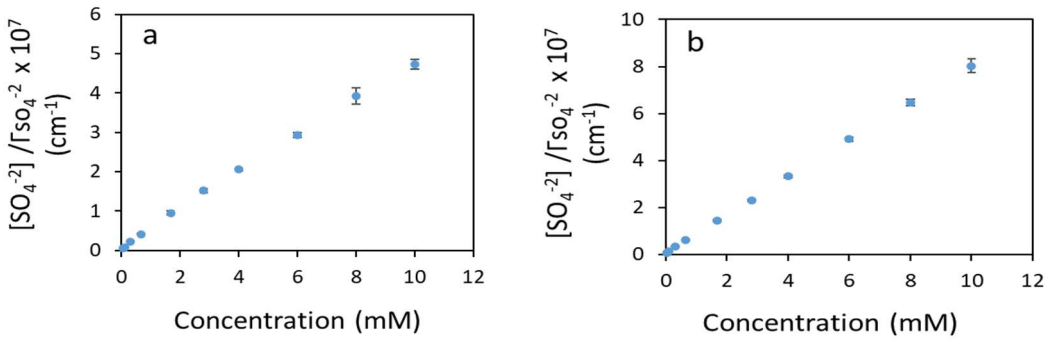

Figure 5.3.1.16: $[SO_4^{-2}]/\Gamma_{SO_4^{-2}}$ *vs sulphate ion concentration for both (a) forward and (b) reverse scan with tren-bCF$_3$ ionophore at 27.5 µm radius pipette. [Pipette radius with Equations 2.3.1.2 and 2.3.1.3 are also given in Appendix B.]*

Figure 5.3.1.17 shows the change of saturation surface coverage with the size of interface. The general trend for both forward and reverse scan is that the saturation surface coverage decreases with the increase of liquid/liquid interface size.

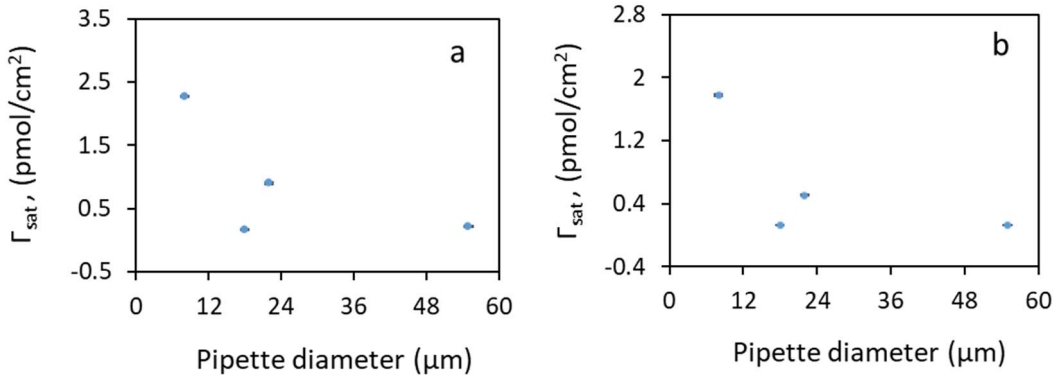

Figure 5.3.1.17: *Saturation of surface coverage for (a) forward and (b) reverse direction vs tips diameter of different pipettes for tren-bCF$_3$ ionophore.*

5.3.2 Cyclic voltammetry experiment with tri-squaramide TEB-tri-bCF$_3$ ionophore

Another tri-squaramide ionophore TEB-tri-bCF$_3$ (Figure 5.3.2.1) has been evaluated for electrochemical detection of sulphate ions at the ITIES by using 4 different size of micropipettes. Figure 5.3.2.2 illustrates the facilitated transfer of sulphate anions by TEB-tri-bCF$_3$ ionophore from the aqueous phase (10 mM SO_4^{-2} ion) to the organic phase at a 25 µm radius tip. 0.25 mM ionophore was introduced in the organic phase for this process. This sulphate ion transfers with the formation of ionophore-sulphate complex under electrochemical control. Because in the absence of ionophore there is no response (black line) shown in CV (Figure 5.3.2.2 a), but there is a good response to sulphate ions in presence of the ionophore. Figure 5.3.2.2 (b) shows the background subtracted voltammogram. The potential axis was calibrated with TEA^+. It is noticeable that the transfer potential of sulphate facilitated by two different ionophores are different. Figure 5.3.2.2 shows that the transfer potential of 10 mM

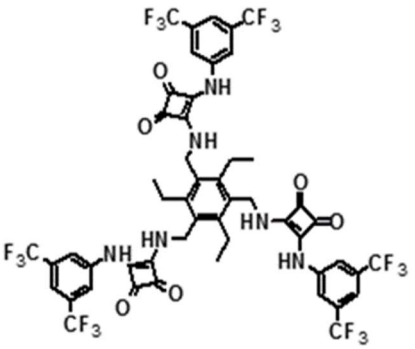

Figure 5.3.2.1: *Structure of tri-squaramide sulphate ionophore TEB-tri-bCF$_3$*

sulphate ions with TEB-tri-bCF$_3$ is ≈ -0.19 V, whereas the transfer potential of 8 mM sulphate ions with Tren-bCF$_3$ is ≈ 0.23 V. From this observation we can say that the sulphate ions transfers through the ITIES by making an interfacial complexation between sulphate and the ionophore, which explains why their transfer potentials differ. The transfer of sulphate ions depends on the concentration of ionophores, not on the sulphate ion concentration which was discussed in previous section with Figure 5.3.1.6.

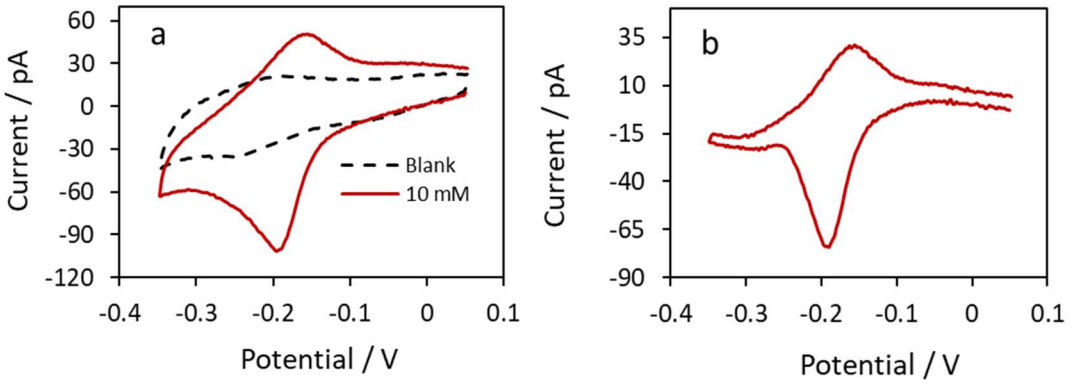

Figure 5.3.2.2: *(a) Cyclic Voltammograms of 10 mM sulphate ions with 0.25 mM TEB-tri-bCF$_3$ ionophore and CV of background electrolyte (black dotted) and (b) background subtracted CV at 25 µm radius pipette. [Pipette radius with Equations 2.3.1.2 and 2.3.1.3 are also given in Appendix B.]*

Figure 5.3.2.3(a) shows the voltammograms of different scan rates and Figure 5.3.2.3(b) shows both forward and reverse current linearly increased with scan rate. Therefore, according to the previous discussions this process is adsorption controlled. The forward and the backward current ratio is nearly ≈ 2.1 and the peak-to-peak separation is ≈ 35 mV.

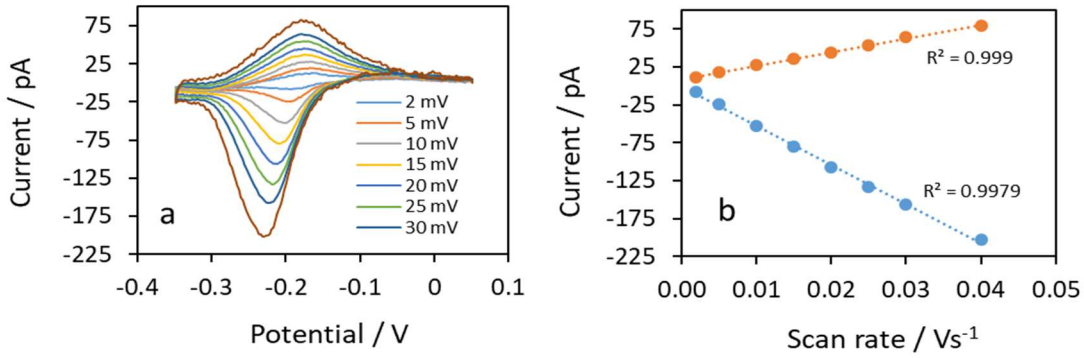

Figure 5.3.2.3: *(a) Cyclic voltammograms of 10 mM sulphate ions at different scan rates with 0.25 mM TEB-tri-bCF₃ ionophore and (b) current vs scan rate for both forward and reverse scan. Radius of the pipette was 25 µm. [Pipette radius with Equations 2.3.1.2 and 2.3.1.3 are also given in Appendix B.]*

This experiment was also done with four different size of pipettes to check how the electrochemical properties changes with the size of interface for ionophore TEB-tri-bCF$_3$. Figure 5.3.2.4 shows the background subtracted voltammograms of different concentrations of SO_4^{-2} with 0.25 mM TEB-tri-bCF$_3$ at a 15 µm radius pipette. Table 5.3.2.1 shows the concentrations used for this experiment and all experiments for each concentrations are done at least for three times. From the background subtracted CVs of different concentrations, the total charge or peak area (Q) and moles of adsorbed ions (m) were calculated. These data were then used to calculate the surface coverage (Γ) for both forward and reverse directions. Data listed in the Table 5.3.2.1 are the average data which are calculated from three different experiments for each concentration.

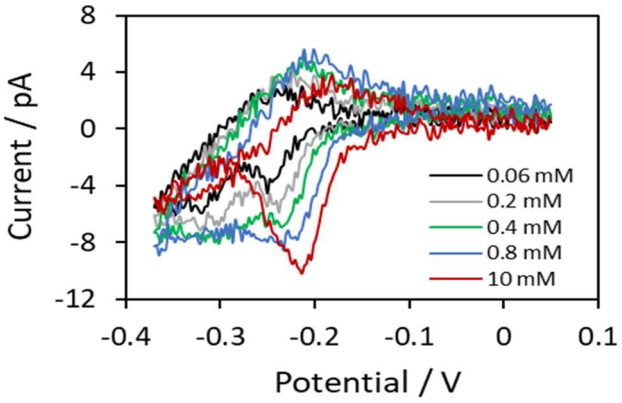

Figure 5.3.2.4: *Cyclic Voltammograms of sulphate ions of concentration 0.06, 0.2, 0.4, 0.8 and 10.0 mM with 0.25 mM TEB-tri-bCF₃ ionophore at 15 µm radius pipette. [Pipette radius with Equations 2.3.1.2 and 2.3.1.3 are also given in Appendix B.]*

Table 5.3.2.1: *Charge or area of the peak, number of molecules and surface coverage for both forward and reverse peaks for CV experiments of sulphate ions at different concentrations with 0.25 mM TEB-tri-bCF$_3$ ionophore at 15 µm radius pipette.*

Conc. (mM)	average area of the forward peak, Q^f x 10^{-14} (coulomb)	average area of the reverse peak, Q^r x 10^{-14} (coulomb)	average number of moles, $m^f = Q^f/Z_i F$ x 10^{-19}	average number of moles, $m^r = Q^r/Z_i F$ x 10^{-19}	surface coverage, $\Gamma^f = m^f$/area of the surface (p.mol/cm^2)	surface coverage, $\Gamma^r = m^r$/area of the surface (p.mol/cm^2)
0.02	5.94	4.42	3.08	2.29	0.042	0.032
0.06	6.56	4.86	3.40	2.52	0.047	0.035
0.2	6.94	5.35	3.60	2.77	0.050	0.038
0.4	7.73	5.92	4.01	3.07	0.055	0.042
0.8	8.31	6.19	4.30	3.21	0.059	0.044
4	8.74	6.77	4.53	3.51	0.063	0.048
6	8.65	6.59	4.48	3.41	0.062	0.047
8	8.85	6.80	4.58	3.53	0.063	0.049
10	8.83	6.78	4.57	3.51	0.063	0.049

By using the data from Table 5.3.2.1 surface coverage vs sulphate ion concentration was plotted for both forward and reverse direction shown in Figure 5.3.2.5 (a) and (b) respectively. The Figures also shows that the TEB-tri-bCF$_3$ follows the Langmuir isotherm ideally. At very low concentration of sulphate (lower than the ionophore), surface coverage increased sharply with the increase of concentration and became a plateau after a certain concentration (nearly about ionophore concentration) for both directions like ionophore tren-bCF$_3$. Earlier we discussed that the monolayer formation for a phospholipid at W/DCE interface was reported as 2.3×10^{-10} mol/cm^2 [304], 2.71×10^{-10} mol/cm^2 [305] and 2.5×10^{-10} mol/cm^2 . So, from the Figure 5.3.2.5 and the data extracted from scans in both directions and according to the previous discussion in tren-bCF$_3$ ionophore section, we can say that the sulphate-ionophore transfer process forms a sub-monolayer at the interface for this case also. Like tren-bCF$_3$ ionophore, the sulphate ions transfer across the ITES controlled by the TEB-tri-bCF$_3$ ionophore.

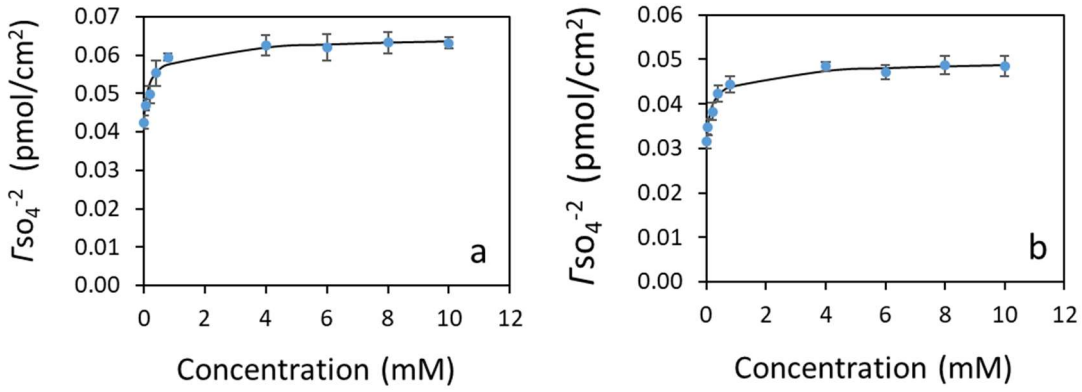

Figure 5.3.2.5: *Surface coverage vs sulphate ion concentration for both (a) forward and (b) reverse scan with TEB-tri-bCF$_3$ ionophore at 15 µm radius pipette. [Pipette radius with Equations 2.3.1.2 and 2.3.1.3 are also given in Appendix B.]*

Figure 5.3.2.6 shows $[SO_4^{-2}]/\Gamma_{SO_4^{-2}}$ *vs* $[SO_4^{-2}]$ graph gives a straight line which follows the linearization of the Langmuir isotherm. We calculated saturation surface coverage for both forward and reverse CV scans from the slope of the graph, which are 6.33 and 4.86 pmol/cm^2 respectively. Adsorption coefficients (β) for both scans were also calculated from the intercept of the graphs, which are 23 x 10^6 cm^3/mol and 37 x 10^6 cm^3/mol respectively.

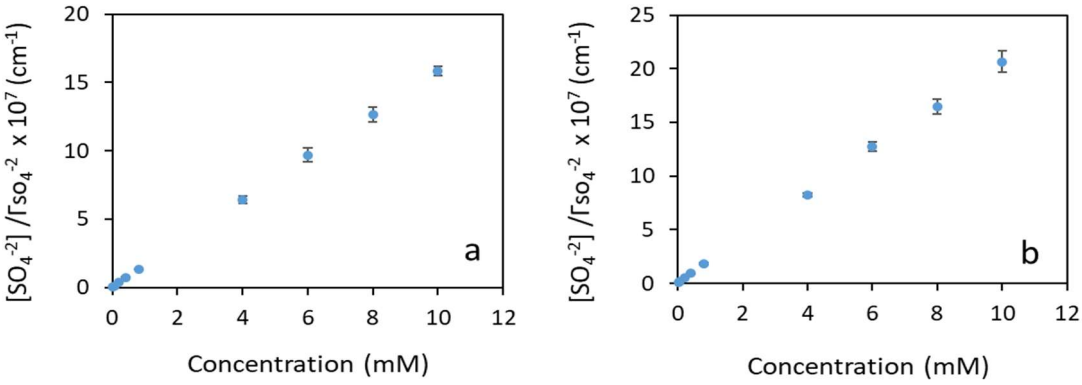

Figure 5.3.2.6: $[SO_4^{-2}]/\Gamma_{SO_4^{-2}}$ *vs sulphate ion concentration for both (a) forward and (b) reverse scan with TEB-tri-bCF$_3$ ionophore at 15 µm radius pipette. [Pipette radius with Equations 2.3.1.2 and 2.3.1.3 are also given in Appendix B.]*

Figure 5.3.2.7 shows the background subtracted voltammograms for different concentrations of sulphate ions with 0.25 mM TEB-tri-bCF$_3$ in organic phase at 20 µm radius pipette. Table 5.3.2.2 shows the concentrations used for this experiment and all the experiments for each concentration are done at least for three times. From the

background subtracted CVs of different concentrations, the total charge (Q) which is equivalent to peak area and moles of adsorbed ions (m) were calculated. Those values were used to calculate the surface coverage (Γ) for both forward and reverse directions. Data listed in the Table 5.3.2.2 are the average results which are calculated from three different experiments for each concentration.

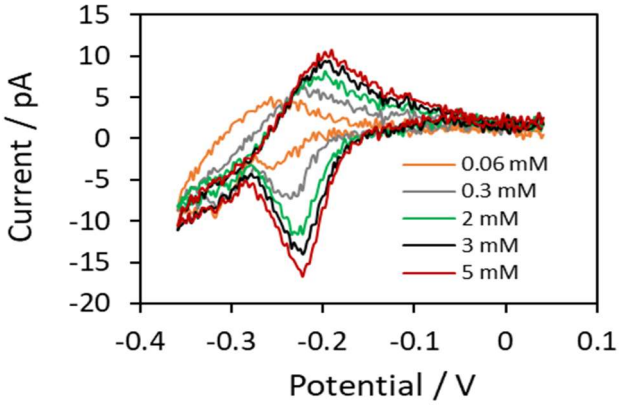

Figure 5.3.2.7: *Cyclic Voltammograms of sulphate ions of concentration 0.06, 0.3, 2.0, 3.0 and 5.0 mM with 0.25 mM TEB-tri-bCF$_3$ ionophore at 20 µm radius pipette.* *[Pipette radius with Equations 2.3.1.2 and 2.3.1.3 are also given in Appendix B.]*

Table 5.3.2.2: *Charge or area of the peak, number of molecules and surface coverage for both forward and reverse peaks for CV experiments of sulphate ions at different concentrations with 0.25 mM TEB-tri-bCF$_3$ ionophore at 20 µm radius pipette.*

Conc. (mM)	average area of the forward peak, Q^f x 10^{-14} (coulomb)	average area of the reverse peak, Q^r x 10^{-14} (coulomb)	average number of moles, $m^f = Q^f/Z_i F$ x 10^{-19}	average number of moles, $m^r = Q^r/Z_i F$ x 10^{-19}	surface coverage, $\Gamma^f = m^f$/area of the surface (p.mol/cm^2)	surface coverage, $\Gamma^r = m^r$/area of the surface (p.mol/cm^2)
0.02	5.02	3.49	2.60	1.81	0.0206	0.0143
0.06	6.04	4.30	3.13	2.23	0.0248	0.0176
0.15	7.02	4.86	3.64	2.52	0.0288	0.0199
0.30	8.23	5.70	4.27	2.95	0.0337	0.0233
1.00	10.03	6.38	5.20	3.31	0.0411	0.0261
2.00	11.08	6.88	5.74	3.56	0.0454	0.0282
3.00	11.09	7.17	5.75	3.71	0.0454	0.0294
5.00	11.90	7.31	6.17	3.79	0.0487	0.0299
7.00	12.39	7.35	6.42	3.81	0.0508	0.0301
8.00	12.22	7.41	6.33	3.84	0.0501	0.0303
9.00	12.32	7.39	6.38	3.83	0.0505	0.0303

Figure 5.3.2.8 (a) and (b) shows surface coverage vs sulphate ion concentrations for both forward and reverse direction respectively. The Figure also shows that the TEB-tri-bCF$_3$ facilitated sulphate in transfer follows the Langmuir isotherm ideally. Like previous, at very low concentration of sulphate, surface coverage increased sharply with the increase of concentration and became plateau after a certain concentration (nearly at equal concentration of ionophore) for both directions. According to the previous explanation, from Figure 5.3.2.8 we can also say that sulphate-ionophore complex forms a sub-monolayer at the interface for this transfer.

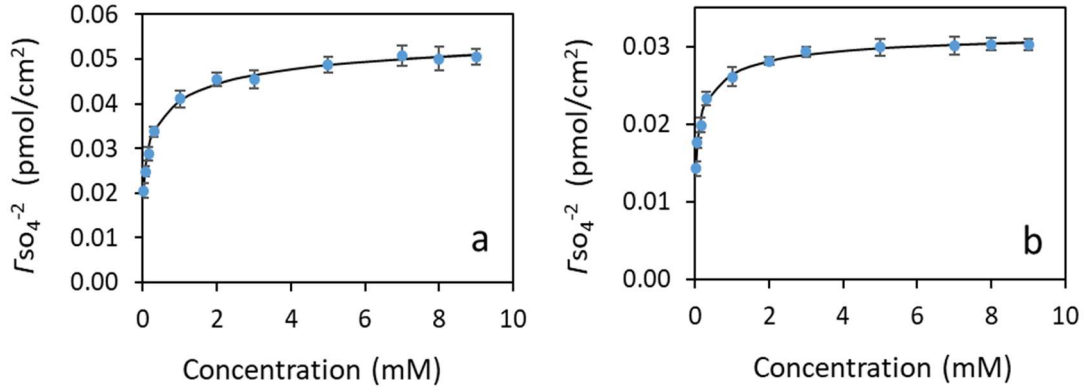

Figure 5.3.2.8: *Surface coverage vs sulphate ion concentration for both (a) forward and (b) reverse scan with TEB-tri-bCF$_3$ ionophore at 20 µm radius pipette. [Pipette radius with Equations 2.3.1.2 and 2.3.1.3 are also given in Appendix B.]*

Figure 5.3.2.9 shows $[SO_4^{-2}]/\Gamma_{SO_4^{-2}}$ *vs* $[SO_4^{-2}]$ graph gives a straight line which follows the linearization of the Langmuir isotherm. Saturation surface coverage was calculated for both forward and reverse scan from the slope of the graph which are 5.11 and 3.06 pmol/cm^2 respectively for this pipette. The calculated adsorption coefficients (β) from the intercept of the graphs for both scans are 7 x 10^6 cm^3/mol and 11 x 10^6 cm^3/mol respectively.

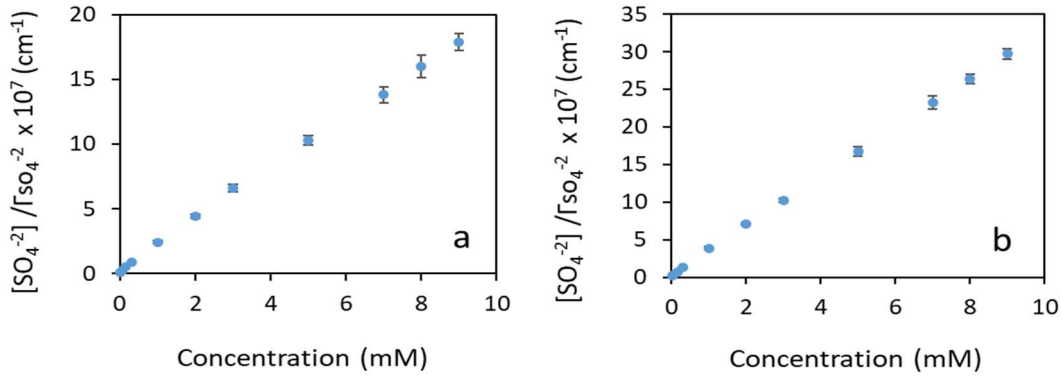

Figure 5.3.2.9: *$[SO_4^{-2}]/\Gamma_{SO_4^{-2}}$ vs sulphate ion concentration for both (a) forward and (b) reverse scan with TEB-tri-bCF₃ ionophore at 20 µm radius pipette. [Pipette radius with Equations 2.3.1.2 and 2.3.1.3 are also given in Appendix B.]*

Figure 5.3.2.10 shows the background subtracted voltammograms for different concentrations of sulphate ion with 0.25 mM TEB-tri-bCF$_3$ ionophore at 25 µm radius pipette. Table 5.3.2.3 shows the concentrations used for this experiment and all experiments for each concentration are done at least for three times. From the background subtracted CVs of different concentrations, the total charge (Q) which is equivalent to the peak area and moles of adsorbed ions (m) were calculated. Those values were used to calculate the surface coverage (Γ) for both forward and reverse directions. Data listed in the Table 5.3.2.3 are the average values which are calculated from three different experiments for each concentration.

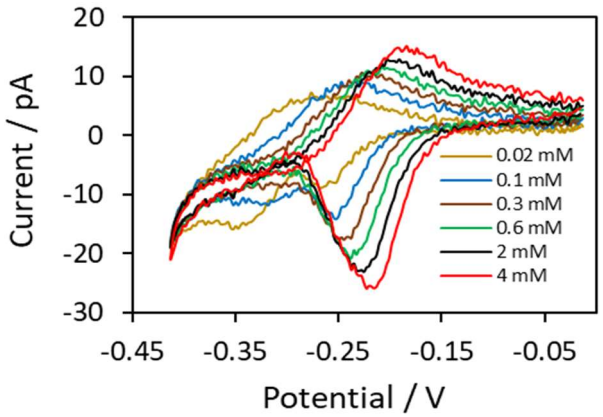

Figure 5.3.2.10: *Cyclic Voltammograms of sulphate ions of concentration 0.02, 0.1, 0.3, 0.6, 2.0 and 4.0 mM with 0.25 mM TEB-tri-bCF₃ ionophore at 25 µm radius pipette. [Pipette radius with Equations 2.3.1.2 and 2.3.1.3 are also given in Appendix B.]*

Table 5.3.2.3: *Charge or area of the peak, number of molecules and surface coverage for both forward and reverse peaks for CV experiments of sulphate ions at different concentrations with 0.25 mM TEB-tri-bCF$_3$ ionophore at 25 µm radius pipette.*

Conc. (mM)	average area of the forward peak, Q^f x 10^{-13} (coulomb)	average area of the reverse peak, Q^r x 10^{-13} (coulomb)	average number of moles, $m^f = Q^f/Z_i F$ x 10^{-19}	average number of moles, $m^r = Q^r/Z_i F$ x 10^{-19}	surface coverage, $\Gamma^f = m^f$/area of the surface (p.mol/cm^2)	surface coverage, $\Gamma^r = m^r$/area of the surface (p.mol/cm^2)
0.02	1.78	0.71	9.23	3.70	0.0476	0.0191
0.04	2.07	0.86	10.73	4.45	0.0554	0.0230
0.1	2.15	0.94	11.16	4.88	0.0576	0.0252
0.2	2.32	0.98	12.03	5.05	0.0621	0.0261
0.3	2.41	1.05	12.47	5.46	0.0644	0.0282
0.6	2.50	1.13	12.95	5.86	0.0668	0.0302
2.0	2.74	1.31	14.22	6.78	0.0734	0.0350
4.0	2.87	1.35	14.87	7.01	0.0767	0.0362
5.0	2.95	1.37	15.28	7.12	0.0789	0.0368
6.0	2.96	1.38	15.34	7.13	0.0792	0.0368
8.0	2.98	1.40	15.42	7.24	0.0796	0.0374
10.0	2.99	1.40	15.49	7.27	0.0799	0.0375

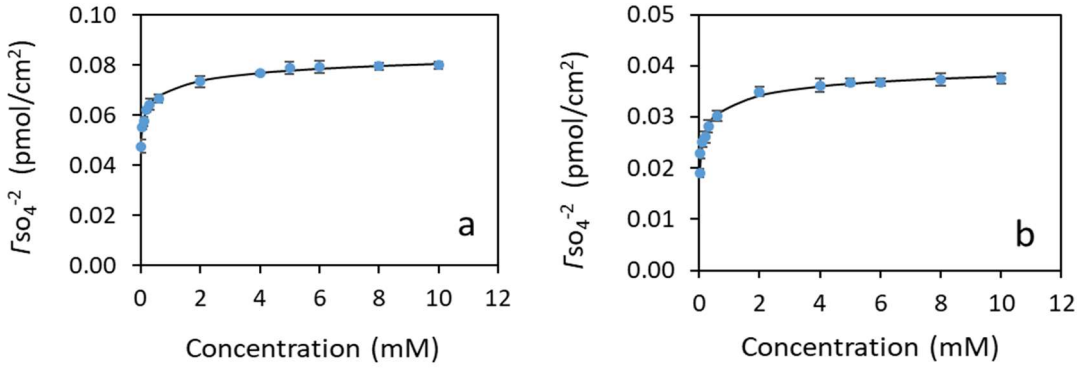

Figure 5.3.2.11: *Surface coverage vs sulphate ion concentration for both (a) forward and (b) reverse scan with TEB-tri-bCF$_3$ ionophore at 25 µm radius pipette. [Pipette radius with Equations 2.3.1.2 and 2.3.1.3 are also given in Appendix B.]*

Figure 5.3.2.11 (a) and (b) shows surface coverage vs sulphate ion concentrations for both forward and reverse direction respectively at 25 µm radius interface. The Figure also shows that the sulphate-TEB-tri-bCF$_3$ complex follows the Langmuir isotherm ideally. Surface coverage increased sharply at very low concentration (compare with

ionophore concentration) with the increase of concentration and became plateau for both directions when the sulphate concentration nearly equals to the ionophore concentration like previous results. Form the Figure 5.3.2.11 we can also say that sulphate-ionophore complex forms a sub-monolayer for both directions according to the monolayer formation data discussed previously.

Figure 5.3.2.12 shows $[SO_4^{-2}]/\Gamma_{SO_4^{-2}}$ *vs* $[SO_4^{-2}]$ graph gives a straight line which follows the linearization of the Langmuir isotherm. Saturation surface coverage was calculated for both forward and reverse scan from the slope of the graph which are 8.01 and 3.76 pmol/cm^2 respectively for this pipette. Adsorption coefficients (β) for both scans also calculated from the intercept of the graphs which are 13 x 10^6 cm^3/mol and 11 x 10^6 cm^3/mol respectively.

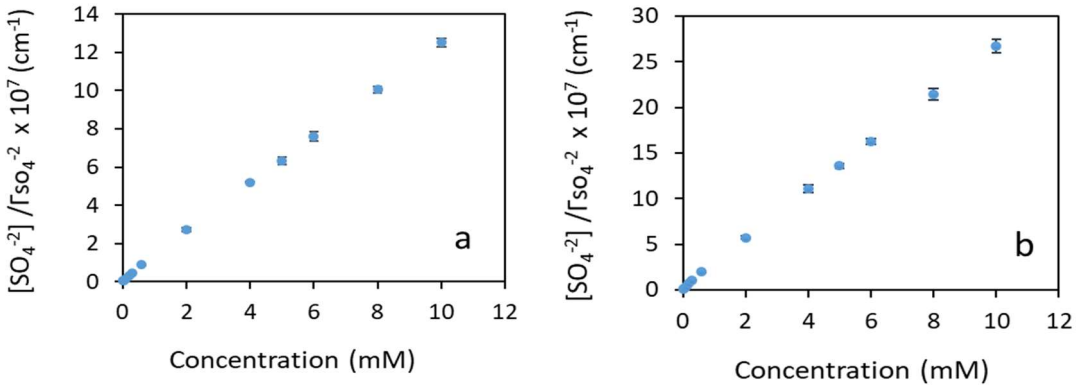

Figure 5.3.2.12: $[SO_4^{-2}]/\Gamma_{SO_4^{-2}}$ *vs sulphate ion concentration for both (a) forward and (b) reverse scan with TEB-tri-bCF$_3$ ionophore at 25 µm radius pipette. [Pipette radius with Equations 2.3.1.2 and 2.3.1.3 are also given in Appendix B.]*

Figure 5.3.2.13 shows the background subtracted voltammograms for different concentrations of sulphate ions facilitated by 0.25 mM TEB-tri-bCF$_3$ ionophore at 62.5 µm radius pipette. Table 5.3.2.4 shows the concentrations of sulphate ions used for this experiment and all experiments for each concentration are done at least for three times. From the background subtracted CVs of different concentrations, the total charge (Q) which is equivalent to the peak area and moles of adsorbed ions (m) are calculated. Those values are used to calculate the surface coverage (Γ) for both forward and reverse directions. Data listed in the Table 5.3.2.4 are the average results which are calculated from three different experiments for each concentration.

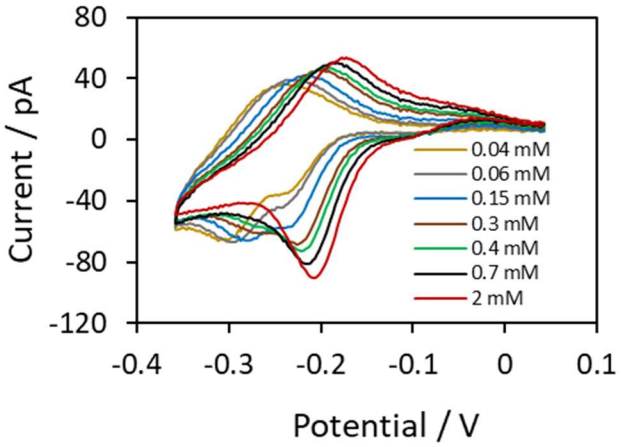

Figure 5.3.2.13: *Cyclic Voltammograms of sulphate ions of concentration 0.04, 0.06, 0.15, 0.3, 0.4, 0.7 and 2.0 mM with 0.25 mM TEB-tri-bCF₃ ionophore at 62.5 µm radius pipette. [Pipette radius with Equations 2.3.1.2 and 2.3.1.3 are also given in Appendix B.]*

Table 5.3.2.4: *Charge or area of the peak, number of molecules and surface coverage for both forward and reverse peaks for CV experiments of sulphate ions at different concentrations with 0.25 mM TEB-tri-bCF₃ ionophore at 62.5 µm radius pipette.*

Conc. (mM)	average area of the forward peak, Q^f x 10^{-13} (coulomb)	average area of the reverse peak, Q^r x 10^{-13} (coulomb)	average number of moles, $m^f = Q^f/Z_i F$ x 10^{-18}	average number of moles, $m^r = Q^r/Z_i F$ x 10^{-18}	surface coverage, $\Gamma^f = m^f$/area of the surface (p.mol/cm^2)	surface coverage, $\Gamma^r = m^r$/area of the surface (p.mol/cm^2)
0.02	3.96	2.12	2.05	1.10	0.0165	0.0088
0.04	5.54	2.92	2.87	1.51	0.0230	0.0121
0.06	6.83	3.23	3.54	1.67	0.0284	0.0134
0.10	8.08	3.96	4.19	2.05	0.0336	0.0165
0.15	10.59	4.53	5.49	2.35	0.0441	0.0188
0.20	11.57	5.07	5.99	2.63	0.0481	0.0211
0.30	13.32	5.51	6.90	2.85	0.0554	0.0229
0.40	14.13	5.35	7.32	2.77	0.0588	0.0223
0.70	14.41	5.58	7.47	2.89	0.0600	0.0232
2.00	15.95	5.76	8.27	2.98	0.0664	0.0239
5.00	17.71	5.84	9.18	3.03	0.0737	0.0243
7.00	17.39	6.08	9.01	3.15	0.0723	0.0253
9.00	18.50	6.00	9.59	3.11	0.0770	0.0249
10.0	18.66	6.11	9.67	3.17	0.0776	0.0254

Figure 5.3.2.14 (a) and (b) shows surface coverage vs sulphate ion concentrations for both forward and reverse direction respectively at 62.5 µm radius interface. The Figures show that the sulphate-ionophore complex follows the Langmuir isotherm ideally. Surface coverage increased sharply with the increase of sulphate concentration (when the sulphate concentration is lower than the ionophore concentration) and became plateau for both directions when the sulphate ion concentration became equal or more than the ionophore concentration. According to the previous discussions, from Figure 5.3.2.14 we can say that sulphate-TEB-tri-bCF$_3$ complex forms sub-monolayer for both directions.

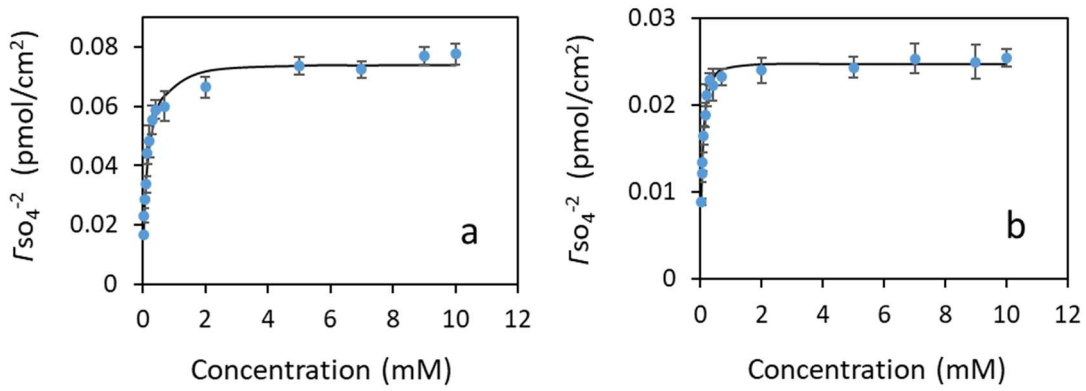

Figure 5.3.2.14: *Surface coverage vs sulphate ion concentration for both (a) forward and (b) reverse scan with TEB-tri-bCF$_3$ ionophore at 62.5 µm radius pipette. [Pipette radius with Equations 2.3.1.2 and 2.3.1.3 are also given in Appendix B.]*

Figure 5.3.2.15 shows $[SO_4^{-2}]/\Gamma_{SO_4^{-2}}$ *vs* $[SO_4^{-2}]$ graph gives a straight line which follows the linearization of Langmuir isotherm. The saturation surface coverage for both forward and reverse scan was calculated from the slopes of the graphs which are 7.72 and 2.52 pmol/cm^2 respectively for this pipette. Adsorption coefficients (β) for both scans also calculated from the intercept of the graphs which are 7 x 10^6 cm^3/mol and 19 x 10^6 cm^3/mol respectively.

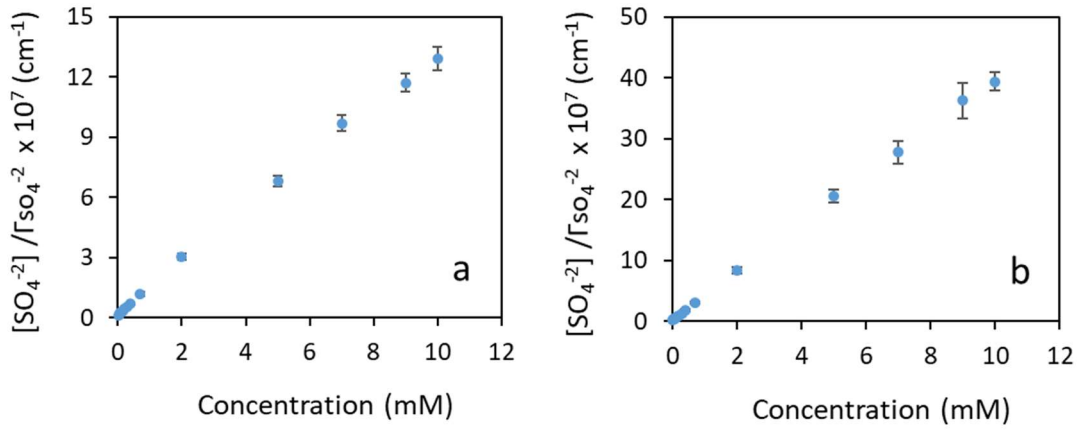

Figure 5.3.2.15: *$[SO_4^{-2}]/\Gamma_{SO_4^{-2}}$ vs sulphate ion concentration for both (a) forward and (b) reverse scan with TEB-tri-bCF₃ ionophore at 62.5 µm radius pipette. [Pipette radius with Equations 2.3.1.2 and 2.3.1.3 are also given in Appendix B.]*

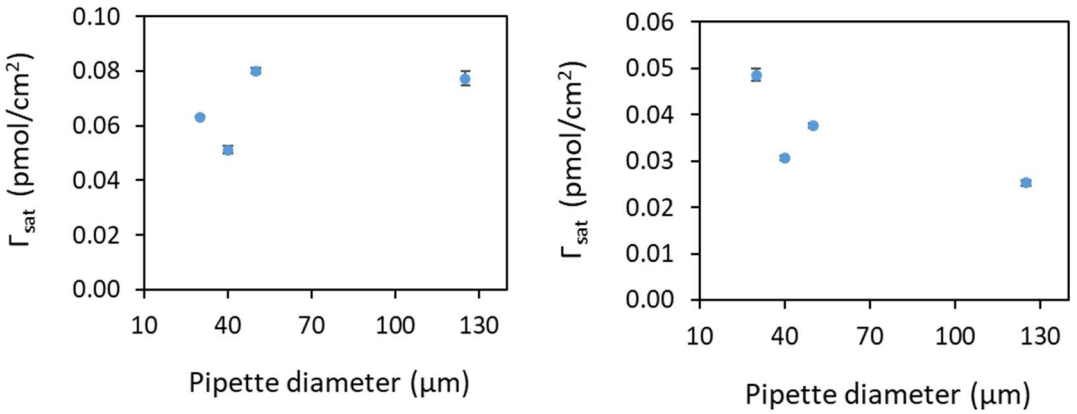

Figure 5.3.2.16: *Saturation of surface coverage for (a) forward and (b) reverse direction vs tips radius of different pipettes for TEB-tri-bCF₃ ionophore.*

Figure 5.3.2.16 shows the change of saturation surface coverage for sulphate-TEB-tri-bCF$_3$ complex with the size of interface. The saturation surface coverage decreases with the increase of liquid/liquid interface size for the reverse scan which is similar trend as seen with the sulphate-tren-bCF$_3$ complex.

Table 5.3.2.5: *Saturation surface coverage (Γ_{sat}) and adsorption coefficient (β) at different radius of pipettes for Tren-bCF$_3$ and TEB-tri-bCF$_3$.*

Tren-bCF$_3$						**TEB-tri-bCF$_3$**				
d (µm)	**Γ_{sat} (pmol/cm^2)**		**β x 10^6 (cm^3/mol)**			**d (µm)**	**Γ_{sat} (pmol/cm^2)**		**β x 10^6 (cm^3/mol)**	
	Forward	Reverse	Forward	Reverse			Forward	Reverse	Forward	Reverse
8	2.28	1.78	21	21		30	0.063	0.049	23	37
18	0.17	0.12	3	3		40	0.051	0.031	7	11
22	0.90	0.50	4	5		50	0.080	0.038	13	11
55	0.21	0.13	5	11		125	0.077	0.025	7	19

From Table 5.3.2.5 we can see that there is a general trend for saturation surface coverage which decreases with the increase of pipette radius. But the adsorption coefficient did not follow any pattern for different size of interfaces.

5.3.3 Cyclic voltammetry experiment with di-squaramide TEB-bis-CF_3 ionophore

Figure 5.3.3.1 shows a structure of di-squaramide ionophore which gives a different response than the previous two tri-squaramide ionophores. Figure 5.3.3.2 (a) shows the CV response for TEB-bis-CF_3 ionophore, where there is no response for blank. Figure 5.3.3.2 (b) shows the background subtracted voltammogram. Figure 5.3.3.3 (a) shows the voltammograms for different scan rates and Figure 5.3.3.3 (b) shows both forward and backward current is linearly dependent with square root of scan rate ($v^{1/2}$). So facilitated sulphate transfer with this ionophore is diffusion controlled [292, 294], while the previous two were adsorption controlled processes.

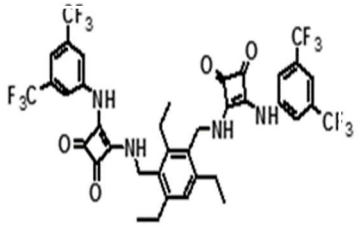

Figure 5.3.3.1: *Structure of di-squaramide sulphate ionophore TEB-bis-CF_3*

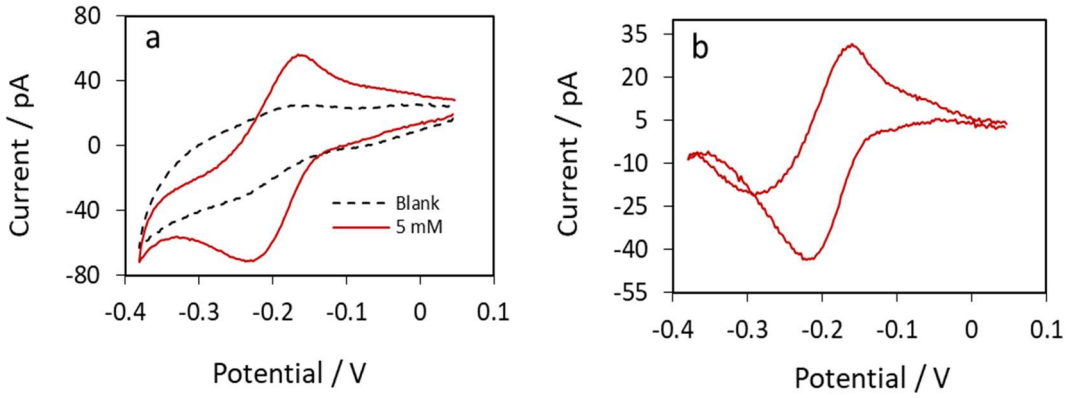

Figure 5.3.3.2: *(a) Cyclic Voltammograms of 5 mM sulphate ions with 0.25 mM TEB-bis-CF_3 ionophore and CV of background electrolyte (black dotted) and (b) background subtracted CV at 35 µm radius pipette. [Pipette radius with Equations 2.3.1.2 and 2.3.1.3 are also given in Appendix B.]*

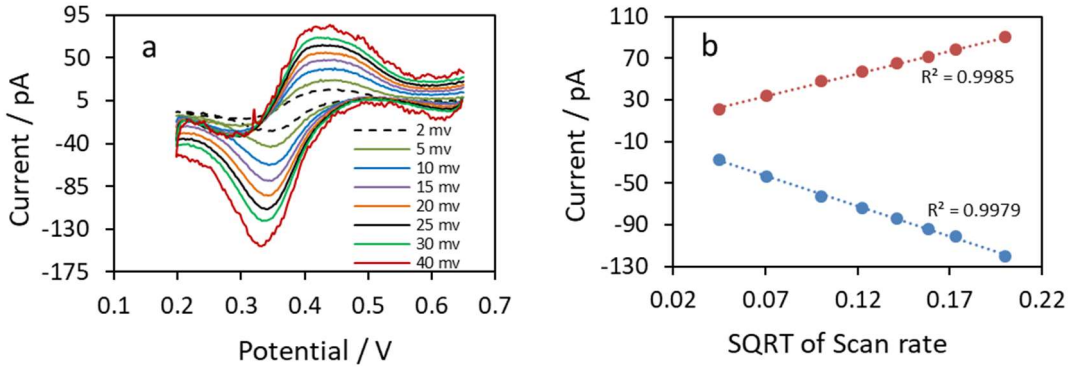

Figure 5.3.3.3: *(a) Cyclic voltammograms of 10 mM sulphate ions at different scan rates with 0.25 mM TEB-bis-CF_3 ionophore and (b) current vs scan rate for both forward and reverse scan. Radius of the pipette was 25 µm. [Pipette radius with Equations 2.3.1.2 and 2.3.1.3 are also given in Appendix B.]*

Peak to peak separation (ΔE) for this case is ≈ 58 mV and current ratio for forward and reverse peak is 1.11. This also satisfy the reversibility criteria, assuming that the ion transferring is HSO_4^- [292, 294]. As the process is reversible, the binding constant or association constant (K_a^o) was calculated for this ionophore. K_a^o was studied in an excess of sulphate in the aqueous solution ($C_{SO_4^{2-}} >> C_L$) according to Equation 5.3.3.1.

$$\Delta_o^w \emptyset_{1/2} = \Delta_o^w \emptyset_{SO_4^{2-}}^{o\prime} - \frac{2.303RT}{zF} \log(K_a^o \, c_{SO_4^{2-}}^w) \qquad \text{(Eq. 5.3.3.1)}$$

where $\Delta_o^w \emptyset_{SO_4^{2-}}^{o\prime}$ is the formal transfer potential of sulphate.

According to equation 5.3.3.1, plotting the half-wave potential ($\Delta_o^w \emptyset_{1/2}$) for the ion transfer process versus log($c_{SO_4^{2-}}^w$) gave a straight line (Figure 5.3.3.5). K_a^o was calculated from the y-axis intercept ($i_{y\text{-int}}$) of that straight line and using the equation 5.3.3.2.

$$i_{y-i} \quad = \Delta_o^w \emptyset_{SO_4^{2-}}^{o\prime} - \frac{2.303RT}{zF} \log(K_a^o) \qquad \text{(Eq. 5.3.3.2)}$$

However, there is uncertainty related to the formal potential of transfer of sulphate as it has not been previously reported at w/NPOE interfaces. At w/DCE interfaces, $\Delta_{DCE}^w \emptyset_{SO_4^{2-}}^{o\prime}$ has been reported as <-0.600 V [306] whilst $\Delta_{NPOE}^w \emptyset_{Br^-}^{o\prime}$ has been reported as -0.613 V [307] and $\Delta_{NPOE}^w \emptyset_{H_2PO_4^-}^{o\prime}$ as <-0.620 V [308]. For that reason, $\Delta_o^w \emptyset_{SO_4^{2-}}^{o\prime}$

was assumed to be ≤-0.62 V on the Galvani potential scale based on its large free energy of hydration [309] and its position in the Hofmeister series [310] with respect to the monovalent anions (i.e. dihydrogenphosphate or bromide).

Like trisquaramide ionophores this experiment was also done with four different size of micropipettes to check how the electrochemical properties changes with the size of the interface. Figure 5.3.3.4 shows the background subtracted voltammograms for different concentrations of sulphate ion at a 17.5 µm radius pipette. Table 5.3.3.1 shows the calculated data for half-wave potential at different concentrations. By using this data, half-wave potential vs log of sulphate concentration is plotted which gave a straight line (Figure 5.3.3.5). The value of the intercept of this straight line is 0.2095. The association constant (K_a^o) calculated using Equation 5.3.3.2 is 7.6 x 10^{13} M^{-1} for a 17.5 µm radius pipette. Diffusion coefficient (D) of the ionophore, which controls this transfer process was calculated 7.18 x 10^{-6} cm^2/s, by using the Equation 5.3.1.1 for this pipette.

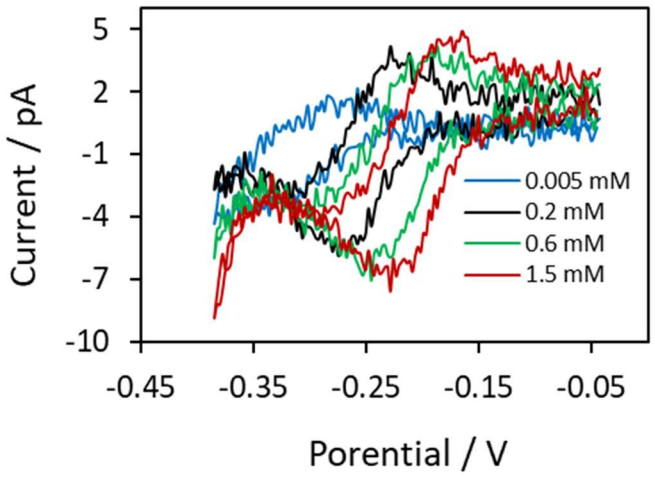

Figure 5.3.3.4: *Cyclic Voltammograms of sulphate ions of concentration 0.005, 0.2, 0.6 and 1.5 mM with 0.25 mM TEB-bis-CF_3 ionophore at 17.5 µm radius pipette. [Pipette radius with Equations 2.3.1.2 and 2.3.1.3 are also given in Appendix B.]*

Table 5.3.3.1: *Half-wave potential from cyclic voltammetry experiments of sulphate ions at different concentrations with 0.25 mM TEB-bis-CF_3 ionophore at a 17.5 µm radius pipette.*

Conc. (mM)	log (conc.) (mM)	Forward peak potential, E_1, (V)	Reverse peak potential E_2, (V)	$(E_1-E_2)/2$ (V)	1/2 E (V)
0.005	-2.301	-0.346	-0.272	-0.037	-0.309
0.02	-1.699	-0.312	-0.250	-0.031	-0.281
0.04	-1.398	-0.294	-0.238	-0.028	-0.266
0.08	-1.097	-0.279	-0.231	-0.024	-0.255
0.2	-0.699	-0.268	-0.221	-0.024	-0.245
0.4	-0.398	-0.26	-0.211	-0.025	-0.236
0.6	-0.222	-0.246	-0.192	-0.027	-0.219
0.8	-0.097	-0.231	-0.182	-0.025	-0.207
1.5	0.176	-0.226	-0.175	-0.026	-0.201

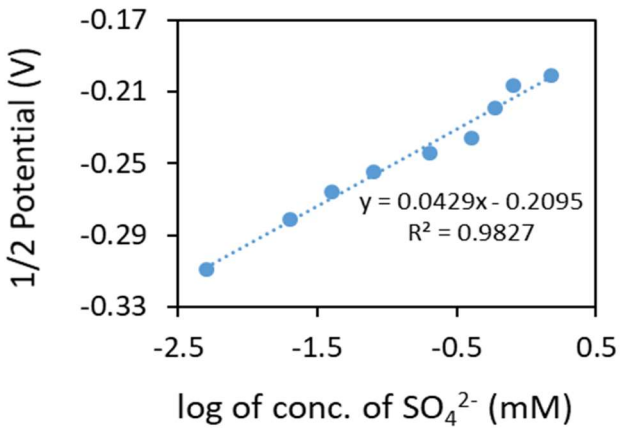

Figure 5.3.3.5: *Half-wave potential vs log of sulphate ion concentration for 17.5 µm radius pipette. [Pipette radius with Equations 2.3.1.2 and 2.3.1.3 are also given in Appendix B.]*

Figure 5.3.3.6 shows the background subtracted voltammograms of different concentrations of sulphate ion at 25 µm radius pipette. Table 5.3.3.2 shows the calculated data for half-wave potential at different concentrations. By using this data half-wave potential vs log of sulphate concentration is plotted which gave a straight line (Figure 5.3.3.7). Value of the intercept of this straight line is 0.1848. Association constant (K_a^o) calculated using Equation 5.3.3.2 is 5.2 x 10^{14} M^{-1} and the diffusion

coefficient (D) of the ionophore, which controls this transfer process was calculated 7.00 x 10^{-6} cm^2/s, by using the Equation 5.3.1.1 for this pipette.

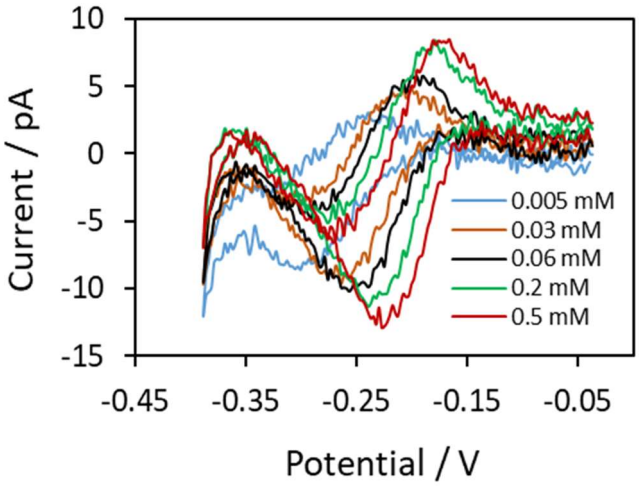

Figure 5.3.3.6: *Cyclic Voltammograms of sulphate ions of concentration 0.005, 0.03, 0.06, 0.2, 0.6 and 0.5 mM with 0.25 mM TEB-bis-CF_3 ionophore at 25 µm radius pipette. [Pipette radius with Equations 2.3.1.2 and 2.3.1.3 are also given in Appendix B.]*

Table 5.3.3.2: *Half-wave potential from cyclic voltammetry experiments of sulphate ions at different concentrations with 0.25 mM TEB-bis-CF_3 ionophore at 25 µm radius pipette.*

Conc. (mM)	log (conc.) (mM)	Forward peak potential, E_1, (V)	Reverse peak potential E_2, (V)	$(E_1-E_2)/2$ (V)	1/2 E (V)
0.005	-2.301	-0.301	-0.240	-0.031	-0.270
0.015	-1.824	-0.281	-0.223	-0.029	-0.252
0.03	-1.523	-0.264	-0.208	-0.028	-0.236
0.06	-1.222	-0.249	-0.196	-0.027	-0.223
0.1	-1.000	-0.237	-0.193	-0.022	-0.215
0.2	-0.699	-0.232	-0.183	-0.024	-0.208
0.3	-0.523	-0.227	-0.181	-0.023	-0.204
0.5	-0.301	-0.225	-0.171	-0.027	-0.198
1.0	0.000	-0.215	-0.162	-0.027	-0.188

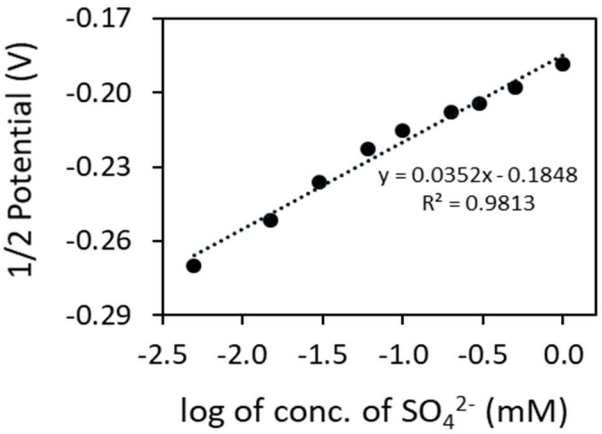

Figure 5.3.3.7: *Half-wave potential vs log of sulphate ion concentration for 25 µm radius pipette. [Pipette radius with Equations 2.3.1.2 and 2.3.1.3 are also given in Appendix B.]*

Figure 5.3.3.8 shows the background subtracted voltammograms for different concentrations of sulphate ions at a 35 µm radius pipette. Table 5.3.3.3 shows the calculated data for half-wave potential at different concentrations. By using this data half-wave potential vs log of sulphate concentration is plotted which gave a straight line (Figure 5.3.3.9). Value of the intercept of this straight line is 0.2089. Association constant (K_a^o) calculated using Equation 5.3.3.2 is 8.6 x 10^{13} M^{-1} and the diffusion coefficient (D) of the ionophore, which controls this transfer process was calculated 6.69 x 10^{-6} cm^2/s, by using the Equation 5.3.1.1 for this 35 µm radius pipette.

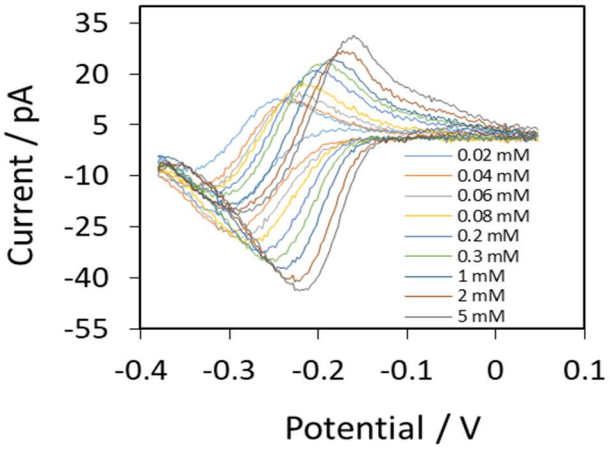

Figure 5.3.3.8: *Cyclic Voltammograms of sulphate ions of concentration 0.02, 0.04, 0.06, 0.08, 0.2, 0.3, 1.0, 2.0 and 5.0 mM with 0.25 mM TEB-bis-CF_3 ionophore at 35 µm radius pipette. [Pipette radius with Equations 2.3.1.2 and 2.3.1.3 are also given in Appendix B.]*

Table 5.3.3.3: *Half-wave potential from cyclic voltammetry experiments of sulphate ions at different concentrations with 0.25 mM TEB-bis-CF_3 ionophore at 35 µm radius pipette.*

Conc. (mM)	log (conc.) (mM)	Forward peak potential, E_1, (V)	Reverse peak potential E_2, (V)	$(E_1-E_2)/2$ (V)	1/2 E (V)
0.02	-1.699	-0.305	-0.239	-0.033	-0.272
0.04	-1.398	-0.297	-0.229	-0.034	-0.263
0.06	-1.222	-0.287	-0.217	-0.035	-0.252
0.08	-1.097	-0.275	-0.212	-0.032	-0.244
0.2	-0.699	-0.263	-0.200	-0.032	-0.232
0.3	-0.523	-0.248	-0.195	-0.027	-0.222
1	0.000	-0.236	-0.180	-0.028	-0.208
2	0.301	-0.222	-0.170	-0.026	-0.196
5	0.699	-0.219	-0.163	-0.028	-0.191

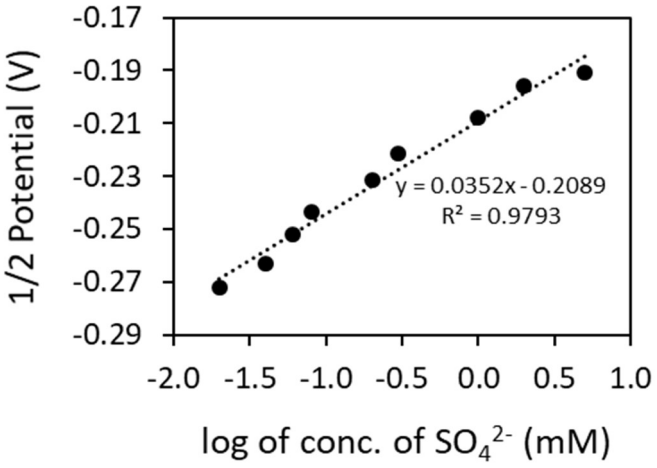

Figure 5.3.3.9: *Half-wave potential vs log of sulphate ion concentration for 35 µm radius pipette. [Pipette radius with Equations 2.3.1.2 and 2.3.1.3 are also given in Appendix B.]*

Figure 5.3.3.10 shows the background subtracted voltammograms for different concentrations of sulphate ions at 62.5 µm radius pipette. Table 5.3.3.4 shows the calculated data for half-wave potential at different concentrations. By using this data half-wave potential vs log of sulphate concentration is plotted which gave a straight line (Figure 5.3.3.11). Value of the intercept of this straight line is 0.2537. Association

constant (K_a^o) calculated using Equation 5.3.3.2 is 2.4 x 10^{12} M^{-1} and the diffusion coefficient (D) of the ionophore, which controls this transfer process was calculated 8.22 x 10^{-6} cm^2/s, by using the Equation 5.3.1.1 for this 62.5 µm radius pipette.

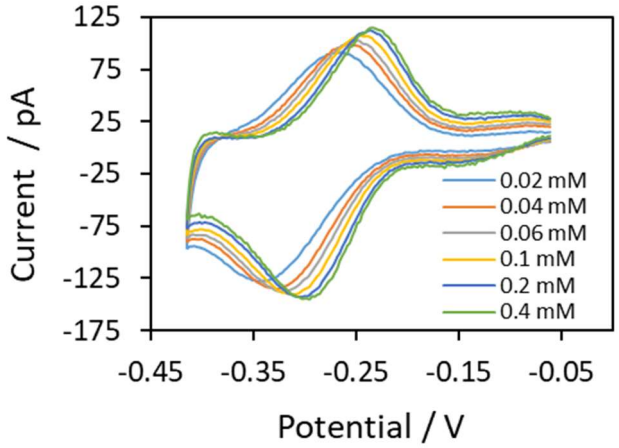

Figure 5.3.3.10: *Cyclic Voltammograms of sulphate ions of concentration 0.02, 0.04, 0.06, 0.1, 0.2 and 0.4 mM with 0.25 mM TEB-bis-CF_3 ionophore at 62.5 µm radius pipette. [Pipette radius with Equations 2.3.1.2 and 2.3.1.3 are also given in Appendix B.]*

Table 5.3.3.4: *Half-wave potential from cyclic voltammetry experiments of sulphate ions at different concentrations with 0.25 mM TEB-bis-CF_3 ionophore at 62.5 µm radius pipette.*

Conc. (mM)	log (conc.) (mM)	Forward peak potential, E_1, (V)	Reverse peak potential E_2, (V)	$(E_1-E_2)/2$ (V)	1/2 E (V)
0.02	-1.70	-0.337	-0.266	-0.035	-0.301
0.04	-1.40	-0.327	-0.254	-0.037	-0.290
0.06	-1.22	-0.320	-0.249	-0.035	-0.284
0.1	-1.00	-0.310	-0.243	-0.033	-0.276
0.2	-0.70	-0.302	-0.234	-0.034	-0.268
0.4	-0.40	-0.295	-0.232	-0.032	-0.263
0.7	-0.15	-0.293	-0.227	-0.033	-0.260
1	0.00	-0.288	-0.224	-0.032	-0.256

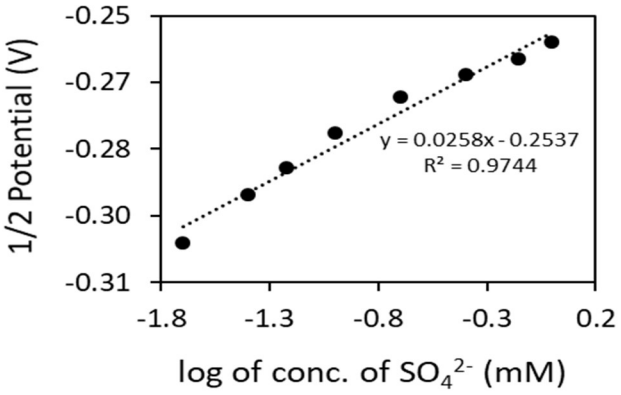

Figure 5.3.3.11: *Half-wave potential vs log of sulphate ion concentration for 62.5 µm radius pipette. [Pipette radius with Equations 2.3.1.2 and 2.3.1.3 are also given in Appendix B.]*

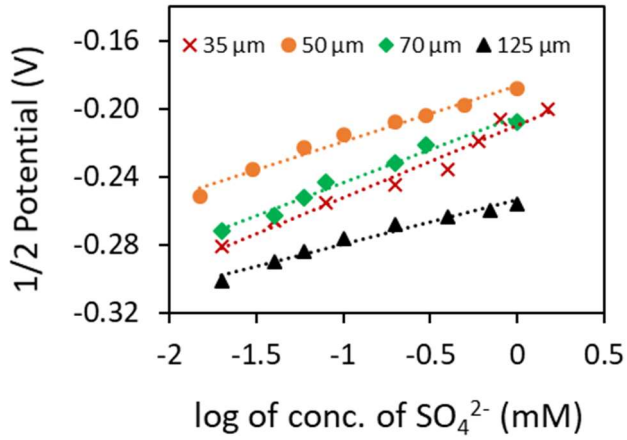

Figure 5.3.3.12: *Half-wave potential vs log of sulphate ion concentration for 17.5, 25, 35 and 62.5 µm radius pipettes. [Pipette radius with Equations 2.3.1.2 and 2.3.1.3 are also given in Appendix B.]*

Table 5.3.3.5: *Association constants (K_a) from the y-intercept of half-wave potential vs log of sulphate ion concentration graph and the diffusion coefficient (D) for 17.5, 25, 35 and 62.5 µm radius pipette.*

Size (µm)	**y-int**	***K_a (M^{-1})***	**log *K_a* (M^{-1})**	**Average log *K_a* (M^{-1})**	***D* cm^2/s**
35	-0.210	7.6×10^{13}	13.9	13.7 (± 0.98)	7.18×10^{-6}
50	-0.185	5.2×10^{14}	14.7		7.00×10^{-6}
70	-0.208	8.6×10^{13}	13.9		6.69×10^{-6}
125	-0.254	2.4×10^{12}	12.4		8.22×10^{-6}

Figure 5.3.3.12 shows the half-wave potential vs log of concentration of sulphate for all four experiments in different radius pipettes. Calculated association constants with y-axis intercept for all experiments are summarized in Table 5.3.3.5. The diffusion coefficient of ionophore for four different size ITIES were also summarized in the table. From the results it has been seen that the diffusion coefficient increases with the decreases of the interface size.

Overall, for this detection of sulphate analysis we observed, all the three ionophores can detect the sulphate ions at ITIES. But the transfer of sulphate mechanism varies, depending on the structure of ionophores. The tripodal ionophores like tren-bCF_3 and TEB-tri-bCF_3 transfer sulphate ions by adsorption mechanism, whereas the dipodal ionophore (TEB-bis-CF_3) transfer sulphate ions by diffusion mechanism. As the sulphate transfers across the interface by making a complex with the ionophore and the investigation showed that the same transfer mechanism followed for the same structure of ionophores, so, it is clear that the transfer mechanism depends on structure of ionophore and structure of ionophore-sulphate complex. The transfer potential of sulphate with three different ionophores are different, but same for the same ionophore with different size of pipettes. This also proves that the sulphate transfers via a complexation reaction with ionophores and as the transfer potential depends on the nature of the ionophore-sulphate complex substances. It has been also observed from this investigation that for the adsorption process, the calculated values of adsorption coefficient has no consistency or did not follow any sequence. This could be for the error of the extracting values from the experimental data or could be for the differences of the experimental setup, environmental conditions.

5.4 Conclusion

The electrochemical characterization for three different new squaramide ionophores for sulfate detection were examined utilizing cyclic voltammetry at single μITIES on the tip of pipettes. All three ionophores gave very good response. The tripodal ionophores (tren-bCF_3 & TEB-tri-bCF_3) show the transfer of sulphate through the interface via adsorption mechanism [292]. These also follows the Langmuir adsorption isotherm as well as linearization of Langmuir isotherm and both of those form sub-monolayers at the interface [300-302]. However the dipodal ionophore (TEB-bis-CF_3) shows diffusion control mechanism [292]. Thermodynamic parameters like the

association constant was investigated at four different size of micro-interface for this dipodal ionophore and the results from four different size interfaces shows close agreement. The values of diffusion coefficient of ionophore shows that it increases with the decrease of interface size.

Chapter 6

General Conclusions

6.1 General Conclusions

The aim of this research work was to evaluate the electrochemical properties of various types of chemical species at micro-ITIES supported at the tip of micropipettes. The single micro-ITIES immerged as a strong platform for the electrochemical characteristics of ionized molecules. By using this platform, we have investigated four different types of species, namely PFAS molecules, four generation of dendrimers, sulphate anions and metal ions. One of the major task for the research was to create stable and reproducible micro-ITIES at the tip of the micropipettes in order to get reliable and comparable data. Because of this, pipette preparation and characterization was a very important part throughout this research work.

Different sizes of pipettes have been prepared from borosilicate or quartz glass capillaries by using P2000 CO_2 laser-based pipette puller. The size and shape of the pipettes depend on the five pulling parameters, namely heat (H), filament (F), velocity (V), delay (D) and pull (P). The inner side of the pipettes were converted to hydrophobic nature by a silanization process to provide a stable ITIES at the tip of the pipettes. Here we described and utilized a new silanization process which makes this process easier. Silanization of the pipettes was checked by electrochemical analysis and compared with electrochemical results from nonsilanized pipettes. This analysis showed that the silanized pipettes create stable ITIES and reproducible data, whereas the ITIES at nonsilanized pipettes were unstable, which demonstrates that the new simple process of silanization works perfectly. The reproducibility of the pipettes of different size was checked by both scanning electron microscopy (SEM) and electrochemical measurements. Five different sizes of pipettes were produced by five different pulling programs at different times. Among these five programs, two were for micropipettes and three for nanopipettes. The different types of micropipettes were examined by both electrochemical and SEM measurements and the three sets of nanopipettes were examined by SEM. Eight micropipettes prepared by pulling parameters H: 400; F: 4; V: 20; D: 200 and P: 70 were examined by CV analysis and the measured diameter was 2.81 (± 0.35) µm with 12.32% relative standard deviation (RSD). Ten micropipettes with the same pulling parameters were measured by SEM where the average diameter was calculated as 2.95 (± 0.25) µm with 8.34% RSD. Another set of micropipettes was prepared with pulling parameters H: 550; F: 2; V:

30; D: 130 and P: 75. The average diameter of this type of micro-pipettes measured by electrochemical and SEM techniques are 2.94 (± 0.25) µm and 2.65 (± 0.21) µm with RSD 8.58% and 7.80% respectively. The tip size of the three different types of nanopipettes were examined by SEM and the average tip diameters were 447 (± 32.5) nm, 296 (± 12.7) nm and 129 (± 5.7) nm with RSD 7.26%, 4.30% and 4.39% respectively. The pipette preparation and analysis were continued throughout the thesis work, which proved the reproducibility of the prepared pipettes by P2000 pipette puller.

Four per- and polyfluoroalkyl (PFAS) substances (i.e. PFOA, PFBS, PFHxS & PFOS) have been studied at micro-ITIES formed at the tips of the prepared micropipettes by applying cyclic voltammetry and differential pulse voltammetry. All four PFAS substances were successfully detected at micro-ITIES by both CV and DPV. The transfer potential of the four different substances changed according to their lipophilicity, which depends on the carbon number and also on the functional groups present in that particular substances. Diffusion coefficients of the PFAS substances in aqueous solution were calculated from CV measurements by using the Saito equation. The LOD was also calculated for both CV and DPV methods and it has been found that the LOD by DPV technique gave 7-to-32 times lower compared to the CV method. Another major investigation for this study was to observe the selectivity in the mixture solution. It has been observed that DPV could detect the PFAS molecules from a mixture of solution, except for the mixtures PFOA - PFBS and PFHxS - PFOS, which gave only a single big peak, instead of two separate peaks, because their transfer potentials are very close together.

PAMAM dendrimers can be viewed as the model molecules of proteins. Dendrimers have amine groups which are protonated in aqueous solution at different pH according to their p*Ka* values, which makes them amenable to detection at the ITIES. This is the first electrochemical investigation of four generations of PAMAM dendrimers at the ITIES formed at micropipettes with a wide range of pH variation. We applied both cyclic voltammetry and differential pulse voltammetry to study the transfer mechanism and other kinetic parameters. The CV experiments showed all four generation dendrimers follow diffusion mechanism transfer from aqueous to organic phase at all pH. However, the transfer from organic to aqueous phase varies with both

pH and the generation of dendrimer. G2 and G3 follow an adsorption mechanism at pH 3.5 to lower pH and follow a diffusion-controlled mechanism from pH 6.0 to higher pH. On the other hand, smaller dendrimers, G0 and G1 always follow diffusion mechanism at all pH values although they did not have any response at very high or at very low pH and maximum signal was obtained at pH 3.5. But G2 and G3 show better responses at lower pH 1.75 and 2.75, respectively. Results show that the diffusion coefficient increases gradually with the increase of pH and decreases with the increase of generation number within the same pH. The LOD by CV analysis has been found in ranges 0.24 – 0.72 μM for G0 to G3, whereas the LOD by DPV analysis was between 0.05 – 0.09 μM, which are 5 to 8 times lower than CV measurements.

Electrochemical detection of sulphate ion has been also investigated at the μITIES formed at the tip of pipettes. Three new squaramide ionophores were examined utilizing cyclic voltammetry. It has been found that all three ionophores have very good capability to bind with sulphate ions. Among the three, the two tripodal ionophores tren-bCF_3 & TEB-tri-bCF_3 transfer sulphate ions through the interface via an adsorption mechanism. They also follow the Langmuir adsorption. Is has also been observed that a sub-monolayer was formed at the interface for both of these tripodal ionophores. All the experiments for this two ionophores has been undertaken at four different size of micro-interfaces. One the other hand, diffusion control transfer mechanism was observed for sulphate ion transfer by the dipodal ionophore TEB-bis-CF_3. AS a result, the thermodynamic parameter association constant (K_a) has been investigated at different size of micro-interface for the sulphate-dipodal ionophore transfer process.

This investigation on electrochemical detection and characterization of different species at single μITIES using micropipettes demonstrate that the research on μITIES has emerged as a powerful technique in analytical electrochemistry. The applications of various types of micro- and nanoscopic L/L interfaces have blossomed in the past few decades in various research fields such as for the detection and characterization of inorganic ions, drug molecules, proteins, neurotransmitters, enzyme-catalyzed reaction, DNA detection, carbohydrate detection and so on. According to this research in different projects, it shows that the ITIES is a powerful technology that can be used to investigate a wide range of analytes. Using single nano-ITIES it might be possible to detect single macromolecules like protein, DNA etc. However, the ITIES could be

an alternative platform for electrochemists to develop sensors/biosensors. There are lots of other opportunities to develop devices using arrays of micro/nano-ITIES to achieve the required LODs. For example, in our PFAS detection with single micro-ITIES, LOD is much higher than established safety limits. But by employing the arrays nano/micro-ITIES, it could be possible to reach the desired LODs. Likewise, the ITIES could offer scope for a better gas sensor, as the soft interface is much more sensitive and capable to react with gaseous substances. Scanning electrochemical microscopy (SECM) with the tip of a micro- or nano- pipette also has become a useful scanning probe technique for quantitative monitoring of chemical reactivity as well as enabling the imaging of the electrochemical properties of a surface or interface with an ion. Currently SECM has become a powerful method for chemists to investigate electrochemical processes happening in living cells.

For fundamental research, single μITIES have become a useful and reliable platform because of its simple instrumentation, low cost, needed low amounts of chemicals, as well as suitable for in field application. It overcomes lots of limitations faced in conventional and macro-ITIES, especially for various kinetic and thermodynamic parameters. This thesis work is a fundamental research to elucidate the electrochemical behaviour of the molecules at the liquid/liquid interface, which will show the path for future analysis, such as, sensor development, better understanding the transfer mechanism at biological membranes etc. Nevertheless, there are also some limitations, such as the glass micropipettes are too much fragile to handle, very difficult to clean and reuse the same pipette. Still there is lots of opportunities to strengthen this research area.

Appendix A

Electrochemical Detection and Extraction of Metal Ions.

This is a preliminary work, that's why added as an appendix.

A.1 Introduction

Separation or extraction of metals from solutions is a challenging task. Solvent extraction has been an extensively used method for analytical investigation of separation of metals. In conventional solvent extraction method, use of extractants or ionophores either in organic solvents or in aqueous phase is an important industrial technique for the recovery and refining of metals from dilute solutions [311-314].

Electro-assisted extraction across a liquid/liquid interface can be a novel method for metal extraction. David J. Schffrin and his group [315] reported about the successful separation of Ni^{2+}, Cu^{2+} and Cd^{2+} ions at ITIES. They used 2, 2'; 6', 2''-terpyridine as an extractant or facilitator in organic solvent 2-heptanone. Additionally the transfer of heavy and transition metal ions (Cd^{2+}, Co^{2+}, Cu^{2+}, Mn^{2+}, Ni^{2+}, Zn^{2+}) at a water/2-octanone interface facilitated by terpyridine has been reported by Cheng and Schffrin [316]. Terpyridine also used to transfer metal ions Fe, Co, Ni, Cu and Zn at water/2-octanone interface [317].

Acorga M5640 is one of the most widely used effective solvents for recovery of copper from aqueous solutions [318-322]. Acorga M5640 consists of 5-nonylsalicylaldoxime (5-nonyl-2-hydroxy-benzaldoxime) as an active substance and a fatty ester as a modifier [320, 323] and is highly selective for copper over iron [320, 321, 324]. Yang et al. [320] used 10% (v/v) Acorga M5640 and 2% (v/v) trialkyl phosphine oxides (TRPO) for copper and nickel extraction and reported that more than 99.96% of copper could be recovered from the solution.

In this investigation, initially we have used Acorga M5640 as an extractant or facilitator for Co^{2+} and Ni^{2+} ions transfer across the DCE/water micro-interface supported by a micropipette. We added Acorga to the organic solvent DCE in different compositions and applied cyclic voltammetry to observe the Co^{2+}/Ni^{2+}ion transfer at various pHs of aqueous solution. Mixed organic solvent (DCE & 1-decanol) also used to characterized the liquid/liquid interface.

A.2 Experimental

A.2.1 Reagents

Acorga M5640 was supplied by Cytec Australia. All other reagents were purchased from Sigma-Aldrich Australia Ltd. and used as received unless otherwise indicated. The organic electrolyte bis(triphenylphosphoranylidene)ammonium tetrakis(4-chlorophenyl)borate (BTPPATPBCl) was prepared by metathesis of equimolar amounts of bis(triphenylphosphoranylidene)ammonium chloride (BTPPACl) and potassium tetrakis(4-chlorophenyl)borate (KTPBCl) as reported earlier [77]. BTPPATPBCl (0.01 M) solutions were prepared in 1,2-dichloroethane (DCE). Chlorotrimethylsilane was used for silanization of pipettes. All aqueous solutions (e.g. LiCl solution) were prepared in purified water from a USF Purelab plus UV (resistivity: 18.2 MΩ cm). 10 mM $CoSO_4.7H_2O$ and 10 mM $NiSO_4.6H_2O$ was prepared as stock solution**.**

A.2.2 Electrochemical cell

Electrochemical measurements were conducted by using an Autolab PGSTAT302N electrochemical analyser (Metrohm Autolab, Utrecht, The Netherlands) running with NOVA software. The organic electrolyte phase was introduced into the pipette which comes up to the tip and the organic reference solution (saturated BTPPACl in 10 mM LiCl) was placed on the top of the organic phase. Then the pipette was immersed into the aqueous phase so that an ITIES formed at the tip of the pipette. As this was a miniaturized interface, so a two-electrode system was employed for this electrochemical cell. An Ag/AgCl electrode was in the aqueous solution and another Ag/AgCl electrode used in the organic reference solution. The micro-interface was polarised by imposing a potential difference between these two electrodes. Unless stated otherwise, 10 mVs^{-1} scan rate was applied to carry out cyclic voltammetry (CV) experiments. The pH of the aqueous LiCl solution was adjusted by using NaOH or HCl solution. The cell is described in the following scheme.

$$\text{Ag} \,\big|\, \text{AgCl} \,\big|\, \begin{matrix}\text{Sat'd BTPPACl} \\ \text{in 10 mM LiCl}\end{matrix} \,\big|\, \begin{matrix}\text{10 mM BTPPATPBCl in} \\ \text{DCE + x \% acorga}\end{matrix} \,\big\|\, \begin{matrix}\text{x } \mu\text{M } CoSO_4 \text{ / } NiSO_4 \\ \text{in 10 mM LiCl at diff. pH}\end{matrix} \,\big|\, \text{AgCl} \,\big|\, \text{Ag}$$

A.3 Results and discussions

A.3.1 Detection of Co^{2+} ions at ITIES by applying Cyclic Voltammetry

The transfer of cobalt ions across the microinterface between water and DCE formed at the tip of a glass micropipette was studied by cyclic voltammetry to analyse the electrochemical behaviour of Co^{2+} at different aqueous phase pHs. Acorga M5640 was added to the organic phase at different percentages to examine the impact on transfer process. pH of the aqueous solution also varied to check at which pH is good for Co^{2+} transfer. The cyclic voltammograms starts from a low potential and the forward scan was in a positive direction. The potential window is limited by the transfer of background electrolyte at low and high potentials. Figure A.3.1.1 shows the CVs of tetraethylammonium ion (TEA) transfer to check the interface without Acorga and with 50% Acorga in the organic phase. Without Acorga (only DCE organic phase), it shows the blank response is good and that 40 µM TEA gave an ideal voltammetric response. However, when 50% Acorga was added in the DCE phase, then the Figure shows that the blank scan becomes very resistive. It may be because the Acorga molecules block the interface that is why the molecules could not transfer through the ITIES. Figure A.3.1.1 also shows that there is no response for 80 µM TEA. This means that the interface becomes block with Acorga molecules.

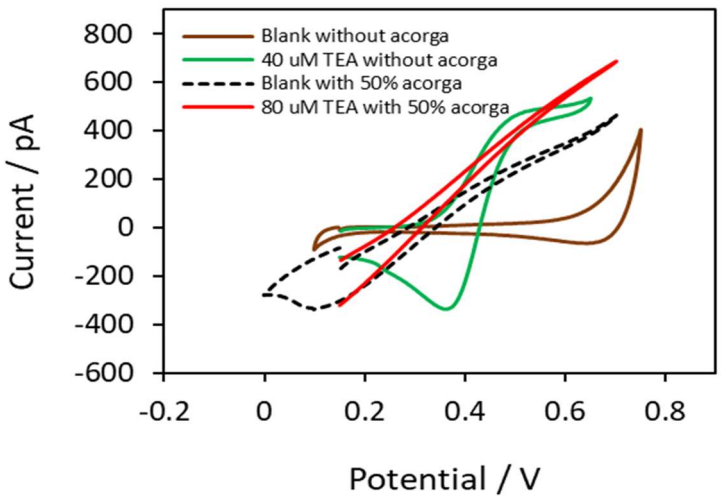

Figure A.3.1.1: *The brown CV response for the blank with DCE only in the organic phase, the green CV is for 40 µM TEA response in that ITIES, the black dashed line CV is for DCE with 50% Acorga and the red one is for 80 µM TEA across the interface with Acorga.*

The percentage of Acorga was then decreased from 50% to 10%. Figure A.3.1.2 shows the TEA response with 10% Acorga in the organic phase. The black dashed voltammogram is for the background voltammogram where no Acorga was added. The green voltammogram is also for the background with 10% Acorga in the organic phase DCE. It shows that the background CV with Acorga changed and decreased the potential window at higher potential. But still it is good and stable compared to the previous blank with 50% Acorga. Then 60 µM TEA was added in the aqueous solution to check the ion transfer behaviour of this ITIES. The red voltammogram is for the transfer for the TEA and its shape looks like an ideal transfer of TEA at DCE/water interface, which indicate that the system is working well.

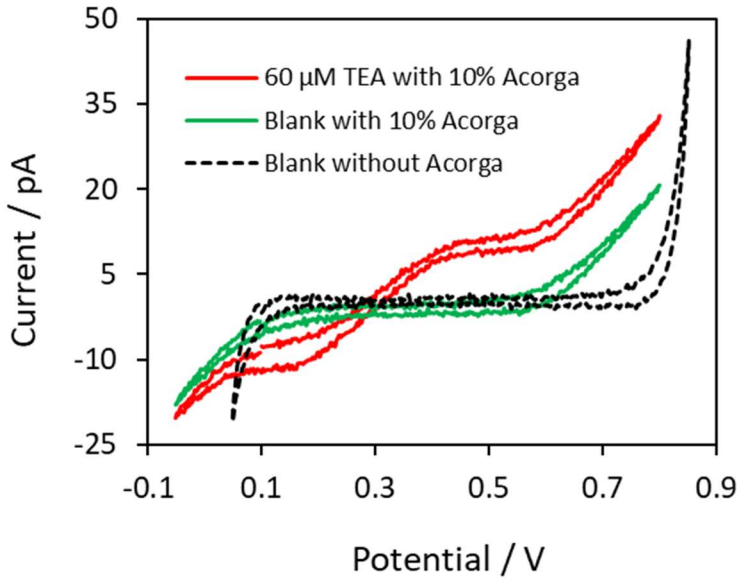

Figure A.3.1.2: *The black dotted voltammogram is the response for the background electrolytes without Acorga, the green one is also for the background electrolytes with 10% Acorga at DCE organic phase and the red CV is for the 60 µM TEA transfer at ITIES with 10% Acorga in DCE.*

A.3.2 pH effect

To check the electrochemical properties of metal ion cobalt (Co^{2+}) at the ITIES we apply cyclic voltammetry at different pH of the aqueous solution. In Figure A.3.2.1, the CV response for 10 mM $CoSO_4$ shows that at pH 3.5, no Co^{2+} ions transfer happens

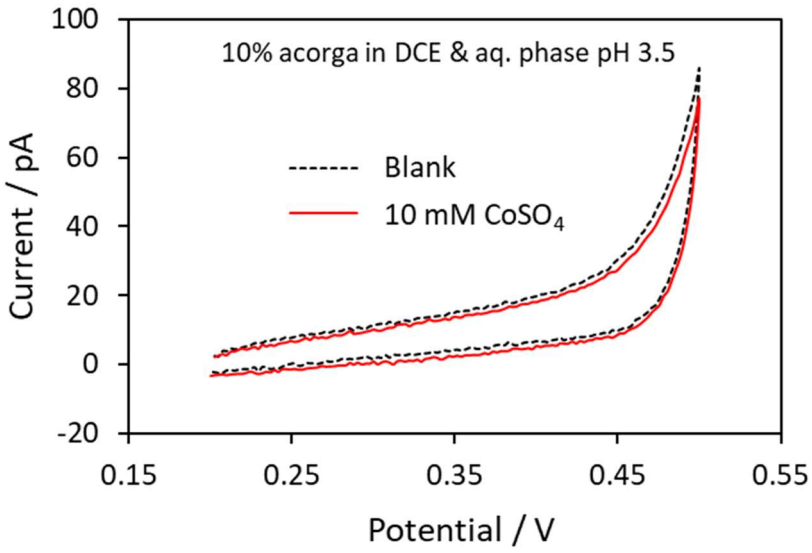

Figure A.3.2.1: *Cyclic voltammogram of background electrolytes (black) and 10 mM $CoSO_4$ in aqueous phase (red) at pH 3.5 with 10% Acorga in organic phase. The radius of the tip of the pipette was 5 µm.*

at ITIES. Similar results were obtained at a higher pH as well. Figure A.3.2.2 shows the cyclic voltammograms of background electrolytes (black) and for 10 mM $CoSO_4$ (red). The two CVs are identical, which means no Co^{2+} ion transfers at ITIES at pH 11.0.

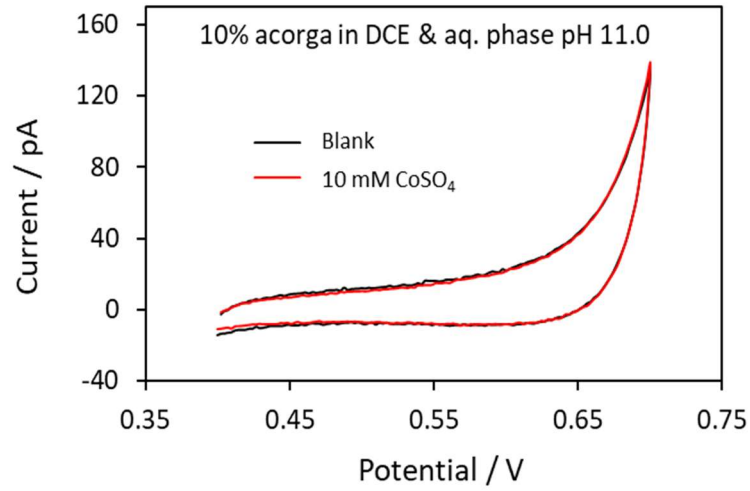

Figure A.3.2.2: *Cyclic voltammogram of background electrolytes (black) and 10 mM $CoSO_4$ in aqueous phase (red) at pH 11 with 10% Acorga in organic phase. The radius of the tip of the pipette was 5 µm.*

At pH A.0, the Co^{2+} ions gave a response at ITIES with 10% Acorga in the organic phase. That means, at this pH, when potential is applied then the Co^{2+} ions transfer between the two phases. Figure A.3.2.3 shows the cyclic voltammograms of 0.2, 0.5, 1.0 5.0 and 10.0 mM Co^{2+} ions. It also shows that the current increases up to 5 mM.

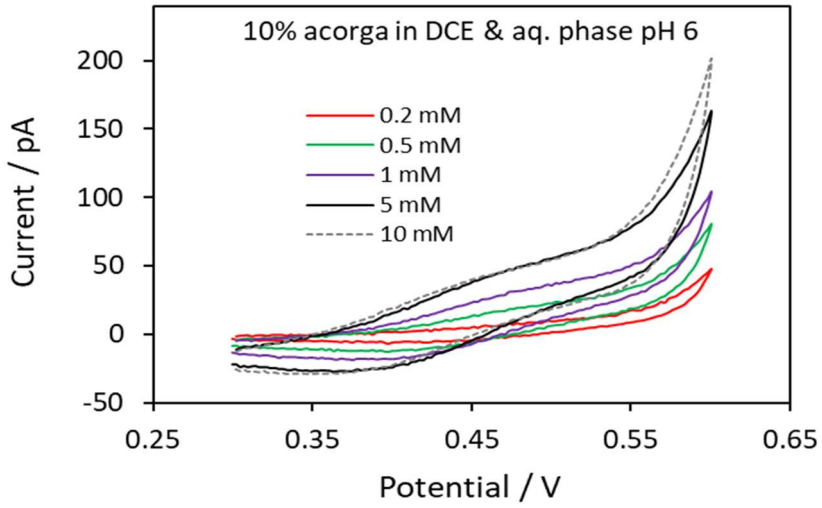

Figure A.3.2.3: *Cyclic voltammograms of 0.2, 0.5, 1, 5 and 10 mM $CoSO_4$ at pH 6 with 10% Acorga in organic phase. The radius of the tip of the pipette was 5 µm.*

We also checked the Co^{2+} ions electrochemical properties across the ITIES at pH 9.0 and we got a slightly higher response at this pH compared to the response of pH A. Figure A.3.2.4 shows the background subtracted CVs of 3 mM and 15 mM $CoSO_4$ with the presence of 10% Acorga in the organic phase. The shape of the voltammogram for Co^{2+} transfer at the ITIES did not match with any ideal voltammogram at ITIES. From the Figures A.3.2.3 and A.3.2.4, we can see that the transfer started around at 0.35 V and the current increases linearly until it reaches the background electrolyte transfer. Normally, a forward transfer process at a micro-ITIES formed at the tip of a pipette, occurs with radial diffusion control (from outside to the inside of the pipette) and gives a sigmoidal voltammogram or a steady state current (as seen for TEA transfer in Figures A.3.1.1 and A.3.1.2). But for this case, it gave almost a linear increase.

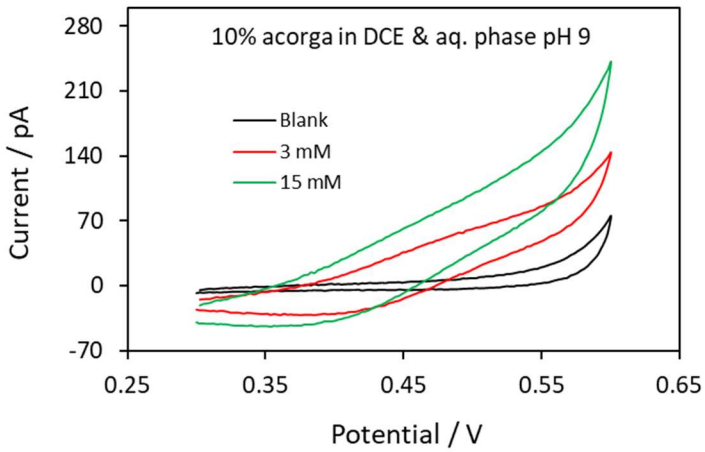

Figure A.3.2.4: *Background subtracted cyclic voltammograms of 3 mM and 15 mM $CoSO_4$ at pH 9 with 10% Acorga in organic phase. The radius of the tip of the pipette was 5 µm.*

Figure A.3.2.5 shows the background subtracted CVs of 0.1, 0.5, 1.0, 3.0, 5.0, 10.0 and 15.0 mM $CoSO_4$. Earlier it has been seen that for pH 6, the current increased up to 5 mM $CoSO_4$ (Figure A.3.2.3). But for pH 9, the Figure A.3.2.5 shows that the current increased linearly with concentration. So, from this investigation at four different pH, it has been found that at very low pH 3.5 and at very high pH 11.0, the Co^{2+} ion is not active at the ITIES. Whereas at pH A.0 and pH 9.0, Co^{2+} ion transfer across the ITIES and CV response is little bit higher at pH 9.0.

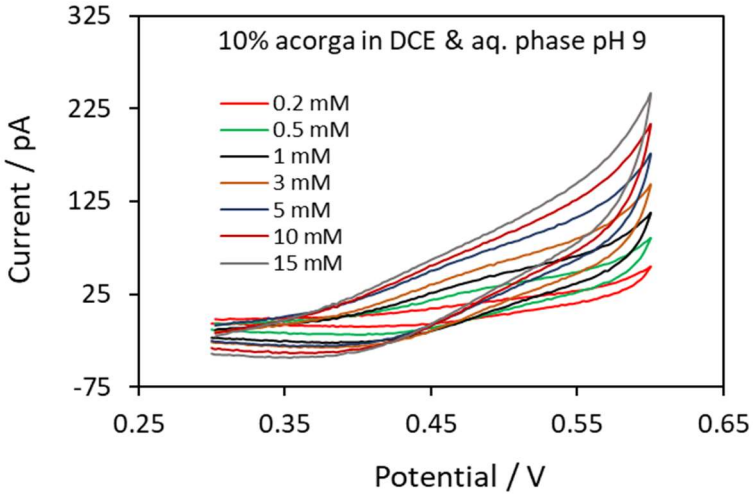

Figure A.3.2.5: *Background subtracted cyclic voltammograms of 0.2, 0.5, 1, 3, 5, 10 and 15 mM $CoSO_4$ at pH 9 with 10% Acorga in organic phase. The radius of the tip of the pipette was 5 µm.*

As pH 9.0 gave the best result, so, at this pH, we investigated the Acorga and DCE composition to identify the better composition for Co^{2+} ion transfer. Figure A.3.2.6 shows the voltammogram for 15 mM $CoSO_4$ transfer with 5% Acorga in the organic phase. If we compare the Co^{2+} ion transfer with 5% Acorga and with 10% Acorga (Figure A.3.2.4) in the organic phase, then it clearly indicates that the current response for Co^{2+} ion transfer with 10% Acorga is higher than with 5% Acorga at the same micro size interface.

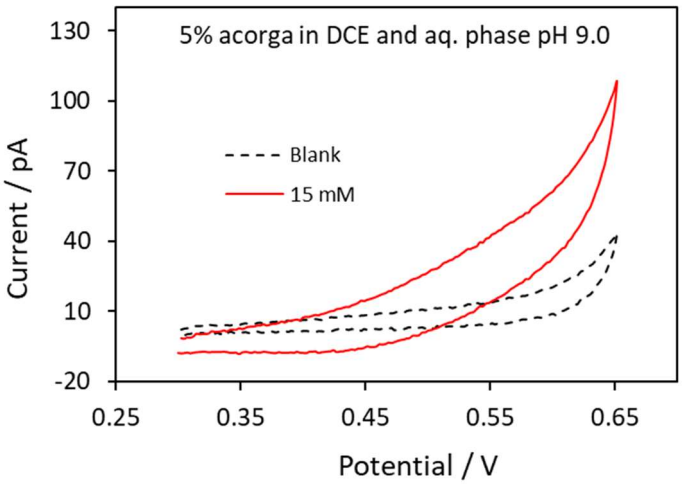

Figure A.3.2.6: *Cyclic voltammograms of 15 mM $CoSO_4$ (red) and CV for background electrolytes (blank) at pH 9 with 5% Acorga in organic phase. The radius of the tip of the pipette was 5 µm.*

Figure A.3.2.7 shows the background subtracted CVs of 0.1, 0.5, 1, 4, 10 and 15 mM Co^{2+} ions transfer at the micro-ITIES with 5% Acorga in organic phase. Like the transfer with 10% Acorga (Figure A.3.2.5), in this case also, the current response increased linearly with concentrations. But mentioned earlier (Figure A.3.2.5) that this current responses are lower than that of current responses with 10% Acorga.

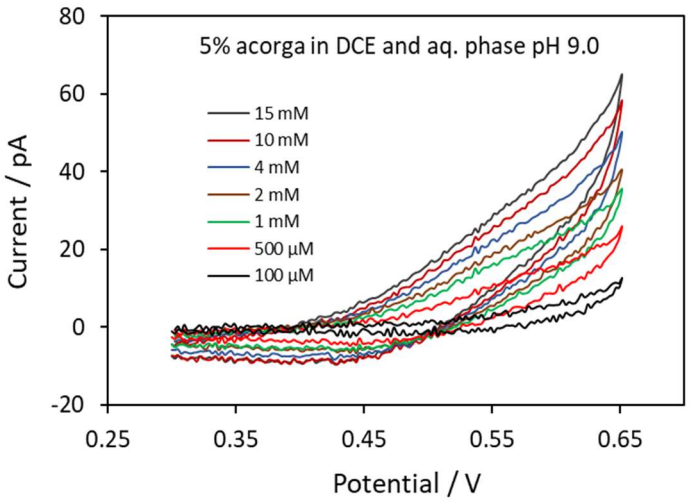

Figure A.3.2.7: *Background subtracted cyclic voltammograms of 0.1, 0.5, 1, 2, 4, 10 and 15 mM $CoSO_4$ at pH 9 with 5% Acorga in organic phase. The radius of the tip of the pipette was 5 µm.*

A similar experiment was carried out with 1% Acorga in the organic phase. Figure A.3.2.8 shows the shows the CVs of 0.1, 0.4, 2, 8 and 15 mM Co^{2+} ions transfer at the microITIES with 1% Acorga in the organic phase. It is clear that the current response again decreased with the decrease of Acorga in organic phase.

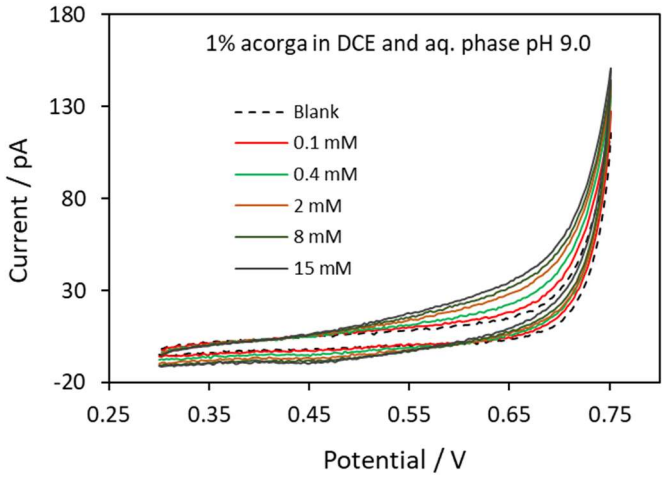

Figure A.3.2.8: *Background subtracted cyclic voltammograms of 0.1, 0.4, 2, 8 and 15 mM $CoSO_4$ at pH 9 with 1% Acorga in organic phase. The radius of the tip of the pipette was 5 µm.*

A.3.3 Mixed organic solvent

Conventionally, the ITIES is formed with a relatively more dense organic solvent than the aqueous phase and with relative permittivity around 10-15. A variety of organic solvents like nitrobenzene (NB), 1,2-dichloroethane (DCE), acetophenone, 1,2-dichlorobenzene (DCB), 1,6-dichlorohexane and 1,1-dichlorobutane are widely using in electrochemical studies at the ITIES. There are some limitations for the wider applications of these solvents and toxicity is one of them. For last two decades the use of mixed organic solvents has attracted attention, because of the opportunity to use lower density organic solvents with lower toxicity as well as to achieve a higher permittivity. In this study, we mixed 1-decanol with DCE in the organic phase to check the electrochemical properties of such an ITIES and the transfer of Co^{2+} ions across that ITIES. All the experiments with mixed organic solvents has been performed at pH 9, as this pH gave the better result for Co^{2+} ion transfer. Figure A.3.3.1 shows the CVs of background electrolytes and 10 mM $CoSO_4$, where 20% 1-decanol was mixed in the DCE organic phase with 10% Acorga. The CV shows that no signal or response was observed for Co^{2+} ion transfer. The potential window was smaller compared to a DCE-only organic phase.

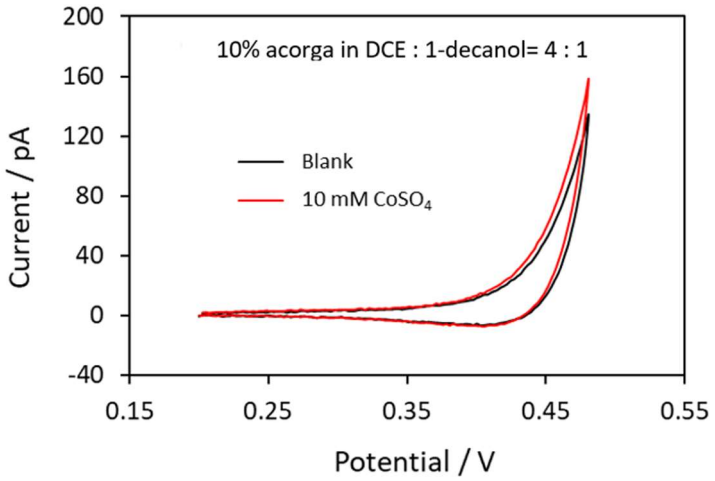

Figure A.3.3.1: *Cyclic voltammogram of background electrolytes (black) and 10 mM $CoSO_4$ in aqueous phase (red) with mixed organic solvents (10% Acorga in DCE:1-decanol = 4:1) at pH 9. The radius of the tip of the pipette was 5 µm.*

The percentage of 1-decanol was increased from 20% to 50% in the organic phase. Figure A.3.3.2 shows the CVs of background electrolytes and 10 mM $CoSO_4$ in that interface. In this case, also no signal or response was observed for Co^{2+} ion transfer and the potential window became more shorter than 20% 1-decanol.

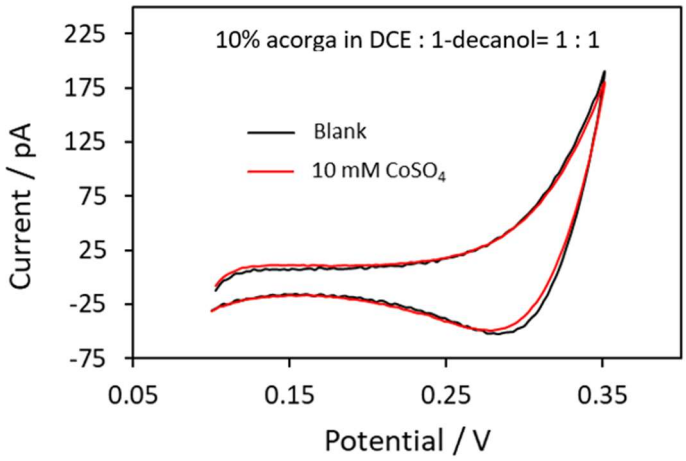

Figure A.3.3.2: *Cyclic voltammogram of background electrolytes (black) and 10 mM $CoSO_4$ in aqueous phase (red) with mixed organic solvents (10% Acorga in DCE:1-decanol = 1:1) at pH 9. The radius of the tip of the pipette was 5 µm.*

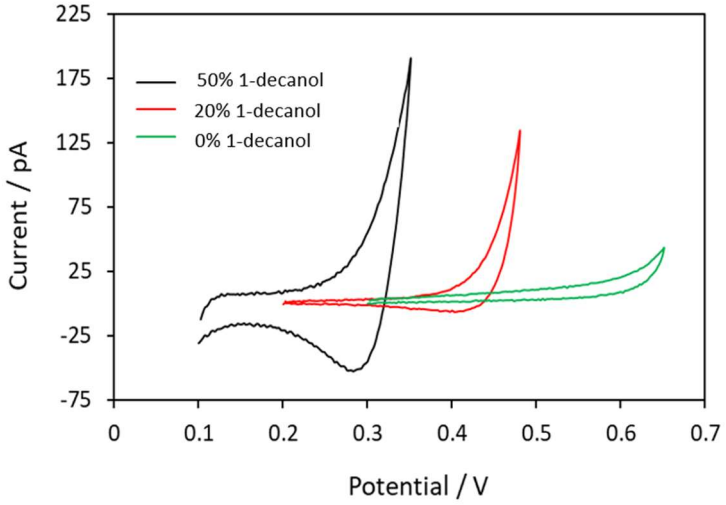

Figure A.3.3.3: *Cyclic voltammogram of background electrolytes at different composition of organic phase. The green on is for only DCE, the red one is for 20% 1-decanol and the black one is for 50% 1-propanol. The aqueous phase pH was 9 and radius of the tip of the pipette was 5 µm.*

Figure A.3.3.3 shows the CVs of background electrolytes for different composition of organic phase. It shows that as the 1-decanol added the potential window shifts to the left or to the lower potential. The potential window also became shorter as more as 1-decanol was added.

A.3.4 Detection of Ni^{2+} ions at ITIES by applying Cyclic Voltammetry

The transfer of Ni^{2+} ions was investigated at liquid/liquid interface with 10% Acorga in DCE organic phase and the pH of the aqueous phase was 9, as because, Co^{2+} ions gave the better response at this conditions.. The same conditions were applied for Ni^{2+} ion transfer and detection at the micro-ITIES. But for this case, no response has been observed. Figure A.3.4.1 shows the cyclic voltammograms of background electrolytes (black) and aqueous 5 mM $NiSO_4$. This Figure shows that there is no electrochemical response for nickel observed at this ITIES.

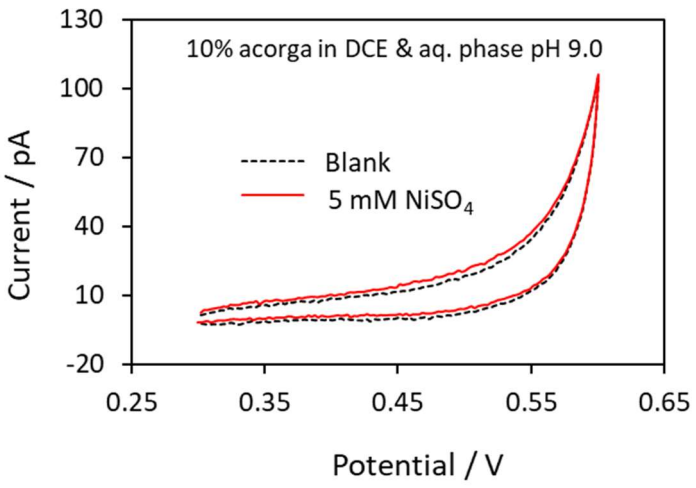

Figure A.3.4.1: *Cyclic voltammogram of background electrolytes (black) and 5 mM $NiSO_4$ in aqueous phase (red) at pH 9 with 10% Acorga in organic phase. The radius of the tip of the pipette was 5 µm.*

A.4 Conclusion

In this study, the extraction of metal ions Co^{2+} and Ni^{2+} with the help of Acorga M5640 was investigated at liquid/liquid micro-interface by applying cyclic voltammetry. Different percentages of Acorga were added into the organic phase DCE and various

pH values of the aqueous solution were used to investigate suitable conditions. When the percentage of Acorga was much higher, nearly 50%, no response was observed, even for TEA transfer. This suggests that the liquid/liquid interface was nearly blocked by the presence of 50% Acorga. The electrochemical investigation has been performed for 10%, 5%, 1% Acorga as well and it was observed that the Co^{2+} ions response for 10% Acorga in DCE was the best. From the pH investigation of aqueous solution, it has been seen that the Co^{2+} ions response at pH 9 is better than the pH A. However, no transfer of Co^{2+} ions was observed at lower or higher pH (3.5 & 11.0). A mixed organic solvent of 1-butanol & DCE was also investigated to observe the effect on the ITIES. It has been found that there was no transfer of Co^{2+} ions across the ITIES when 1-butanol was added and that available potential window decreased with an increased content of 1-butanol.

Appendix B

Pipette Radius Calculated by Three Different Equations

Table B.1: *Calculated tip diameters of pipettes from CV experiments using three different* Equations 2.3.1.1 ($I_{ss} = 4|z_i|FD_iC_ir_a$), 2.3.1.2 ($I_{ss} = 3.35\pi|z_i|FD_iC_ir_a$) and 2.3.1.3 ($I_{ss} = 2\pi|z_i|FD_iC_ir_a$) with pulling parameters *H: 400; F: 4; V: 20; D: 200 and P: 70.*

Pipette number	**Tip diameter (µm)**		
	$\boldsymbol{I_{ss} = 4\|z_i\|FD_iC_ir_a}$	$\boldsymbol{3.35\pi\|z_i\|FD_iC_ir_a}$	$\boldsymbol{I_{ss} = 2\pi\|z_i\|FD_iC_ir_a}$
1	3.1	1.18	1.97
2	3.12	1.19	1.98
3	2.51	0.95	1.59
4	2.28	0.87	1.45
5	3.12	1.19	1.98
6	2.82	1.08	1.79
7	3.09	1.18	1.96
8	2.47	0.94	1.57

Table B.2: *Calculated tip diameters of pipettes from CV experiments using three different* Equations 2.3.1.1 ($I_{ss} = 4|z_i|FD_iC_ir_a$), 2.3.1.2 ($I_{ss} = 3.35\pi|z_i|FD_iC_ir_a$) and 2.3.1.3 ($I_{ss} = 2\pi|z_i|FD_iC_ir_a$) with pulling parameters *H: 550; F: 2; V: 30; D: 130 and P: 75.*

Pipette number	**Tip diameter (µm)**		
	$\boldsymbol{I_{ss} = 4\|z_i\|FD_iC_ir_a}$	$\boldsymbol{3.35\pi\|z_i\|FD_iC_ir_a}$	$\boldsymbol{I_{ss} = 2\pi\|z_i\|FD_iC_ir_a}$
1	2.72	1.03	1.72
2	2.83	1.08	1.79
3	2.98	1.13	1.89
4	3.09	1.18	1.96
5	2.72	1.04	1.73
6	3.02	1.15	1.92
7	2.46	0.94	1.56
8	3.31	1.27	2.14
9	3.13	1.19	1.99
10	3.11	1.18	1.97

Table B.3: *Calculated tip radius of the pipettes using three different* Equations 2.3.1.1 ($I_{ss} = 4|z_i|FD_iC_ir_a$), 2.3.1.2 ($I_{ss} = 3.35\pi|z_i|FD_iC_ir_a$) and 2.3.1.3 ($I_{ss} = 2\pi|z_i|FD_iC_ir_a$), those were *used throughout the thesis for different experiments*.

Pipette radius (µm)		
$I_{ss} = 4z_iFDCr$	**$I_{ss} = 3.35\pi z_iFDCr$**	**$I_{ss} = 2\pi\ z_iFDCr$**
Pipettes used in chapter 3		
25	9.5	15.8
23	8.8	14.7
24.5	9.4	15.6
Pipettes used in chapter 4		
23	8.8	14.7
26	10	16.5
24	9.2	15.3
22	8.4	14
21	8	13.4
22.5	8.6	14.3
25	9.5	15.8
27	10.3	17.2
23.5	8.95	14.9
Pipettes used in chapter 5		
25	9.5	15.8
11	4.2	7
4	1.5	2.5
9	3.5	5.8
27.5	10.5	17.5
15	5.7	9.5
17.5	6.7	11.1
20	7.7	12.8
35	13.3	22.2
62.5	23.8	39.7

References

[1] C. Gavach, T. Mlodnicka, and J. Guastalla, "Possibility of Excess Pressure Phenomena at Interface between Organic Solutions and Aqueous Solutions," *Comptes rendus Hebdomadaires Des Seances De L Academie Des Sciences Serie C,* vol. 266, no. 16, pp. 1196, 1968.

[2] Z. Samec, "Electrochemistry at the interface between two immiscible electrolyte solutions (IUPAC Technical Report)," *Pure and applied chemistry,* vol. 76, no. 12, pp. 2147-2180, 2004.

[3] D. W. Arrigan, "Bioanalytical detection based on electrochemistry at interfaces between immiscible liquids," *Analytical letters,* vol. 41, no. 18, pp. 3233-3252, 2008.

[4] Á. Molina, C. Serna, J. A. Ortuño, and E. Torralba, "Studies of ion transfer across liquid membranes by electrochemical techniques," *Annual Reports Section" C"(Physical Chemistry),* vol. 108, pp. 126-176, 2012.

[5] Z. Samec, V. Mareček, J. Koryta, and M. Khalil, "Investigation of ion transfer across the interface between two immiscible electrolyte solutions by cyclic voltammetry," *Journal of Electroanalytical Chemistry and Interfacial Electrochemistry,* vol. 83, no. 2, pp. 393-397, 1977.

[6] G. Taylor, and H. H. J. Girault, "Ion transfer reactions across a liquid-liquid interface supported on a micropipette tip," *Journal of Electroanalytical Chemistry and Interfacial Electrochemistry,* vol. 208, no. 1, pp. 179-183, 1986/08/08/, 1986.

[7] Y. Shao, M. Osborne, and H. Girault, "Assisted ion transfer at micro-ITIES supported at the tip of micropipettes," *Journal of electroanalytical chemistry and interfacial electrochemistry,* vol. 318, no. 1-2, pp. 101-109, 1991.

[8] A. Sherburn, M. Platt, D. W. Arrigan, N. M. Boag, and R. A. Dryfe, "Selective silver ion transfer voltammetry at the polarised liquid/liquid interface," *Analyst,* vol. 128, no. 9, pp. 1187-1192, 2003.

[9] G. C. Lillie, S. M. Holmes, and R. A. Dryfe, “Electrochemistry of Cytochrome c at the Liquid-Liquid Interface,” *The Journal of Physical Chemistry B,* vol. 106, no. 47, pp. 12101-12103, 2002.

[10] T. Sugihara, H. Hotta, and T. Osakai, “Electrochemical control of glucose oxidase-catalyzed redox reaction using an oil/water interface,” *Physical Chemistry Chemical Physics,* vol. 6, no. 13, pp. 3563-3568, 2004.

[11] S. Liu, Q. Li, and Y. Shao, “Electrochemistry at micro and nanoscopic liquid/liquid interfaces,” *Chemical Society Reviews,* vol. 40, no. 5, pp. 2236-2253, 2011.

[12] W. Nernst, and E. Riesenfeld, “Ueber elektrolytische Erscheinungen an der Grenzfläche zweier Lösungsmittel,” *Annalen der Physik,* vol. 313, no. 7, pp. 600-608, 1902.

[13] L. Sanchez Vallejo, J. Ovejero, R. Fernández, and S. Dassie, “Simple ion transfer at liquid / liquid interfaces,” *International Journal of Electrochemistry,* vol. 2012, 2012.

[14] M. Blank, and S. Feig, “Electric fields across water-nitrobenzene interfaces,” *Science,* vol. 141, no. 3586, pp. 1173-1174, 1963.

[15] D. L. Nelson, and M. M. Cox, “Lehninger principles of biochemistry,” (4th ed.), W.H. Freeman, *New York,* 2005.

[16] J. Koryta, P. Vanýsek, and M. Březina, “Electrolysis with electrolyte dropping electrode: II. Basic properties of the system,” *Journal of Electroanalytical Chemistry and Interfacial Electrochemistry,* vol. 75, no. 1, pp. 211-228, 1977.

[17] H. Girault, "Charge Transfer across Liquid-Liquid Interfaces," *Modern Aspects of Electrochemistry*, no. 25, edited by John O'M. Bockris *et al,* pp. 1-62: Springer, 1993.

[18] Z. Samec, V. Mareček, and J. Weber, “Detection of an electron transfer across the interface between two immiscible electrolyte solutions by cyclic voltammetry with four-electrode system,” *Journal of Electroanalytical Chemistry and Interfacial Electrochemistry,* vol. 96, no. 2, pp. 245-247, 1979.

[19] P. Vanýsek, and L. Basáez Ramírez, “Interface between two immiscible liquid electrolytes: a review,” *Journal of the Chilean Chemical Society,* vol. 53, no. 2, pp. 1455-1463, 2008.

[20] S. Amemiya, X. Yang, and T. L. Wazenegger, “Voltammetry of the phase transfer of polypeptide protamines across polarized liquid/liquid interfaces,” *Journal of the American Chemical Society,* vol. 125, no. 39, pp. 11832-11833, 2003.

[21] S. Senthilkumar, R. A. Dryfe, and R. Saraswathi, “Size-selective voltammetry: modification of the interface between two immiscible electrolyte solutions by zeolite Y,” *Langmuir,* vol. 23, no. 6, pp. 3455-3461, 2007.

[22] H. H. Girault, “Electrochemistry at liquid-liquid interfaces,” *Electroanalytical chemistry,* edited by Allen J. Bard and Cynthia G. Zoski, vol. 23, pp. 1-104, Taylor & Francis Group, 2010.

[23] E. Alvarez de Eulate, and D. W. Arrigan, “Adsorptive stripping voltammetry of hen-egg-white-lysozyme via adsorption–desorption at an array of liquid / liquid microinterfaces,” *Analytical chemistry,* vol. 84, no. 5, pp. 2505-2511, 2012.

[24] A. Kontturi, K. Kontturi, J. Manzanares, S. Mafe, and L. Murtomäki, “Ion Pairing in the Analysis of Voltammetric Data at the ITIES: RbTPB and RbTPBCl in 1, 2-dichloroethane,” *Berichte der Bunsengesellschaft für physikalische Chemie,* vol. 99, no. 9, pp. 1131-1136, 1995.

[25] S. Tan, R. Dryfe, and H. H. Girault, “Electrochemical Study of Phase-Transfer Catalysis Reactions: The Williamson ether synthesis,” *Helvetica chimica acta,* vol. 77, no. 1, pp. 231-242, 1994.

[26] D. W. Arrigan, M. Ghita, and V. Beni, “Selective voltammetric detection of dopamine in the presence of ascorbate,” *Chemical Communications*, no. 6, pp. 732-733, 2004.

[27] S. Wilke, H. Franzke, and H. Müller, “Simultaneous determination of nitrate and chloride by means of flow-injection amperometry at the membrane-

stabilized water/nitrobenzene interface," *Analytica chimica acta,* vol. 268, no. 2, pp. 285-292, 1992.

[28] H. J. Lee, C. M. Pereira, A. F. Silva, and H. H. Girault, "Pulse amperometric detection of salt concentrations by flow injection analysis using ionodes," *Analytical chemistry,* vol. 72, no. 22, pp. 5562-5566, 2000.

[29] B. Liu, and M. V. Mirkin, "Electrochemistry at microscopic liquid-liquid interfaces," *Electroanalysis:* vol. 12, no. 18, pp. 1433-1446, 2000.

[30] G. Herzog, W. Moujahid, J. Strutwolf, and D. W. Arrigan, "Interactions of proteins with small ionised molecules: electrochemical adsorption and facilitated ion transfer voltammetry of haemoglobin at the liquid/liquid interface," *Analyst,* vol. 134, no. 8, pp. 1608-1613, 2009.

[31] M. l. D. Scanlon, G. Herzog, and D. W. Arrigan, "Electrochemical Detection of Oligopeptides at Silicon-Fabricated Micro-Liquid/Liquid Interfaces," *Analytical chemistry,* vol. 80, no. 15, pp. 5743-5749, 2008.

[32] Y. Yuan, and S. Amemiya, "Facilitated protamine transfer at polarized water/1, 2-dichloroethane interfaces studied by cyclic voltammetry and chronoamperometry at micropipet electrodes," *Analytical chemistry,* vol. 76, no. 23, pp. 6877-6886, 2004.

[33] Y. Chen, Y. Yuan, M. Zhang, F. Li, P. Sun, Z. Gao, and Y. Shao, "Systematic study of the transfer of amino acids across the water/l, 2-dichloroethane interface facilitated by dibenzo-18-crown-6," *Science in China Series B: Chemistry,* vol. 47, no. 1, pp. 24-33, 2004.

[34] H. Alemu, "Voltammetry of drugs at the interface between two immiscible electrolyte solutions," *Pure and Applied Chemistry,* vol. 76, no. 4, pp. 697-705, 2004.

[35] J. Ortuno, A. Gil, C. Serna, and A. Molina, "Voltammetry of some catamphiphilic drugs with solvent polymeric membrane ion sensors," *Journal of Electroanalytical Chemistry,* vol. 605, no. 2, pp. 157-161, 2007.

[36] J. A. Ribeiro, F. Silva, and C. M. Pereira, “Electrochemical study of the anticancer drug daunorubicin at a water/oil interface: drug lipophilicity and quantification,” *Analytical chemistry,* vol. 85, no. 3, pp. 1582-1590, 2013.

[37] C. J. Collins, A. Berduque, and D. W. Arrigan, “Electrochemically modulated liquid / liquid extraction of ionized drugs under physiological conditions,” *Analytical chemistry,* vol. 80, no. 21, pp. 8102-8108, 2008.

[38] S. M. Ulmeanu, H. Jensen, G. Bouchard, P. A. Carrupt, and H. H. Girault, “Water-oil partition profiling of ionized drug molecules using cyclic voltammetry and a 96-well microfilter plate system,” *Pharmaceutical research,* vol. 20, no. 8, pp. 1317-1322, 2003.

[39] V. Beni, M. Ghita, and D. W. Arrigan, “Cyclic and pulse voltammetric study of dopamine at the interface between two immiscible electrolyte solutions,” *Biosensors and Bioelectronics,* vol. 20, no. 10, pp. 2097-2103, 2005.

[40] A. Berduque, R. Zazpe, and D. W. Arrigan, “Electrochemical detection of dopamine using arrays of liquid/liquid micro-interfaces created within micromachined silicon membranes,” *Analytica chimica acta,* vol. 611, no. 2, pp. 156-162, 2008.

[41] D. Zhan, S. Mao, Q. Zhao, Z. Chen, H. Hu, P. Jing, M. Zhang, Z. Zhu, and Y. Shao, “Electrochemical investigation of dopamine at the water/1, 2-dichloroethane interface,” *Analytical chemistry,* vol. 76, no. 14, pp. 4128-4136, 2004.

[42] G. Herzog, V. Kam, A. Berduque, and D. W. Arrigan, “Detection of food additives by voltammetry at the liquid/liquid interface,” *Journal of agricultural and food chemistry,* vol. 56, no. 12, pp. 4304-4310, 2008.

[43] J. Guo, Y. Yuan, and S. Amemiya, “Voltammetric detection of heparin at polarized blood plasma/1, 2-dichloroethane interfaces,” *Analytical chemistry,* vol. 77, no. 17, pp. 5711-5719, 2005.

[44] T. Osakai, H. Komatsu, and M. Goto, “Cationic-surfactant transfer facilitated by DNA adsorbed on a polarized 1, 2-dichloroethane/water interface,” *Journal of Physics: Condensed Matter,* vol. 19, no. 37, pp. 375103, 2007.

[45] H. J. Lee, C. Beriet, and H. H. Girault, “Amperometric detection of alkali metal ions on micro-fabricated composite polymer membranes,” *Journal of Electroanalytical Chemistry,* vol. 453, no. 1-2, pp. 211-219, 1998.

[46] M. M. Hossain, S. H. Lee, H. H. Girault, V. Devaud, and H. J. Lee, “Voltammetric studies of hexachromic anion transfer reactions across micro-water/polyvinylchloride-2-nitrophenyloctylether gel interfaces for sensing applications,” *Electrochimica Acta,* vol. 82, pp. 12-18, 2012.

[47] Z. Samec, V. Mareček, and M. P. Colombini, “Standard Gibbs energies of transfer of alkali metal cations from water to 1, 2-dichloroethane: A critique,” *Journal of electroanalytical chemistry and interfacial electrochemistry,* vol. 257, no. 1-2, pp. 147-154, 1988.

[48] G. Lagger, L. Tomaszewski, M. D. Osborne, B. J. Seddon, and H. H. Girault, “Electrochemical extraction of heavy metal ions assisted by cyclic thioether ligands,” *Journal of Electroanalytical Chemistry,* vol. 451, no. 1-2, pp. 29-37, 1998.

[49] E. Verwey, and K. Niessen, “XL. The electrical double layer at the interface of two liquids,” *The London, Edinburgh, and Dublin Philosophical Magazine and Journal of Science,* vol. 28, no. 189, pp. 435-446, 1939.

[50] J. Wang, “Analytical electrochemistry,” Third edition, *Hoboken, New Jersey: A John Wiley & sons, inc.*, 2006.

[51] C. Gavach, P. Seta, and B. D'epenoux, “The double layer and ion adsorption at the interface between two non miscible solutions: Part I. Interfacial tension measurements for the water / nitrobenzene tetraalkylammonium bromide systems,” *Journal of Electroanalytical Chemistry and Interfacial Electrochemistry,* vol. 83, no. 2, pp. 225-235, 1977.

[52] H. Girault, and D. Schiffrin, “Thermodynamic surface excess of water and ionic solvation at the interface between immiscible liquids,” *Journal of Electroanalytical Chemistry and Interfacial Electrochemistry,* vol. 150, no. 1-2, pp. 43-49, 1983.

[53] Z. Samec, V. Mareček, and D. Homolka, “Double layers at liquid/liquid interfaces,” *Faraday Discussions of the Chemical Society,* vol. 77, pp. 197-208, 1984.

[54] H. Girault, and D. Schiffrin, “Theory of the kinetics of ion transfer across liquid/liquid interfaces,” *Journal of electroanalytical chemistry and interfacial electrochemistry,* vol. 195, no. 2, pp. 213-227, 1985.

[55] D. M. Mitrinović, A. M. Tikhonov, M. Li, Z. Huang, and M. L. Schlossman, “Noncapillary-wave structure at the water-alkane interface,” *Physical review letters,* vol. 85, no. 3, pp. 582, 2000.

[56] D. M. Mitrinovic, Z. Zhang, S. M. Williams, Z. Huang, and M. L. Schlossman, “X-ray reflectivity study of the water / hexane interface,” *The Journal of Physical Chemistry B,* vol. 103, no. 11, pp. 1779-1782, 1999.

[57] G. Luo, S. Malkova, J. Yoon, D. G. Schultz, B. Lin, M. Meron, I. Benjamin, P. Vanýsek, and M. L. Schlossman, “Ion distributions near a liquid-liquid interface,” *Science,* vol. 311, no. 5758, pp. 216-218, 2006.

[58] N. Laanait, M. Mihaylov, B. Hou, H. Yu, P. Vanýsek, M. Meron, B. Lin, I. Benjamin, and M. L. Schlossman, “Tuning ion correlations at an electrified soft interface,” *Proceedings of the National Academy of Sciences,* vol. 109, no. 50, pp. 20326-20331, 2012.

[59] J. Strutwolf, A. L. Barker, M. Gonsalves, D. J. Caruana, P. R. Unwin, D. E. Williams, and J. R. Webster, “Probing liquid| liquid interfaces using neutron reflection measurements and scanning electrochemical microscopy,” *Journal of Electroanalytical Chemistry,* vol. 483, no. 1-2, pp. 163-173, 2000.

[60] G. C. Gschwend, and H. H. Girault, “Discrete Helmholtz model: a single layer of correlated counter-ions. Metal oxides and silica interfaces, ion-exchange and

biological membranes," *Chemical Science,* vol. 11, no. 38, pp. 10304-10312, 2020.

[61] C. Collins, "Liquid-liquid Electrochemistry for the Extraction and Detection of Drug Molecules," PhD thesis, University College Cork, Cork, Ireland, 2010.

[62] M. C. Henstridge, and R. G. Compton, "Mass Transport to micro-and nanoelectrodes and their arrays: a review," *The Chemical Record,* vol. 12, no. 1, pp. 63-71, 2012.

[63] P. Peljo, and H. Girault, "Electrochemistry at liquid/liquid interfaces," *Encyclopedia of Analytical Chemistry*, John Wiley & Sons, Ltd., 2012, doi:10.1002/9780470027318.a5306.pub2.

[64] F. Reymond, D. Fermın, H. J. Lee, and H. H. Girault, "Electrochemistry at liquid/liquid interfaces: methodology and potential applications," *Electrochimica acta,* vol. 45, no. 15-16, pp. 2647-2662, 2000.

[65] S. Amemiya, Y. Wang, and M. V. Mirkin, "Nanoelectrochemistry at the liquid/liquid interfaces," *Specialist periodical reports in electrochemistry,* vol. 12, pp. 1, 2013.

[66] D. Arrigan, G. Herzog, M. Scanlon, and J. Strutwolf, "Bioanalytical applications of electrochemistry at liquid/liquid microinterfaces," *Electroanalytical Chemistry: A Series of Advances:* edited by A. Bard, C. G. Zoski, Volume 25, pp. 105-178: CRC Press, 2013.

[67] Y. Shao, and M. V. Mirkin, "Fast kinetic measurements with nanometer-sized pipets. Transfer of potassium ion from water into dichloroethane facilitated by dibenzo-18-crown-6," *Journal of the American Chemical Society,* vol. 119, no. 34, pp. 8103-8104, 1997.

[68] M. D. Scanlon, J. Strutwolf, A. Blake, D. Iacopino, A. J. Quinn, and D. W. Arrigan, "Ion-transfer electrochemistry at arrays of nanointerfaces between immiscible electrolyte solutions confined within silicon nitride nanopore membranes," *Analytical chemistry,* vol. 82, no. 14, pp. 6115-6123, 2010.

[69] M. D. Scanlon, and D. W. Arrigan, "Enhanced Electroanalytical Sensitivity via Interface Miniaturisation: Ion Transfer Voltammetry at an Array of Nanometre Liquid/Liquid Interfaces," *Electroanalysis,* vol. 23, no. 4, pp. 1023-1028, 2011.

[70] F. O. Laforge, P. Sun, and M. V. Mirkin, "Shuttling mechanism of ion transfer at the interface between two immiscible liquids," *Journal of the American Chemical Society,* vol. 128, no. 46, pp. 15019-15025, 2006.

[71] P. Sun, F. O. Laforge, and M. V. Mirkin, "Ion transfer at nanointerfaces between water and neat organic solvents," *Journal of the American Chemical Society,* vol. 127, no. 24, pp. 8596-8597, 2005.

[72] P. Sun, F. O. Laforge, and M. V. Mirkin, "Role of trace amounts of water in transfers of hydrophilic and hydrophobic ions to low-polarity organic solvents," *Journal of the American Chemical Society,* vol. 129, no. 41, pp. 12410-12411, 2007.

[73] P. D. Beattie, A. Delay, and H. H. Girault, "Investigation of the kinetics of assisted potassium ion transfer by dibenzo-18-crown-6 at the micro-ITIES by means of steady-state voltammetry," *Journal of Electroanalytical Chemistry,* vol. 380, no. 1, pp. 167-175, 1995/01/03/, 1995.

[74] Y. Tong, P. Sun, Z. Zhang, and Y. Shao, "Fabrication of agar-gel microelectrodes and their application in the study of ion transfer across the agar-water/1,2-dichloroethane interface," *Journal of Electroanalytical Chemistry,* vol. 504, no. 1, pp. 52-58, 2001.

[75] Y. Shao, and M. V. Mirkin, "Voltammetry at Micropipet Electrodes," *Analytical Chemistry,* vol. 70, no. 15, pp. 3155-3161, 1998/08/01, 1998.

[76] B. Kralj, and R. A. Dryfe, "Membrane voltammetry: The interface between two immiscible electrolyte solutions," *Physical Chemistry Chemical Physics,* vol. 3, no. 23, pp. 5274-5282, 2001.

[77] H. J. Lee, P. D. Beattie, B. J. Seddon, M. D. Osborne, and H. H. Girault, "Amperometric ion sensors based on laser-patterned composite polymer

membranes," *Journal of Electroanalytical Chemistry,* vol. 440, no. 1, pp. 73-82, 1997/12/20/, 1997.

[78] J. Campbell, and H. Girault, "Steady state current for ion transfer reactions at a micro liquid/liquid interface," *Journal of electroanalytical chemistry and interfacial electrochemistry,* vol. 266, no. 2, pp. 465-469, 1989.

[79] J. Strutwolf, M. D. Scanlon, and D. W. Arrigan, "Electrochemical ion transfer across liquid/liquid interfaces confined within solid-state micropore arrays simulations and experiments," *Analyst,* vol. 134, no. 1, pp. 148-158, 2009.

[80] M. D. Scanlon, J. Strutwolf, and D. W. Arrigan, "Voltammetric behaviour of biological macromolecules at arrays of aqueous/organogel micro-interfaces," *Physical Chemistry Chemical Physics,* vol. 12, no. 34, pp. 10040-10047, 2010.

[81] E. Alvarez de Eulate, J. Strutwolf, Y. Liu, K. O'Donnell, and D. W. Arrigan, "An electrochemical sensing platform based on liquid/liquid microinterface arrays formed in laser-ablated glass membranes," *Analytical Chemistry,* vol. 88, no. 5, pp. 2596-2604, 2016.

[82] R. Zazpe, C. Hibert, J. O'Brien, Y. H. Lanyon, and D. W. Arrigan, "Ion-transfer voltammetry at silicon membrane-based arrays of micro-liquid/liquid interfaces," *Lab on a Chip,* vol. 7, no. 12, pp. 1732-1737, 2007.

[83] P. Borgul, P. Pawlak, K. Rudnicki, K. Sipa, P. Krzyczmonik, A. Trynda, S. Skrzypek, G. Herzog, and L. Poltorak, "Ephedrine sensing at the electrified liquid-liquid interface supported with micro-punched self-adhesive polyimide film," *Sensors and Actuators B: Chemical*, pp. 130286, 2021.

[84] R. A. Dryfe, and B. Kralj, "Voltammetric ion transfer in the presence of a nanoporous material," *Electrochemistry communications,* vol. 1, no. 3-4, pp. 128-130, 1999.

[85] M. Platt, R. A. Dryfe, and E. P. Roberts, "Voltammetry with liquid/liquid microarrays: characterization of membrane materials," *Langmuir,* vol. 19, no. 19, pp. 8019-8025, 2003.

[86] M. Rimboud, R. D. Hart, T. Becker, and D. W. Arrigan, “Electrochemical behaviour and voltammetric sensitivity at arrays of nanoscale interfaces between immiscible liquids,” *Analyst,* vol. 136, no. 22, pp. 4674-4681, 2011.

[87] C. Dekker, “Solid-state nanopores,” *Nature nanotechnology,* vol. 2, no. 4, pp. 209-215, 2007.

[88] M. Sairi, N. Chen-Tan, G. Neusser, C. Kranz, and D. W. Arrigan, “Electrochemical Characterisation of Nanoscale Liquid/Liquid Interfaces Located at Focused Ion Beam-Milled Silicon Nitride Membranes,” *ChemElectroChem,* vol. 2, no. 1, pp. 98-105, 2015.

[89] D. W. Arrigan, “Nanoelectrodes, nanoelectrode arrays and their applications,” *Analyst,* vol. 129, no. 12, pp. 1157-1165, 2004.

[90] D. W. Arrigan, and Y. Liu, “Electroanalytical ventures at nanoscale interfaces between immiscible liquids,” *Annual Review of Analytical Chemistry,* vol. 9, pp. 145-161, 2016.

[91] J. A. Campbell, A. A. Stewart, and H. H. Girault, “Determination of the kinetics of facilitated ion transfer reactions across the micro interface between two immiscible electrolyte solutions,” *Journal of the Chemical Society, Faraday Transactions 1: Physical Chemistry in Condensed Phases,* vol. 85, no. 4, pp. 843-853, 1989.

[92] B. Horrocks, and M. Mirkin, “Cation binding to DNA studied by ion-transfer voltammetry at micropipets,” *Analytical Chemistry,* vol. 70, no. 22, pp. 4653-4660, 1998.

[93] M. Y. Vagin, S. A. Trashin, A. A. Karyakin, and M. Mascini, “Label-free detection of DNA hybridization at a liquid/liquid interface,” *Analytical chemistry,* vol. 80, no. 4, pp. 1336-1340, 2008.

[94] F. Kivlehan, M. Lefoix, H. A. Moynihan, D. Thompson, V. I. Ogurtsov, G. Herzog, and D. W. Arrigan, “Interaction of acridine-calix [4] arene with DNA at the electrified liquid/liquid interface,” *Electrochimica acta,* vol. 55, no. 9, pp. 3348-3354, 2010.

[95] J. A. Ribeiro, C. M. Pereira, and F. Silva, “Electrochemistry of the interaction between bioactive drugs daunorubicin and dopamine and DNA at a water/oil interface,” *Electrochimica Acta,* vol. 180, pp. 687-694, 2015.

[96] B. M. B. Felisilda, and D. W. Arrigan, “Electroactivity of aptamer at soft microinterface arrays,” *Analytical chemistry,* vol. 90, no. 14, pp. 8470-8477, 2018.

[97] C. J. Collins, and D. W. Arrigan, “Ion-transfer voltammetric determination of the β-blocker propranolol in a physiological matrix at silicon membrane-based liquid/liquid microinterface arrays,” *Analytical chemistry,* vol. 81, no. 6, pp. 2344-2349, 2009.

[98] C. J. Collins, C. Lyons, J. Strutwolf, and D. W. Arrigan, “Serum-protein effects on the detection of the β-blocker propranolol by ion-transfer voltammetry at a micro-ITIES array,” *Talanta,* vol. 80, no. 5, pp. 1993-1998, 2010.

[99] M. Sairi, and D. W. Arrigan, “Electrochemical detection of ractopamine at arrays of micro-liquid/liquid interfaces,” *Talanta,* vol. 132, pp. 205-214, 2015.

[100] S. H. I. Hamid, “Liquid/liquid interface ion-transfer amperometric sensors for tenofovir as a model nucleoside/nucleotide anti-retroviral drug,” thesis, University of the Western Cape, 2014. http://hdl.handle.net/11394/3999

[101] H. R. Kim, C. M. Pereira, H. Y. Han, and H. J. Lee, “Voltammetric studies of topotecan transfer across liquid/liquid interfaces and sensing applications,” *Analytical chemistry,* vol. 87, no. 10, pp. 5356-5362, 2015.

[102] T. Osakai, H. Jensen, H. Nagatani, D. J. Fermín, and H. H. Girault, “Mechanistic aspects associated with the oxidation of l-ascorbic acid at the 1, 2-dichloroethane/water interface,” *Journal of Electroanalytical Chemistry,* vol. 510, no. 1-2, pp. 43-49, 2001.

[103] H. Ohde, K. Maeda, Y. Yoshida, and S. Kihara, “Redox reactions between NADH and quinone derivatives at a liquid/liquid interface,” *Electrochimica acta,* vol. 44, no. 1, pp. 23-28, 1998.

[104] E. M. Almbrok, N. A. Yusof, J. Abdullah, and R. M. Zawawi, "Electrochemical Behavior and Detection of Diclofenac at a Microporous Si_3N_4 Membrane Modified Water/1,6-dichlorohexane Interface System," *Chemosensors,* vol. 8, no. 1, pp. 11, 2020.

[105] K. Rudnicki, L. Poltorak, S. Skrzypek, and E. J. Sudhölter, "Ion transfer voltammetry for analytical screening of fluoroquinolone antibiotics at the water/1,2-dichloroethane interface," *Analytica chimica acta,* vol. 1085, pp. 75-84, 2019.

[106] G. Lu, C. Despas, L. Liu, and G. Herzog, "Ametryn detection by proton assisted transfer at a single micro-interface between two immiscible electrolyte solutions," *Journal of Electroanalytical Chemistry,* vol. 877, pp. 114745, 2020.

[107] R. Kataky, and P. Lopes, "Chiral detection at a liquid/liquid interface," *Chemical communications*, no. 12, pp. 1490-1492, 2009.

[108] P. Lopes, and R. Kataky, "Chiral interactions of the drug propranolol and α_1-acid-glycoprotein at a micro liquid/liquid interface," *Analytical chemistry,* vol. 84, no. 5, pp. 2299-2304, 2012.

[109] B. Huang, B. Yu, P. Li, M. Jiang, Y. Bi, and S. Wu, "Vitamin B_1 ion-selective microelectrode based on a liquid-liquid interface at the tip of a micropipette," *Analytica chimica acta,* vol. 312, no. 3, pp. 329-335, 1995.

[110] Q. Qian, G. S. Wilson, and K. Bowman-James, "MicroITIES detection of adenosine phosphates," *Electroanalysis,* vol. 16, no. 16, pp. 1343-1350, 2004.

[111] T. J. Davies, and R. G. Compton, "The cyclic and linear sweep voltammetry of regular and random arrays of microdisc electrodes: Theory," *Journal of Electroanalytical Chemistry,* vol. 585, no. 1, pp. 63-82, 2005.

[112] P. Vanýsek, and Z. Sun, "Bovine serum albumin adsorption on a water/nitrobenzene interface," *Journal of electroanalytical chemistry and interfacial electrochemistry,* vol. 298, no. 2, pp. 177-194, 1990.

[113] A. Trojánek, J. Langmaier, E. Samcová, and Z. Samec, “Counterion binding to protamine polyion at a polarised liquid/liquid interface,” *Journal of Electroanalytical Chemistry,* vol. 603, no. 2, pp. 235-242, 2007.

[114] S. O'Sullivan, and D. W. Arrigan, “Electrochemical behaviour of myoglobin at an array of microscopic liquid/liquid interfaces,” *Electrochimica acta,* vol. 77, pp. 71-76, 2012.

[115] S. G. Booth, B. M. B. Felisilda, E. Alvarez de Eulate, O. J. Gustafsson, M. Arooj, R. L. Mancera, R. A. Dryfe, M. J. Hackett, and D. W. Arrigan, “Secondary Structural Changes in Proteins as a Result of Electroadsorption at Aqueous-Organogel Interfaces,” *Langmuir,* vol. 35, no. 17, pp. 5821-5829, 2019.

[116] H. B. Lamichhane, T. G. Henares, M. J. Hackett, and D. W. Arrigan, “Structural Changes in Insulin at a Soft Electrochemical Interface,” *Analytical Chemistry*, vol. 93, no. 26, 9094-9102, 2021.

[117] Z. Samec, A. Trojánek, J. Langmaier, and E. Samcová, “Cyclic voltammetry of biopolymer heparin at PVC plasticized liquid membrane,” *Electrochemistry communications,* vol. 5, no. 10, pp. 867-870, 2003.

[118] P. Jing, Y. Kim, and S. Amemiya, “Voltammetric extraction of heparin and low-molecular-weight heparin across 1, 2-dichloroethane/water interfaces,” *Langmuir,* vol. 25, no. 23, pp. 13653-13660, 2009.

[119] B. M. B. Felisilda, E. A. de Eulate, D. N. Stringer, J. H. Fitton, and D. W. Arrigan, “Electrochemical behaviour at a liquid-organogel microinterface array of fucoidan extracted from algae,” *Analyst,* vol. 142, no. 17, pp. 3194-3202, 2017.

[120] B. M. B. Felisilda, A. D. Payne, and D. W. M. Arrigan, “Electrochemical Behavior and Detection of Sulfated Sucrose at a Liquid/Organogel Microinterface Array,” *Analytical Chemistry,* vol. 90, no. 17, pp. 10256-10262, 2018/09/04, 2018.

[121] M. Senda, and Y. Yamamoto, "Urea biosensor based on amperometric ammonium ion electrode," *Electroanalysis,* vol. 5, no. 9-10, pp. 775-779, 1993.

[122] Y. Yamamoto, and M. Senda, "Amperometric ammonium ion sensor and its application to biosensors," *Sensors and Actuators B: Chemical,* vol. 13, no. 1-3, pp. 57-60, 1993.

[123] M. D. Osborne, and H. H. Girault, "The liquid/liquid micro-interface for the amperometric detection of urea," *Electroanalysis,* vol. 7, no. 8, pp. 714-721, 1995.

[124] C. M. Pereira, J. M. Oliveira, R. M. Silva, and F. Silva, "Amperometric glucose biosensor based on assisted ion transfer through gel-supported microinterfaces," *Analytical chemistry,* vol. 76, no. 18, pp. 5547-5551, 2004.

[125] M. M. Hossain, S. N. Faisal, C. S. Kim, H. J. Cha, S. C. Nam, and H. J. Lee, "Amperometric proton selective strip-sensors with a microelliptic liquid/gel interface for organophosphate neurotoxins," *Electrochemistry Communications,* vol. 13, no. 6, pp. 611-614, 2011.

[126] M. M. Hossain, C. S. Kim, H. J. Cha, and H. J. Lee, "Amperometric Detection of Parathion and Methyl Parathion with a Microhole-ITIES," *Electroanalysis,* vol. 23, no. 9, pp. 2049-2056, 2011.

[127] R. Akter, and D. W. Arrigan, "Detection of prostate specific membrane antigen at picomolar levels using biocatalysis coupled to assisted ion transfer voltammetry at a liquid/organogel microinterface array," *Analytical chemistry,* vol. 88, no. 23, pp. 11302-11305, 2016.

[128] K. Mohan, K. C. Donavan, J. A. Arter, R. M. Penner, and G. A. Weiss, "Sub-nanomolar detection of prostate-specific membrane antigen in synthetic urine by synergistic, dual-ligand phage," *Journal of the American Chemical Society,* vol. 135, no. 20, pp. 7761-7767, 2013.

[129] J. A. Arter, J. E. Diaz, K. C. Donavan, T. Yuan, R. M. Penner, and G. A. Weiss, "Virus-polymer hybrid nanowires tailored to detect prostate-specific membrane antigen," *Analytical chemistry,* vol. 84, no. 6, pp. 2776-2783, 2012.

[130] B. V. Chikkaveeraiah, A. Bhirde, R. Malhotra, V. Patel, J. S. Gutkind, and J. F. Rusling, "Single-wall carbon nanotube forest arrays for immunoelectrochemical measurement of four protein biomarkers for prostate cancer," *Analytical chemistry,* vol. 81, no. 21, pp. 9129-9134, 2009.

[131] Y.-C. Chen, D. G. De Oteyza, Z. Pedramrazi, C. Chen, F. R. Fischer, and M. F. Crommie, "Tuning the band gap of graphene nanoribbons synthesized from molecular precursors," *ACS nano,* vol. 7, no. 7, pp. 6123-6128, 2013.

[132] S. Zannah, and D. W. Arrigan, "Electrochemistry of catalase at a liquid/liquid micro-interface array," *Bioelectrochemistry,* vol. 138, pp. 107694, 2021.

[133] M. L. Colombo, J. V. Sweedler, and M. Shen, "Nanopipet-based liquid-liquid interface probes for the electrochemical detection of acetylcholine, tryptamine, and serotonin via ionic transfer," *Analytical chemistry,* vol. 87, no. 10, pp. 5095-5100, 2015.

[134] G. Herzog, B. McMahon, M. Lefoix, N. D. Mullins, C. J. Collins, H. A. Moynihan, and D. W. M. Arrigan, "Electrochemistry of dopamine at the polarised liquid/liquid interface facilitated by an homo-oxo-calix[3]arene ionophore," *Journal of Electroanalytical Chemistry,* vol. 622, no. 1, pp. 109-114, 2008/10/01/, 2008.

[135] A. Berduque, R. Zazpe, and D. W. M. Arrigan, "Electrochemical detection of dopamine using arrays of liquid/liquid micro-interfaces created within micromachined silicon membranes," *Analytica Chimica Acta,* vol. 611, no. 2, pp. 156-162, 2008/03/24/, 2008.

[136] M. L. Colombo, S. McNeil, N. Iwai, A. Chang, and M. Shen, "Electrochemical detection of dopamine via assisted ion transfer at nanopipet electrode using cyclic voltammetry," *Journal of The Electrochemical Society,* vol. 163, no. 4, pp. H3072, 2015.

[137] N. T. Iwai, M. Kramaric, D. Crabbe, Y. Wei, R. Chen, and M. Shen, "GABA detection with nano-ITIES pipet electrode: a new mechanism, water/DCE–octanoic acid interface," *Analytical chemistry,* vol. 90, no. 5, pp. 3067-3072, 2018.

[138] X. Wang, T. Xu, Y. Zhang, N. Gao, T. Feng, S. Wang, and M. Zhang, "In Vivo Detection of Redox-Inactive Neurochemicals in the Rat Brain with an Ion Transfer Microsensor," *ACS sensors*, 6, 7, 2757-2762, 2021.

[139] A. Bard, "In Scanning Electrochemical Microscopy, " A. J. Bard, M. V. Mirkin, Eds, *Mercel Dekker: New York*, pp. 1-17, 2001.

[140] A. J. Bard, X. Li, and W. Zhan, "Chemically imaging living cells by scanning electrochemical microscopy," *Biosensors and Bioelectronics,* vol. 22, no. 4, pp. 461-472, 2006.

[141] S. Amemiya, J. Guo, H. Xiong, and D. A. Gross, "Biological applications of scanning electrochemical microscopy: chemical imaging of single living cells and beyond," *Analytical and bioanalytical chemistry,* vol. 386, no. 3, pp. 458-471, 2006.

[142] D. Zhan, X. Li, W. Zhan, F.-R. F. Fan, and A. J. Bard, "Scanning electrochemical microscopy. 58. Application of a micropipet-supported ITIES tip to detect Ag^+ and study its effect on fibroblast cells," *Analytical chemistry,* vol. 79, no. 14, pp. 5225-5231, 2007.

[143] P. Sun, Z. Zhang, Z. Gao, and Y. Shao, "Probing fast facilitated ion transfer across an externally polarized liquid–liquid interface by scanning electrochemical microscopy," *Angewandte Chemie,* vol. 114, no. 18, pp. 3595-3598, 2002.

[144] C. Cai, Y. Tong, and M. V. Mirkin, "Probing Rapid Ion Transfer Across a Nanoscopic Liquid/Liquid Interface," *The Journal of Physical Chemistry B,* vol. 108, no. 46, pp. 17872-17878, 2004.

[145] M. Shen, R. Ishimatsu, J. Kim, and S. Amemiya, "Quantitative imaging of ion transport through single nanopores by high-resolution scanning electrochemical microscopy," *Journal of the American Chemical Society,* vol. 134, no. 24, pp. 9856-9859, 2012.

[146] J. Koryta, “Electrochemical polarization phenomena at the interface of two immiscible electrolyte solutions,” *Electrochimica Acta,* vol. 24, no. 3, pp. 293-300, 1979.

[147] M. Imoto, T. Sakaki, and T. Osakai, “Sophisticated design of PVC membrane ion-selective electrodes based on the mixed potential theory,” *Analytical chemistry,* vol. 85, no. 9, pp. 4753-4760, 2013.

[148] Q. Li, S. Xie, Z. Liang, X. Meng, S. Liu, H. H. Girault, and Y. Shao, “Fast Ion-Transfer Processes at Nanoscopic Liquid/Liquid Interfaces,” *Angewandte Chemie International Edition,* vol. 48, no. 43, pp. 8010-8013, 2009.

[149] R. Cui, Q. Li, D. E. Gross, X. Meng, B. Li, M. Marquez, R. Yang, J. L. Sessler, and Y. Shao, “Anion transfer at a micro-water/1, 2-dichloroethane interface facilitated by β-octafluoro-meso-octamethylcalix [4] pyrrole,” *Journal of the American Chemical Society,* vol. 130, no. 44, pp. 14364-14365, 2008.

[150] J. A. Ribeiro, F. Silva, and C. M. Pereira, “Electrochemical sensing of ammonium ion at the water/1, 6-dichlorohexane interface,” *Talanta,* vol. 88, pp. 54-60, 2012.

[151] S. H. Lee, J. Sumranjit, P. Tongkate, B. H. Chung, and H. J. Lee, “Voltammetric studies of Cu (II) ion transfer reaction with picolinamide-phenylenevinylene across liquid/liquid interfaces and their sensing applications,” *Electrochimica Acta,* vol. 123, pp. 198-204, 2014.

[152] H. J. Lee, D. W. M. Arrigan, M. Nurul Karim, H. Kim, “Amperometric Ion Sensing Approaches at Liquid/Liquid Interfaces for Inorganic, Organic and Biological Ions,” D.W.M. Arrigan (Ed.), *Electrochem. Strateg. Detect. Sci.*, Royal Society of Chemistry, Cambridge (2016), pp. 296-340, 10.1039/9781782622529-00296

[153] T. Stockmann, J. Zhang, and J. Wren, “unpublished results; b) TJ Stockmann, Z. Ding,” *Anal. Chem,* vol. 83, pp. 7542-7549, 2011.

[154] S. Zhang, M. Li, B. Su, and Y. Shao, "Fabrication and Use of Nanopipettes in Chemical Analysis," *Annual Review of Analytical Chemistry,* vol. 11, pp. 265-286, 2018.

[155] P-2000 Laser Based Micropipette Puller System, "Operation Manual," 2010, Rev. 2.2 (20100629), Sutter Instrument, One Digital Drive, Novato, CA 94949.

[156] C. R. Vistas, A. C. Águas, and G. N. Ferreira, "Silanization of glass chips-A factorial approach for optimization," *Applied surface science,* vol. 286, pp. 314-318, 2013.

[157] Y. Liu, M. Sairi, G. Neusser, C. Kranz, and D. W. Arrigan, "Achievement of Diffusional Independence at Nanoscale Liquid/Liquid Interfaces within Arrays," *Analytical chemistry,* vol. 87, no. 11, pp. 5486-5490, 2015.

[158] M. Sairi, J. Strutwolf, R. A. Mitchell, D. S. Silvester, and D. W. Arrigan, "Chronoamperometric response at nanoscale liquid-liquid interface arrays," *Electrochimica Acta,* vol. 101, pp. 177-185, 2013.

[159] H. Katano, and M. Senda, "Voltammetry at 1, 6-dichlorohexane/water interface," *Analytical sciences,* vol. 17, no. 9, pp. 1027-1029, 2001.

[160] P. Beattie, A. Delay, and H. Girault, "Investigation of the kinetics of assisted potassium ion transfer by dibenzo-18-crown-6 at the micro-ITIES by means of steady-state voltammetry," *Journal of Electroanalytical Chemistry,* vol. 380, no. 1-2, pp. 167-175, 1995.

[161] Y. Shao, and M. V. Mirkin, "Probing ion transfer at the liquid/liquid interface by scanning electrochemical microscopy (SECM)," *The Journal of Physical Chemistry B,* vol. 102, no. 49, pp. 9915-9921, 1998.

[162] J. Langmaier, K. Stejskalová, and Z. Samec, "Evaluation of the standard ion transfer potentials for PVC plasticized membranes from voltammetric measurements," *Journal of Electroanalytical Chemistry,* vol. 496, no. 1, pp. 143-147, 2001/01/19/, 2001.

[163] X. Li, and D. F. Shantz, “PFG NMR Investigations of Tetraalkylammonium-Silica Mixtures,” *The Journal of Physical Chemistry C,* vol. 114, no. 18, pp. 8449-8458, 2010.

[164] Z. Samec, and P. Papoff, “Electrolyte dropping electrode polarographic studies. Solvent effect on stability of crown ether complexes of alkali-metal cations,” *Analytical Chemistry,* vol. 62, no. 10, pp. 1010-1015, 1990.

[165] Y. Wang, J. Velmurugan, M. V. Mirkin, P. J. Rodgers, J. Kim, and S. Amemiya, “Kinetic study of rapid transfer of tetraethylammonium at the 1, 2-dichloroethane/water interface by nanopipet voltammetry of common ions,” *Analytical Chemistry,* vol. 82, no. 1, pp. 77-83, 2010.

[166] D. Perry, D. Momotenko, R. A. Lazenby, M. Kang, and P. R. Unwin, “Characterization of nanopipettes,” *Analytical chemistry,* vol. 88, no. 10, pp. 5523-5530, 2016.

[167] R. Chen, R. J. Balla, A. Lima, and S. Amemiya, “Characterization of nanopipet-supported ITIES tips for scanning electrochemical microscopy of single solid-state nanopores,” *Analytical chemistry,* vol. 89, no. 18, pp. 9946-9952, 2017.

[168] C. Lau, "Perfluorinated compounds," *Molecular, clinical and environmental toxicology*, 101, pp. 47-86, Springer, New York, 2012, DOI: 10.1007/978-3-7643-8340-4_3

[169] S. Liu, R. Yang, N. Yin, and F. Faiola, “The short-chain perfluorinated compounds PFBS, PFHxS, PFBA and PFHxA, disrupt human mesenchymal stem cell self-renewal and adipogenic differentiation,” *Journal of Environmental Sciences,* vol. 88, pp. 187-199, 2020.

[170] N. Marchetti, R. Guzzinati, M. Catani, A. Massi, L. Pasti, and A. Cavazzini, “New insights into perfluorinated adsorbents for analytical and bioanalytical applications,” *Analytical and bioanalytical chemistry,* vol. 407, no. 1, pp. 17-21, 2015.

[171] C. A. Barton, M. A. Botelho, and M. A. Kaiser, "Solid vapor pressure and enthalpy of sublimation for perfluorooctanoic acid," *Journal of Chemical & Engineering Data,* vol. 53, no. 4, pp. 939-941, 2008.

[172] G. Lewandowski, E. Meissner, and E. Milchert, "Special applications of fluorinated organic compounds," *Journal of hazardous materials,* vol. 136, no. 3, pp. 385-391, 2006.

[173] C. A. Moody, J. W. Martin, W. C. Kwan, D. C. Muir, and S. A. Mabury, "Monitoring perfluorinated surfactants in biota and surface water samples following an accidental release of fire-fighting foam into Etobicoke Creek," *Environmental science & technology,* vol. 36, no. 4, pp. 545-551, 2002.

[174] H.-J. Lehmler, "Synthesis of environmentally relevant fluorinated surfactants-a review," *Chemosphere,* vol. 58, no. 11, pp. 1471-1496, 2005/03/01/, 2005.

[175] K. Prevedouros, I. T. Cousins, R. C. Buck, and S. H. Korzeniowski, "Sources, Fate and Transport of Perfluorocarboxylates," *Environmental Science & Technology,* vol. 40, no. 1, pp. 32-44, 2006/01/01, 2006.

[176] P. A. Fair, B. Wolf, N. D. White, S. A. Arnott, K. Kannan, R. Karthikraj, and J. E. Vena, "Perfluoroalkyl substances (PFASs) in edible fish species from Charleston Harbor and tributaries, South Carolina, United States: Exposure and risk assessment," *Environmental research,* vol. 171, pp. 266-277, 2019.

[177] Y. J. Jeong, S. Bang, J. Kim, S. H. Chun, S. Choi, J. Kim, M. S. Chung, G. J. Kang, Y. W. Kang, and J. Kim, "Comparing levels of perfluorinated compounds in processed marine products," *Food and Chemical Toxicology,* vol. 126, pp. 199-210, 2019.

[178] M. C. Huang, A. L. Dzierlenga, V. G. Robinson, S. Waidyanatha, M. J. DeVito, M. A. Eifrid, C. A. Granville, S. T. Gibbs, and C. R. Blystone, "Toxicokinetics of perfluorobutane sulfonate (PFBS), perfluorohexane-1-sulphonic acid (PFHxS), and perfluorooctane sulfonic acid (PFOS) in male and female Hsd:Sprague Dawley SD rats after intravenous and gavage administration," *Toxicology Reports,* vol. 6, pp. 645-655, 2019.

[179] R. C. Buck, "Toxicology data for alternative “short-chain” fluorinated substances," In J. C. DeWitt (Ed.), *Toxicological effects of perfluoroalkyl and polyfluoroalkyl substances,* 2015 (pp. 451-477), Humana Press. https://doi.org/10.1007/978-3-319-15518-0

[180] C. Lau, J. L. Butenhoff, and J. M. Rogers, “The developmental toxicity of perfluoroalkyl acids and their derivatives,” *Toxicology and applied pharmacology,* vol. 198, no. 2, pp. 231-241, 2004.

[181] C. Lau, K. Anitole, C. Hodes, D. Lai, A. Pfahles-Hutchens, and J. Seed, “Perfluoroalkyl acids: a review of monitoring and toxicological findings,” *Toxicological sciences,* vol. 99, no. 2, pp. 366-394, 2007.

[182] S. S. White, A. M. Calafat, Z. Kuklenyik, L. Villanueva, R. D. Zehr, L. Helfant, M. J. Strynar, A. B. Lindstrom, J. R. Thibodeaux, and C. Wood, “Gestational PFOA exposure of mice is associated with altered mammary gland development in dams and female offspring,” *Toxicological Sciences,* vol. 96, no. 1, pp. 133-144, 2007.

[183] B. L. Upham, J.-S. Park, P. Babica, I. Sovadinova, A. M. Rummel, J. E. Trosko, A. Hirose, R. Hasegawa, J. Kanno, and K. Sai, "Structure-activity-dependent regulation of cell communication by perfluorinated fatty acids using in vivo and in vitro model systems," National Institute of Environmental Health Sciences, Vol. 117, No. 4, 2009. https://doi.org/10.1289/ehp.11728

[184] M. Houde, A. O. De Silva, D. C. Muir, and R. J. Letcher, “Monitoring of perfluorinated compounds in aquatic biota: an updated review: PFCs in aquatic biota,” *Environmental science & technology,* vol. 45, no. 19, pp. 7962-7973, 2011.

[185] M. Houde, J. W. Martin, R. J. Letcher, K. R. Solomon, and D. C. Muir, “Biological monitoring of polyfluoroalkyl substances: a review,” *Environmental science & technology,* vol. 40, no. 11, pp. 3463-3473, 2006.

[186] B. F. Scott, C. A. Moody, C. Spencer, J. M. Small, D. C. Muir, and S. A. Mabury, “Analysis for perfluorocarboxylic acids/anions in surface waters and precipitation using GC-MS and analysis of PFOA from large-volume

samples," *Environmental science & technology,* vol. 40, no. 20, pp. 6405-6410, 2006.

[187] F. Xiao, P. C. Sasi, B. Yao, A. Kubátová, S. A. Golovko, M. Y. Golovko, and D. Soli, "Thermal Decomposition of PFAS: Response to Comment on "Thermal Stability and Decomposition of Perfluoroalkyl Substances on Spent Granular Activated Carbon"," *Environmental Science & Technology Letters,* vol. 8, no. 4, pp. 364-365, 2021.

[188] M. Takino, S. Daishima, and T. Nakahara, "Determination of perfluorooctane sulfonate in river water by liquid chromatography/atmospheric pressure photoionization mass spectrometry by automated on-line extraction using turbulent flow chromatography," *Rapid Communications in Mass Spectrometry,* vol. 17, no. 5, pp. 383-390, 2003.

[189] M. Surma, M. Piskuła, W. Wiczkowski, and H. Zieliński, "The perfluoroalkyl carboxylic acids (PFCAs) and perfluoroalkane sulfonates (PFSAs) contamination level in spices," *European Food Research and Technology,* vol. 243, no. 2, pp. 297-307, 2017.

[190] C. Tang, J. Tan, C. Wang, and X. Peng, "Determination of perfluorooctanoic acid and perfluorooctane sulfonate in cooking oil and pig adipose tissue using reversed-phase liquid–liquid extraction followed by high performance liquid chromatography tandem mass spectrometry," *Journal of chromatography A,* vol. 1341, pp. 50-56, 2014.

[191] S. Poothong, S. K. Boontanon, and N. Boontanon, "Determination of perfluorooctane sulfonate and perfluorooctanoic acid in food packaging using liquid chromatography coupled with tandem mass spectrometry," *Journal of hazardous materials,* vol. 205, pp. 139-143, 2012.

[192] P. Giusto, P. Lova, G. Manfredi, S. Gazzo, P. Srinivasan, S. Radice, and D. Comoretto, "Colorimetric detection of perfluorinated compounds by all-polymer photonic transducers," *ACS omega,* vol. 3, no. 7, pp. 7517-7522, 2018.

[193] N. Cennamo, G. D'Agostino, F. Sequeira, F. Mattiello, G. Porto, A. Biasiolo, R. Nogueira, L. Bilro, and L. Zeni, "A simple and low-cost optical fiber

intensity-based configuration for perfluorinated compounds in water solution," *Sensors,* vol. 18, no. 9, pp. 3009, 2018.

[194] T. Takayanagi, H. Yamashita, S. Motomizu, J. Musijowski, and M. Trojanowicz, "Preconcentration and decomposition of perfluorinated carboxylic acids on an activated charcoal cartridge with sodium biphenyl reagent and its determination at μg L-1 level on the basis of flow injection-fluorimetric detection of fluoride ion," *Talanta,* vol. 74, no. 5, pp. 1224-1230, 2008.

[195] M. Liu, G. Zhao, Y. Tang, Z. Yu, Y. Lei, M. Li, Y. Zhang, and D. Li, "A simple, stable and picomole level lead sensor fabricated on DNA-based carbon hybridized TiO_2 nanotube arrays," *Environmental science & technology,* vol. 44, no. 11, pp. 4241-4246, 2010.

[196] G. Hernandez-Vargas, J. E. Sosa-Hernández, S. Saldarriaga-Hernandez, A. M. Villalba-Rodríguez, R. Parra-Saldivar, and H. Iqbal, "Electrochemical biosensors: A solution to pollution detection with reference to environmental contaminants," *Biosensors,* vol. 8, no. 2, pp. 29, 2018.

[197] L. D. Chen, C. Z. Lai, L. P. Granda, M. A. Fierke, D. Mandal, A. Stein, J. A. Gladysz, and P. Bühlmann, "Fluorous membrane ion-selective electrodes for perfluorinated surfactants: Trace-level detection and in situ monitoring of adsorption," *Analytical chemistry,* vol. 85, no. 15, pp. 7471-7477, 2013.

[198] J. Li, H. Feng, J. Cai, L. Yuan, N. Wang, and Q. Cai, "Molecularly imprinted polymer modified TiO_2 nanotube arrays for photoelectrochemical determination of perfluorooctane sulfonate (PFOS)," *Sensors and Actuators B: Chemical,* vol. 190, pp. 745-751, 2014.

[199] P. Jing, P. J. Rodgers, and S. Amemiya, "High lipophilicity of perfluoroalkyl carboxylate and sulfonate: implications for their membrane permeability," *Journal of the American Chemical Society,* vol. 131, no. 6, pp. 2290-2296, 2009.

[200] M. B. Garada, B. Kabagambe, Y. Kim, and S. Amemiya, "Ion-transfer voltammetry of perfluoroalkanesulfonates and perfluoroalkanecarboxylates:

picomolar detection limit and high lipophilicity," *Analytical chemistry,* vol. 86, no. 22, pp. 11230-11237, 2014.

[201] B. N. Viada, L. M. Yudi, and D. Arrigan, "Detection of perfluorooctane sulfonate by ion-transfer stripping voltammetry at an array of microinterfaces between two immiscible electrolyte solutions," *Analyst*, 145**,** 5776-5786, 2020.

[202] Y. Saito, "A theoretical study on the diffusion current at the stationary electrodes of circular and narrow band types," *Review of Polarography,* vol. 15, no. 6, pp. 177-187, 1968.

[203] J. E. Randles, "A cathode ray polarograph. Part II. The current-voltage curves," *Transactions of the Faraday Society,* vol. 44, pp. 327-338, 1948.

[204] C. E. Schaefer, D. M. Drennan, D. N. Tran, R. Garcia, E. Christie, C. P. Higgins, and J. A. Field, "Measurement of aqueous diffusivities for perfluoroalkyl acids," *Journal of Environmental Engineering,* vol. 145, no. 11, pp. 06019006, 2019.

[205] S. Kihara, M. Suzuki, M. Sugiyama, and M. Matsui, "The transfer of carboxylate and sulphonate anions at the aqueous/organic solution interface studied by polarography with the electrolyte solution dropping electrode," *Journal of electroanalytical chemistry and interfacial electrochemistry,* vol. 249, no. 1-2, pp. 109-122, 1988.

[206] J. Beauvais, "Lifetime Health Advisories and Health Effects Support Documents for Perfluorooctanoic Acid and Perfluoroctane Sulfonate In Federal Register," *Federal Register,* vol. 81, pp. 33250-33251, 2016.

[207] A. J. Bard, and L. R. Faulkner, "Fundamentals and applications," *Electrochemical Methods,* vol. 2, no. 482, pp. 580-632, 2001.

[208] S. Thakur, P. Kesharwani, R. K. Tekade, and N. K. Jain, "Impact of pegylation on biopharmaceutical properties of dendrimers," *Polymer,* vol. 59, pp. 67-92, 2015.

[209] P. Kesharwani, R. K. Tekade, and N. K. Jain, "Generation dependent cancer targeting potential of poly (propyleneimine) dendrimer," *Biomaterials,* vol. 35, no. 21, pp. 5539-5548, 2014.

[210] B. Birdhariya, P. Kesharwani, and N. K. Jain, "Effect of surface capping on targeting potential of folate decorated poly (propylene imine) dendrimers," *Drug development and industrial pharmacy,* vol. 41, no. 8, pp. 1393-1399, 2015.

[211] P. Kesharwani, and A. K. Iyer, "Recent advances in dendrimer-based nanovectors for tumor-targeted drug and gene delivery," *Drug discovery today,* vol. 20, no. 5, pp. 536-547, 2015.

[212] D. A. Bosman, H. Janssen, and E. Meijer, "About dendrimers: structure, physical properties, and applications," *Chemical reviews,* vol. 99, no. 7, pp. 1665-1688, 1999.

[213] B. Klajnert, and M. Bryszewska, "Dendrimers: properties and applications," *Acta biochimica polonica,* vol. 48, no. 1, pp. 199-208, 2001.

[214] S. M. Fatemi, S. J. Fatemi, and Z. Abbasi, "PAMAM dendrimer-based macromolecules and their potential applications: recent advances in theoretical studies," *Polymer Bulletin*, pp. 1-21, 2020.

[215] E. Abbasi, S. F. Aval, A. Akbarzadeh, M. Milani, H. T. Nasrabadi, S. W. Joo, Y. Hanifehpour, K. Nejati-Koshki, and R. Pashaei-Asl, "Dendrimers: synthesis, applications, and properties," *Nanoscale research letters,* vol. 9, no. 1, pp. 1-10, 2014.

[216] B. Klajnert, L. Stanisławska, M. Bryszewska, and B. Pałecz, "Interactions between PAMAM dendrimers and bovine serum albumin," *Biochimica et Biophysica Acta (BBA)-Proteins and Proteomics,* vol. 1648, no. 1-2, pp. 115-126, 2003.

[217] P. K. Maiti, T. Çağın, G. Wang, and W. A. Goddard, "Structure of PAMAM dendrimers: Generations 1 through 11," *Macromolecules,* vol. 37, no. 16, pp. 6236-6254, 2004.

[218] F. Vögtle, G. Richardt, and N. Werner, *Dendrimer chemistry: concepts, syntheses, properties, applications*: Wiley-CVH Gmbh & Co, 2009.

[219] N. T. Pourianazar, P. Mutlu, and U. Gunduz, "Bioapplications of poly (amidoamine)(PAMAM) dendrimers in nanomedicine," *Journal of Nanoparticle Research,* vol. 16, no. 4, pp. 2342, 2014.

[220] K. Gardikis, M. Micha-Screttas, C. Demetzos, and B. R Steele, "Dendrimers and the development of new complex nanomaterials for biomedical applications," *Current medicinal chemistry,* vol. 19, no. 29, pp. 4913-4928, 2012.

[221] K. Bezouška, "Design, functional evaluation and biomedical applications of carbohydrate dendrimers (glycodendrimers)," *Reviews in Molecular Biotechnology,* vol. 90, no. 3-4, pp. 269-290, 2002.

[222] S. D. Konda, M. Aref, S. Wang, M. Brechbiel, and E. C. Wiener, "Specific targeting of folate-dendrimer MRI contrast agents to the high affinity folate receptor expressed in ovarian tumor xenografts," *Magnetic resonance materials in physics, Biology and Medicine,* vol. 12, no. 2-3, pp. 104-113, 2001.

[223] E. Markatou, V. Gionis, G. D. Chryssikos, S. Hatziantoniou, A. Georgopoulos, and C. Demetzos, "Molecular interactions between dimethoxycurcumin and Pamam dendrimer carriers," *International journal of pharmaceutics,* vol. 339, no. 1-2, pp. 231-236, 2007.

[224] S. Choudhary, L. Gupta, S. Rani, K. Dave, and U. Gupta, "Impact of dendrimers on solubility of hydrophobic drug molecules," *Frontiers in pharmacology,* vol. 8, pp. 261, 2017.

[225] G. A. Pilkington, J. S. Pedersen, and W. H. Briscoe, "Dendrimer nanofluids in the concentrated regime: from polymer melts to soft spheres," *Langmuir,* vol. 31, no. 11, pp. 3333-3342, 2015.

[226] L. J. Twyman, A. E. Beezer, R. Esfand, M. J. Hardy, and J. C. Mitchell, "The synthesis of water soluble dendrimers, and their application as possible drug delivery systems," *Tetrahedron Letters,* vol. 40, no. 9, pp. 1743-1746, 1999.

[227] D. Shcharbin, M. Bryszewska, S. Mignani, X. Shi, and J. P. Majoral, "Phosphorus dendrimers as powerful nanoplatforms for drug delivery, as fluorescent probes and for liposome interaction studies: A concise overview," *European Journal of Medicinal Chemistry*, pp. 112788, 2020.

[228] G. S. Yu, Y. M. Bae, H. Choi, B. Kong, I. S. Choi, and J. S. Choi, "Synthesis of PAMAM dendrimer derivatives with enhanced buffering capacity and remarkable gene transfection efficiency," *Bioconjugate chemistry,* vol. 22, no. 6, pp. 1046-1055, 2011.

[229] D. Luong, P. Kesharwani, R. Deshmukh, M. C. I. M. Amin, U. Gupta, K. Greish, and A. K. Iyer, "PEGylated PAMAM dendrimers: enhancing efficacy and mitigating toxicity for effective anticancer drug and gene delivery," *Acta biomaterialia,* vol. 43, pp. 14-29, 2016.

[230] J. D. Eichman, A. U. Bielinska, J. F. Kukowska-Latallo, and J. R. Baker Jr, "The use of PAMAM dendrimers in the efficient transfer of genetic material into cells," *Pharmaceutical science & technology today,* vol. 3, no. 7, pp. 232-245, 2000.

[231] J. van Haasteren, S. C. Hyde, and D. R. Gill, "Lessons learned from lung and liver in-vivo gene therapy: implications for the future," *Expert opinion on biological therapy,* vol. 18, no. 9, pp. 959-972, 2018.

[232] L. J. Fox, R. M. Richardson, and W. H. Briscoe, "PAMAM dendrimer-cell membrane interactions," *Advances in Colloid and Interface Science,* vol. 257, pp. 1-18, 2018.

[233] P. Kesharwani, S. Banerjee, U. Gupta, M. C. I. M. Amin, S. Padhye, F. H. Sarkar, and A. K. Iyer, "PAMAM dendrimers as promising nanocarriers for RNAi therapeutics," *Materials Today,* vol. 18, no. 10, pp. 565-572, 2015.

[234] G. M. Pavan, P. Posocco, A. Tagliabue, M. Maly, A. Malek, A. Danani, E. Ragg, C. V. Catapano, and S. Pricl, "PAMAM dendrimers for siRNA delivery: computational and experimental insights," *Chemistry-A European Journal,* vol. 16, no. 26, pp. 7781-7795, 2010.

[235] J. Li, S. Xue, and Z. W. Mao, "Nanoparticle delivery systems for siRNA-based therapeutics," *Journal of Materials Chemistry B,* vol. 4, no. 41, pp. 6620-6639, 2016.

[236] S. Sheikh, M. A. Nasseri, M. Chahkandi, A. Allahresani, and O. Reiser, "Functionalized magnetic PAMAM dendrimer as an efficient nanocatalyst for new synthesis strategy of xanthene pigments," *Journal of Hazardous Materials*, pp. 122985, 2020.

[237] Y. Liao, J. Gao, Y. Zhang, Y. Zhou, R. Yuan, and W. Xu, "Proximity ligation-responsive catalytic hairpin assembly-guided DNA dendrimers for synergistically amplified electrochemical biosensing," *Sensors and Actuators B: Chemical,* vol. 322, pp. 128566, 2020.

[238] M. Zhang, H. Yang, S. Wang, W. Zhang, Q. Hou, D. Guo, F. Liu, T. Chen, X. Wu, and J. Wang, "PAMAM Based Dendrimers with Different Alkyl Chains Self-Assemble on Silica Surfaces: Controllable Layer Structure and Molecular Aggregation," *The Journal of Physical Chemistry B,* vol. 122, no. 25, pp. 6648-6655, 2018.

[239] K. R. Raghupathi, J. Guo, O. Munkhbat, P. Rangadurai, and S. Thayumanavan, "Supramolecular disassembly of facially amphiphilic dendrimer assemblies in response to physical, chemical, and biological stimuli," *Accounts of chemical research,* vol. 47, no. 7, pp. 2200-2211, 2014.

[240] K. Inoue, "Functional dendrimers, hyperbranched and star polymers," *Progress in Polymer Science,* vol. 25, no. 4, pp. 453-571, 2000/05/01/, 2000.

[241] M. P. G. Armada, J. Losada, M. Zamora, B. Alonso, I. Cuadrado, and C. M. Casado, "Electrocatalytical properties of polymethylferrocenyl dendrimers and their applications in biosensing," *Bioelectrochemistry,* vol. 69, no. 1, pp. 65-73, 2006.

[242] J. M. Frechet, and D. A. Tomalia (eds.), “Dendrimers and other dendritic polymers, ” *John Wiley & Sons*, Chichester, New York, USA, 2001.

[243] D. A. Tomalia, H. Baker, J. Dewald, M. Hall, G. Kallos, S. Martin, J. Roeck, J. Ryder, and P. Smith, “A new class of polymers: starburst-dendritic macromolecules,” *Polymer journal,* vol. 17, no. 1, pp. 117-132, 1985.

[244] D. Cakara, J. Kleimann, and M. Borkovec, “Microscopic protonation equilibria of poly (amidoamine) dendrimers from macroscopic titrations,” *Macromolecules,* vol. 36, no. 11, pp. 4201-4207, 2003.

[245] Y. Niu, L. Sun, and R. M. Crooks, “Determination of the intrinsic proton binding constants for poly (amidoamine) dendrimers via potentiometric pH titration,” *Macromolecules,* vol. 36, no. 15, pp. 5725-5731, 2003.

[246] S. O'Sullivan, E. A. de Eulate, Y. H. Yuen, E. Helmerhorst, and D. W. Arrigan, “Stripping voltammetric detection of insulin at liquid/liquid microinterfaces in the presence of bovine albumin,” *Analyst,* vol. 138, no. 20, pp. 6192-6196, 2013.

[247] G. Herzog, V. Kam, and D. W. Arrigan, “Electrochemical behaviour of haemoglobin at the liquid/liquid interface,” *Electrochimica acta,* vol. 53, no. 24, pp. 7204-7209, 2008.

[248] Y. Imai, T. Sugihara, and T. Osakai, “Electron transfer mechanism of cytochrome c at the oil/water interface as a biomembrane model,” *The Journal of Physical Chemistry B,* vol. 116, no. 1, pp. 585-592, 2012.

[249] E. Alvarez de Eulate, S. O'Sullivan, and D. W. Arrigan, “Electrochemically induced formation of cytochrome c oligomers at soft interfaces,” *ChemElectroChem,* vol. 4, no. 4, pp. 898-904, 2017.

[250] A. Berduque, M. D. Scanlon, C. J. Collins, and D. W. Arrigan, “Electrochemistry of non-redox-active poly (propylenimine) and poly (amidoamine) dendrimers at liquid/liquid interfaces,” *Langmuir,* vol. 23, no. 13, pp. 7356-7364, 2007.

[251] H. Nagatani, T. Ueno, and T. Sagara, “Spectroelectrochemical analysis of ion-transfer and adsorption of the PAMAM dendrimer at a polarized liquid/liquid interface,” *Electrochimica acta,* vol. 53, no. 22, pp. 6428-6433, 2008.

[252] M. Calderon, L. M. Monzón, M. Martinelli, A. V. Juarez, M. C. Strumia, and L. M. Yudi, “Electrochemical study of a dendritic family at the water/1, 2-dichloroethane interface,” *Langmuir,* vol. 24, no. 12, pp. 6343-6350, 2008.

[253] G. Herzog, S. Flynn, C. Johnson, and D. W. Arrigan, “Electroanalytical behavior of poly-l-lysine dendrigrafts at the interface between two immiscible electrolyte solutions,” *Analytical chemistry,* vol. 84, no. 13, pp. 5693-5699, 2012.

[254] L. Poltorak, K. Morakchi, G. Herzog, and A. Walcarius, “Electrochemical characterization of liquid/liquid micro-interfaces modified with mesoporous silica,” *Electrochimica Acta,* vol. 179, pp. 9-15, 2015.

[255] M. Li, P. He, Z. Yu, S. Zhang, C. Gu, X. Nie, Y. Gu, X. Zhang, Z. Zhu, and Y. Shao, “Investigation of Dendrimer Transfer Behaviors at the Micro-Water/1, 2-Dichloroethane Interface Facilitated by Dibenzo-18-Crown-6,” *Analytical Chemistry,* vol. 93, no. 3, pp. 1515-1522, 2020.

[256] P. K. Maiti, T. Çağın, S. T. Lin, and W. A. Goddard, “Effect of solvent and pH on the structure of PAMAM dendrimers,” *Macromolecules,* vol. 38, no. 3, pp. 979-991, 2005.

[257] P. J. Rodgers, and S. Amemiya, “Cyclic voltammetry at micropipet electrodes for the study of ion-transfer kinetics at liquid/liquid interfaces,” *Analytical chemistry,* vol. 79, no. 24, pp. 9276-9285, 2007.

[258] V. A. Jiménez, J. A. Gavín, and J. B. Alderete, “Scaling trend in diffusion coefficients of low generation G0-G3 PAMAM dendrimers in aqueous solution at high and neutral pH,” *Structural Chemistry,* vol. 23, no. 1, pp. 123-128, 2012.

[259] N. Štambuk-Giljanović, “The quality of water resources in Dalmatia,” *Environmental monitoring and assessment,* vol. 104, pp. 235-268, 2005.

[260] M. Shakirullah, I. Ahmad, K. Mehmood, A. Khan, H. Rehman, S. Alam, and A. Shah, "Physicochemical study of drinking water from Dir districts," *Journal-Chemical Society of Pakistan,* vol. 27, no. 4, pp. 374, 2005.

[261] P. D. Beer, and P. A. Gale, "Anion Recognition and Sensing: The State of the Art and Future Perspectives," *Angewandte Chemie International Edition,* vol. 40, no. 3, pp. 486-516, 2001.

[262] T. Nakanishi, Y. Otaki, Y. Hasuike, M. Nanami, R. Itahana, K. Miyagawa, H. Nishikage, M. Izumi, and Y. Takamitsu, "Association of hyperhomocysteinemia with plasma sulfate and urine sulfate excretion in patients with progressive renal disease," *American Journal of Kidney Diseases,* vol. 40, no. 5, pp. 909-915, 2002.

[263] E. L. C. Silveira, L. B. de Caland, and M. Tubino, "Simultaneous quantitative analysis of the acetate, formate, chloride, phosphate and sulfate anions in biodiesel by ion chromatography," *Fuel,* vol. 124, pp. 97-101, 2014/05/15/, 2014.

[264] P. Gołębiewski, B. Puciłowski, F. Sommer, S. Kubik, M. Daniels, W. Dehaen, U. Sivasankaran, K. G. Kumar, H. Radecka, and J. Radecki, "Electrochemical sensing of sulfate in aqueous solution with a cyclopeptide-dipyrromethene-Cu(II) or Co(II) complex attached to a gold electrode," *Sensors and Actuators B: Chemical,* vol. 285, pp. 536-545, 2019/04/15/, 2019.

[265] D. W. Smith, "Ionic hydration enthalpies," *Journal of Chemical Education,* vol. 54, no. 9, pp. 540, 1977.

[266] P. Kubáň, P. Kubáň, and V. Kubáň, "Flow injection-capillary electrophoresis system with contactless conductivity detection and hydrostatic pressure generated flow. Application to the quantitative analysis of inorganic anions in water samples," *Electrophoresis,* vol. 24, no. 12-13, pp. 1935-1943, 2003.

[267] P. Kosobucki, and B. Buszewski, "Application of isotachophoresis for quality control of drinking and mineral waters," *Journal of liquid chromatography & related technologies,* vol. 29, no. 13, pp. 1951-1960, 2006.

[268] C. Park, and H. Simmons, “Macrobicyclic amines. III. Encapsulation of halide ions by in, in-1,(k+ 2)-diazabicyclo [klm] alkane ammonium ions,” *Journal of the American Chemical Society,* vol. 90, no. 9, pp. 2431-2432, 1968.

[269] D. Shriver, and M. Biallas, “Observation of the chelate effect with a bidentate Lewis acid, $F_2BCH_2CH_2BF_2$,” *Journal of the American Chemical Society,* vol. 89, no. 5, pp. 1078-1081, 1967.

[270] T. K. Ghorpade, M. Patri, and S. P. Mishra, “Highly sensitive colorimetric and fluorometric anion sensors based on mono and di-calix[4]pyrrole substituted diketopyrrolopyrroles,” *Sensors and Actuators B: Chemical,* vol. 225, pp. 428-435, 2016/03/31/, 2016.

[271] B. Sen, M. Mukherjee, S. Pal, S. Sen, and P. Chattopadhyay, “A water soluble copper (II) complex as a HSO^{4-} ion selective turn-on fluorescent sensor applicable in living cell imaging,” *RSC Advances,* vol. 5, no. 62, pp. 50532-50539, 2015.

[272] J. Singh, M. Yadav, A. Singh, and N. Singh, “Zinc metal complex as a sensor for simultaneous detection of fluoride and HSO^{4-} ions,” *Dalton Transactions,* vol. 44, no. 28, pp. 12589-12597, 2015.

[273] D. Zhao, C. Chen, L. Lu, F. Yang, and X. Yang, “A label-free colorimetric sensor for sulfate based on the inhibition of peroxidase-like activity of cysteamine-modified gold nanoparticles,” *Sensors and Actuators B: Chemical,* vol. 215, pp. 437-444, 2015/08/01/, 2015.

[274] T. Guinovart, P. Blondeau, and F. J. Andrade, “Sulphate-selective optical microsensors: overcoming the hydration energy penalty,” *Chemical Communications,* vol. 51, no. 52, pp. 10377-10380, 2015.

[275] M. McDonnell, and P. Vadgama, “Membranes-Separation Principles and Sensing,” *Selective electrode reviews,* vol. 11, no. 1, pp. 17-67, 1989.

[276] P. Bühlmann, E. Pretsch, and E. Bakker, “Carrier-based ion-selective electrodes and bulk optodes. 2. Ionophores for potentiometric and optical sensors,” *Chemical Reviews,* vol. 98, no. 4, pp. 1593-1688, 1998.

[277] M. Fibbioli, M. Berger, F. P. Schmidtchen, and E. Pretsch, "Polymeric membrane electrodes for monohydrogen phosphate and sulfate," *Analytical Chemistry,* vol. 72, no. 1, pp. 156-160, 2000.

[278] P. D. Beer, J. Cadman, J. M. Lloris, R. Martínez-Máñez, M. E. Padilla, T. Pardo, D. K. Smith, and J. Soto, "Selective electrochemical recognition of sulfate over phosphate and phosphate over sulfate using polyaza ferrocene macrocyclic receptors in aqueous solution," *Journal of the Chemical Society, Dalton Transactions*, no. 2, pp. 127-134, 1999.

[279] C. Coll, R. H. Labrador, R. M. Mañez, J. Soto, F. Sancenón, M. J. Seguí, and E. Sanchez, "Ionic liquids promote selective responses towards the highly hydrophilic anion sulfate in PVC membrane ion-selective electrodes," *Chemical Communications*, no. 24, pp. 3033-3035, 2005.

[280] M. J. Berrocal, A. Cruz, I. H. A. Badr, and L. G. Bachas, "Tripodal ionophore with sulfate recognition properties for anion-selective electrodes," *Analytical Chemistry,* vol. 72, no. 21, pp. 5295-5299, 2000.

[281] S. Firouzabadi, I. Razavipanah, R. Zhiani, M. Ghanei-Motlagh, and M. R. Salavati, "Sulfate-selective electrode based on a bis-thiourea ionophore," *Monatshefte für Chemie-Chemical Monthly,* vol. 144, no. 2, pp. 113-120, 2013.

[282] S. Nishizawa, P. Bühlmann, K. P. Xiao, and Y. Umezawa, "Application of a bis-thiourea ionophore for an anion selective electrode with a remarkable sulfate selectivity," *Analytica Chimica Acta,* vol. 358, no. 1, pp. 35-44, 1998/01/20/, 1998.

[283] Y. Liu, Y. Qin, and D. Jiang, "Squaramide-based tripodal ionophores for potentiometric sulfate-selective sensors with high selectivity," *Analyst,* vol. 140, no. 15, pp. 5317-5323, 2015.

[284] R. B. Elmes, K. K. Y. Yuen, and K. A. Jolliffe, "Sulfate-Selective Recognition by Using Neutral Dipeptide Anion Receptors in Aqueous Solution," *Chemistry-A European Journal,* vol. 20, no. 24, pp. 7373-7380, 2014.

[285] F. Kivlehan, W. J. Mace, H. A. Moynihan, and D. W. M. Arrigan, "Potentiometric evaluation of calix[4]arene anion receptors in membrane electrodes: Phosphate detection," *Analytica Chimica Acta,* vol. 585, no. 1, pp. 154-160, 2007/02/28/, 2007.

[286] S. Nishizawa, T. Yokobori, R. Kato, K. Yoshimoto, T. Kamaishi, and N. Teramae, "Hydrogen-bond forming ionophore for highly efficient transport of phosphate anions across the nitrobenzene-water interface," *Analyst,* vol. 128, no. 6, pp. 663-669, 2003.

[287] T. Shioya, S. Nishizawa, and N. Teramae, "Anion recognition at the liquid/liquid interface. Sulfate transfer across the 1,2-dichloroethane/water interface facilitated by hydrogen- bonding ionophores," *Journal of the American Chemical Society,* vol. 120, no. 44, pp. 11534-11535, 1998.

[288] R. A. W. Dryfe, S. S. Hill, A. P. Davis, J. B. Joos, and E. P. L. Roberts, "Electrochemical quantification of high-affinity halide binding by a steroid-based receptor," *Organic and Biomolecular Chemistry,* vol. 2, no. 19, pp. 2716-2718, 2004.

[289] E. A. de Eulate, F. Busetti, and D. W. M. Arrigan, "Evaluation of interfacial sulfate complexation by a bis-thiourea ionophore at water-organic interfaces using microelectrochemistry and high resolution mass spectrometry," *Microchemical Journal,* vol. 131, pp. 36-42, 2017.

[290] T. Shioya, S. Nishizawa, and N. Teramae, "Anion Recognition at the Liquid/Liquid Interface. Sulfate Transfer across the 1,2-Dichloroethane/ Water Interface Facilitated by Hydrogen-Bonding Ionophores," *Journal of the American Chemical Society,* vol. 120, no. 44, pp. 11534-11535, 1998/11/01, 1998.

[291] O. Valent, J. Koryta, and M. Panoch, "Voltammetric study of ion transfer across the water/o-nitrophenyloctyl ether interface: Part I. Reversible process," *Journal of Electroanalytical Chemistry and Interfacial Electrochemistry,* vol. 226, no. 1, pp. 21-25, 1987/07/10/, 1987.

[292] A. Bard, and L. Faulkner, "Electrochemical Methods: Fundamental and Applications," 2nd Edition, Wiley & Sons Inc, *New York, capitulo,* vol. 5, 2001.

[293] J. M. Savéant, "Elements of molecular and biomolecular electrochemistry: an electrochemical approach to electron transfer chemistry, " *John Wiley & Sons*, Hoboken, NJ, 2006.

[294] N. Elgrishi, K. J. Rountree, B. D. McCarthy, E. S. Rountree, T. T. Eisenhart, and J. L. Dempsey, "A Practical Beginner's Guide to Cyclic Voltammetry," *Journal of Chemical Education,* vol. 95, no. 2, pp. 197-206, 2018/02/13, 2018.

[295] M. I. Prodromidis, A. B. Florou, S. M. Tzouwara-Karayanni, and M. I. Karayannis, "The importance of surface coverage in the electrochemical study of chemically modified electrodes," *Electroanalysis,* vol. 12, no. 18, pp. 1498-1501, 2000.

[296] T. J. Duffin, N. Nerngchamnong, D. Thompson, and C. A. Nijhuis, "Direct measurement of the local field within alkyl-ferrocenyl-alkanethiolate monolayers: Importance of the supramolecular and electronic structure on the voltammetric response and potential profile," *Electrochimica Acta,* vol. 311, pp. 92-102, 2019.

[297] R. J. Forster, "Kinetic separation of amperometric sensor responses," *Analyst,* vol. 121, no. 6, pp. 733-741, 1996.

[298] A. L. Eckermann, D. J. Feld, J. A. Shaw, and T. J. Meade, "Electrochemistry of redox-active self-assembled monolayers," *Coordination chemistry reviews,* vol. 254, no. 15-16, pp. 1769-1802, 2010.

[299] A. Itodo, H. Itodo, and M. Gafar, "Estimation of specific surface area using Langmuir isotherm method," *Journal of Applied Sciences and Environmental Management,* vol. 14, no. 4, 2010.

[300] V. S. Markin, M. I. Volkova-Gugeshashvili, and A. G. Volkov, "Adsorption at liquid interfaces: the generalized Langmuir isotherm and interfacial structure," *The Journal of Physical Chemistry B,* vol. 110, no. 23, pp. 11415-11420, 2006.

[301] I. Langmuir, “The adsorption of gases on plane surfaces of glass, mica and platinum,” *Journal of the American Chemical society,* vol. 40, no. 9, pp. 1361-1403, 1918.

[302] E. Laviron, “Electroanalytical chemistry,” *Bard AJ (ed),* vol. 12, pp. 53-151, 1982.

[303] Y. Bayrak, “Application of Langmuir isotherm to saturated fatty acid adsorption,” *Microporous and Mesoporous Materials,* vol. 87, no. 3, pp. 203-206, 2006/01/09/, 2006.

[304] Y. Yoshida, K. Maeda, and O. Shirai, “The complex formation of ions with a phospholipid monolayer adsorbed at an aqueous/1,2-dichloroethane interface,” *Journal of Electroanalytical Chemistry,* vol. 578, no. 1, pp. 17-24, 2005/04/15/, 2005.

[305] J. Li, R. Miller, and H. Möhwald, “Characterisation of phospholipid layers at liquid interfaces. 1. Dynamics of adsorption of phospholipids at the chloroform/water interface,” *Colloids and Surfaces A: Physicochemical and Engineering Aspects,* vol. 114, pp. 113-121, 1996/08/20/, 1996.

[306] F. Reymond, and H. H. Girault, “Electrochemistry at Liquid/liquid interfaces,” *Encyclopedia of Analytical Chemistry:* John Wiley & Sons: Hoboken, 2006.

[307] M. M. Hossain, H. H. Girault, and H. J. Lee, “Voltammetric studies of anion transfer reactions across a microhole array-water/PVC-NPOE gel interface,” *Bulletin of the Korean Chemical Society,* vol. 33, no. 5, pp. 1734-1740, 2012.

[308] L. A. Chrisstoffels, F. de Jong, and D. N. Reinhoudt, “Facilitated transport of salts by neutral anion carriers,” *Chemistry-A European Journal,* vol. 6, no. 8, pp. 1376-1385, 2000.

[309] Y. Marcus, “Thermodynamics of solvation of ions. Part 5. Gibbs free energy of hydration at 298.15 K,” *Journal of the Chemical Society, Faraday Transactions,* vol. 87, no. 18, pp. 2995-2999, 1991.

[310] E. Thormann, “On understanding of the Hofmeister effect: how addition of salt alters the stability of temperature responsive polymers in aqueous solutions,” *Rsc Advances,* vol. 2, no. 22, pp. 8297-8305, 2012.

[311] C. S. Brooks, “Recovery of nonferrous metals from metal finishing industry wastes,” *Separation science and technology,* vol. 28, no. 1-3, pp. 579-593, 1993.

[312] M. Ismael, and C. Tondre, “Transition metal complexes with 8-hydroxyquinoline and Kelex 100 in micellar systems. Stoichiometry of the complexes and kinetics of dissociation in acid media,” *Separation science and technology,* vol. 29, no. 5, pp. 651-662, 1994.

[313] J. D. S. Benedetto, M. L. D. L. Soares, I. Grewal, and D. B. Dreisinger, “Recovery of rare metals with a new organophosphorus extractant,” *Separation science and technology,* vol. 30, no. 17, pp. 3339-3349, 1995.

[314] H. Matsuyama, Y. Miyamoto, M. Teramoto, M. Goto, and F. Nakashio, “Selective separation of rare earth metals by solvent extraction in the presence of new hydrophilic chelating polymers functionalized with ethylenediaminetetraacetic acid. I. Development of new hydrophilic chelating polymers and their adsorption properties for rare earth metals,” *Separation science and technology,* vol. 31, no. 5, pp. 687-704, 1996.

[315] I. Bustero, Y. Cheng, J. C. Mugica, T. Fernández-Otero, A. F. Silva, and D. J. Schiffrin, “Electro-assisted solvent extraction of Cu^{2+}, Ni^{2+} and Cd^{2+},” *Electrochimica acta,* vol. 44, no. 1, pp. 29-38, 1998.

[316] Y. Cheng, and D. J. Schiffrin, “A study of 2-heptanone and 2-octanone as solvents for two-phase electrochemistry: Part 2. Facilitated ion transfers,” *Journal of Electroanalytical Chemistry,* vol. 429, no. 1-2, pp. 37-45, 1997.

[317] H. Alemu, B. Hundhammer, and T. Solomon, “Transfer of transition metal-terpyridine complexes across the water/nitrobenzene interface,” *Journal of electroanalytical chemistry and interfacial electrochemistry,* vol. 294, no. 1-2, pp. 165-177, 1990.

[318] V. Sridhar, and J. Verma, “Extraction of copper, nickel and cobalt from the leach liquor of manganese-bearing sea nodules using LIX 984N and ACORGA M5640,” *Minerals Engineering,* vol. 24, no. 8, pp. 959-962, 2011.

[319] F. J. Alguacil, F. Lopez, and I. García-Díaz, “Copper removal from acidic wastewaters using 2-hydroxy-5-nonylbenzaldehyde oxime as ionophore in pseudo-emulsion membrane with strip dispersion (PEMSD) technology,” *Journal of Industrial and Engineering Chemistry,* vol. 18, no. 1, pp. 255-259, 2012.

[320] R. Yang, S. Wang, H. Duan, X. Yuan, Z. Huang, H. Guo, and X. Yang, “Efficient separation of copper and nickel from ammonium chloride solutions through the antagonistic effect of TRPO on Acorga M5640,” *Hydrometallurgy,* vol. 163, pp. 18-23, 2016.

[321] L. Wang, Q. Li, X. Sun, and L. Wang, “Separation and recovery of copper from waste printed circuit boards leach solution using solvent extraction with Acorga M5640 as extractant,” *Separation Science and Technology,* vol. 54, no. 8, pp. 1302-1311, 2019.

[322] J. Vander Linden, and R. De Ketelaere, “Selective recuperation of copper by supported liquid membrane (SLM) extraction,” *Journal of membrane science,* vol. 139, no. 1, pp. 125-135, 1998.

[323] S. Agarwal, M. T. A. Reis, M. R. C. Ismael, M. J. N. Correia, and J. M. Carvalho, “Modeling of the extraction equilibrium of copper from sulfate solutions with Acorga M5640,” *Solvent Extraction and Ion Exchange,* vol. 30, no. 5, pp. 536-551, 2012.

[324] S. Agarwal, A. E. Ferreira, S. M. Santos, M. T. A. Reis, M. R. C. Ismael, M. J. N. Correia, and J. M. Carvalho, “Separation and recovery of copper from zinc leach liquor by solvent extraction using Acorga M5640,” *International Journal of Mineral Processing,* vol. 97, no. 1-4, pp. 85-91, 2010.